DESIGN AND STRUCTURAL CHARACTERIZATION OF MONOMETALLIC AND BIMETALLIC CLUSTERS FOR SELECTIVE HETEROGENEOUS CATALYSIS

A Thesis Submitted to the
College of Graduate and Postdoctoral Studies
In Partial Fulfillment of the Requirements
For the Degree of Doctor of Philosophy
In the Department of Chemistry
University of Saskatchewan
Saskatoon

By

KAZEEM OLUDARE SULAIMAN

PERMISSION TO USE

In presenting this thesis/dissertation in partial fulfillment of the requirements for a Postgraduate degree from the University of Saskatchewan, I agree that the Libraries of this University may make it freely available for inspection. I further agree that permission for copying of this thesis/dissertation in any manner, in whole or in part, for scholarly purposes may be granted by the professor or professors who supervised my thesis/dissertation work or, in their absence, by the Head of the Department or the Dean of the College in which my thesis work was done. It is understood that any copying or publication or use of this thesis/dissertation or parts thereof for financial gain shall not be allowed without my written permission. It is also understood that due recognition shall be given to me and to the University of Saskatchewan in any scholarly use which may be made of any material in my thesis/dissertation.

DISCLAIMER

Reference in this thesis/dissertation to any specific commercial products, process, or service by trade name, trademark, manufacturer, or otherwise, does not constitute or imply its endorsement, recommendation, or favoring by the University of Saskatchewan. The views and opinions of the author expressed herein do not state or reflect those of the University of Saskatchewan, and shall not be used for advertising or product endorsement purposes.

Requests for permission to copy or to make other uses of materials in this thesis/dissertation in whole or part should be addressed to:

Head of the Department of Chemistry
Thorvaldson Building, 110 Science Place
University of Saskatchewan
Saskatoon, Saskatchewan S7N 5C9 Canada

OR

Dean
College of Graduate and Postdoctoral Studies
University of Saskatchewan
116 Thorvaldson Building, 110 Science Place
Saskatoon, Saskatchewan S7N 5C9 Canada

ABSTRACT

The development of catalysts for industrial use can take advantage of the design of clusters with a more abundant and relatively less expensive metal (i.e. silver (Ag)) rather than gold (Au)). Atom-precise $Ag_{25}(SR)_{18}^-$ clusters are attractive as they have a similar structure to the Au analogue, $Au_{25}(SR)_{18}^-$, which has been well studied in the literature. This thesis documents the rational synthesis and structural characterization of Ag monometallic and silver-palladium (AgPd) bimetallic clusters for use as selective oxidation and hydrogenation catalysts. Clusters were synthesized and purified via solution-based synthetic strategies, followed by deposition of the clusters onto carbon supports. Atom-precise $Ag_{25}(SPhMe_2)_{18}^-$ clusters on carbon supports were activated at a mild temperature of 250 °C without the formation of Ag_2O or Ag_2S, albeit with a slight growth in cluster size. A sequential deposition (SD) strategy towards the rational synthesis of supported-bimetallic clusters catalysts based on atom-precise monometallic Ag cluster precursors was investigated and contrasted with a direct synthesis approach. The SD approach resulted in AgPd bimetallic catalysts with cluster-in-cluster atomic arrangements and could incorporate variable amounts of dopant Pd atoms. In contrast, the direct synthesis approach predominantly formed atom-precise $Ag_{24}Pd_1(SPhMe_2)_{18}^{2-}$ bimetallic clusters with the single Pd dopant occupying a non-central position in the clusters. These bimetallic clusters were used as model catalysts to reveal the correlation between catalyst performance and their structures. The isolation of active Pd sites suppressed the over-hydrogenation of alkynols to alkanols by Pd catalysts and the AgPd bimetallic catalysts prepared by both methods were selective for intermediate hydrogenation products. Electron microscopy and X-ray spectroscopy were found to be good characterization tools to elucidate structures of the synthesized Ag-based clusters before and after activation for catalysis. Pair distribution function (PDF) analyses based on total scattering data also allowed insight into the structural changes that occur during the thermal activation process. Furthermore, differential PDF analysis clearly shows the structural transformation of atom-precise Ag and Au clusters to nanoparticles with bulk fcc-like structures at intermediate temperatures, while the Ag system behaves significantly differently than the analogous Au system at high temperatures.

ACKNOWLEDGEMENTS

All praise is due to the Almighty God for giving me sound health, knowledge, perseverance, and patience to successfully navigate this challenging phase of my academic pursuit. Special thanks to my supervisor Dr. Robert Scott for his timely advice, passionate guidance, inspiring encouragement, and kind understanding during my Ph.D. program. I am very grateful to Dr. Matthew Paige, Dr. Stephen Foley, and Dr. Gap Soo Chang for their valuable suggestions to my research work. I thank Dr. Andrew Grosvenor, Dr. Richard Bowles, and Dr. David Sanders for attending meetings to discuss my research progress. I also thank Dr. Timothy Kelly, Dr. Randy Purves, and Dr. Eric Price for giving me access to their research laboratories when needed most. I am beholden to the University of Saskatchewan and the Department of Chemistry for giving the golden opportunity to complete my Ph.D. program. The teaching guidance, support, and feedback that I received from my laboratory managers: Dr. Alexandra Bartole-Scott, Dr. Valerie MacKenzie, and Dr. Adrian Clark, deserve my deepest gratitude. I appreciate timely responses and professional handlings of my requests by administrative and stores staff: Amber Bornhorst, Erin Wasylow, Bonita Wong, Leah Hildebrandt, and Linda Duxbury. I am also indebted to other faculty members and my colleague in the graduate program, especially past and present members of Scott Research Group, for upholding conducive environment for learning and research in the University. I acknowledge financial assistance from the National Sciences and Engineering Research Council of Canada (NSERC) through Discovery grant awarded to Dr. Scott. I also thank beamline (BXDS-WHE, BioXAS, HXMA, and SXRMB) scientists and their associates at Canadian Light Source, for their assistance while using synchrotron facilities for my research work. I sincerely acknowledge the cheerful moments I experienced with receiving several travel awards, especially the prestigious Kokes award, special Graduate Teaching Fellowship, and Dr. O. Kenneth Johannson Scholarship. I am grateful to all that found me worthy of receiving these awards and scholarships. I also acknowledge the facilitators of the 4th US School on Total Scattering for providing hands-on training with total scattering analysis software. Beyond academics, I appreciate all kinds of support I received from family and friends, too numerous to mention, both at the motherland and in diasporas. Finally, my heartfelt gratitude goes to my immediate family members (Ubaidah, Fawzan, and Roheemah) for their kind understanding, fervent encouragement, and unflinching support. You are all indispensable components of whatever I can refer to as my academic achievements. Thank you all!

DEDICATION

To the glory of God,
to those who encourage and support me, and
to the benefit of humanity for the love of foundational science.

TABLE OF CONTENTS

LIST OF TABLES

LIST OF FIGURES

LIST OF ABBREVIATIONS

11-MUA	11-Mercaptoundecanoic Acid
BA	Benzaldehyde
BE	Binding Energy
BioXAS	Biological X-ray Absorption Spectroscopy
BXDS-HEW	Brockhouse X-ray Diffraction and Scattering - High Energy Wiggler
CCEM	Canadian Centre for Electron Microscopy
CFIA	Canadian Food Inspection Agency
CLS	Canadian Light Source
CN	Coordination Number
CNT	Carbon Nanotube
CR	Co-Reduction
DCM	Dichloromethane
DFT	Density Functional Theory
DMF	Dimethylformamide
DMSO	Dimethylsulfoxide
DNA	Deoxyribonucleic Acid
DRIFTS	Diffuse Reflectance Infrared Fourier Transform Spectroscopy
dPDF	Differential Pair Distribution Function
E-HE	E-3-Hexen-1-ol
EO	Ethylene oxide
ESI-MS	Electro-Spray Ionization Mass Spectrometry
EXAFS	Extended X-ray Absorption Fine Structure
F127	$EO_{106}PO_{70}EO_{106}$ triblock copolymer

fcc	Face-Centred Cubic
FT	Fourier Transform
FWHM	Full Width at Half Maximum
GSH	Glutathione
GUI	Graphical User Interface
HA	Hexanol
HAADF-STEM	High-Angle Annular Dark-Field Scanning Transmission Electron Microscopy
HAS	Hemi-Spherical Analyzer
HE	3-Hexen-1-ol
HESI	Heated Electro Spray Ionization
HOMO	Highest Occupied Molecular Orbital
HRTEM	High-Resolution Transmission Electron Microscopy
$HSPhMe_2$	2,4-dimethylbenzenethiol
HXMA	Hard X-ray Micro Analysis
HY	3-hexyn-1-ol
KE	Kinetic Energy
LUMO	Lowest Unoccupied Molecular Orbital
MALDI-TOF	Matrix Assisted Laser Desorption Ionization Time-of-Fight
MBA	2-methyl-2-butanol
MBE	2-methyl-3-buten-2-ol
MBY	2-methyl-3-butyn-2-ol
MHA	6-Mercaptohexanoic acid
MC	Mesoporous Carbon
MS	Mass Spectrometry

NMR	Nuclear Magnetic Resonance
NPs	Nanoparticles
NSERC	National Sciences and Engineering Research Council of Canada
PAGE	Polyacrylamide Gel Electrophoresis
PDF	Pair Distribution Function
p-MBA	*p*-Mercaptobenzoic acid
PO	Propylene oxide
PVP	Poly(N-vinylpyrrolidone)
RP-HPLC	Reversed-Phase High-Performance Liquid Chromatography
SC-XRD	Single Crystal X-ray Diffraction
SD	Sequential Deposition
SMA	Spherical Mirror Analyzer
StO	Styrene Oxide
SR	Thiolate Ligands
STEM	Scanning Transmission Electron Microscopy
STM	Scanning Tunneling Microscopy
SXRMB	Soft X-ray Micro Characterization Beamline
TBHP	Tert-butyl hydroperoxide
TEM	Transmission Electron Microscopy
TEOS	Tetraethylorthosilicate
TGA	Thermal Gravimetric Analysis
THF	Tetrahydrofuran
TOAB	Tetraoctylammonium bromide
TON	Turnover Number
UV-Vis	Ultraviolet-Visible

XANES	X-ray Absorption Near Edge Structure
XAS	X-ray Absorption Spectroscopy
XPS	X-ray Photoelectron Spectroscopy
XRD	X-ray Diffraction
Z-HE	Z-3-Hexen-1-ol

Chapter 1

General Introduction

1.1 Metal Clusters for Nanocatalysis

Noble metal particles with sizes in nanoscale generally exhibit excellent catalytic activity because of their enhanced surface-to-volume ratio which gives more active sites, as well as modified surface geometric and electronic properties compared in bulk materials.[1,2] By tailoring the size as well as the morphology, robust nanocatalysts with excellent catalytic activity and selectivity can be achieved.[2] Metal clusters, often referred to as nanoclusters, are a sub-class of metal nanoparticles (NPs) that exhibit molecule-like properties and typically have a metal core size of ≤ 3 nm.[3,4] Clusters have fewer numbers of atoms and unique packing structures that have many low-coordination atoms at the surface compared to NPs and bulk materials.[5] Unlike NPs that exhibit quasi-continuous electronic states, clusters show size dependent discrete electronic transitions.[6-8] The molecule-like features of clusters further account for some fascinating physical and chemical properties that have made them excellent functional materials in sensor designs, biomedicine, drug delivery, energy conversion and catalyst development.[9-12] Furthermore, the development of bimetallic clusters can enable the integration of the physicochemical properties of two constituent metal species and allow for tailoring of the catalytic properties by manipulating the structure, size, and composition of bimetallic clusters at the atomic level.[13,14] Non-uniformity in the particle size distribution and composition that results from the traditional wetness impregnation method for the synthesis of supported-nanoparticle heterogeneous catalysts encourages the design of nanocatalysts with atom-precise compositions and structures. The use of atom-precise clusters as model catalysts can enable correlations between the intrinsic properties of the individual nanocatalysts and their overall catalytic performance.[15] However, this assumes that the resulting atom-precise clusters can be activated for catalysis with no change in their underlying structure, which can be challenging.

1.2 Atom-Precise, Thiolate-Protected Au and Ag Metal Clusters

Atom-precise, ligand-protected metal clusters, especially those comprised of Au and Ag atoms, have received significant research attention owing to developments in synthetic strategies and high stability of specific cluster compositions, which in turn has supported their wide applications in catalysis.[16] Atom-precise metal clusters can be prepared by solution chemistry methods in polar and non-polar reaction environments. The available synthesis approaches in the literature typically adopt modified Brust-Schiffrin methods which generally entail reduction of metal precursors by a reducing agent in the presence of protecting ligands.[4,17] Among other factors, the type of ligand influences reaction conditions for the successful synthesis of ligand-protected metal clusters.[18-21] Unprotected clusters are thermodynamically unstable and chemically reactive due to their ultrasmall size and stabilization of their structures can be achieved with protection by ligands such as thiolates, selenolates, tellurolates, phosphenes, carbenes, dendrimers, proteins, and DNA.[21-25] The choice of ligand strongly influences the properties, including the stability and catalytic performance, of the protected metal clusters.[22,23,26] Notably, thiolate-protected clusters are widely studied due to strong sulfur-metal interactions that enable good stability of the clusters in solution, facile synthesis, and controlled cluster composition as well as functionalization of stable clusters.[21,27,28]

Atom-precise thiolate-protected metal clusters are commonly designated as $M_n(SR)_m$, where M is the metal (e.g. Au, Ag, etc.), n is the number of metal atoms, and m is the number of protecting thiolate ligands (-SR) in the cluster composition. Atom-precise Au clusters were first synthesized and characterized and have been extensively studied, while Ag and other metal cluster systems have received more research attention in the last five years. Many reports on the synthesis, characterization, and applications of atom-precise thiolate ligand protected Au clusters such as $Au_{144}(SR)_{60}$, $Au_{102}(SR)_{44}$, $Au_{38}(SR)_{24}$, $Au_{25}(SR)_{18}$, $Ag_{25}(SR)_{18}$, and $Ag_{44}(SR)_{30}$ can be found in literature.[29-34] The structures of many of these clusters have been determined by X-ray crystallography, and typically clusters have core-shell morphologies, wherein the metal core has a certain geometrical structure that gives unique physicochemical properties to the whole cluster, and the shell consists of metal-thiolate complexes (or “staples”) that offer protection to the core structure.[16,29-32] Xie and co-workers emphasized that the presence of protecting thiolate ligands on metal clusters enables both atomic precision and well-defined structures and influences the

physicochemical and catalytic properties of Au clusters of different cluster sizes.[21] $Au_{25}(SR)_{18}^-$ clusters remain the most researched atom-precise metal cluster family owing to its early discovery, facile preparation, great stability, and ease of functionalization.[34] In fact, the high stability against degradation in solution and etching reactions by thiols has enabled extensive study of thiolate-protected Au_{25} clusters.[34,35] Using thiolate-protected Au_{25} clusters as the starting material, many non-thiolate ligand-protected Au_{25} clusters have been prepared via a ligand-exchange approach. For example, Meng *et al.* prepared selenophenolate-protected Au_{25} clusters from phenylethanethiolate-protected Au_{25} clusters via a complete thiolate to selenolate ligand exchange, as established by results from MALDI-MS, UV-Vis absorption spectroscopy, TGA, and ^{1}H and ^{13}C-NMR analyses.[36] Improved purification of clusters has been achieved with different forms of chromatographic separation techniques. Pradeep and co-workers purified a variety of Au clusters using normal-phase thin-layer chromatography by taking advantage of differences in polarity and the affinity of different clusters towards a stationary phase.[37] Niihori *et al.* reported reversed-phase high-performance liquid chromatography (RP-HPLC) as an efficient separation method for different sizes of clusters with water-soluble ligands.[38] Notably, non-chromatographic methods like polyacrylamide gel electrophoresis (PAGE) have also been used to successfully separate clusters of different sizes.[39,40] Our group also reported a purification strategy that involves deprotonation and re-protonation of the mercaptoundecanoic acid-protected Au_{25} clusters for the isolation of clusters.[41]

Unlike Au cluster systems, the design and development of Ag clusters are still limited, possibly due to greater susceptibility of Ag to oxidation. However, Ag cluster systems are gaining interest given the higher relative abundance and lower cost of Ag compared to Au. For example, $Ag_{44}(SR)_{30}^{4-}$ clusters with different water-soluble thiolate ligands have been prepared,[31,42,43] and $Ag_{44}(SR)_{30}^{4-}$ clusters with 5-mercapto-2-nitrobenzoic acid ligands have been shown to be highly stable in aqueous solution for at least 9 months under ambient conditions as shown by the preservation of UV-Vis optical features.[43] Desireddy *et al.* reported a simple synthetic procedure for achieving nearly quantitative yields of pure and ultrastable Ag_{44} clusters with *p*-mercaptobenzoic acid (*p*-MBA), and found that the Ag_{44}(*p*-MBA)$_{30}^{4-}$ clusters are more stable than Au clusters of the same size and structure.[31] The synthesis method involves solubilization of a Ag(I)-*p*-MBA precursor by adjusting the solution pH with CsOH, followed by reduction with aqueous $NaBH_4$ in the presence of a coordinating solvent.[31] Later, Bakr and co-workers reported

the successful synthesis of 2,4-dimethylbenzenethiolate-protected $Ag_{25}(SR)_{18}^-$ clusters that have similar (but not identical) atomic arrangements and ligand counts to well-studied $Au_{25}(SR)_{18}^-$ clusters.[32] Their synthesis involves the reduction of a Ag(I)-thiolate complex using $NaBH_4$ as reducing agent in a CH_3OH/CH_2Cl_2 mixture in the presence of Ph_4PBr in an ice-bath. It was noted that the stability of Ag_{25} clusters relies on the nature of the protecting ligands, the coordinating solvent and temperature, and therefore, these parameters are needed to be strategically optimized to achieve Ag_{25} clusters of comparable stability to Au_{25} clusters.[28,32] Recently, Xie and co-workers reported the successful synthesis of water-soluble Ag_{25} clusters using 6-mercaptohexanoic acid as a ligand,[44,45] using a NaOH-mediated $NaBH_4$-reduction method.[46] The group also noted that the ligand structure can control the size and structure of thiolate-protected Ag clusters in aqueous solution.[44] In similar synthesis conditions, a bulky thiol-containing tri-peptide ligand (i.e. glutathione (GSH)) gave $Ag_{9\text{-}15}(SR)_{5\text{-}10}$ clusters, a medium-sized aromatic-thiol (*p*-mercaptobenzoic acid (*p*-MBA)) afforded $Ag_{44}(SR)_{30}$ clusters, while a smaller alkane-thiol (6-mercaptohexanoic acid (MHA) led to the formation of $Ag_{25}(SR)_{18}$ clusters. Other thiolate ligands like 5-mercapto-2-nitobenzoic acid, 4-fluorothiophenol, 3-fluorothiophenol, 2-fluorothiophenol, (2-mercapto-5-methylphenyl) methanol, and 4-methylbenzene-1,2-dithiol have been reported for the synthesis of $Ag_{44}(SR)_{30}^{4-}$ clusters.[43,47] However, only 2,4-dimethylbenzenethiol, 3-mercaptopropionic acid, 4-mercaptobutyric acid, and 6-mercaptohexanoic acid ligands have been used to prepare atom-precise Ag_{25} clusters.[32,44] Generally, the cluster community has witnessed significant progress in the development and total-structure determination of atom-precise, thiolate-protected noble metal clusters in the last decade. Advances in the syntheses include improvements in purification and isolation of these clusters with relatively high yields as well more detailed characterization to reveal their unique properties.

1.2.1 Structural Description of Atom-Precise, Thiolate-Protected Au and Ag Metal Clusters

Atom-precise, thiolate-protected $Au_{25}(SR)_{18}^-$ clusters have core-shell structures as revealed by single crystal X-ray diffraction (SC-XRD) analysis. The X-ray crystal structure of $Au_{25}(SR)_{18}^-$ clusters shows the presence of an icosahedral Au_{13} core where 12 of the 20 Au_3 facets anchor six dimeric $Au_2(SR)_3$ staple-like motifs that also cap the Au_{13} core.[29,48] Challenges in both making and crystallizing monodisperse clusters limits a comprehensive study of the relative X-ray crystal

structures of ligand protected clusters as one moves from Au to Ag clusters.[24,49] However, there are reports on the total structure determination of both $Ag_{25}(SR)_{18}^-$ and $Ag_{44}(SR)_{30}^{4-}$ clusters, which are shown in Figure 1.1. The $Ag_{25}(SR)_{18}^-$ clusters are the Ag analogue of well-studied $Au_{25}(SR)_{18}^-$ clusters; both $Au_{25}(SR)_{18}^-$ and $Ag_{25}(SR)_{18}^-$ have comparable atomic arrangements, charges, core structures, and ligand counts, and their optical absorption spectra have some common features.[32] Both have M_{13} icosahedral cores (M = Au or Ag) having 12 vertices, 20 triangular faces, and 30 edges but a more careful comparison of their crystal structures shows that there are differences in the arrangement of metal atoms around the cluster core. In contrast to the situation in $Au_{25}(SR)_{18}^-$ clusters, where all the twelve non-icosahedral "staple" Au atoms occupy the center of the triangular face centers of the Au_{13} icosahedral core, the $Ag_{25}(SR)_{18}^-$ structure has three of the non-icosahedral Ag atoms lying away from the triangular face centers, while the remaining nine non-icosahedral Ag atoms are lying on the triangular face centers of the Ag_{13} icosahedral core.[32] This kind of atomic arrangement enables Ag to be in the proximity of anchoring thiolates of different v-shaped -S-Ag-S-Ag-S- staple motifs in the $Ag_{25}(SR)_{18}^-$ clusters and thus facilitates weak intermotif interactions which are absent in $Au_{25}(SR)_{18}^-$ clusters. Furthermore, the crystal structure of $Ag_{25}(SR)_{18}^-$ clusters shows four larger voids that allow possible solvent coordination to give better stability to the clusters, depending on the choice of the coordinating solvent.[28,32] Unlike the $Ag_{25}(SR)_{18}^-$ clusters, a single-crystal analysis of $Ag_{44}(SR)_{30}^{4-}$ clusters showed that each cluster has a Keplerate (a two-shell structure with one shell inside the other) $Ag_{12}@Ag_{20}$ core whose surface is protected by six $Ag_2(SR)_5$ units. The first shell of the core is a hollow Ag_{12} icosahedral cage whose faces are fully capped by twenty Ag atoms to form a concentric icosahedral and dodecahedral Ag core. The Keplerate cage of $Ag_{12}@Ag_{20}$ is surrounded by six $Ag_2(SR)_5$ staple units. Through Ag-SR interactions, each $Ag_2(SR)_5$ unit is connected to an edge of the Ag_{20} pentagonal dodecahedron and the Ag_{20} sub-shell offers extra stabilization to the hollow Ag_{12} icosahedral core.[31] The difference in the atomic arrangement in the structures of Ag clusters is reflected in their optical properties as each of them shows distinct absorption fingerprint in the visible region of light, which is discussed in more detail below.

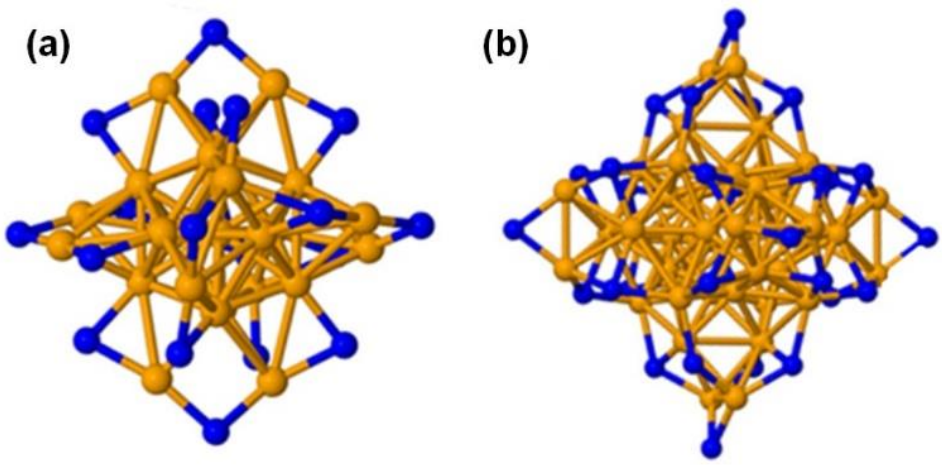

Figure 1.1. The single-crystal structures of (a) $Ag_{25}(SR)_{18}^-$ and (b) $Ag_{44}(SR)_{30}^{4-}$ clusters; Ag: Orange, S: Blue. Only the S atoms of thiolate ligands are shown and charge balancing cations are omitted for clarity. Reprinted from ref. 16 with permission from the Royal Society of Chemistry.

1.2.2 Optical Features of Atom-Precise Ag Clusters versus Ag Nanoparticles

The surface plasmon resonance is observed in metal NPs owing to the collective oscillation of electrons in their incompletely filled band,[50] and the size, shape and dielectric constant of the metal nanoparticle and its environment determine the resonance condition.[51] Unlike Ag nanoparticles that exhibit quasi-continuous electronic states, atom-precise Ag clusters have discrete energy levels that lead to the clusters having unique molecule-like absorption behavior in the visible region of light.[31,32,52] Specific clusters can show multiple features across the entire visible range in their optical absorption spectra that are defined by their core structures. The total structure determination analysis shows that, in addition to the difference in the atom compositions, $Ag_{25}(SR)_{18}^-$ clusters have a non-hollow metal core while $Ag_{44}(SR)_{30}^{4-}$ clusters have a hollow metal core.[53] This difference in core structures is reflected in the optical fingerprints displayed by each of these atom-precise Ag clusters as compared to spherical Ag nanoparticles that show a plasmon band in the region of ca. 400-420 nm (Figure 1.2). $Ag_{44}(SR)_{30}^{4-}$ clusters exhibit broad multiband optical absorptions with six main peaks at around 374 nm, 411 nm, 483 nm, 535 nm, 641 nm, and 833 nm, and two shoulder peaks at 590 nm and 689 nm. Yang *et al.* noted that these absorption peaks are the same regardless of the nature of thiolate ligands in the structure, to suggest that there is little or no influence of the type of thiolate ligands used on the absorption spectra of $Ag_{44}(SR)_{30}^{4-}$

clusters.[54] In contrast, $Ag_{25}(SR)_{18}^-$ clusters show a typical absorption spectrum with four characteristic peaks at 334 nm, 392 nm, 490 nm, and 678 nm, where the broad peak at around 678 nm is due to the HOMO-LUMO transition from the Ag_{13} icosahedral core in the Ag_{25} structure.[32] The distinct optical fingerprints of atom-precise thiolate-protected Ag clusters in the visible region of light allow the use of UV-Vis absorption spectroscopy as a facile technique to follow the synthesis of Ag clusters in solution.

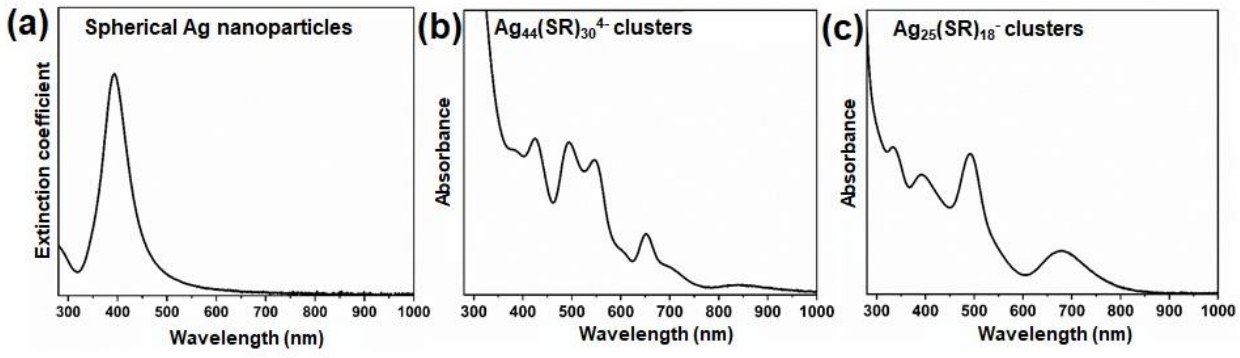

Figure 1.2. UV-Vis absorption spectra of (a) spherical Ag nanoparticles in H_2O, (b) $Ag_{44}(SR)_{30}^{4-}$ clusters in DMF, and (c) $Ag_{25}(SR)_{18}^-$ clusters in DCM. Unpublished work, Kazeem O. Sulaiman.

1.2.3 Site-Specific Electronic Properties of $Ag_{25}(SR)_{18}^-$ Clusters

Information about the oxidation states and local environment of constituent metal atoms in a specific site of the cluster structure can be crucial for understanding the structure and electronic properties of the metal clusters. Like its Au analogue, $Ag_{25}(SR)_{18}^-$ clusters are comprised of a well-defined thirteen-atom icosahedral core surrounded by a shell containing six $Ag_2(SR)_3^{2-}$ staple species.[29,32] Even though the SC-XRD method cannot typically directly afford information about electronic properties of metal clusters,[55] information from this technique about the atomic arrangement is crucial to the description of site-specific electronic properties of $Ag_{25}(SR)_{18}^-$ clusters. Figure 1.3 shows the breakdown of the structural model of $Ag_{25}(SR)_{18}^-$ clusters; Chen *et al.* observed about a 0.20 eV positive shift in the XPS spectrum of $Ag_{25}(SR)_{18}^-$ clusters as compared to Ag foil,[56] and similar positive shifts have been measured for metal nanoparticles and clusters which can be attributed to either the metal-ligand charge transfer and/or quantum size effects.[57,58] The multiple-component core-level XPS analysis of $Ag_{25}(SR)_{18}^-$ clusters shows that the center Ag atom is mostly metallic with an oxidation state of 0, the surface Ag atoms have a mixture of both

non-metallic and metallic natures with oxidation states between 0 and +1, while the Ag atoms at the staple sites have a +1 oxidation state.[56] As expected, the relative peak area ratio for Ag speciation is 1:12:12 for center:surface:staple sites. The tuning of the electronic properties of metal clusters is typically achieved via introduction of dopant atom(s) into parent clusters. A single atom replacement in the parent cluster structure with a foreign atom often leads to change in electronic properties of the parent clusters.[28,59,60] For typical $Ag_{25}(SR)_{18}^-$ clusters with a well-defined structure, single atom doping can position the dopant atom to one of three sites in the clusters: core center, core surface, or staples (Figure 1.3), and the use of element-specific characterization techniques, such as a combination of XPS and XAS, is essential for probing the possible location of dopants which typically cause modulation of the electronic properties of the parent metal clusters.

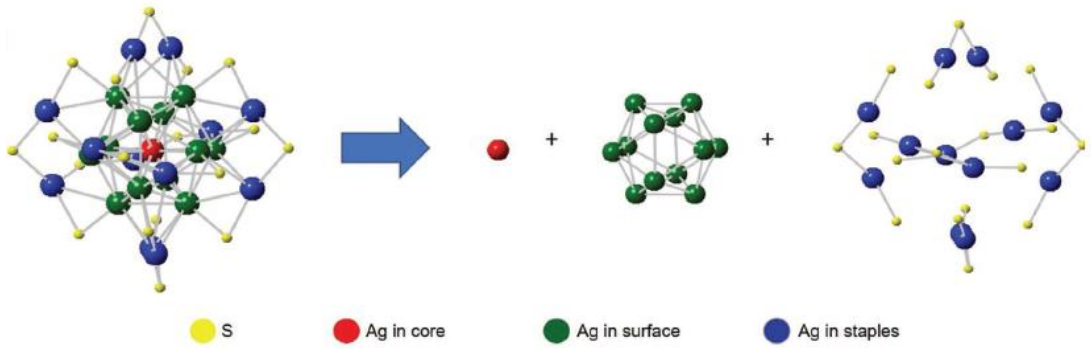

Figure 1.3. Structural model of $Ag_{25}(SR)_{18}^-$ broken down into the center (red), surface (green), and staple sites (blue); the -R parts of thiolate ligand are omitted for clarity. Reprinted with permission from ref. 56. Copyright 2021, Wiley-VCH GmbH.

1.3 Design and Structural Description of Bimetallic Cluster Catalysts

In the last 12 years, the metal cluster community has witnessed the emergence of bimetallic atom-precise clusters which contain two metal species in a cluster.[27,28,61-64] The design of bimetallic clusters allows the integration of the physicochemical properties of the two constituent metal species and tuning of the overall electronic structures by manipulating the structure, size, and composition of the bimetallic clusters at the atomic level.[13,26,27] Bimetallic atom-precise clusters constitute a class of promising functional clusters with rich surface chemistry and unique electronic structures that can enable improved catalytic applications. They can also serve as model

bimetallic catalysts to allow for a better understanding of structure-property relationships in bimetallic systems. Remarkably, bimetallic clusters show significant differences in their structures and physicochemical properties when parent clusters are doped with even a single foreign metal atom.[28,58,63] Several synthesis protocols have been developed and reported for making monodisperse atom-precise bimetallic clusters,[28,58,60,63] and research efforts are being geared towards synthesizing novel and high-quality bimetallic clusters with distinct sizes and structures.[27] Thiolate-protected bimetallic clusters are well studied owing to their facile synthesis, controlled cluster composition, rich surface chemistry, as well as strong metal-thiolate interactions that allows good stability of the clusters in solution.[26-28] Based on the synthetic procedures, the synthesis of thiolate-protected bimetallic clusters can be generally classified as either direct syntheses or post-treatment syntheses. The former entails simultaneous reduction of two metal ions in the presence of the protecting ligand while the latter involves two distinct processes, the first involving the preparation of a monometallic precursor/intermediate and the second post-treatment of the precursor/intermediate with a second metal species.[27]

1.3.1 Direct Synthesis Approach to Preparing Bimetallic Clusters

In the direct synthesis (also sometimes referred to as single-pot co-reduction) method, metal precursors of the two metals are reduced simultaneously using a reducing agent in the presence of the protecting ligands. This method has been largely reported for the synthesis of three most common species of thiolate-protected bimetallic clusters containing 25, 38, and 144 metal atoms.[58,59,62-64] In this method, the interaction between the different metal atoms, their atomic radii and redox potentials, and the ligand affinity of thiolates for each of the metals are crucial factors that determine the metal incorporation ratio (i.e. composition) of the bimetallic clusters and the location of each metal within the cluster.[27] Similar sizes of atomic radii and strong metal-pair interactions can help minimize distortions in the cluster structure while similar reduction kinetics discourages phase separation of the constituent metals. Several examples of atom-precise singly doped clusters, including $M_1Au_{24}(SR)_{18}$ (M = Pd or Pt),[58,60,63,65] and $M_1Ag_{24}(SR)_{18}^{2-}$ (M = Pd or Pt),[28,66] have been prepared via a direct synthesis single-pot method. Notably, bimetallic clusters with a mixture of compositions, $[Ag_{25-x}Au_x(SR)_{18}]^-$ (x = 1-8), were produced in an attempt to make $Au_1Ag_{24}(SR)_{18}^-$ bimetallic clusters using a co-reduction method.[28] Despite their low synthesis yield and difficulties in purification, several examples of bimetallic clusters prepared by direct syntheses

showing interesting catalytic activities have been reported in the literature.[27] Examples of catalytic applications of atom-precise bimetallic clusters are discussed in section 1.4 (see below).

Both the parent clusters ($Au_{25}(SR)_{18}$ and $Ag_{25}(SR)_{18}$) and the singly doped clusters (M_1Au_{24} and M_1Ag_{24}) show core-shell structures as earlier described, with the dopant atom occupying either a core, surface, or staple position. The formation of doped clusters is commonly confirmed by mass spectrometry measurements while SC-XRD and computational methods are often employed to give information about the position of the dopant atom in the parent cluster structure. $Au_{25}(SR)_{18}^-$ clusters have the largest number of structurally elucidated doped analogues, with the single atom dopant occupying the central core position in most cases and elsewhere in a few cases.[60,63,65-68] For instance, a Cd dopant occupies the surface of the icosahedral core in the $Au_{24}Cd_1(SR)_{18}$ cluster while a Hg dopant atom is in the staple position in $Au_{24}Hg_1(SR)_{18}$ clusters.[68] SC-XRD analysis of thiolate-protected M_1Ag_{24} (where M is Pd, Pt, or Au) bimetallic clusters suggested that M replaces the central Ag atom in Ag_{25} clusters.[28,66,69] Intuitively, an element-specific technique will be more suitable to probe the dopant position in Pd_1Ag_{24}, as SC-XRD cannot typically distinguish elements such as Ag and Pd due to similarity in their atomic numbers. Positioning catalytically active dopant atoms in a non-central position in $Ag_{25}(SR)_{18}$ clusters is desirable and this has been observed for its isostructural $Au_{25}(SR)_{18}$ clusters.[68,70] There continues to be much research interest in developing synthetic methods for the fabrication of high-yield, compositionally and structurally pure bimetallic clusters, especially with the catalytic metal on the exterior surface of clusters.

1.3.2 Post-Synthesis Treatments of Monometallic Clusters to Synthesize Bimetallic Clusters

Several groups have employed indirect methods that involve post-synthesis treatments of monometallic parent atom-precise clusters to prepare bimetallic clusters. The most common method is referred to as a metal exchange strategy, wherein the metal precursor of the dopant is added to the solution of the parent cluster in a controlled manner.[67,71] For such metal exchange reactions, Murray and co-workers proposed a redox model wherein the metal clusters act as reductants toward the metal ions for the reaction between $Au_{25}(SR)_{18}^-$ clusters and metal ions (Ag^+, Cu^{2+}, and Pb^{2+}).[72] Various doped metal clusters with atomic precision have been prepared via both galvanic and antigalvanic exchange strategies.[28,67,71-74] In a galvanic metal exchange, noble-metal

cations (such as Au^{+}, Pd^{2+}, etc.) are reduced by the less noble parent clusters (e.g. $Ag_{25}(SR)_{18}^{-}$ host) with a favorable redox driving force. In an antigalvanic metal exchange reaction, however, a noble parent cluster (e.g. $Au_{25}(SCH_2CH_2Ph)_{18}^{-}$ clusters) can reduce less noble metal ions (e.g. Ag ions) to form bimetallic clusters (e.g. $Ag_xAu_{25-x}(SCH_2CH_2Ph)_{18}^{-}$).[28,73] Wang *et al.* noted the presence of $NaBH_4$ in the metal exchange reaction between $Cu(SR)_2$ and $Au_{25}(SC_2H_4Ph)_{18}^{-}$ allowed the successful preparation of $Cu_xAu_{25-x}(SC_2H_4Ph)_{18}^{-}$ bimetallic clusters.[71] Previous work from our group employed *in situ* X-ray Absorption Spectroscopy (XAS) methods to follow the reactions of $Au_{25}(SC_8H_9)_{18}^{-}$ clusters with Ag^{+} and Pd^{2+} ions.[75] Results showed that Pd^{2+} reacts with the staple motifs of the $Au_{25}(SC_8H_9)_{18}^{-}$ clusters and forms Pd(II) thiolate species, while Ag^{+} reduces to Ag on the cluster core, rather than forming Ag(I) thiolate species.

Single atom doping of other metals like Au, Pd, Pt, and Ni into parent Ag_{25} clusters has also been successfully realized via metal exchange methods.[76-78] Using $Ag_{25}(SPhMe_2)_{18}^{-}$ as a template, Bootharaju *et al.* employed the galvanic metal exchange method to successfully synthesize $Au_1Ag_{24}(SR)_{18}^{-}$ bimetallic clusters that could not be prepared via a co-reduction method.[76] The process involves reduction of Au^{+} ions (from $AuPPh_3Cl$ as a gold precursor salt) to Au^{0} by Ag atoms of the Ag_{25} cluster, due to the difference in electrochemical potentials of the two species. They noted that the choice of metal precursors is very crucial for such a process. In a similar galvanic synthesis, $Pd_1Ag_{24}(SPhMe_2)_{18}^{2-}$ clusters were prepared using $Ag_{25}(SPhMe_2)_{18}^{-}$ clusters as the reducing agent.[76,77] In both cases the single dopant atom (Au or Pd) was reported to be located at the center of the icosahedron core. Recently, Kim *et al.* reported the high-yield synthesis of centrally doped $M_1Ag_{24}(SR)_{18}$ (M = Ni, Pd, Pt) clusters with the aid of a co-reductant (BH_4^{-}) and a counterion (Ph_4P^{+}).[78] The authors proposed the dopant deposition followed by host dissolution as two mechanistic steps of the metal exchange process that led to the replacement of the central Ag atom of the Ag_{25} clusters with a dopant atom.

Both core-shell and cluster-in-cluster architectures have been reported for small-sized AgPd bimetallic nanoparticles prepared via an indirect synthesis approach that involves sequential reduction of a second metal onto the preformed host metal clusters/seeds. Our group reported the preparation of AgPd bimetallic nanoparticles through galvanic exchange reactions by varying the ratio of Ag nanoparticle seeds and amount of K_2PdCl_4 in the presence of PVP stabilizer.[79] The structure of the resulting bimetallic catalysts was best described as a cluster-in-cluster structure as

revealed by extended X-ray absorption fine structure (EXAFS) analysis. Mitsudome *et al.* prepared Pd@Ag core@shell nanoparticles via reduction of $AgNO_3$ onto Pd nanoparticle seeds using ascorbic acid.[80] The Pd@Ag catalyst showed high chemoselectivity towards a wide range of alkenes with high Z-selectivity under mild reaction conditions (room temperature and 1 atm H_2) for the semihydrogenation of a wide range of terminal and internal alkynes containing hydroxyl, carboxylic acid, ester, amine, cyano, and halogen groups.

1.4 Catalysis by Atom-Precise Monometallic and Bimetallic Clusters

Atom-precise $Au_{25}(SR)_{18}$ clusters have been evaluated as either catalysts or precursors for catalysts for chemical conversions involving oxidation and reduction reactions.[81-87] Zhu *et al.* showed that silica-supported $Au_{25}(SR)_{18}$ clusters were active for styrene oxidation in the presence of oxygen to give benzaldehyde as a major product.[81] They observed that $Au_{25}(SR)_{18}$ clusters are more active than $Au_{38}(SR)_{24}$ and $Au_{144}(SR)_{60}$ clusters on the same silica support under the same reaction conditions, which indicated size-dependent activity of atom-precise Au cluster catalysts. In another study, glutathione-stabilized Au_{25} clusters on hydroxyapatite supports were found to be active for selective styrene to styrene oxide reactions using tert-butyl hydroperoxide (TBHP) as an oxidant.[82] Notably, the activated clusters showed 100% conversion and 92% selectivity towards styrene oxide using TBHP as an oxidant in toluene at 80 ˚C. The reduction of 4-nitrophenol to 4-aminophenol using $NaBH_4$ as a reducing agent is another interesting reaction that has been used a model reaction for evaluation of metal cluster and nanoparticle catalysts.[83-88] Our group and several other groups have observed that intact Au clusters are an active catalyst for this particular reduction reaction.[83-87] In a comparison study of the catalytic activity of thiolate-protected $Au_{25}(SR)_{18}^-$ clusters with different chain lengths of ligands ($-SC_{12}H_{25}$, $-SC_6H_{13}$, and $-SC_8H_9$) for the 4-nitrophenol reduction to 4-aminophenol reaction, an increase in the rate constant was observed with a decrease in chain length to suggest that there are reduced mass transfer issues associated with shorter thiolate chain lengths.[84]

Compared to monometallic catalysts, bimetallic catalysts often show superior physicochemical and catalytic properties due to synergy of properties of the constituent metals,[27,28,60,67,69] and careful syntheses and purification allow for the fabrication of atom-precise to bimetallic clusters with controlled cluster sizes, compositions, and structures. [28,60,63] Single foreign metal atom doping of atom-precise metal clusters is attracting great interest, as such subtle

atom replacement can afford bimetallic clusters with significantly different physicochemical and catalytic properties. Several studies have shown that a single atom doping of $Au_{25}(SR)_{18}^-$ clusters leads to both improved cluster stability and enhanced catalytic efficiency. [28,58,60,63,89] For instance, Jin and co-workers observed an increase in substrate conversion from 58.9 % to 90.8% for the styrene oxidation reaction when $Au_{25}(SC_2H_4Ph)_{18}$ clusters were singly doped to form $Pt_1Au_{24}(SC_2H_4Ph)_{18}$ cluster catalysts in which Pt was in the central core position.[60] Meanwhile, Qian *et al.* observed similar catalytic activity for intact $Pd_1Au_{24}(SC_2H_4Ph)_{18}$ and $Au_{25}(SC_2H_4Ph)_{18}$ clusters for the selective hydrogenation of α,β-unsaturated ketones to α,β-unsaturated alcohol, to show that the central Pd atom is not the active site of the catalyst, and thus could not significantly affect the catalytic properties.[90] Conversely, Xie *et al.* observed no catalytic activity for intact $Pd_1Au_{24}(SC_{12}H_{25})_{18}$/CNT and $Au_{25}(SC_{12}H_{25})_{18}$/CNT catalysts, whereas thermally activated catalysts were active for benzyl alcohol oxidation reactions and single Pd atom doping significantly improved the catalytic performance of activated clusters.[89] These different observations show that the enhanced catalytic performance by $Pd_1Au_{24}(SR)_{18}$ clusters with a single Pd atom at the central position is still an open debate.

Catalytic studies of atom-precise Ag and Ag-based bimetallic catalysts are presently much more scarce in the literature, perhaps due to the later discovery of the monometallic Ag cluster system as compared to Au-based clusters. Similar to the Au system, enhancements in stability and catalytic performance have been observed for $M_1Ag_{24}(SR)_{18}^{2-}$ clusters when compared with monometallic $Ag_{25}(SR)_{18}^-$ clusters.[28,66,69] Zhu and co-workers studied the effects of strategic replacement of central core atoms of atom-precise Ag_{25} clusters with a single foreign atom (Au, Pd, and Pt) on the catalytic properties of the resulting atom-precise bimetallic clusters with the protecting thiolate ligands intact.[69] The centrally doped bimetallic clusters demonstrated superior catalytic performances for the carboxylation reaction of CO_2 with terminal alkynes via C-C bond formation to give propiolic acid. Significant synergistic enhancements in the catalytic efficiency were observed in the order of Au > Pd ~ Pt > Ag for doping atoms. It is noted that the presence of Cs_2CO_3 was necessary to facilitate the adsorption and activation of the terminal C≡C bond of the alkyne on the clusters and the possibility of distinct chemical adsorption of CO_2 on the clusters may account for different reactivities observed for the studied catalysts.[69] It is noteworthy that the Ag-based bimetallic clusters were used as catalysts without activation, and the presence of ligands on the cluster surfaces can influence their catalytic properties. At present, there is no information

on the nature of Ag-based bimetallic clusters upon activation as there is possibility of metal oxidation, sintering, or phase separation upon activation at high temperatures. Moreover, more catalytic evaluations of Ag clusters and singly doped Ag-based bimetallic clusters need to be carried out.

Hydrogenation reactions over heterogeneous metal catalysts is typically described by the Langmuir-Hinshelwood mechanism which involves adsorption of two reacting molecules onto neighboring sites of the catalyst, followed by a bimolecular reaction of the adsorbed molecules. [91] For some metal catalysts studied in the literature, stronger adsorption of alkynes than alkenes is often a factor in the thermodynamic selectivity towards semi-hydrogenation products.[92] Selective hydrogenation of alkynes is a chemical conversion of industrial interest.[92,93] Metals like Au and Ag have low reactivity towards H_2 but show high alkene selectivity, albeit with much lower activity that other metals.[93] Pd catalysts are highly active hydrogenation catalysts but suffer from intrinsic poor selectivity for selective alkyne hydrogenations to alkenes. The selectivity of Pd can be improved by the addition of nitrogen based additives (such as ammonia, pyridine, and quinoline) but this often necessitates additional steps, like separation, which can be costly.[94] Improved selectivity can be also attained when Pd is diluted with other metals (Zn, Cu, Au, Ag, etc.) to form bimetallic catalysts.[79,80,95-98] This promising strategy involves atomic distribution of Pd in the matrix of second metal, and such catalysts are known as single-atom alloys at low Pd loadings.[66,69,89,90] The atomic composition and method of preparation are important tunable factors towards the final catalyst structure which is essential for optimum activity and selectivity of bimetallic systems.[67,69,98] The presence of protecting ligands on the surface of the metal catalyst can also affect the catalytic performance by limiting the accessibility of metal active sites by the substrates. Thus, achieving a controlled desorption of ligands without significant compromise of structure and composition can enable higher activities and selectivities for bimetallic cluster catalysts. It is of great interest to assess both ligand-on and ligand-off $Ag_{24}Pd_1$ cluster catalysts as selective hydrogenation catalysts.

1.4.1 Controlled Desorption of Thiolate Ligands from Atom-Precise Metal Clusters

While some groups have observed catalytic activity over intact ligand-protected cluster catalysts in various chemical reactions, there are cases where partial or complete removal of ligand often leads to improved catalytic performance as the substrates have improved access to active

sites on the cluster surface.[89,99] For example, Yoskamtorn *et al.* studied thiolate-protected Au_{25} clusters on porous carbon nanosheets as catalysts for benzyl alcohol oxidation and observed no catalytic activity for thiolate-protected Au_{25} clusters whereas the thiolate-free Au_{25} clusters showed efficient conversion which suggests that thiolate ligands acted as a site-blocking agent and thus supressed the catalytic activity.[99] They noted improved selectivity for benzaldehyde, although with reduced activity, for catalysts having residual thiolates on Au_{25} clusters. For the same benzyl alcohol oxidation reaction, the ligand-on Pd_1Au_{24}/CNT catalyst showed no activity while the ligand-free Pd_1Au_{24}/CNT catalyst showed a conversion of 74%.[89] The removal of thiolate ligands from carbon-supported $Au_{25}(SC_8H_9)_{18}^-$ clusters via calcination at 250 ˚C under air for 1.5 h led to an enhancement in the catalytic activity for the reduction of 4-nitrophenol to 4-aminophenol using $NaBH_4$ as a reducing agent, albeit deactivation of the catalyst was noted for catalysts treated at higher temperatures due to cluster sintering.[100] Similarly, thermal treatment of $Ag_{44}(SC_6H_4F)_{30}^{4-}$ clusters on mesoporous carbon (MC) supports at 300 °C under vacuum for 2 hrs produced ligand-free Ag_{44} clusters, and the resulting Ag_{44}/MC catalyst was active for dehydrogenation of ammonia-borane in the presence of oxygen.[101] The removal of ligands likely enhanced the accessibility of reactants to the active sites on the metal surface, whereas at higher temperatures the decrease in available catalyst surface area led to lower activities. Our research group recently published a comprehensive review of the activation of atom-precise metal clusters for catalysis.[16] Therein, we described the available methods of activation with examples of their applications and limitations. Generally, methods of activation of metal clusters for catalysis include heat treatment (thermal calcination) methods, chemical methods with oxidizing agents or reducing agents, and oxidation via light irradiation. Thermal activation is the simplest and most widely used method of activating clusters for catalysis.[16] Slight or significant particle size growth may occur upon deprotection of metal clusters due to sintering, particularly at high temperatures.

Both our group, and others, have shown that EXAFS is a valuable tool for following the activation of metal clusters.[85,100-102] Figure 1.4 shows the EXAFS spectra of $Au_{25}(SR)_{18}^-$ clusters on carbon supports calcined at different temperatures; there is a progressive decrease/disappearance of metal-thiol interactions and increase in the intensity of the Au-Au interaction as the calcination temperature is increased.[100] The data shows that as the metal thiolate interactions are completely removed, cluster sintering becomes significant. Besides sintering due to agglomeration of metal clusters upon oxidization of metal-thiolate bonds during heat treatments,

the fate of oxidized ligands is also of concern. Using S K-edge XANES analysis, Zhang *et al.* reported that the thiolate ligand oxidation products (sulfides, sulfonates, and sulfates) migrate from the Au clusters to the oxide support after thermal treatment and noted that the presence of these sulfur-containing species could limit the role of redox active supports in catalytic reactions.[103] Conversely, Alkmukhlifi *et al.* showed that the presence of trace amount of sulfates on inorganic support surfaces after the thermal activation of thiolate-stabilized Au nanoparticles at 340 ˚C did not affect the activity of resulting catalysts for hydrocarbon oxidation reactions.[104] Nevertheless, it is crucial to carefully select activation conditions that enable good stability of metal clusters upon thiolate removal, i.e. and prevent of particle agglomeration and sintering. In addition, oxidized ligands can potentially influence the catalytic performance in some reactions, and thus routes to remove these species would be beneficial.

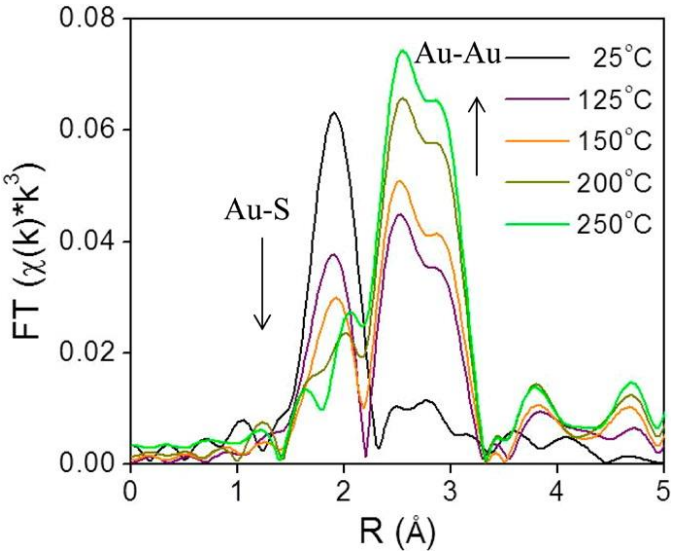

Figure 1.4. Au L_3-edge EXAFS spectra in R space of $Au_{25}(SR)_{18}$ clusters on carbon (no phase shift correction). Reprinted with permission from ref. 100. Copyright 2013, American Chemical Society.

1.5 Characterization Techniques

Generally, the successful synthesis of materials, including metal clusters, is followed with detailed structural characterization to enable an understanding of the structure-property relationships of the materials. Both UV-Vis absorption spectroscopy and mass spectrometry can confirm the formation of both monometallic and bimetallic clusters, but these techniques do not

give information about the position of the foreign metal atoms in the structure of bimetallic clusters. Knowing the exact location of atoms in a cluster is essential to understanding and tuning their properties. Several modern characterization techniques can enable thorough structural elucidation of atom-precise clusters. Amongst the available techniques, SC-XRD is the most direct method of revealing the structure of clusters.[29,32,65,66,105] However, crystalline samples of monodisperse clusters are needed for X-ray crystallographic analysis, and it can be difficult to obtain high-quality single crystals of metal clusters. Metal clusters are typically immobilized onto supports for their use in heterogeneous catalysis, and SC-XRD techniques are not suitable for such supported cluster samples.[55,105] Many advanced techniques have been developed and subsequently explored to capture the structural changes of supported-cluster catalysts. Synchrotron-based X-ray methods (both absorption and scattering) can play critical roles in revealing structural information about cluster chemistry.[105-107] Synchrotron radiation can provide energy-tunable high intensity monochromatic X-rays. This can allow analysis of nearly all elements by scanning over specific absorption edges of each element. X-ray absorption spectroscopy (XAS) is an element-specific technique which can be used to determine the average local structure of absorbing atoms.[105,108,109] For structural characterization of supported metal clusters, both XAS and X-ray total scattering measurements, alongside with Transmission Electron Microscopy (TEM) and X-ray Photoelectron Spectroscopy (XPS), are used in studies documented in subsequent chapters of this thesis. This section briefly describes some essential characterization techniques used in the thesis to monitor structural changes to metal clusters, particularly when they are thermally activated for catalysis.

1.5.1 Transmission Electron Microscopy (TEM)

Transmission electron microscopy (TEM) is broadly used to measure the size of nanomaterials. A TEM instrument uses monochromatic high-energy electrons in a vacuum chamber to provide high-resolution, two-dimensional images of a sample. The electron gun component of the TEM instrument generates monochromatic electrons that then pass through a condenser to produce an electron beam directed at the sample. Depending on the sample density and thickness, the beam is scattered or absorbed as it passes through the sample, and the transmitted electrons form a two-dimensional negative projection of the sample. This sample projection is then magnified by the electron optics to produce a bright field image. Conversely, dark field images can also be obtained by reconstructing scattered electron beams on some instruments, which are

slightly off angle from the transmitted beam. Typically, high vacuum ($\geq 10^{-6}$ Torr) is required within the specimen chamber to eliminate the energy loss of electrons due to collisions with gaseous atoms.

In this thesis, bright field TEM images of high magnification and resolution were taken, and the imaging of metal clusters enables an evaluation of the average core size of the clusters. It is noteworthy that clusters are sometimes unstable with respect to the electron beam and caution must be taken in collecting reliable images of these small-sized clusters. The electron beam is a type of ionizing radiation, and the protecting ligands on cluster surfaces can be particularly susceptible to beam damage.[110,111] Good practice involves using a moderate voltage TEM source and ensuring that a distinct sample position on the grid does not remain illuminated by the beam too long before taking the image. In addition, several images are usually taken for different portions of the TEM grid and the average size of clusters in each image are thoroughly sampled to determine average cluster sizes and standard deviations.

1.5.2 X-ray Photoelectron Spectroscopy (XPS)

XPS is a surface sensitive technique that is based on the photoelectric effect. Upon irradiating a sample surface with an incident X-ray with sufficient energy ($h\upsilon$), core level electrons are excited, and an eventual photoelectron is released with a certain kinetic energy (KE). The binding energy is the energy required to move an electron from its ground state orbital to the Fermi edge, while the work function is the energy required to move electron from Fermi level to vacuum. The kinetic energy of the photoelectron is related to the binding energy (BE) as described by Einstein equation (1.1).

$$KE = h\upsilon - BE - \varphi \qquad (\mathbf{1.1})$$

Where h is Planck's constant, υ is the frequency of exciting radiation, and φ is the work function.

Common X-ray sources for XPS measurements are Al K_α (1487 eV), Mg K_α (1254 eV), and tunable synchrotron radiation. Through an electron lens, the ejected photoelectrons are directed to an electron energy analyzer and then get separated based on their kinetic energies, before finally hitting the detector. XPS survey spectra (wide scan but low resolution) analysis can provide compositional information about various elements, except H and He, on surfaces of a

sample. On the other hand, the analysis of high-resolution spectra of each elemental component affords direct information on the oxidation state of the components of the sample surface. In XPS nomenclature, the peak label (1s, $2p_{3/2}$, $3d_{5/2}$, etc.) depends on the final state configuration and spin-orbit coupling occurs when $l > 0$. The orientation of the unpaired electron in the orbital after photoionization determines the peak label. For instance, $2p_{3/2}$ ($j = l + s$) has a spin-up unpaired electron left, while $2p_{1/2}$ ($j = l - s$) has a spin-down unpaired electron after photoionization. Also, for a final state with multiple degenerate states, there is a fixed peak area ratio, regardless of the sample. 2p peaks have area ratio of 2:1 for $2p_{3/2}$: $2p_{1/2}$, while 3d peaks have area ratios of 3:2 for $3d_{5/2}$: $3d_{3/2}$. XPS can enable the identification of atoms of an element in different chemical environments and with different oxidation states. In addition, the presence of an electron-withdrawing adjacent atom in bimetallic clusters can lead to higher binding energies for the metal atom of interest.[112,113] Element-specific XPS analysis is used throughout the thesis as a valuable tool in determining metal speciation in monometallic and bimetallic clusters.

1.5.3 X-ray Absorption Spectroscopy (XAS)

X-ray absorption occurs when the energy of an incident X-ray photon has energy that is greater than a core binding energy of an electron in a given element, and this causes a sharp rise in the absorption coefficient at the absorption edge. XAS measures the energy dependence of the X-ray absorption coefficient $\mu(E)$ at and above the absorption edge, and can be collected in either transmission or fluorescence mode. According to the Beer-Lambert law, the absorption coefficient is related to sample thickness (t), the intensity of incident photon (I_0) and transmitted photon (I_t) as expressed in Equation 1.2 below.

$$I_t/I_0 = e^{-\mu t} \quad \textbf{(1.2)}$$

The absorption coefficient (μ) varies with the sample density (ρ), the atomic number (Z), the atomic mass (A), and the X-ray energy (E) as expressed in Equation 1.3.

$$\mu = \rho Z^4/AE^3 \quad \textbf{(1.3)}$$

The X-ray absorption energy corresponds to the binding energy of the electron energy levels in the atom. The edges are named according to the principal quantum number core electron that is excited, such that when the origin of the excited core electrons are from 1s orbitals (n=1),

2s or 2p orbitals (n=2), or 3s/3p/3d orbitals (n=3), we have K-, L-, or M-edge measurements, respectively. In this thesis, the K- and L_3-edges of elements such as Ag, Pd, and S are analyzed. K-edges represent the excitation of electrons from 1s to (n+1)p orbitals and L_3 edges represent the $2p_{3/2} \rightarrow$nd transition.

A typical XAS spectrum comprises of two regions called the X-ray absorption near edge structure (XANES) and the extended X-ray absorption fine structure (EXAFS) regions as shown in Figure 1.5(a). The XANES region comprises of a pre-edge, absorption edge, and all the features within ~50 eV above the absorption edge. The electronic transition from the core level to unoccupied valence states of the absorbing atom gives rise to the white line in the XANES region. At the L_3-edge, the white line peak intensity is inversely related to the valence d-electron count of the absorbing atom, and a positive shift of absorption edge and increasing intensity of the white line suggests higher oxidation states of the absorbing atom. On the other hand, the EXAFS region consists of all the features in the spectrum from 50 eV to up to 1000 eV above the absorption edge. Transitions near the end of the XANES region and early in the EXAFS region are often due to the multiple scattering of photoelectrons at low kinetic energy.[114] EXAFS is the attenuation of the absorption spectra beyond the edge due to backscattering of photoelectrons from neighbouring atoms. The EXAFS χ(k) signal contains sum of contributions arising from all the scattering paths, as expressed in Equation 1.4. The derivation of this EXAFS equation can be found elsewhere.[115,116]

$$\chi(k) = \Sigma_J S_0^2 N_J \frac{|f_J(k)|}{KR_J^2}\, e^{-2R_J/\lambda(k)} e^{-2\sigma_J^2 k^2} \sin\left(2kR_J + \delta_c(k) + \delta_J(k)\right) \qquad \textbf{(1.4)}$$

where S_0^2 is the amplitude reduction factor which is due to the relaxation of all other electrons in the absorbing atom to the hole in the core level, and it is completely correlated with N_J, the coordination number or the degeneracy of a particular scattering path J. The term f_J represents the scattering amplitude, the term $e^{-2R_J/\lambda(k)}$ is due to the inelastic loss in the scattering process, while the mean free path of the ejected photoelectron from the absorber atom is designated by the term $\lambda(k)$. The amplitude of the EXAFS waves depends on the coordination number and the backscattering power of neighbouring atoms. The frequency of the EXAFS oscillation is inversely proportional to the average interatomic distance between the neighboring atoms. Dampening of the EXAFS wave is seen at higher k-ranges due to thermal disorder (σ), and the term $e^{-2\sigma_J^2 k^2}$

accounts for the k-dependent dampening of the EXAFS wave. The phase shift due to the central atom and the phase shift due to the neighboring atoms are represented by the terms $\delta_c(k)$ and $\delta_J(k)$, respectively. The interaction of the photoelectron with the positively charged nucleus of the absorbing atom and neighboring atoms leads to energy losses and increased wavelength of the photoelectron, and thus causes the phase shift. The phase shift is responsible for the typically smaller interatomic distances observed in the EXAFS spectrum as compared to the theoretical values. The Fourier transformation of the k-space data provides a photoelectron scattering profile as a function of the radial distance from the absorber (also known as R-space).

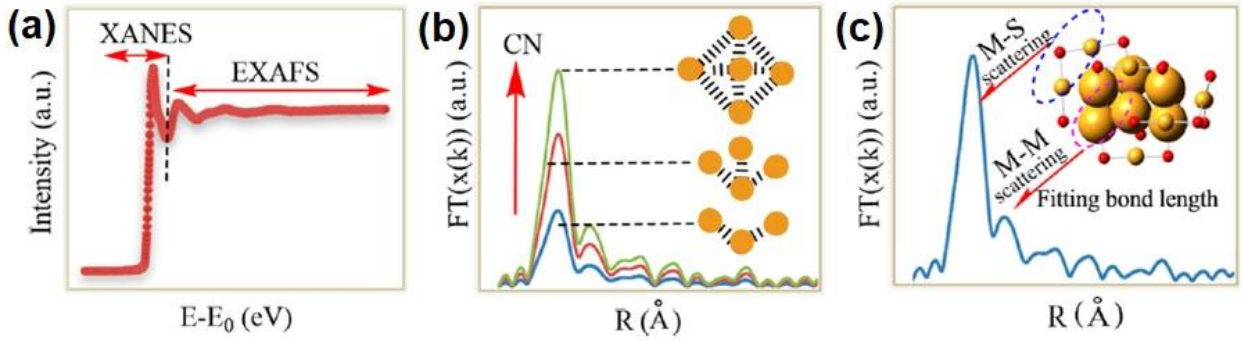

Figure 1.5. (a) Description of XANES and EXAFS regions of a XAS spectrum. (b) Simulated EXAFS spectra in R-space correlating peak intensity with coordination number (CN). (c) EXAFS spectra in R-space identifying different scattering path. Reprinted, with slight modification, from ref. 105. Copyright 2021, American Chemical Society.

EXAFS analysis entails calculating the theoretical EXAFS spectrum using a model structure and refining structural parameters (N_J, delR, σ^2, ΔE_0) to best match the experimental data. The term N_J gives the number of neighbouring atoms at a distance R_J, while the term delR measures the difference between first neighbor distance from the model and fitted distance. The term σ^2 accounts for both static and thermal disorder in the neighbouring atom position, while the term ΔE_0, measures the difference between chosen edge and fitted edge, and it is used to align the energy scale of the theoretical spectrum to match the measured spectrum. The relative fit of the model and experimental data is reported over the fitting range by an R-factor. Modelling involves determining all possible scattering paths of photoelectrons from a selected absorbing atom. In this thesis, EXAFS data treatments (background subtraction, normalization of EXAFS oscillations, k-space transformations, and Fourier transform of k-space data into R-space) and EXAFS data

modeling were done using the Demeter software package.[117] The details of EXAFS fitting procedures can be found elsewhere.[115,117] In addition to the R-factor to be typically less than 5% for a meaningful fit, it is also important to critically evaluate the physical significance of the modelled data. For instance, the amplitude reduction factor (S_0^2) should typically have a value between 0.7 and 1, while the mean square disorder (σ^2) must a positive value and most often be less than 0.01 (except for high temperature systems). Also, the ΔE_0 value must be less than 10 eV, as there is no physical reality in shifting the sine wave of the theoretical model by more than a period to better match experimental data. The delR value should be small, typically < ±0.05 Å, otherwise the wrong theoretical model was likely used. Finally, low correlations, typically less than 85%, between the parameters (N and S_0^2, and ΔE_0 and R) are required for an acceptable fit.

EXAFS is a bulk technique and does not require long-range order.[108,116] It is suitable for different kinds of samples including crystals, amorphous samples, solutions, as well as gas-phase samples. EXAFS analysis gives average values over all absorbing atoms in a sample, and thus homogeneity of sample composition is essential. Unlike SC-XRD, EXAFS can typically distinguish transition metals of similar atomic number due to its element-specific nature. EXAFS fitting analysis provides local structure information like coordination numbers (CNs) and interatomic bond distances between the absorbing atom and its neighbouring atoms. An atom in the bulk of face-centred cubic (fcc) materials such as Ag, Au, Pd, etc. has 12 first shell neighboring atoms, while surface atoms of nanoparticles typically have much lower CN values as a certain number of neighboring atoms are missing on the surface. A greater number of atoms are exposed to the surface as the particle size decreases from the bulk to clusters. The EXAFS peak intensity is directly related to the CN value as shown in Figure 1.5(b), and small-sized clusters typically have low CNs that correspond to weaker EXAFS peak intensities. An increase in EXAFS peak intensity, and thus CN value, occurs when there is growth in the average cluster size, for example, due to sintering. The Fourier-transformed EXAFS peaks in R-space relate to the scattering paths of the photoelectron waves in different shells, and multi-shell EXAFS fittings can give bond distances of different bonding pairs in a sample (Figure 1.5(c)). By extension, more structural information can be obtained by conducting multi-element and multi-edge XAS measurements, as was done in this thesis. EXAFS is a remarkable tool for monitoring the structural changes in metal clusters, and it is best complemented with other experimental techniques like TEM, XPS, and

theoretical simulations to achieve detailed insights into the structure-property correlations of metal clusters.

1.5.4 Pair Distribution Function (PDF)

Pair distribution function (PDF) analysis is a total scattering technique that can provide structural information about amorphous materials, disordered crystallites, and nanomaterials as atomic periodicity is not required for PDF analysis.[118,119] While the long-range order of atoms is deduced from the Bragg peaks, the local atomic structure (i.e. short-range order) is obtained from the broad and less-defined features arising from underlying diffuse scattering in an X-ray diffractogram.[118-120] Total scattering is an excellent probe of local structure, but also of intermediate length scales which are not accessible by many techniques. For instance, EXAFS analysis mainly probes just the first coordination sphere, and possibly the second or third to a lesser extent thus giving limited information about the studied materials. PDF analysis can cover much longer length scales (>200 Å) and provide unparalleled structural information that may not be available from most other techniques.[120,121] PDF analysis can be used to learn about the structures of clusters and nanoparticles which are too small to produce Bragg peaks, making it a very suitable technique for metallic cluster materials.[122-124] Quantitatively, atomic PDF analysis describes the local structure by measuring/providing the probability of finding two atoms separated by a certain distance in a material under investigation. It is a radial distribution G(r) function, and the peaks are not sharp delta functions because of the thermal motion of the atoms.[108,120,121] The intensity of a point in G(r) is proportional to the number of pairs of atoms at that r value weighted by products of the scattering powers of the pairs. In contrast to EXAFS, PDF analysis enables non-element specific and long order measurements along with quick data collection.[108] Nevertheless, both EXAFS and PDF analyses are bulk techniques and can complement each other.

1.5.4.1 Obtaining Experimental PDF: Instrumentation, Sample Preparation, Total Scattering Measurements, and PDF Generation

To obtain a decent spatial resolution for the local structure of the material, the diffraction data acquisition must be done at large Q-range (high diffraction angles, $Q = 4\pi\sin\theta/\lambda$) using high energy (very short wavelength) X-ray radiation, with both excellent counting statistics and optimum background containment (to give an almost clean and featureless background).[118,123]

These requirements necessitate exclusive reliance on high-quality X-ray beams that are obtainable at synchrotron facilities. The total scattering measurements in this thesis were performed at the recently commissioned Brockhouse X-ray Diffraction and Scattering - High Energy Wiggler (BXDS-HEW) beamline at the Canadian Light Source (CLS), Saskatoon, Canada. Sample preparation involves careful sample packing into a one-end-closed quartz capillary (0.8 mm in diameter) and the loaded capillary is positioned between a heating filament along the beam direction. Importantly, beam alignment is necessary to ensure that beam hits the sample through the capillary only, but not the heating filament and/or temperature probe as these materials can contribute significantly to beam scattering. The whole set-up can be monitored closely throughout the measurement using in-house cameras installed inside the beamline hutch. While the temperature probe reads the actual sample temperature, the temperature of the heating filament is controlled remotely outside the beamline hutch. Both the set and measured temperature are in close agreement with ca. 3% error at temperature below 200 °C and ca. 1% error at higher temperatures. This set-up enables *in situ* heating of samples while measuring total scattering.

Figure 1.6 qualitatively describes the steps involved in obtaining experimental PDF data from a total scattering pattern acquired for a Ni sample using GSAS-II software.[125] The 2D scattering pattern is subjected to azimuthal integration to give I(Q) data, which is called intensity profile of the 2D scattering pattern. Then, necessary corrections and data normalization are applied to ensure I(Q) goes to 1 at high Q. This normalized function is referred to as the structure function, S(Q), and it is further processed to give the F(Q) which is a reduced structure function in reciprocal space. The Fourier transform of the function F(Q) converts the data from reciprocal space to real space giving the G(r) function. The underlying mathematical operations are not trivial and the quantitative descriptions of generating PDF data can be found in literature.[123] There are several excellent software options, both open-sourced and commercial, that can be used for these exercises. GSAS-II and PDFgetX3 were employed to process the PDF data reported in this thesis.[125,126]

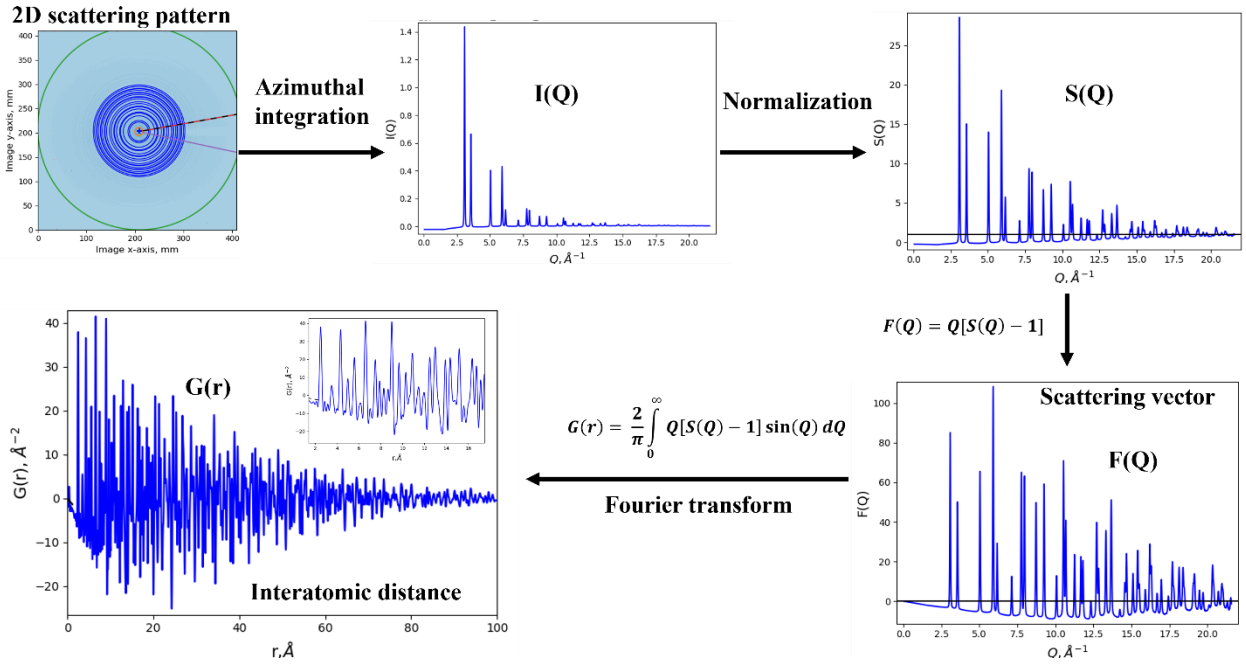

Figure 1.6. Steps in obtaining experimental PDF data from a 2D scattering pattern image of a standard nickel sample. Unpublished work, Kazeem O. Sulaiman.

1.5.4.2 Differential PDF of Supported Metal Clusters

Analyzing the PDF data of supported metal catalysts can be challenging as it contains information about both the support and the supported metal components, and the use of the differential PDF (dPDF) concept is commonly adopted to circumvent this challenge.[127-129] For example, Harrington *et al.* subtracted the PDF of ferrihydrite from the PDF of ferrihydrite with arsenate adsorbed on the surface to reveal the bidentate binuclear binding mechanism in agreement with previously reported EXAFS data.[127] Similar dPDF analysis was employed to investigate the interfacial structure of arsenate oxyanions adsorbed onto gamma-alumina nanoparticles, and the results indicated a bidentate binuclear coordination environment to the octahedral Al of γ-alumina in agreement with density functional theory (DFT) calculations.[128] With respect to heterogeneous catalysts, the dPDF approach assumes that PDF data from the support can be accurately subtracted from the catalyst PDF data to obtain dPDF data that reflects only the local atomic ordering of the supported particles. It is noteworthy that any noticeable changes in the structure of the support during active metal deposition and thermal treatment can lead to difficulties in obtaining adequate dPDF data for analysis. This represents a major limitation of the differential approach, but it can

be overcome by treating the support material under similar conditions, such as thermal treatment at the same temperature.[129]

1.5.4.3 PDF Data Reduction, Modelling, and Analysis

There are few reports that have shown the usefulness of PDF analysis in the characterization of Au nanoparticles,[120-122,131,132] and this thesis extends this technique to the characterization of atom-precise $M_{25}(SR)_{18}$ (M is Ag or Au) clusters. One important variable with respect to sample preparation is to have a high loading of metal clusters on a weakly scattering support. This leads to significant improvement in the separation of cluster scattering peaks from that of the support in the dPDF approach. There are several ways of modelling/analyzing the obtained dPDF; visual inspection, small box modelling, R-dependent refinements, cluster/nanoparticle modeling/refinement, Reverse Monte Carlo methods, and machine learning.[133-135] Visual inspection is usual the first step and sometimes it is the only thing required to get necessary information from the data. Small box and R-dependent modelling can be done using PDFgui software,[133] while cluster/nanoparticle modeling can be done with DISCUS software.[135] The dPDF data in this thesis were modeled and analyzed using both visual inspection and small box refinement with PDFgui software. The dPDF data clearly showed the structural evolution of metal clusters upon thermal oxidation of protecting thiolate ligands off the metal surfaces.

1.6 Research Objectives

The major goal of this research work is the structural characterization of atom-precise Ag, Au, and AgPd bimetallic clusters for selective heterogeneous catalysis. The main hypotheses of this thesis were: (i) that low-temperature activation of thiolate-protected Ag clusters might prevent significant sintering and metal oxide/sulfide formation; (ii) that mildly activated Ag clusters on carbon support might be good templates for sequential deposition of Pd to synthesize AgPd bimetallic clusters; (iii) that dopant Pd atoms can be positioned in surface/staple positions of clusters for better accessibility for catalysis by controlling the reduction kinetics of metal-thiolate precursors in a direct synthesis method; and (iv) that total scattering measurements with pair distribution function analysis might complement XAS measurements in following the structural transformations that occur upon thermal activation of such atom-precise metal clusters. These

hypotheses were tested with a focus on Ag and Ag-based bimetallic clusters, while Au clusters were used as a control in the last experimental chapter. Specific objectives for each of the experimental chapters are described below.

Atom-precise $Au_{25}(SR)_{18}^-$ clusters have been extensively studied as catalysts and precursors for Au-based bimetallic catalysts for various chemical reactions of industrial and commercial importance. Thus, there was research interest in the development of similar atom-precise clusters of catalytically active noble metals other than Au. Considering its lower cost and higher relative abundance when compared to Au, Ag is a remarkably good choice but its susceptibility to oxidation imposes possible limitations on the development of heterogeneous catalysts based on thiolate-protected Ag clusters. In late 2015, the successful synthesis and crystal structure of $Ag_{25}(SR)_{18}^-$ clusters was reported. The $Ag_{25}(SR)_{18}^-$ clusters have a similar (but not identical) atomic arrangements and ligand counts as $Au_{25}(SR)_{18}^-$ clusters. At that time, there was a knowledge gap as to whether $Ag_{25}(SR)_{18}^-$ clusters could be activated and used for catalysis. So, the first research objective was to follow the activation of the 2,4-dimethylbenzenethiolate-protected Ag_{25} clusters using element specific XAS and other characterization techniques. The selective oxidation of styrene to styrene oxide was chosen as a model chemical reaction to assess the particle size-dependent activity of the Ag clusters on carbon supports. The results of this study are presented in Chapter 2 and titled, 'Activation of Atom-Precise Silver Clusters on Carbon Supports for Styrene Oxidation Reactions'.

Results documented in Chapter 2 clearly showed that Ag-thiol bonds are selectively oxidized from the clusters upon mild heat treatments without formation of Ag_2O or Ag_2S, and thus the activated Ag clusters on carbon supports were hypothesized to be good starting materials for the design of Ag-based bimetallic clusters with other metals. Pd was considered as the second metal as Ag is a poor hydrogenation catalyst by itself and Pd, while being an excellent hydrogenation catalyst, is often unable to selectively reduce alkynes to alkenes. The second objective was to employ mildly activated Ag_{25} clusters on carbon supports as a precursor for designing AgPd bimetallic clusters and using these clusters as selective catalysts for hydrogenation reactions. By sequential deposition of Pd onto Ag clusters there is no practical limit to the number of Pd atoms that can be incorporated into the final AgPd bimetallic clusters. Chapter 3 of this thesis

contains the details of this study and is titled, 'Atom-Precise Ag Clusters as Precursors for Bimetallic AgPd Heterogeneous Catalysts'.

A wide range of bimetallic clusters have been prepared using co-reduction strategies, but this strategy is often constrained by purification challenges. Following recent developments in the synthesis and purification of atom-precise bimetallic clusters, the co-reduction method was reconsidered in a quest to prepare AgPd bimetallic clusters with atom-precision and a limited number of dopant metal atoms (Pd) in the matrix of the host metal (Ag) clusters. Previous literature reported that a single-atom Pd dopant was found in atom-precise $PdAg_{24}(SR)_{18}^{2-}$ bimetallic clusters prepared by the co-reduction method, and SC-XRD measurements indicated Pd occupied the central core position.[28,66] Typically, crystallography methods cannot unambiguously distinguish transition metals of similar atomic numbers (like Ag and Pd). The third research objective was to see what the maximum loading of Pd was in Ag clusters and perform structural characterization of atom-precise $Ag_{24}Pd_1(SR)_{18}^{2-}$ bimetallic clusters using element-specific spectroscopic methods (XPS and XAS) to determine their actual structures. Mass spectrometry data confirmed that only the singly doped $Ag_{24}Pd$ species could be synthesized, and spectroscopy data showed that the Pd atoms in such clusters are actually present in a thiolate environment which indicates that the Pd occupies the non-central position of atom-precise $Ag_{24}Pd_1(SR)_{18}^{2-}$ bimetallic clusters. The details of this work are presented in Chapter 4 and titled, 'Exploring the Structure of Atom-Precise Silver-Palladium Bimetallic Clusters Prepared via Improved Single-Pot Co-reduction Synthesis Protocol'.

With the establishment of the Pd loading limit and the position of the Pd dopant in $Ag_{24}Pd_1(SR)_{18}^{2-}$ bimetallic clusters, insight into the structure-activity relationships for these atom-precise $Ag_{24}Pd_1(SR)_{18}^{2-}$ clusters as heterogeneous catalysts was possible. Intuitively, atomically isolated Pd atoms on Ag cluster surfaces would be more accessible for catalysis. Earlier work in Chapter 3 established that AgPd bimetallic systems were excellent catalysts for the selective hydrogenations of alkynes to alkenes, though it was difficult to control the structures of the final catalysts. Thus, the singly-doped $Ag_{24}Pd_1$ bimetallic clusters were expected to be improved model catalysts for selective alkyne hydrogenation reactions. The fourth research objective was to investigate the thermal activation of carbon-supported $Ag_{24}Pd_1(SR)_{18}^{2-}$ bimetallic clusters in comparison with carbon-supported $Ag_{25}(SR)_{18}^{-}$ monometallic clusters and evaluate their

performance as heterogeneous catalysts for the selective hydrogenation of alkynols to alkenols. The results of this study are documented in Chapter 5 and titled, 'Atom-Precise Silver-Palladium Bimetallic Clusters on Carbon Supports as Selective Hydrogenation Catalysts'.

Many research groups, including ours, have demonstrated that TEM and XAS are good techniques for monitoring particle size growth upon thermal activation of supported metal clusters. Unlike TEM, XAS is mostly a bulk technique that can be used to probe both chemical bonding and local structure properties of metal clusters both with and without thiolate ligands. However, EXAFS modelling often mainly probes the first coordination sphere, and thus giving somewhat limited information about the clusters. Pair distribution function (PDF) analysis is a total scattering technique that allow long order measurements with quick data collection, and it is suitable for probing the structures of metal clusters that are too small to produce Bragg peaks. While others have performed PDF analysis to characterize Au nanoparticles, PDF work had yet to be done on atom-precise metal clusters which have smaller sizes than nanoparticles. The fifth research objective was to assess the potential of differential PDF analyses towards the structural characterization of metallic atom-precise Au and Ag clusters upon activation. Interestingly, the Ag and Au systems behave very differently upon calcination at higher temperatures. The results of this study are reported in Chapter 6 and titled, 'Taking A Different Road: Following Ag_{25} and Au_{25} Clusters Activation via *In Situ* Differential Pair Distribution Function Analysis'.

1.7 Thesis Organization and Scope

This PhD thesis discusses the synthesis and structural characterization of atom-precise Ag, Au, and AgPd bimetallic cluster-based catalysts for selective catalysis. It is divided into seven chapters, and Chapters 2 and 4 are adapted from articles published in different journals. Chapters 3, 5, and 6 are manuscripts to be submitted for publication in the near future. The Chapter 1 gives an overview of the literature of the subject of study and highlights the identified knowledge gaps that were investigated in the subsequent chapters of the thesis. In Chapter 2, atom-precise $Ag_{25}(SPhMe_2)_{18}^-$ clusters were prepared and immobilized onto carbon supports, followed by a thermal activation study to produce activated clusters on carbon supports without sintering or formation of Ag_2O or Ag_2S. The outcome of this study revealed that atom-precise thiolate-protected Ag clusters could be carefully activated on carbon supports without significant particle growth under mild heat treatment. In Chapter 3, the mildly activated Ag clusters on carbon

supports were used as precursors to make AgPd bimetallic clusters via sequential reduction of Pd ions onto Ag clusters. It was found out that there was no limit to the amount of Pd that could be incorporated, and X-ray absorption spectroscopy analysis revealed cluster-in-cluster atomic arrangements in the bimetallic AgPd heterogenous catalysts prepared via sequential reduction approach. The Pd sites changed from subsurface to surface with increased Pd loading and these structural changes were reflected in the catalytic performance of the clusters as model catalysts for selective hydrogenation of alkynol substrates. In Chapter 4, direct synthesis was used to prepare AgPd bimetallic clusters with the precise atom composition of $Ag_{24}Pd_1(SPhMe_2)_{18}^{2-}$ as revealed by mass spectrometry data. These atom-precise bimetallic clusters species were the only atom-precise bimetallic system formed which indicated that a limited amount of Pd could be incorporated into Ag clusters via the direct synthesis approach. Element-specific structural analysis of the $Ag_{24}Pd_1(SPhMe_2)_{18}^{2-}$ bimetallic clusters suggested that the single Pd dopant occupied the non-central position of clusters. This was followed with the catalytic studies of carbon-supported $Ag_{24}Pd_1(SPhMe_2)_{18}^{2-}$ bimetallic clusters with and without activation for selective hydrogenation of alkynol substrates (Chapter 5). In Chapter 6, total scattering measurements of the clusters was done in order to gain insight into the activation of atom-precise thiolate-protected metal clusters, $Au_{25}(SR)_{18}^{-}$ and $Ag_{25}(SR)_{18}^{-}$, on alumina supports using *in situ* differential pair distribution function analysis. Chapter 7 wraps up this thesis with a summary of research outcomes and lessons learned in all these studies, along with proposals for future resarch directions with proof of concept studies.

1.8 References

1. J. Zeng, Q. Zhang, J. Chen, Y. Xia. A Comparison Study of the Catalytic Properties of Au-Based Nanocages, Nanoboxes, and Nanoparticles, *Nano Lett.* 2010, **10**, 30-35.

2. G. Yue, S. Su, N. Li, M. Shuai, X. Lai, D. Astruc, P. Zhao. Gold Nanoparticles as Sensors in the Colorimetric and Fluorescence Detection of Chemical Warfare Agents, *Coord. Chem. Rev.* 2016, **311**, 75-84.

3. Z. Wang, X. Pan, S. Qian, G. Yang, F. Du, X. Yuan. The Beauty of Binary Phases: A Facile Strategy for Synthesis, Processing, Functionalization, and Application of Ultrasmall Metal Nanoclusters, *Coord. Chem. Rev.* 2021, **438**, 213900.

4. Q. Zhu, X. Huang, Y. Zeng, K. Sun, L. Zhou, Y. Liu, L. Luo, S. Tian, X. Sun. Controllable Synthesis and Electrocatalytic Applications of Atomically Precise Gold Nanoclusters, *Nanoscale Adv.* 2021, **3**, 6330-6341.

5. W.A. de Heer. The Physics of Simple Metal Clusters: Experimental Aspects and Simple Models, *Rev. Mod. Phys.* 1993, **65**, 611-676.

6. L. Shang, S. Dong, G.U. Nienhaus. Ultra-Small Fluorescent Metal Nanoclusters: Synthesis and Biological Applications, *Nano Today* 2011, **6**, 401-418.

7. I. Díez, R.H.A. Ras. Fluorescent Silver Nanoclusters, *Nanoscale* 2011, **3**, 1963-1970.

8. S. Choi, R.M. Dickson, J. Yu. Developing Luminescent Silver Nanodots for Biological Applications, *Chem. Soc. Rev.* 2012, **41**, 1867-1891.

9. Y. Zhu, H. Qian, R. Jin. Catalysis Opportunities of Atomically Precise Gold Nanoclusters, *J. Mater. Chem.* 2011, **21**, 6793-6799.

10. Y.-S. Chen, H. Choi, P.V. Kamat. Metal-Cluster-Sensitized Solar Cells. A New Class of Thiolated Gold Sensitizers Delivering Efficiency Greater Than 2%, *J. Am. Chem. Soc.* 2013, **135**, 8822-8825.

11. X. Yuan, Y. Tay, X. Dou, Z. Luo, D.T. Leong, J. Xie. Glutathione-Protected Silver Nanoclusters as Cysteine-Selective Fluorometric and Colorimetric Probe, *Anal. Chem.* 2013, **85**, 1913-1919.

12. X. Yuan, M.I. Setyawati, D.T. Leong, J. Xie. Ultrasmall Ag^{+}-rich Nanoclusters as Highly Efficient Nanoreservoirs for Bacterial Killing, *Nano Res.* 2014, **7**, 301-307.

13. Q. Zhang, J. Xie, J. Liang, J.Y. Lee. Synthesis of Monodisperse Ag-Au Alloy Nanoparticles with Independently Tunable Morphology, Composition, Size, and Surface Chemistry and Their 3-D Superlattices, *Adv. Funct. Mater.* 2009, **19**, 1387-1398.

14. J. Huang, Y. Zhu, M. Lin, Q. Wang, L. Zhao, Y. Yang, K.X. Yao, Y. Han. Site-Specific Growth of Au-Pd Alloy Horns on Au Nanorods: A Platform for Highly Sensitive Monitoring of Catalytic

Reactions by Surface Enhancement Raman Spectroscopy, *J. Am. Chem. Soc.* 2013, **135**, 8552-8561.

15. A.S.K. Hashmi, G.J. Hutchings. Gold catalysis, *Angew. Chem. Int. Ed. Engl.* 2006, **45**, 7896-7936.

16. V. Sudheeshkumar, K.O. Sulaiman, R.W.J. Scott. Activation of Atom-Precise Clusters for Catalysis, *Nanoscale Adv.* 2020, **2**, 55-69.

17. P.J.G. Goulet, R.B. Lennox. New Insights into Brust-Schiffrin Metal Nanoparticle Synthesis, *J. Am. Chem. Soc.* 2010, **132**, 9582-9584.

18. M. Zhu, E. Lanni, N. Garg, M.E. Bier, R. Jin. Kinetically Controlled, High-Yield Synthesis of Au_{25} Clusters, *J. Am. Chem. Soc.* 2008, **130**, 1138-1139.

19. S. Campisi, M. Schiavoni, C.E. Chan-Thaw, A. Villa. Untangling the Role of the Capping Agent in Nanocatalysis: Recent Advances and Perspectives, *Catalysts* 2016, **6**, 185.

20. I. Chakraborty, T. Pradeep. Atomically Precise Clusters of Noble Metals: Emerging Link between Atoms and Nanoparticles, *Chem. Rev.* 2017, **117**, 8208-8271.

21. R.R. Nasaruddin, T. Chen, N. Yan, J. Xie. Roles of Thiolate Ligands in the Synthesis, Properties and Catalytic Application of Gold Nanoclusters, *Coord. Chem. Rev.* 2018, **368**, 60-79.

22. L. Liu, A. Corma. Metal Catalysts for Heterogeneous Catalysis: From Single Atoms to Nanoclusters and Nanoparticles, *Chem. Rev.* 2018, **118**, 4981-5079.

23. J. Yan, B.K. Teo, N. Zheng. Surface Chemistry of Atomically Precise Coinage-Metal Nanoclusters: From Structural Control to Surface Reactivity and Catalysis, *Acc. Chem. Res.* 2018, 51, **12**, 3084-3093.

24. A. Mathew, P.R. Sajanlal, T. Pradeep. A Fifteen-Atom Silver Cluster Confined in Bovine Serum Albumin, *J. Mater. Chem.* 2011, **21**, 11205-11212.

25. G. Liu, Y. Shao, K. Ma, Q. Cui, F. Wu, S. Xu. Synthesis of DNA-Templated Fluorescent Gold Nanoclusters, *Gold Bull.* 2012, **45**, 69-74.

26. J. Fang, B. Zhang, Q. Yao, Y. Yang, J. Xie, N. Yan. Recent Advances in The Synthesis and Catalytic Applications of Ligand-Protected, Atomically Precise Metal Nanoclusters, *Coord. Chem. Rev.* 2016, **322**, 1-29.

27. X. Yuan, X. Dou, K. Zheng, J. Xie. Recent Advances in the Synthesis and Applications of Ultrasmall Bimetallic Nanoclusters, *Part. Part. Syst. Charact.* 2015, **32**, 613-629.

28. M.S. Bootharaju, C.P. Joshi, M.R. Parida, O.F. Mohammed, O.M. Bakr, Angew. Templated Atom-Precise Galvanic Synthesis and Structure Elucidation of a $[Ag_{24}Au(SR)_{18}]^-$ Nanocluster, *Angew. Chem. Int. Ed.* 2016, **55**, 922-926.

29. M.W. Heaven, A. Dass, P.S. White, K.M. Holt, R.W. Murray. Crystal Structure of the Gold Nanoparticle $[N(C_8H_{17})_4][Au_{25}(SCH_2CH_2Ph)_{18}]$, *J. Am. Chem. Soc.* 2008, **130**, 3754-3755.

30. O. Lopez-Acevedo, J. Akola, R.L. Whetten, H. Grönbeck, H. Häkkinen. Structure and Bonding in the Ubiquitous Icosahedral Metallic Gold Cluster $Au_{144}(SR)_{60,}$ *J. Phys. Chem. C* 2009, **113**, 5035-5038.

31. A. Desireddy, B.E. Conn, J. Guo, B. Yoon, R.N. Barnett, B.M. Monahan, K. Kirschbaum, W.P. Griffith, R. L. Whetten, U. Landman, T.P. Bigioni. Ultrastable Silver Nanoparticles, *Nature* 2013, **501**, 399-402.

32. C.P. Joshi, M.S. Bootharaju, M.J. Alhilaly, O.M. Bakr. $[Ag_{25}(SR)_{18}]^-$: The "Golden" Silver Nanoparticle, J. *Am. Chem. Soc.* 2015, **137**, 11578-11581.

33. K.L.D.M. Weerawardene, E.B. Guidez, C.M. Aikens. Photoluminescence Origin of $Au_{38}(SR)_{24}$ and $Au_{22}(SR)_{18}$ Nanoparticles: A Theoretical Perspective, *J. Phys. Chem. C* 2017, **121**, 15416-15423.

34. X. Kang, H. Chong, M. Zhu. $Au_{25}(SR)_{18}$: The Captain of the Great Nanocluster Ship, *Nanoscale* 2018, **10**, 10758-10834.

35. Y. Negishi, K. Nobusada, T. Tsukuda. Glutathione-Protected Gold Clusters Revisited: Bridging the Gap between Gold(I)-Thiolate Complexes and Thiolate-Protected Gold Nanocrystals, *J. Am. Chem. Soc.* 2005, **127**, 5261-5270.

36. X. Meng, Q. Xu, S. Wang, M. Zhu. Ligand-Exchange Synthesis of Selenophenolate-Capped Au_{25} Nanoclusters, *Nanoscale* 2012, **4**, 4161-4165.

37. A. Ghosh, J. Hassinen, P. Pulkkinen, H. Tenhu, R.H.A. Ras, T. Pradeep. Simple and Efficient Separation of Atomically Precise Noble Metal Clusters, *Anal. Chem.* 2014, **86**, 12185-12190.

38. Y. Niihori, Y. Kikuchi, D. Shima, C. Uchida, S. Sharma, S. Hossain, W. Kurashige, Y. Negishi. Separation of Glutathionate-Protected Gold Clusters by Reversed-Phase Ion-Pair High-Performance Liquid Chromatography, *Ind. Eng. Chem. Res.* 2017, **56**, 1029-1035.

39. D. Li, B. Kumari, X. Zhang, C. Wang, X. Mei, V.M. Rotello. Purification and Separation of Ultra-Small Metal Nanoclusters, *Adv. Colloid Interface Sci.* 2019, **276**, 102090.

40. Y. Negishi, S. Hashimoto, A. Ebina, K. Hamada, S. Hossain, T. Kawawaki, Atomic-Level Separation of Thiolate-Protected Metal Clusters, *Nanoscale* 2020, **12**, 8017-8039.

41. A. Shivhare, L. Wang, R.W.J. Scott. Isolation of Carboxylic Acid-Protected Au_{25} Clusters Using a Borohydride Purification Strategy, *Langmuir* 2015, **31**, 1835-1841.

42. K.M. Harkness, Y. Tang, A. Dass, J. Pan, N. Kothalawala, V.J. Reddy, D.E. Cliffel, B. Demeler, F. Stellacci, O.M. Bakr, J.A. McLean. $Ag_{44}(SR)_{30}^{4-}$: A Silver-Thiolate Superatom Complex, *Nanoscale* 2012, **4**, 4269-4274.

43. L.G. AbdulHalim, S. Ashraf, K. Katsiev, A.R. Kirmani, N. Kothalawala, D.H. Anjum, S. Abbas, A. Amassian, F. Stellacci, A. Dass, I. Hussain, O.M. Bakr. A Scalable Synthesis of Highly Stable and Water Dispersible $Ag_{44}(SR)_{30}$ Nanoclusters, *J. Mater. Chem. A* 2013, **1**, 10148-10154.

44. K. Zheng, X. Yuan, J. Xie. Effect of Ligand Structure on the Size Control of Mono- and Bi-Thiolate-Protected Silver Nanoclusters, *Chem. Commun*. 2017, **53**, 9697-9700.

45. K. Zheng, V. Fung, X. Yuan, D-e. Jiang, J. Xie. Real Time Monitoring of the Dynamic Intracluster Diffusion of Single Gold Atoms into Silver Nanoclusters, *J. Am. Chem. Soc.* 2019, **141**, 18977-18983.

46. X. Yuan, B. Zhang, Z. Luo, Q. Yao, D.T. Leong, N. Yan, J. Xie. Balancing the Rate of Cluster Growth and Etching for Gram-Scale Synthesis of Thiolate-Protected Au_{25} Nanoclusters with Atomic Precision, *Angew. Chem. Int. Ed.* 2014, **53**, 4623-4627.

47. O.M. Bakr, V. Amendola, C.M. Aikens, W. Wenseleers, R. Li, L. Dal Negro, G.C. Schatz, F. Stellacci. Silver Nanoparticles with Broad Multiband Linear Optical Absorption, *Angew. Chem. Int. Ed.* 2009, **48**, 5921-5926.

48. M. Zhu, C.M. Aikens, F.J. Hollander, G.C. Schatz, R. Jin. Correlating the Crystal Structure of a Thiol-Protected Au_{25} Cluster and Optical Properties, *J. Am. Chem. Soc.* 2008, **130**, 5883-5885.

49. A. Mathew, T. Pradeep. Noble Metal Clusters: Applications in Energy, Environment, and Biology, *Part. Part. Syst. Char.* 2014, **31**, 1017-1053.

50. S. Eustis, M.A. El-Sayed. Why Gold Nanoparticles Are More Precious Than Pretty Gold: Noble Metal Surface Plasmon Resonance and Its Enhancement of the Radiative and Nonradiative Properties of Nanocrystals of Different Shapes, *Chem. Soc. Rev.* 2006, **35**, 209-217.

51. J. Jana, M. Ganguly, T. Pal. Enlightening Surface Plasmon Resonance Effect of Metal Nanoparticles for Practical Spectroscopic Application, *RSC Adv.* 2016, **6**, 86174-86211.

52. C.M. Aikens. Electronic and Geometric Structure, Optical Properties, and Excited State Behavior in Atomically Precise Thiolate-Stabilized Noble Metal Nanoclusters, *Acc. Chem. Res.* 2018, **51**, 3065-3073.

53. M.S. Bootharaju, C.P. Joshi, M.J. Alhilaly, O.M. Bakr. Switching a Nanocluster Core from Hollow to Nonhollow, *Chem. Mater.* 2016, **28**, 3292-3297.

54. H. Yang, Y. Wang, H. Huang, L. Gell, L. Lehtovaara, S. Malola, H. Häkkinen, N. Zheng. All-Thiol-Stabilized Ag_{44} and $Au_{12}Ag_{32}$ Nanoparticles with Single-Crystal Structures, *Nat. Commun.* 2013, **4**, 2422.

55. L.J. Barbour. Single-Crystal X-Ray Diffraction, *Comprehensive Supramolecular Chemistry II* 2017, 23-43.

56. Z. Chen, A.G. Walsh, X. Wei, M. Zhu, P. Zhang. Site-Specific Electronic Properties of $[Ag_{25}(SR)_{18}]^-$ Nanoclusters by X-Ray Spectroscopy, *Small* 2021, **17**, 2005162.

57. A. Visikovskiy, H. Matsumoto, K. Mitsuhara, T. Nakada, T. Akita, Y. Kido. Electronic d-Band Properties of Gold Nanoclusters Grown on Amorphous Carbon, *Phys. Rev. B* 2011, **83**, 165428.

58. S.L. Christensen, M.A. MacDonald, A. Chatt, P. Zhang, H. Qian, R. Jin. Dopant Location, Local Structure, and Electronic Properties of $Au_{24}Pt(SR)_{18}$ Nanoclusters, *J. Phys. Chem. C* 2012, **116**, 26932-26937.

59. Y. Negishi, T. Iwai, M. Ide. Continuous Modulation of Electronic Structure of Stable Thiolate-Protected Au_{25} Cluster by Ag Doping, *Chem. Commun.* 2010, **46**, 4713-4715.

60. H. Qian, D-e. Jiang, G. Li, C. Gayathri, A. Das, R.R. Gil, R. Jin. Monoplatinum Doping of Gold Nanoclusters and Catalytic Application, *J. Am. Chem. Soc.* 2012, **134**, 16159-16162.

61. M. Walter, M. Moseler. Ligand-Protected Gold Alloy Clusters: Doping the Superatom, *J. Phys. Chem. C* 2009, **113**, 15834-15837.

62. C.A. Fields-Zinna, M.C. Crowe, A. Dass, J.E.F. Weaver, R.W. Murray. Mass Spectrometry of Small Bimetal Monolayer-Protected Clusters, *Langmuir* 2009, **25**, 7704-7710.

63. Y. Negishi, W. Kurashige, Y. Niihori, T. Iwasa, K. Nobusada. Isolation, Structure, and Stability of a Dodecanethiolate-Protected Pd_1Au_{24} Cluster, *Phys. Chem. Chem. Phys.* 2010, **12**, 6219-6225.

64. C. Kumara, A. Dass. AuAg Alloy Nanomolecules with 38 Metal Atoms, *Nanoscale* 2012, **4**, 4084-4086.

65. M.A. Tofanelli, T.W. Ni, B.D. Phillips, C.J. Ackerson. Crystal Structure of the $PdAu_{24}(SR)_{18}^0$ Superatom, *Inorg. Chem.* 2016, **55**, 999-1001.

66. J. Yan, H. Su, H. Yang, S. Malola, S. Lin, H. Häkkinen, N. Zheng. Total Structure and Electronic Structure Analysis of Doped Thiolated Silver $[MAg_{24}(SR)_{18}]^{2-}$ (M = Pd, Pt) Clusters, *J. Am. Chem. Soc.* 2015, **137**, 11880-11883.

67. A. Ghosh, O.F. Mohammed, O.M. Bakr. Atomic-Level Doping of Metal Clusters, *Acc. Chem. Res.* 2018, **51**, 3094-3103.

68. C. Yao, Y.-j. Lin, J. Yuan, L. Liao, M. Zhu, L.-h. Weng, J. Yang, Z. Wu. Mono-cadmium vs Mono-mercury Doping of Au_{25} Nanoclusters, *J. Am. Chem. Soc.* 2015, **137**, 15350-15353.

69. Y. Liu, X. Chai, X. Cai, M. Chen, R. Jin, W. Ding, Y. Zhu. Central Doping of a Foreign Atom into the Silver Cluster for Catalytic Conversion of CO_2 toward C-C Bond Formation, *Angew. Chem. Int. Ed.* 2018, **57**, 9775-9779.

70. C. Garcia, V. Truttmann, I. Lopez, T. Haunold, C. Marini, C. Rameshan, E. Pittenauer, P. Kregsamer, K. Dobrezberger, M. Stöger-Pollach, N. Barrabés, G. Rupprechter. Dynamics of Pd Dopant Atoms inside Au Nanoclusters during Catalytic CO Oxidation, *J. Phys. Chem. C* 2020, **124**, 23626-23636.

71. S. Wang, Y. Song, S. Jin, X. Liu, J. Zhang, Y. Pei, X. Meng, M. Chen, P. Li, M. Zhu, M. Metal Exchange Method Using Au_{25} Nanoclusters as Templates for Alloy Nanoclusters with Atomic Precision, *J. Am. Chem. Soc.* 2015, **137**, 4018-4021.

72. J-P. Choi, C.A. Fields-Zinna, R.L. Stiles, R. Balasubramanian, A.D. Douglas, M.C. Crowe, R.W. Murray. Reactivity of $[Au_{25}(SCH_2CH_2Ph)_{18}]^{1-}$ Nanoparticles with Metal Ions, J. *Phys. Chem. C* 2010, **114**, 15890-15896.

73. Z. Wu. Anti-Galvanic Reduction of Thiolate-Protected Gold and Silver Nanoparticles, *Angew. Chem. Int. Ed.* 2012, **51**, 2934-2938.

74. W. Fei, S. Antonello, T. Dainese, A. Dolmella, M. Lahtinen, K. Rissanen, A. Venzo, F. Maran. Metal Doping of $Au_{25}(SR)_{18}^-$ Clusters: Insights and Hindsights, *J. Am. Chem. Soc.* 2019, **141**, 16033-16045.

75. A. Shivhare, K.E. Lee, Y. Hu, R.W.J. Scott. Following the Reactivity of $Au_{25}(SC_8H_9)_{18}^-$ Clusters with Pd^{2+} and Ag^+ Ions Using *In Situ* X-ray Absorption Spectroscopy: A Tale of Two Metals, *J. Phys. Chem. C* 2015, **119**, 23279-23284.

76. M.S. Bootharaju, L. Sinatra, O.M. Bakr. Distinct Metal-Exchange Pathways of Doped Ag_{25} Nanoclusters, *Nanoscale* 2016, **8**, 17333-17339.

77. X. Kang, S. Chen, S. Jin, Y. Song, Y. Xu, H. Yu, H. Sheng, M. Zhu. Heteroatom Effects on the Optical and Electrochemical Properties of $Ag_{25}(SR)_{18}$ and Its Dopants, *ChemElectroChem* 2016, **3**, 1261-1265.

78. M. Kim, K.L.D.M. Weerawardene, W. Choi, S.M. Han, J. Paik, Y. Kim, M-G. Choi, C.M. Aikens, D. Lee. Insights into the Metal-Exchange Synthesis of $MAg_{24}(SR)_{18}$ (M = Ni, Pd, Pt) Nanoclusters, *Chem. Mater.* 2020, **32**, 10216-10226.

79. C.F. Calver, P. Dash, R.W.J. Scott. Selective Hydrogenations with Ag-Pd Catalysts Prepared by Galvanic Exchange Reactions, *ChemCatChem*, 2011, **3**, 695-697.

80. T. Mitsudome, T. Urayama, K. Yamazaki, Y. Maehara, J. Yamasaki, K. Gohara, Z. Maeno, T. Mizugaki, K. Jitsukawa, K. Kaneda. Design of Core-Pd/Shell-Ag Nanocomposite Catalyst for Selective Semihydrogenation of Alkynes, *ACS Catal.* 2016, **6**, 666-670.

81. Y. Zhu, H. Qian, R. Jin. An Atomic-Level Strategy for Unraveling Gold Nanocatalysis from the Perspective of $Au_n(SR)_m$ Nanoclusters, *Chem. Eur. J.* 2010, **16**, 11455-11462.

82. Y. Liu, H. Tsunoyama, T. Akita, T. Tsukuda. Efficient and Selective Epoxidation of Styrene with TBHP Catalyzed by Au_{25} Clusters on Hydroxyapatite, *Chem. Commun.* 2010, **46**, 550-552.

83. H. Yamamoto, H. Yano, H. Kouchi, Y. Obora, R. Arakawa, H. Kawasaki. *N*,*N*-Dimethylformamide-Stabilized Gold Nanoclusters as a Catalyst for the Reduction of 4-Nitrophenol, *Nanoscale* 2012, **4**, 4148-4154.

84. A. Shivhare, S.J. Ambrose, H. Zhang, R.W. Purves, R.W.J. Scott. Stable and Recyclable Au_{25} Clusters for The Reduction of 4-Nitrophenol, *Chem. Commun.* 2013, **49**, 276-278.

85. V. Sudheeshkumar, A. Shivhare, R.W.J. Scott. Synthesis of Sinter-Resistant Au@silica Catalysts Derived from Au_{25} Clusters, *Catal. Sci. Technol.* 2017, **7**, 272-280.

86. J. Li, R.R. Nasaruddin, Y. Feng, J. Yang, N. Yan, J. Xie. Tuning the Accessibility and Activity of $Au_{25}(SR)_{18}$ Nanocluster Catalysts via Ligand Engineering, *Chem. Eur. J. 2016*, **22**, 14816-14820.

87. D. Hu, S. Jin, Y. Shi, X. Wang, R.W. Graff, W. Liu, M. Zhu, H. Gao. Preparation of Hyperstar Polymers with Encapsulated $Au_{25}(SR)_{18}$ Clusters as Recyclable Catalysts for Nitrophenol Reduction, *Nanoscale*, 2017, **9**, 3629-3636.

88. S. Wunder, F. Polzer, Y. Lu, Y. Mei, M. Ballauff. Kinetic Analysis of Catalytic Reduction of 4-Nitrophenol by Metallic Nanoparticles Immobilized in Spherical Polyelectrolyte Brushes, *J. Phys. Chem. C* 2010, **114**, 8814-8820.

89. S. Xie, H. Tsunoyama, W. Kurashige, Y. Negishi, T. Tsukuda. Enhancement in Aerobic Alcohol Oxidation Catalysis of Au_{25} Clusters by Single Pd Atom Doping, *ACS Catal.* 2012, **2**, 1519-1523.

90. H. Qian, E. Barry, Y. Zhu, R. Jin. Doping 25-Atom and 38-Atom Gold Nanoclusters with Palladium, *Acta Phys.-Chim. Sin.* 2011, **27**, 513-519.

91. W.M. Irvine. Langmuir-Hinshelwood Mechanism. In: M. Gargaud R. Amils, J.C. Quintanilla, H.J. CleavesII, W.M. Irvine, D.L. Pinti, M. Viso (eds) Encyclopedia of Astrobiology. Springer, Berlin, Heidelberg, 2011.

92. J.A. Delgado, O. Benkirane, C. Claver, D. Curulla-Ferré, C. Godard. Advances in the Preparation of Highly Selective Nanocatalysts for the Semi-Hydrogenation of Alkynes Using Colloidal Approaches, *Dalton Trans.* 2017, **46**, 12381-12403.

93. G. Vilé, D. Baudouin, I. Remediakis, C. Copéret, N. López, J. Pérez-Ramírez. Silver Nanoparticles for Olefin Production: New Insights into the Mechanistic Description of Propyne Hydrogenation, *ChemCatChem*, 2013, **5**, 3750-3759.

94. N. Semagina, M. Grasemann, N. Xanthopoulos, A. Renken, L. Kiwi-Minsker. Structured Catalyst of Pd/ZnO on Sintered Metal Fibers for 2-methyl-3-butyn-2-ol Selective Hydrogenation, *J. Catal.* 2007, **251**, 213-222.

95. H. Zhou, X. Yang, L. Li, X. Liu, Y. Huang, X. Pan, A. Wang, J. Li, T. Zhang. PdZn Intermetallic Nanostructure with Pd-Zn-Pd Ensembles for Highly Active and Chemoselective Semi-Hydrogenation of Acetylene, *ACS Catal.* 2016, **6**, 1054-1061.

96. G.X. Pei, X.Y. Liu, A. Wang, A.F. Lee, M.A. Isaacs, L. Li, X. Pan, X. Yang, X. Wang, Z. Tai, K. Wilson, T. Zhang, Ag Alloyed Pd Single-Atom Catalysts for Efficient Selective Hydrogenation of Acetylene to Ethylene in Excess Ethylene, *ACS Catal.* 2015, **5**, 3717-3725.

97. P.A. Sheth, M. Neurock, C.M. Smith. First-Principles Analysis of the Effects of Alloying Pd with Ag for the Catalytic Hydrogenation of Acetylene-Ethylene Mixtures, *J. Phys. Chem. B* 2005, **109**, 12449-12466.

98. M. Luneau, T. Shirman, A.C. Foucher, K. Duanmu, D.M.A. Verbart, P. Sautet, E.A. Stach, J. Aizenberg, R.J. Madix, C.M. Friend. Achieving High Selectivity for Alkyne Hydrogenation at High Conversions with Compositionally Optimized PdAu Nanoparticle Catalysts in Raspberry Colloid-Templated SiO_2, *ACS Catal.* 2020, **10**, 441-450.

99. T. Yoskamtorn, S. Yamazoe, R. Takahata, J.I. Nishigaki, A. Thivasasith, J. Limtrakul, T. Tsukuda. Thiolate-Mediated Selectivity Control in Aerobic Alcohol Oxidation by Porous Carbon-Supported Au_{25} Clusters, *ACS Catal.* 2014, **4**, 3696-3700.

100. A. Shivhare, D.M. Chevrier, R.W. Purves, R.W.J. Scott. Following the Thermal Activation of $Au_{25}(SR)_{18}$ Clusters for Catalysis by X-ray Absorption Spectroscopy, *J. Phys. Chem. C* 2013, **117**, 20007-20016.

101. M. Urushizaki, H. Kitazawa, S. Takano, R. Takahata, S. Yamazoe, T. Tsukuda. Synthesis and Catalytic Application of Ag_{44} Clusters Supported on Mesoporous Carbon, *J. Phys. Chem. C* 2015, **119**, 27483-27488.

102. S. Gaur, J.T. Miller, D. Stellwagen, A. Sanampudi, C.S.S.R. Kumar, J.J. Spivey. Synthesis, Characterization, and Testing of Supported Au Catalysts Prepared from Atomically-Tailored $Au_{38}(SC_{12}H_{25})_{24}$ Clusters, *Phys. Chem. Chem. Phys.* 2012, **14**, 1627-1634.

103. B. Zhang, C. García, A. Sels, G. Salassa, C. Rameshan, J. Llorca, K. Hradil, G. Rupprechter, N. Barrabés, T. Bürgi. Ligand and Support Effects on the Reactivity and Stability of $Au_{38}(SR)_{24}$ Catalysts in Oxidation Reactions, *Catal. Commun.* 2019, **130**, 105768.

104. H.A. Alkmukhlifi, R.C. Burns. Gold Nanoparticles on Metal Oxide Surfaces Derived from N-Alkanethiolate-Stabilized Gold Nanoparticles; Investigations of the Adsorption Mechanism and Sulfate Formation During Subsequent Thermolysis, *Appl. Catal. A* 2015, **502**, 174-187.

105. Z. Zhang, A.G. Walsh, P. Zhang. Dynamic Structure of Metal Nanoclusters from Synchrotron X-ray Spectroscopy, *J. Phys. Chem. C* 2021, **125**, 5982-5994.

106. P. Zhang. X-ray Spectroscopy of Gold-Thiolate Nanoclusters, *J. Phys. Chem. C* 2014, **118**, 25291-25299.

107. S.J.L. Billinge. The Rise of the X-ray Atomic Pair Distribution Function Method: A Series of Fortunate Events, *Phil. Trans. R. Soc. A* 2019, **377**, 20180413.

108. S.J.L. Billinge, I. Levin. The Problem with Determining Atomic Structure at the Nanoscale, Science 2007, **316**, 561-565.

109. D.M. Chevrier, R. Yang, A. Chatt, P. Zhang. Bonding Properties of Thiolate-Protected Gold Nanoclusters and Structural Analogs from X-Ray Absorption Spectroscopy, *Nanotechnol. Rev.* 2015, **4**, 193-206.

110. E. Ortega, A. Ponce, U. Santiago, D. Alducin, A. Benitez-Lara, G. Plascencia-Villa, M. José-Yacamán. Structural Damage Reduction in Protected Gold Clusters by Electron Diffraction Methods, *Adv. Struct. Chem. Imag.* 2016, **2**, 12.

111. H.S. Al Qahtani, R. Higuchi, T. Sasaki, J.F. Alvino, G.F. Metha, V.B. Golovko, R. Adnan, G.G. Andersson, T. Nakayama. Grouping and Aggregation of Ligand Protected Au_9 Clusters on TiO_2 Nanosheets, *RSC Adv.* 2016, **6**, 110765-110774.

112. W.E. Kaden, T. Wu, W.A. Kunkel, S.L. Anderson. Electronic Structure Controls Reactivity of Size-Selected Pd Clusters Adsorbed on TiO_2 Surfaces, *Science* 2009, **326**, 826-829.

113. A. Miller, L. Yu, J. Blickensderfer, R. Akolkar. Electrochemical Copper Metallization of Glass Substrates Mediated by Solution-Phase Deposition of Adhesion-Promoting Layers, *J. Electrochem. Soc.* 2015, **162**, 630-634.

114. M.L. Baker, M.W. Mara, J.J. Yan, K.O. Hodgson, B. Hedman, E.I. Solomon. K and L-edge X-ray Absorption Spectroscopy (XAS) and Resonant Inelastic X-ray Scattering (RIXS) Determination of Differential Orbital Covalency (DOC) of Transition Metal Sites, *Coord. Chem. Rev.* 2017, **345**, 182-208.

115. M. Newville. Fundamentals of XAFS, *Rev. Mineral. Geochem.* 2014, **78**, 33-74.

116. S.T. Chill, R.M. Anderson, D.F. Yancey, A.I. Frenkel, R.M. Crooks, G. Henkelman. Probing the Limits of Conventional Extended X-ray Absorption Fine Structure Analysis Using Thiolated Gold Nanoparticles, *ACS Nano* 2015, **9**, 4036-4042.

117. B. Ravel, M. Newville. ATHENA, ARTEMIS, HEPHAESTUS: Data Analysis for X-ray Absorption Spectroscopy Using IFEFFIT, *J. Synchrotron Radiat.* 2005, **12**, 537-541.

118. B.H. Toby, T. Egami. Accuracy of Pair Distribution Function Analysis Applied to Crystalline and Non-Crystalline Materials, *Acta Cryst.* 1992, **A48**, 336-346.

119. S.J.L. Billinge, M.G. Kanatzidis. Beyond Crystallography: The Study of Disorder, Nanocrystallinity and Crystallographically Challenged Materials with Pair Distribution Functions, *Chem. Commun.* 2004, **7**, 749-760.

120. Th. Proffen, K.L. Page, R. Seshadri, A. Cheetham. Pair Distribution Function for Nanoparticle Studies, *Las Alamos Science* 2006, **30**, 161-163.

121. K. Page, T.C. Hood, Th. Proffen, R.B. Neder. Building and Refining Complete Nanoparticle Structures with Total Scattering Data, *J. Appl. Cryst.* 2011, **44**, 327-336.

122. H. Nakotte, C. Silkwood, K. Page, H-W. Wang, D. Olds, B. Kiefer, S. Manna, D. Karpov, E. Fohtung, E.E. Fullerton. Pair Distribution Function Analysis Applied to Decahedral Gold Nanoparticles, *Phys. Scr.* 2017, **92**, 114002.

123. T.L. Christiansen, S.R. Cooper, K.M.Ø. Jensen. There's No Place Like Real-Space: Elucidating Size Dependent Atomic Structure of Nanomaterials Using Pair Distribution Function Analysis, *Nanoscale Adv.* 2020, **2**, 2234-2254.

124. C.L. Farrow, S.J.L. Billinge. Relationship between the Atomic Pair Distribution Function and Small-Angle Scattering: Implications for Modeling of Nanoparticles, *Acta Cryst.* 2009, **A65**, 232-239.

125. B.H. Toby, R.B. Von Dreele. GSAS-II: The Genesis of a Modern Open-Source All Purpose Crystallography Software Package, *J. Appl. Cryst.* 2013, **46**, 544-549.

126. P. Juhás, T. Davis, C.L. Farrow, S.J.L. Billinge. PDFgetX3: A Rapid and Highly Automatable Program for Processing Powder Diffraction Data into Total Scattering Pair Distribution Functions, *J. Appl. Crystallogr.* 2013, **46**, 560-566.

127. R. Harrington, D.B. Hausner, N. Bhandari, D.R. Strongin, K.W. Chapman, P.J. Chupas, D.S. Middlemiss, C.P. Grey, J.B. Parise. Investigations of Surface Structures by Powder Diffraction: A Differential Pair Distribution Function Study on Arsenate Sorption on Ferrihydrite, *Inorg. Chem.* 2010, **49**, 325-330.

128. W. Li, R. Harrington, Y. Tang, J.D. Kubicki, M. Aryanpour, R.J. Reeder, J.B. Parise, B.L. Phillips. Differential Pair Distribution Function Study of The Structure of Arsenate Adsorbed on Nanocrystalline γ-Alumina, *Environ. Sci. Technol.* 2011, **45**, 9687-9692.

129. V.P. Pakharukova, D.A. Yatsenko, E. Yu. Gerasimov, E.N. Vlasova, G.A. Bukhtiyarova, S.V. Tsybulya. Application of Pair Distribution Function Analysis to Structural Investigation of Alumina Supported MoS_2 Catalysts, *Colloids Interface Sci. Commun.* 2021, **43**, 100454.

130. V. Petkov, Y. Peng, G. Williams, B. Huang, D. Tomalia, Y. Ren. Structure of Gold Nanoparticles Suspended in Water Studied by X-Ray Diffraction and Computer Simulations, *Phys. Rev. B: Condens. Mater. Phys.* 2005, **72**, 195402.

131. K.M.Ø. Jensen, P. Juhás, M.A. Tofanelli, C.L. Heinecke, G. Vaughan, C.J. Ackerson, S.J.L. Billinge. Polymorphism in Magic-Sized $Au_{144}(SR)_{60}$ Clusters, *Nat. Commun*. 2016, **7**, 11859.

132. S. Banerjee, C.-H. Liu, J.D. Lee, A. Kovyakh, V. Grasmik, O. Prymak, C. Koenigsmann, H. Liu, L. Wang, A.M.M. Abeykoon, S.S. Wong, M. Epple, C.B. Murray, S.J.L. Billinge. Improved Models for Metallic Nanoparticle Cores from Atomic Pair Distribution Function (PDF) Analysis, *J. Phys. Chem. C* 2018, **122**, 29498-29506.

133. C.L. Farrow, P. Juhás, J.W. Liu, D. Bryndin, E.S. Bozin, J. Bloch, Th. Proffen, S.J.L. Billinge. PDFfit2 and PDFgui: Computer Programs for Studying Nanostructure in Crystals, J. *Phys.: Condens. Matter* 2007, **19**, 335219.

134. Y. Zhang, M. Eremenko, V. Krayzman, M.G. Tucker, I. Levin. New Capabilities for Enhancement of RMCprofile: Instrumental Profiles with Arbitrary Peak Shapes for Structural Refinements Using the Reverse Monte Carlo Method, *J. Appl. Cryst.* 2020, **53**, 1509-1518.

135. Th. Proffen and R.B. Neder. DISCUS: A Program for Diffuse Scattering and Defect-Structure Simulation, *J. Appl. Crystallogr.* 1997, **30**, 171-175.

Chapter 2

Activation of Atom-Precise Silver Clusters on Carbon Supports for Styrene Oxidation Reactions

In this chapter, the thermal activation of carbon-supported $Ag_{25}(SPhMe_2)_{18}^-$ clusters is discussed. XAS results showed that Ag-thiol bonds are selectively oxidized from the clusters upon mild heat treatment without formation of Ag_2O or Ag_2S. TEM and EXAFS studies showed particle size growth upon activation, and the catalytic studies revealed the particle-size-dependent activity of the Ag clusters catalysts for styrene oxidation reactions.

This chapter is adapted from work published in *RSC Adv.* 2019, **9**, 28019-28027, with permission from the Royal Society of Chemistry. I perfomed all the experimental work in this article. Some preliminary EXAFS analysis was performed with the assistance of Dr. V. Sudheeshkumar. I wrote the complete first draft of the manuscript and this was then edited with the guidance of Prof. Robert W.J. Scott prior to its publication.

2.1 Introduction

The use of well-defined clusters for the development of model heterogeneous catalysis is a very active research area.[1,2] Noble metals with sizes in the nanoscale generally show excellent catalytic activity due to their enhanced surface-to-volume ratio which leads to more active sites, as well as having modified surface geometric and electronic properties compared to bulk materials.[3,4] By tailoring the size as well as the morphology and composition, robust nanocatalysts with excellent catalytic activity and selectivity can be achieved.[4] Atomic-precise thiolate ligand protected clusters are widely studied due to strong sulfur-metal interactions that enable good stability in solution, facile synthesis, and controlled cluster compositions as well as functionalization of stable clusters.[5] Owing to possible influence of the capping ligand on the activity and/or selectivity of ligand-protected clusters in catalytic reactions, it is desirable to have partial or complete ligand removal to enhance contact between the surface metal atoms and reactants, and thus allow higher catalytic activity.[5,6] This leads to a research challenge in preventing or controlling particle aggregation upon removal of ligands from the protected clusters at high loading on supports. Metal-support interactions can play a key role in stabilizing naked clusters, in addition to other strategies that involve creating physical barriers to minimize or prevent particle aggregation.[7,8]

Many research groups, including ours, have extensively studied $Au_{25}(SR)_{18}^-$ clusters for various catalytic reactions.[9-15] X-ray absorption near edge structure (XANES) and extended X-ray absorption fine structure (EXAFS) techniques are components of X-ray absorption spectroscopy (XAS) which are often used in combination to probe chemical bonding and local structure properties of metal clusters with thiol ligands.[12,16,17] Many research groups have demonstrated that XAS is a reliable bulk technique for following particle size growth upon thermal activation of supported Au clusters.[12,18-20] Jin and co-workers showed that Au-thiolate bonds are stable to heating until 125 ºC beyond which the metal clusters become deprotected.[21] A number of research groups have observed sintering of Au clusters upon thermal activation at temperatures above 250 ºC for supported clusters, though some supports show strong interaction with clusters which mitigate sintering.[10,12,22-25] Other activation strategies include chemical approaches, which involve the use of oxidizing and reducing agents, as well as light-induced approaches.[26-30] Both naked and protected Au_{25} clusters have been reported to be active catalysts for styrene oxidation,[10,31] and

others have shown size dependent activity of Au clusters, with high selectivity towards styrene oxide.[10,13] Ag nanoparticles have also shown to be effective catalysts for styrene epoxidation, though the use of secondary promoter is a common practice to achieve high selectivity of the epoxide product.[32,33] Then, selective styrene epoxidation can serve as a good model oxidation reaction to assess the activity of atomic-precise Ag cluster catalysts.

A large number of ligand-protected Ag clusters such as Ag_9, Ag_{10}, Ag_{16}, Ag_{25}, Ag_{29}, Ag_{32} and Ag_{44} have been reported in the literature.[20,34-38] $Ag_{25}(SR)_{18}^-$ clusters have similar (but not identical) atomic arrangements and ligand counts as $Au_{25}(SR)_{18}^-$ clusters. Bakr and co-workers reported the successful synthesis and structural elucidation of $Ag_{25}(SR)_{18}^-$ clusters and noted that the crystal structure has four voids that can allow solvent coordination to give better stability of the clusters.[5,39] The predisposition of silver (Ag) to oxidation, in spite of its lower cost and higher relative abundance (compared to Au), imposes possible limitations on the development of heterogeneous catalysts based on thiolate-protected Ag clusters. Indeed, early work in the field suggested that Ag systems might behave significantly differently than analogous Au systems. Padmos and Zhang showed by XAS that as-synthesized small thiolate protected Ag nanoparticles look to have Ag cores and Ag_2S shells, while dialkylsulfide-stabilized Ag nanoparticles have pure Ag cores.[40] Pradeep and co-workers found that glutathione-stabilized $Ag_{25}L_{18}$ clusters formed Ag_2S materials, as evidenced by PXRD, after heating at 80 °C in solution.[36] However, later work by Tsukuda and co-workers employed XAS techniques to study the behavior of mesoporous carbon supported $[Ag_{44}(SC_6H_4F)_{30}]^-$ clusters upon thermal treatment.[20] They observed sulfur-free Ag clusters upon calcination at 300 °C, which were used as catalysts for the catalytic dehydrogenation of ammonia-borane. At the current time, it is not clear whether such discrepancies in results are due to ligand differences or due to improved purification protocols of Ag cluster materials. This manuscript employs XAS and other techniques to probe the behavior of 2,4-dimethylbenzenethiolate-protected Ag_{25} clusters upon thermal activation for heterogeneous catalysis.

In this study, the structural and morphological properties of the purified $Ag_{25}(SPhMe_2)_{18}^-$ clusters, as catalyst precursors, were evaluated using UV-Vis absorption spectroscopy, thermal gravimetric analysis (TGA), and transmission electron microscopy (TEM), followed by monitoring the effect of choice of coordinating solvents and storage temperature on the stability

of solvent dispersed $Ag_{25}(SPhMe_2)_{18}^-$ clusters. Thereafter, $Ag_{25}(SPhMe_2)_{18}^-$ clusters were supported on carbon supports and activated thermally, followed by examining the carbon supported Ag_{25} clusters using X-ray photoelectron spectroscopy (XPS), TEM, and XAS, and then examined for catalytic activity and selectivity for styrene oxidation reactions. Results show that Ag-thiol bonds are selectively oxidized from the clusters upon mild heat treatments without formation of Ag_2O or Ag_2S, and that the activated Ag clusters on carbon supports showed particle size dependent activity for styrene oxidation reactions.

2.2 Experimental

2.2.1 Materials

All chemicals are commercially available and used as received without any further purification. Silver nitrate ($AgNO_3$, ≥99.0%), styrene (ReagentPlus®, 99.9%), tert-butyl hydroperoxide (tBuOOH, TBHP, 70% in H_2O), high purity acetonitrile (MeCN) and 100% ethanol (EtOH) were purchased from Sigma Aldrich. Dichloromethane (CH_2Cl_2, DCM), methanol (MeOH, HPLC grade), sodium borohydride ($NaBH_4$, 98%), tetrahydrofuran (high purity, THF) were purchased from Fisher Scientific. 2,4-Dimethylbenzenethiol ($HSPhMe_2$, C_8H_9SH, 95%) and tetraphenylphosphonium bromide (Ph_4PBr) were purchased from Alfa Aesar. Dimethylformamide (DMF, HPLC grade), dimethylsulfoxide (DMSO, HPLC grade), and activated carbon (Powder, CX0657-1) were purchased from EMD. Milli-Q (Millipore, Bedford, MA) deionized water (resistivity 18.2 MΩ cm) was used in all experiments.

2.2.2 Synthesis and Purification of the Alkanethiolate-Protected Ag_{25} Clusters

The $Ag_{25}(SPhMe_2)_{18}^-$ clusters were synthesized using a literature procedure,[39] with slight modifications. In a typical synthesis, 2.0 mL of MeOH was used to dissolve 0.22 mmol of $AgNO_3$ in 50 mL flask with 5 min of sonication. Addition of 0.66 mmol of 2,4-dimethylbenzenethiol to this solution gave a thick yellow mixture that became dispersed with the addition of 18 mL of DCM. This solution was kept in an ice-bath with constant stirring at 600 rpm for 30 min before adding a freshly prepared 0.50 mL of methanolic solution containing 0.014 mmol of PPh_4Br. Afterwards, 0.50 mL of an ice-cold aqueous solution containing 0.40 mmol of $NaBH_4$ was added dropwise and the reaction mixture was continuously stirred in an ice-bath for 6 h. Within this period, the colour of the solution changed from deep yellow to light yellow and finally to a dark

red, which indicates the reduction of the silver (I)-thiolate mixture. The crude solution was aged at ~4 ^{o}C for 18 h followed by centrifugation (8500 rpm for 30 min) to remove a solid that presumably constitutes the excess thiol ligands. The supernatant was then concentrated using a rotary evaporator to about 5 mL before adding 20 mL of methanol to precipitate the Ag clusters. The precipitate was collected by centrifugation and extracted into 20 mL of DCM. The DCM solution of the clusters was again centrifuged (8500 rpm for 60 min) to remove an insoluble yellow solid. Then, the deep red colored supernatant was dried under vacuum, and the obtained purified and dried $[Ph_4P][Ag_{25}(SPhMe_2)_{18}]$ clusters were stored in a glass vial under ambient conditions for further studies.

2.2.3 Preparation of Carbon-Supported $Ag_{25}(SPhMe_2)_{18}^-$ Clusters

Immobilization of $Ag_{25}(SPhMe_2)_{18}^-$ clusters onto carbon supports was done via the wetness impregnation method, to give a final metal loading of ca. 4 wt%. Typically, *ca.* 15.5 mg of Ag_{25} clusters was dissolved in 5.0 mL of DCM followed by adding 200 mg of activated carbon and stirring for 24 h. Afterwards, the carbon-supported $Ag_{25}(SPhMe_2)_{18}^-$ clusters (Ag_{25}/carbon) were first dried at 110 ^{o}C for 2 h in an oven, and then thermally treated at 250 ^{o}C, 350 ^{o}C, or 450 ^{o}C, for 2 h, at a ramping rate of 10 ^{o}C/min under air flow using a Lindberg/Blue M furnace. The as-prepared and thermally-treated Ag_{25}/carbon samples were analyzed with TEM, XPS, and XAS (see below).

2.2.4 Characterization Techniques

UV-Vis absorption spectroscopy spectra of the $Ag_{25}(SPhMe_2)_{18}^-$ clusters in solutions were obtained using a Varian Cary 50 UV-Visible spectrophotometer with an optical path length of 1 cm. A small amount of the dried $Ag_{25}(SPhMe_2)_{18}^-$ clusters was dissolved in 2.0 mL of suitable solvent (e.g. DCM) to prepare a sample solution for UV-Vis absorption measurements. Thermal gravimetric analyses (TGA) were performed using a TA Instruments TGA Q5000IR, upon which samples were heated from 25 to 800 ^{o}C under an air flow, with a heating rate of 5 ^{o}C/min. Transmission electron microscopy (TEM) images were collected using a Hitachi HT7700 and HF 3300 TEM operated at 100 kV and 300 kV respectively. TEM samples were prepared by drop casting $Ag_{25}(SPhMe_2)_{18}^-$ cluster solutions onto a carbon coated 300 mesh copper TEM grid (Electron Microscopy Sciences, Hatfield, PA) and dried at ambient condition prior to TEM

analysis. In the case of thermally activated Ag_{25} clusters on carbon, each sample was dispersed in EtOH, and the dispersion was dropped onto a carbon coated copper grid, followed by drying the sample grid at ambient conditions for 2 h prior to TEM analysis. Average particle sizes were typically determined by manually measuring 100 particles from images obtained for each sample using the ImageJ software program.[41]

X-ray photoelectron spectroscopy (XPS) measurements were collected using a Kratos (Manchester, UK) AXIS Supra system at the Saskatchewan Structural Sciences Centre (SSSC). This system is equipped with a 500 mm Rowland circle monochromated Al K-α (1486.6 eV) source and combined hemi-spherical analyzer (HSA) and spherical mirror analyzer (SMA). An accelerating voltage of 15 keV, an emission current of 15 mA, and a hybrid spot size of 300 x 700 microns were used. All survey scan spectra were collected in the -5 to 1200 eV binding energy range in 1 eV steps with a pass energy of 160 eV. High resolution scans of three regions were also conducted using 0.05 eV steps with a pass energy of 20 eV. All binding energies were calibrated to the C 1s of the adventitious carbon at 284.8 eV and spectra were fitted without constraining the full width at half maximum (FWHM) using CasaXPS software.[42]

The Ag K-edge XAS measurements were conducted at the Hard X-ray MicroAnalysis (HXMA) beamline 061D-1 (5-30 keV; resolution 1 x 10^{-4} $\Delta E/E$) at the Canadian Light Source (CLS). Energy selection of the Ag K-edge was done using a Si(220) double-crystal Si monochromator, with a Pt-coated water-cooled collimating KB mirror. Ionization chambers were filled with nitrogen gas. Samples were mixed with boron nitride and measured in fluorescence mode at room temperature using a 32-element detector. The energy of the X-rays was calibrated by using Ag foil (25514 eV). The data processing was performed using the IFEFFIT software package.[43] The X-ray absorption near-edge structure (XANES) spectra were obtained by subtracting the atomic absorption background and normalizing the spectra to the edge height. The k^3-weighted spectra were subjected to a Fourier transform (FT) in R space for the k range of 2.8-12 $Å^{-1}$. Ag fcc bulk lattice parameters were used to fit the Ag-foil spectrum, keeping the first shell coordination number fixed (CN = 12) at first, in order to determine the amplitude reduction factor (S_0^2). From this fitting, the amplitude reduction factor determined for the Ag-foil was 0.80 and was used for the subsequent sample fits.

2.2.5 Catalytic Measurements for Styrene Oxidation Reactions

The catalytic performances of the as-prepared and activated Ag_{25}/carbon samples were evaluated for styrene epoxidation reactions. For each catalyst sample, the catalytic test was conducted inside a 100 mL round bottom flask fitted with a reflux condenser. A typical reaction set-up includes addition of styrene (920 μL, 8.0 mmol), TBHP (3.3 mL, 24 mmol), MeCN (5.0 mL), and catalyst (20 mg) into a flask under reflux and stirring (600 rpm) at reaction temperature of 82 °C for 24 h.[13] Products were then analyzed using a gas chromatograph (7890A, Agilent Technologies) equipped with a HP-5 column and a flame ionization detector.

2.3 Results and Discussion

The formation of a deep-red solution upon addition of sodium borohydride to the Ag(I)-thiolate complex indicates the reduction of Ag(I) ions and formation of thiolate protected silver clusters. Figure 2.1 presents characterization results obtained for purified, unsupported thiolate-protected metal clusters consisting of precisely 25 silver atoms; $Ag_{25}(SPhMe_2)_{18}^-$. Figure 2.1(a) shows the UV-Vis absorption spectrum of purified $Ag_{25}(SPhMe_2)_{18}^-$ clusters in DCM with characteristic peaks at 334 nm, 392 nm, 490 nm, and 678 nm for nearly monodisperse $Ag_{25}(SPhMe_2)_{18}^-$ clusters.[39] Similar to the case for Au_{25} clusters, the broad peak at around 678 nm is due to the HOMO-LUMO transition due to the Ag_{13} icosahedral core in the Ag_{25} structure. Figure 2.1(b) shows the previously determined crystal structure of $Ag_{25}(SPhMe_2)_{18}^-$,[39] as visualized using the VESTA software package,[44] to reflect the atomic arrangement and ligand counts. There is one silver atom (red) at the center and twelve silver atoms (dark blue) on the surface of the icosahedral core. The remaining twelve silver atoms (blue) and eighteen sulfur atoms (yellow), from thiolate ligands, constitute atoms in the staple positions. Figure 2.1(c) shows a TEM image which shows individual $Ag_{25}(SPhMe_2)_{18}^-$ clusters have an average size of 1.0 ± 0.2 nm. This measurement slightly less than a value of 1.5 ± 0.3 nm previously reported for $Ag_{25}(SR)_{18}$,[45] but closer in line to the expected size of the Ag core. The slight difference in measured average particle size can be due to better size separation, due to extra purification step, in our synthesis procedure, as well as moderate voltage imaging at 100 kV on new sample areas to minimize damage to the clusters by the electron beam. The TGA result in Figure 2.1(d) shows no weight loss below 150 ^oC and a major weight loss centering around 250 ^oC, which is presumed to be due to removal of the protecting thiolate ligands from the $Ag_{25}(SPhMe_2)_{18}^-$ clusters upon thermal treatment. The final

weight percent of material leftover is approximately 40%, which is slightly lower than the theoretically estimated *ca.* 47% Ag composition of the clusters and counter ions, *i.e.* $Ph_4P[Ag_{25}(SPhMe_2)_{18}]$.

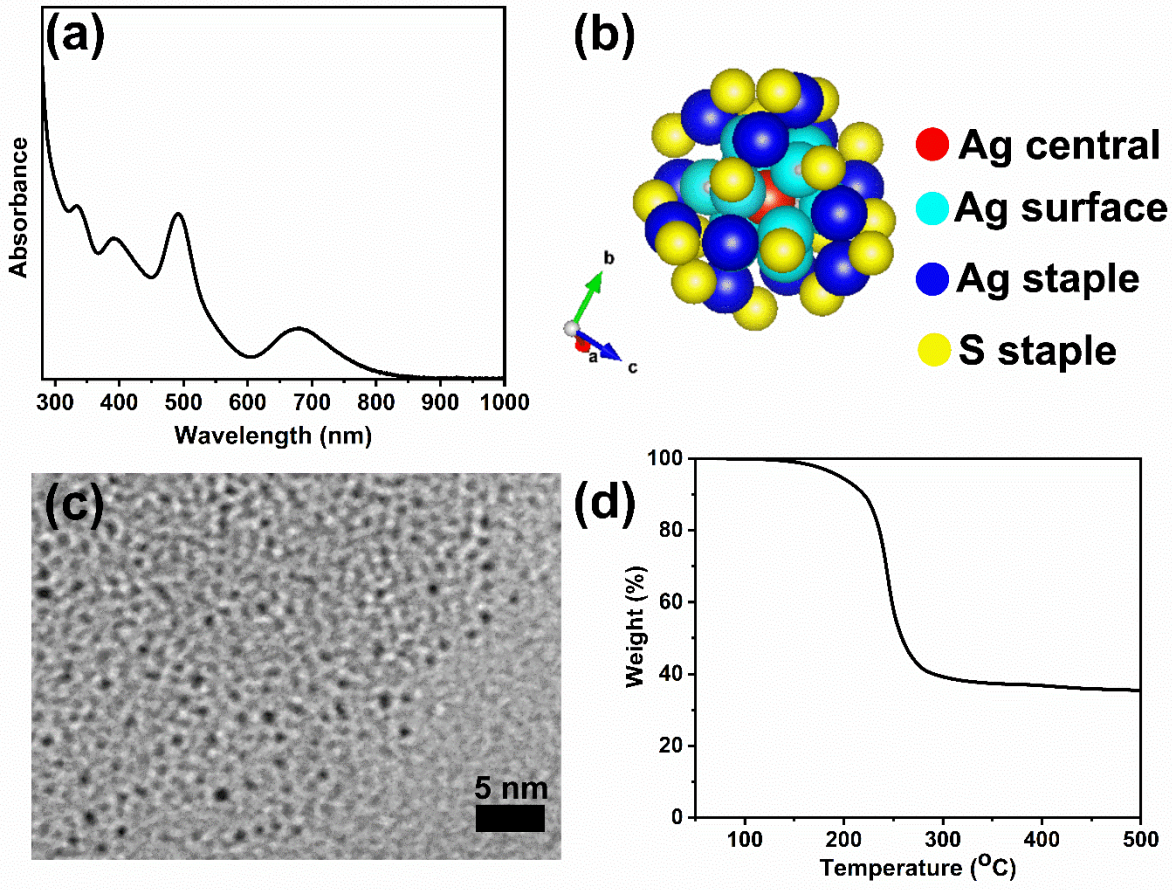

Figure 2.1. Characteristic features of $Ag_{25}(SPhMe_2)_{18}^-$ clusters (a) UV-Vis spectra in DCM, (b) atomic arrangement as visualized using VESTA software,[44] colour scheme is red for the Ag central atom, light blue for Ag surface atoms, dark blue for Ag staple atoms and yellow for sulfur staple atoms. (c) TEM image, and (d) TGA plot.

Table 2.1 summarizes the preservation of UV-Vis absorption spectroscopy fingerprints of $Ag_{25}(SPhMe_2)_{18}^-$ clusters in four different aprotic polar solvents (THF, DMF, DCM, and DMSO), under different storage conditions. Equal concentrations (0.10 mg/mL) of Ag clusters were prepared with different solvents and time-dependent UV-Vis absorption studies were conducted for clusters stored at room (22-24 °C) and cold (~4 °C) temperatures. The fingerprints of $Ag_{25}(SPhMe_2)_{18}^-$ clusters in the UV-Vis absorption measurements turn out to be good features for

evaluating the stability of clusters in these solvents. The voids in the crystal structure of $Ag_{25}(SPhMe_2)_{18}^-$ allow coordination with suitable solvents, and thus can be correlated with the solution-based stability of the $Ag_{25}(SPhMe_2)_{18}^-$ clusters.[5,39] The values of dielectric constant of the selected solvents correlates with the number of days it takes for the precipitation of the $Ag_{25}(SPhMe_2)_{18}^-$ clusters, presumably due to loss of coordination of solvent molecules with the voids in the crystal structure of $Ag_{25}(SPhMe_2)_{18}^-$ clusters. Both the nature of coordinating solvent and storage temperature affect the solution-based stability of $Ag_{25}(SPhMe_2)_{18}^-$ clusters. Importantly, it takes a minimum of 48 h to observe precipitation of $Ag_{25}(SPhMe_2)_{18}^-$ clusters in any of these solvents at room temperature and thus any choice among these solvents is suitable for immobilization of $Ag_{25}(SPhMe_2)_{18}^-$ clusters onto carbon supports via wetness impregnation, a procedure that was completed under 24 h, in making heterogeneous catalysts. DCM solvent was chosen for immobilization procedure as it dries quickly due to its lower boiling point.

Table 2.1. Stability of dispersed $Ag_{25}(SPhMe_2)_{18}^-$ clusters as determined by the preservation of optical transitions in UV-Vis absorption measurements

Solvent property		**Longevity (in days) at different storage temperature**	
Solvent	**Dielectric constant (ε)**	**22-24 °C (ambient)**	**~4 °C (cold)**
THF	7.58	2	24
DCM	8.93	4	31
DMF	36.7	6	120
DMSO	46.7	10	2*
*Freezes up after 2 days.			

The activation of heterogeneous catalysts derived from colloidal precursors often entails partial or complete removal of any protecting ligands to enable access of active sites by reactants.[21,46-48] While the activation can be achieved by several approaches, thermal calcination approaches to activation are quite simple and thus employed in this present study. TEM, XPS, and XAS analyses of the Ag_{25}/carbon samples gave insight into the extent of ligand removal and particle growth at different activation temperatures. Figure 2.2 shows TEM images of thermally-

activated Ag_{25}/carbon catalysts. It is noteworthy that imaging clusters on carbon supports was somewhat difficult due to the small size and poor contrast between the support and clusters. Nevertheless, no appreciable increase in cluster size was noted upon loading the Ag clusters onto carbon supports. This suggests that majority of Ag clusters are effectively adsorbed without structural compromise. Improved contrast was seen between Ag and the carbon support for Ag_{25}/carbon samples calcined at 250 ^{o}C and beyond. Average particle sizes were 1.2 ± 0.3 nm, 2.6 ± 0.4 nm, and 2.8 ± 0.6 nm for activated samples at 250, 350, and 450 ^{o}C, respectively. This shows that very minor growth in the average cluster size is seen for samples calcined at 250 ^{o}C, while the cluster size grows progressively with higher activation temperatures. Thus, particle growth revealed by TEM images may be a consequence of the removal of protecting thiolate ligands upon thermal activation of as-prepared Ag_{25}/carbon catalysts.

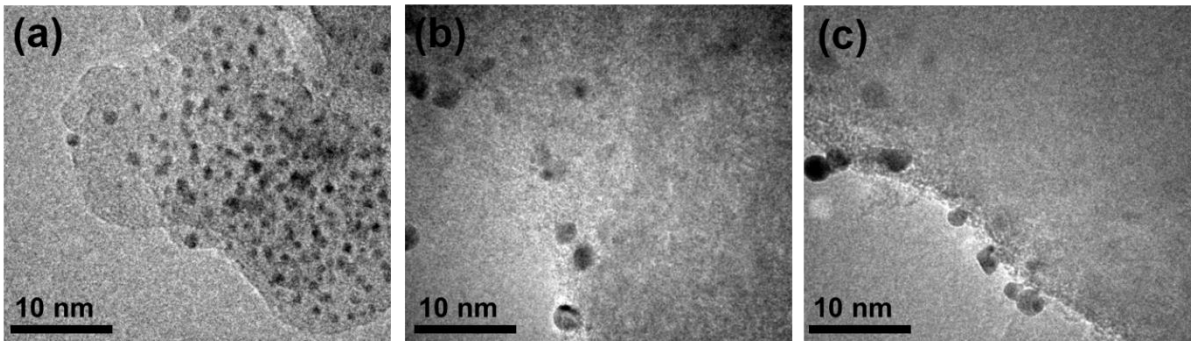

Figure 2.2. TEM images of thermally activated Ag_{25}/carbon catalyst samples at (a) 250 ^{o}C (b) 350 ^{o}C, and (c) 450 ^{o}C.

Figure 2.3 shows the XPS spectra of the constituent elements of the as-prepared Ag_{25}/carbon sample; XPS survey maps show the presence of C, Ag, S, and O as the constituent elements. The C 1s spectrum was fitted with multiple Gaussian components having peaks with binding energies at 284.8 eV, 285.3 eV, and 288.9 eV and these can be attributed to C-C/C-H, C-O, and C=O species, respectively; the latter species are commonly found on activated carbon surfaces.[49] Figure 2.3(b) shows the Ag $3d_{5/2}$ and Ag $3d_{3/2}$ peaks at 368.1 eV and 374.1 eV, respectively, which are consistent with silver atoms in the zerovalent state (Ag $3d_{5/2}$ = ~368.0 eV).[50,51] Deconvolution of the high resolution spectrum of S 2p spectrum, shown in Figure 2.3(c), shows two peaks with spin-orbit splitting of ~1.2 eV indicating the presence of Ag-thiolate species (162.2 eV for S $2p_{3/2}$ and 163.5 eV for S $2p_{1/2}$).[52] The O 1s spectrum shows an asymmetric profile

to suggest the presence of more than one kind of oxygen species (Figure 2.3(d)) on the carbon surface. The deconvolution of the spectrum gives two peaks centering at ~531.2 and 533.1 eV that can be ascribed to C-O and C=O species from the activated carbon surface, respectively, and thus the absence of metal oxide species.[53] Altogether, XPS results indicate that thiolate ligands remain attached to the surface of silver cluster surface and no oxidation of silver atoms occurs in the Ag_{25}/carbon sample prepared via wetness impregnation.

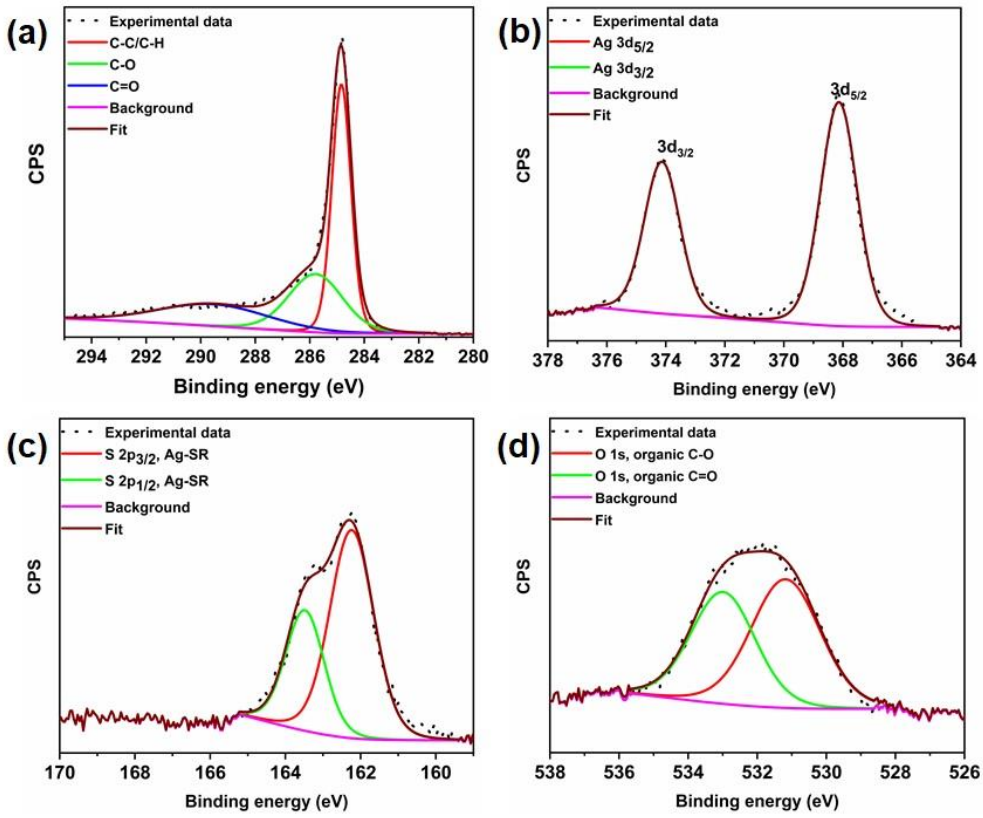

Figure 2.3. XPS spectra for the as-prepared Ag_{25}/carbon catalyst; (a) C 1s (b) Ag 3d, (c) S 2p and (d) O 1s peaks.

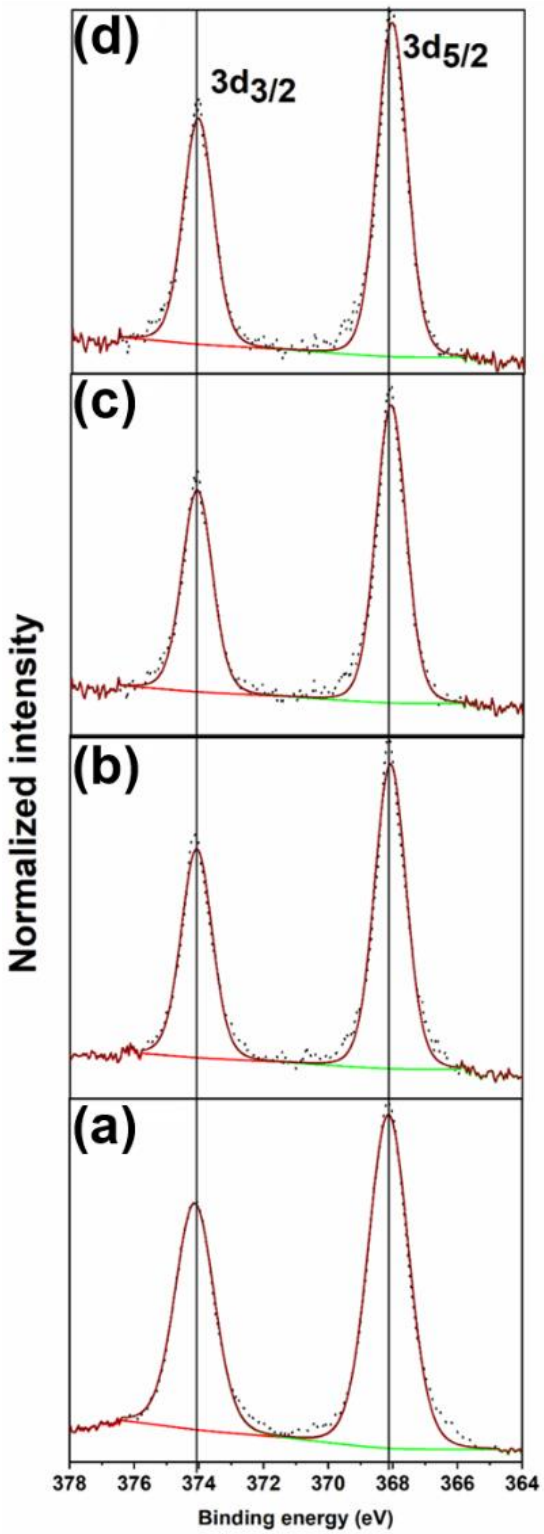

Figure 2.4. XPS spectra of Ag 3d peaks for (a) as-prepared, and the calcined Ag_{25}/carbon catalyst samples at (b) 250 ºC, (c) 350 ºC, and (d) 450 ºC.

Figure 2.4 shows the XPS spectra and fits of the Ag 3d peaks for the calcined Ag_{25}/carbon catalyst samples. In the calcined samples, the Ag $3d_{5/2}$ and Ag $3d_{3/2}$ peaks are at 368.0 eV and 374.0 eV respectively, which show that silver atoms maintain the zerovalent state after calcination. In contrast, analysis of the S 2p spectra of activated samples shows the absence of peaks earlier ascribed to Ag-thiolate species (Figure 2.5). Instead, S 2p peaks appears at higher binding energies and these peaks can be attributed to the organic disulfide and other oxidized sulfur species like sulfonates,[54,55] which are byproducts of oxidative dethiolation. Also, there is no indication of formation of silver oxide or sulfide from both Ag 3d and O 1s spectra obtained for activated samples (Figures 2.4 and 2.5). Also, from the quantification of survey spectra, the amount of sulfur species decreases with an increase in activation temperatures. The sulfur species content was quantified to be 1.4% in the as-prepared sample, and 0.6%, 0.1% and 0% for activated samples at 250 °C, 350 °C, and 450 °C, respectively. These XPS results suggest that thiolate ligands leave the surface of silver clusters upon thermal activation, which is consistent with the TGA results (Figure 2.1(d)). Zhang *et al.* recently reported a similar observation showing migration of protecting ligands from the gold metal surface onto an oxide support upon deposition and oxidative pretreatment.[56] All XPS results suggest Ag clusters remain in the zerovalent state after calcination, and that no significant Ag oxidation is occurring upon calcination.

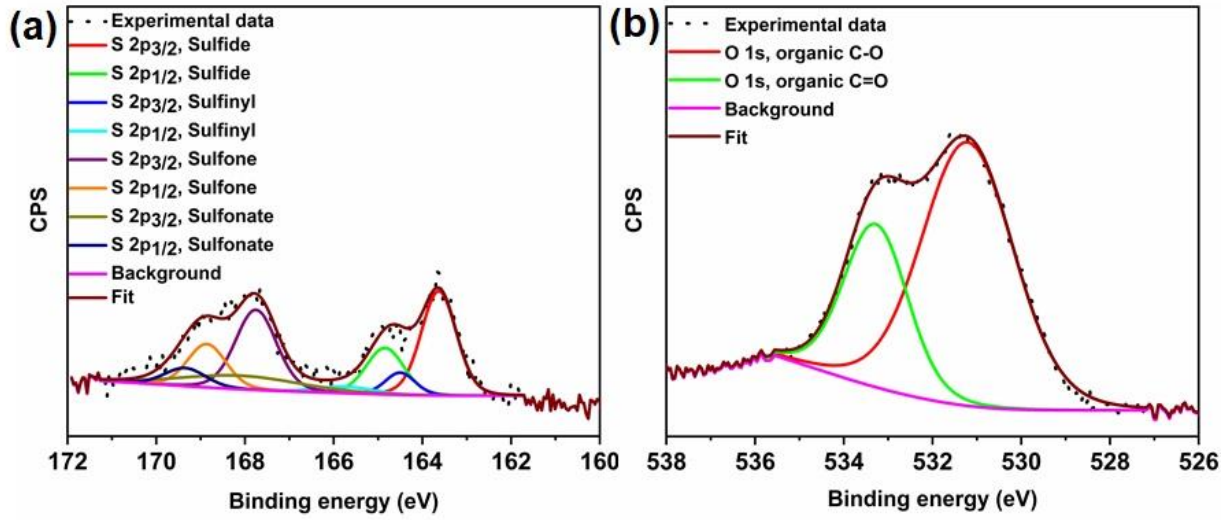

Figure 2.5. XPS spectra for activated Ag_{25}/carbon catalyst at 350 °C; (a) S 2p, and (b) O 1s spectra.

XAS experiments were carried out to further examine the structural integrity of Ag_{25} clusters on carbon supports. While XANES spectroscopy gives information about the oxidation state and local environment, EXAFS spectroscopy affords information about the average coordination number (CN) around metal atoms and bond distances.[57] Figure 2.6 shows the Ag K-edge spectra obtained for as-prepared and activated Ag_{25}/carbon catalysts, alongside that of Ag foil as a reference. The spectra show a strong K-edge feature for Ag at 25514 eV which is attributed to the dipole-allowed 1s to 5p transition.[58] Figure 2.6(a) shows the XANES spectra of the sample; the peak at *ca.* 25550 eV is absent in the as-prepared clusters and grows in intensity with increased activation temperature. A number of groups, including our own, have observed that this multiple scattering feature is a good fingerprint for Au cluster growth in analogous Au cluster samples (*i.e.* small clusters do not have such multiple scattering features given their small size).[12,17,18] This agrees well with previous TEM results from these samples. The as-prepared sample shows distinct near edge features to suggest that the neighboring atoms are different for the as-prepared sample as compared to activated samples. Comparing the near edge features with those of reference Ag foil, it shows that Ag-Ag interactions become more predominant at calcination temperatures above 250 ^{o}C which affirms that cluster sintering becomes problematic beyond 250 ^{o}C. This agrees with the results from both TGA and XPS, confirming the removal of protecting thiolate ligands upon thermal activation of as-prepared Ag_{25}/carbon catalyst. It is noteworthy that the spectra features of all the samples show no detectable Ag_2O or Ag_2S in these samples, in consistent with the XPS results (Figures 2.3, 2.4 and 2.5).

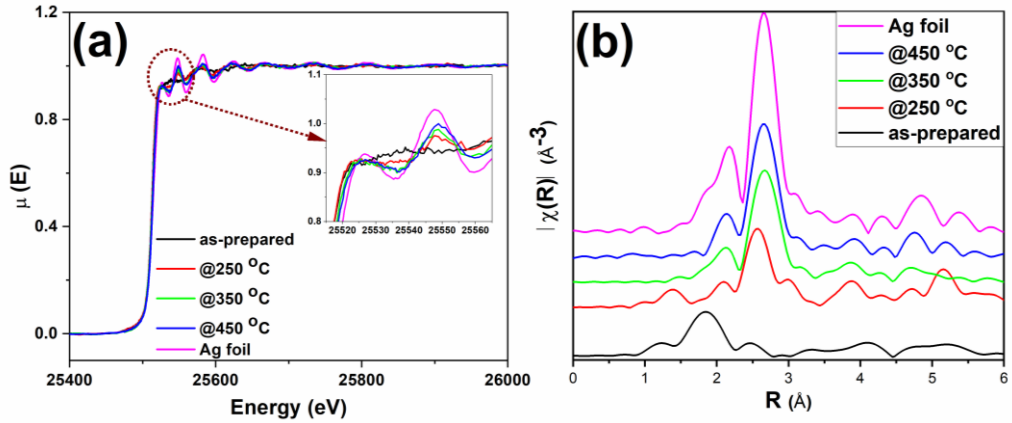

Figure 2.6. Ag K-edge (a) XANES and (b) FT-EXAFS spectra obtained for as-prepared and activated Ag_{25}/carbon catalysts and Ag foil reference.

Figure 2.6(b) shows the Ag K edge EXAFS spectra of the Ag_{25}/carbon samples in R-space. EXAFS measurements are sensitive to the bonding environment of the absorbing atom. All samples, as well as the reference Ag foil, show major peaks at around 2.72 Å (note the plotted data has no phase shift correction) that are characteristic features of first shell Ag-Ag contributions (Figure 2.6(b)), while only the as-prepared sample has a Ag-S feature in the 1.85 Å region. The crystallographic information of $Ag_{25}(SPhMe_2)_{18}^-$ provided in the literature was used to make the theoretical model for fitting the experimental data obtained for as-prepared sample using a two-shell fitting approach.[39] A similar approach was reported for EXAFS fittings of $Ag_{44}(SR)_{30}^{4-}$ clusters.[20] The fitting parameters such as coordination number (CN), nearest neighbour distance (R), Debye Waller factors (σ^2), and energy shift (E_o) are presented in Table 2.2, while the k-space and R-space plots are shown in Figure 2.7. The bond distance of 2.401(6) Å was obtained for the Ag-S contribution from the fit and this value agrees very well with values of 2.382-2.445 Å earlier reported for Ag-S bonds in the crystal structure,[39] and a value of 2.81(2) Å was obtained for the Ag-Ag bond distance in the as-prepared sample. CN values of 1.08(5) and 0.5(1) were obtained for Ag-S and Ag-Ag bonds, respectively. We note that the CN value for first shell Ag-Ag interactions is low, but this can be due to both the presence of multiple first shell Ag-Ag contributions and perhaps low levels of Ag thiolate impurities. Attempts to use multiple Ag-Ag first shells in fitting were unsuccessful as the data quality was not sufficient for such a detailed analysis.[18,59] Nevertheless, the data suggests successful immobilization of $Ag_{25}(SPhMe_2)_{18}^-$ clusters onto carbon supports without compromising their structural integrity.[39] In summary, XPS and XAS data of as-prepared Ag_{25}/carbon catalysts suggest that the structural changes in activated Ag_{25}/carbon samples can be solely due to calcination which causes removal of protecting ligands from $Ag_{25}(SPhMe_2)_{18}^-$ clusters.

Table 2.2. Multi-shell EXAFS fitting parameters for as-prepared Ag_{25}/carbon catalysts.

Bond type	**CN**	**R/Å**	**σ^2/Å^2**	**E_o shift /eV**	**R-factor**
Ag-S	1.08(5)	2.401(6)	0.00272(2)	-4.0(8)	0.0066
Ag-Ag	0.5(1)	2.81(2)	0.00900(3)	-4.0(8)	

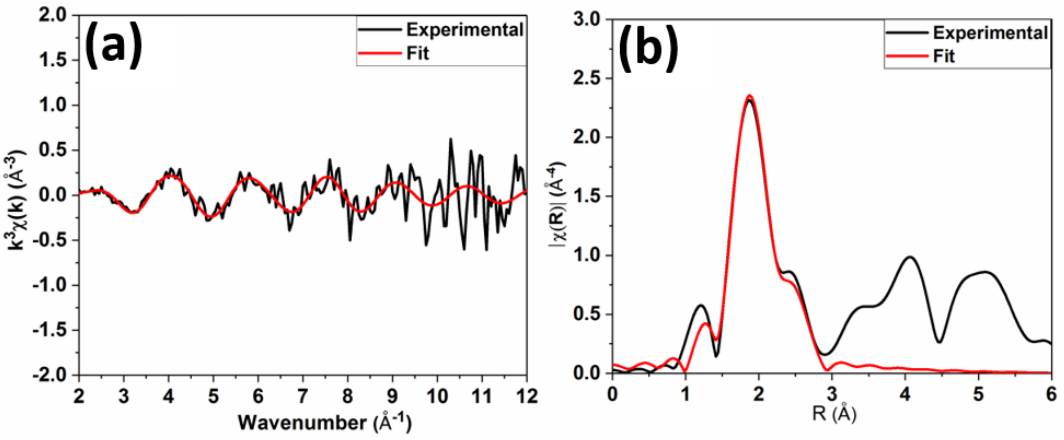

Figure 2.7. EXAFS data in (a) k-space and (b) R-space, for as-prepared Ag_{25}/carbon catalyst.

In addition to the observable changes in the near edge features in XANES spectra (Figure 2.6(a)), a single-shell fit approach is employed to analyze the EXAFS data obtained for thermally treated Ag_{25}/carbon samples to probe the growth in cluster size with increasing activation temperatures. The single-shell fit entails the use of a Ag fcc model and is adopted due to observed growth in cluster size and presence of zerovalent Ag as revealed by the other results. Figure 2.8 shows both k-space and R-space EXAFS spectra at the Ag K-edge for the thermally activated Ag_{25}/carbon samples, and the obtained fitting parameters are presented in Table 2.3. The first shell Ag-Ag coordination number (CN) increases with an increase in activation temperature; this agrees with the increase in the peak intensities of the R-space EXAFS spectra (Figure 2.6(b)). No significant Ag-S contributions were found for any of the calcined samples. For samples thermally activated at 250 ^{o}C, 350 ^{o}C, and 450 ^{o}C, the first shell Ag-Ag CN values are 3.8(7), 6.1(3), and 6.3(3), respectively. A CN value of 3.8(7) for the sample activated at 250 ^{o}C and 6.1(3) for the sample activated at 350 ^{o}C suggest significant structural changes occur at higher calcination temperatures due to sintering of Ag clusters. There is no significant change in the Debye-Waller parameter which indicates that the degree of disorder remains unchanged with increase in activation temperature. However, the Ag-Ag bond distance slightly increases with activation temperature which is also consistent with an increase in cluster size.[20,58,60] Altogether, it can be said that the protecting thiolate ligands are completely removed with little compromise in the size of Ag_{25} clusters by thermal activation at 250 ^{o}C, whereas higher temperature calcination leads to moderate cluster sintering.

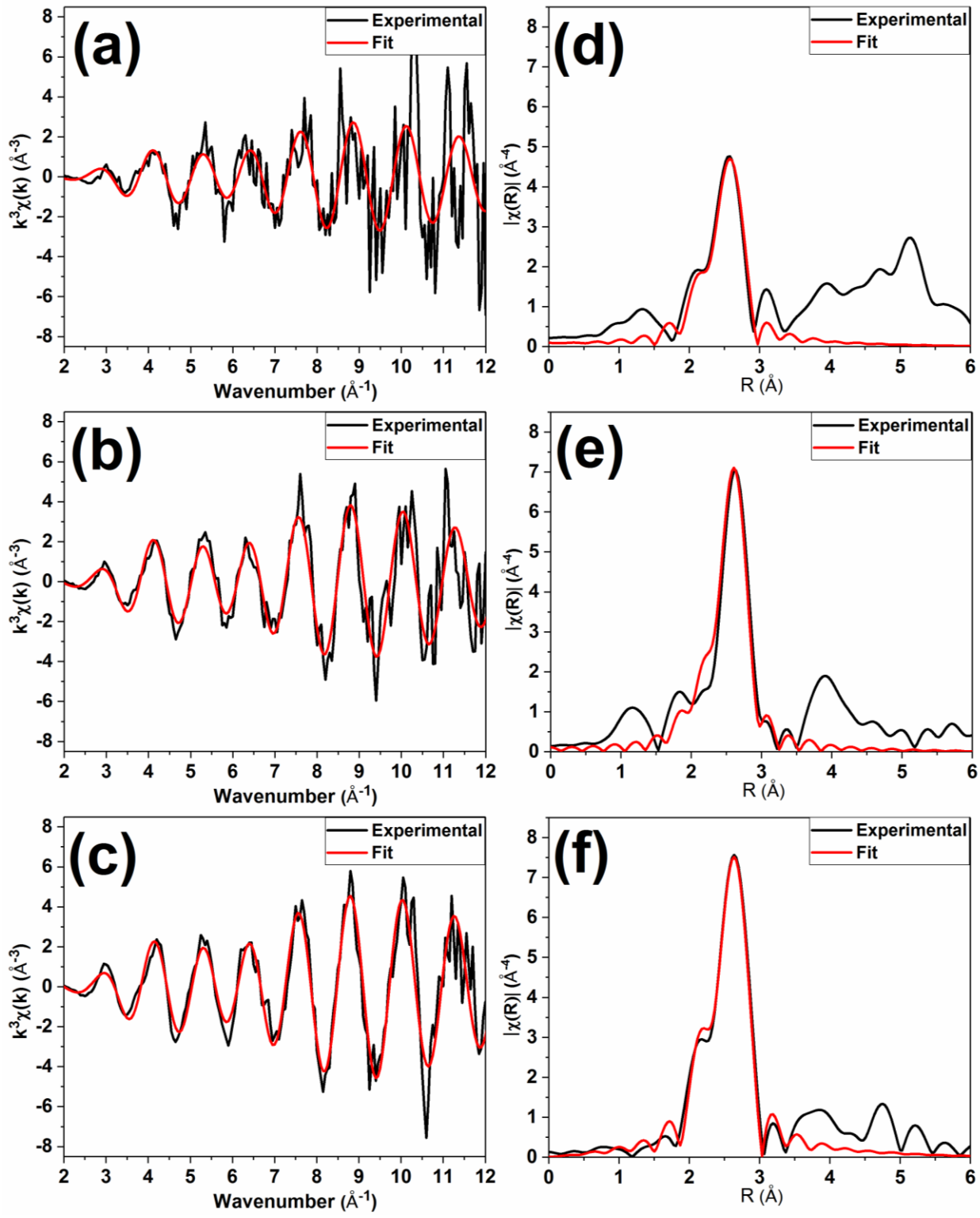

Figure 2.8. EXAFS data in k-space (a-c) and R-space (d-f) for activated Ag_{25}/carbon catalysts at 250 °C (a,d), 350 °C (b,e), and 450 °C (c,f) respectively.

Table 2.3. Single shell EXAFS fitting parameters for activated Ag_{25}/carbon catalysts.

Catalyst	CN (Ag-Ag)	R/Å (Ag-Ag)	σ^2/Å^2 (Ag-Ag)	E_o shift /eV (Ag-Ag)	R-factor
@250 °C	3.8(7)	2.826(6)	0.0080(2)	-3.7(8)	0.017
@350 °C	6.1(3)	2.854(5)	0.0090(7)	-1.9(5)	0.019
@450 °C	6.3(3)	2.859(6)	0.0081(8)	-0.7(6)	0.019

Estimation of average particle sizes (d_{mean}) directly from EXAFS CNs is reported in the literature.[61-63] Recently, Wei *et al.* reported an equation that quantitatively relates the CN from EXAFS fittings to average particle size, in angstroms, using Ag nanoparticle sizes obtained by analyzing STEM images (for particles ranging from 0.8 to 8.7 nm in size).[63] The equation was modified to give Equation 2.1 below that can directly estimate the average particle size in nanometers (nm). Using the concept of error propagation,[64] Equation 2.2 was derived to estimate the error in d_{mean} in Equation 2.1. These two equations enable estimation of size distribution using CN errors from EXAFS fittings.

$$d_{mean}(nm) = 10^{((0.1319 * CN) - 0.5763)} \quad \textbf{(2.1)}$$

$$\sigma_d = |d * (0.1319 * ln(10) * \sigma_{CN})| \quad \textbf{(2.2)}$$

Using the two equations above, the average cluster size was estimated to be 0.84 ± 0.18 nm, 1.69 ± 0.15 nm, and 1.80 ± 0.16 nm for Ag_{25}/carbon samples activated at 250 °C, 350 °C and 450 °C respectively. These values are somewhat consistent with the average cluster sizes measured from TEM images of 1.2 ± 0.3 nm, 2.6 ± 0.4 nm, and 2.8 ± 0.6 nm, respectively (Figure 2.2), though TEM measurements slightly over-represent cluster sizes.[64] Determining precise particle sizes and distributions when dealing with clusters in the nanometer size range by TEM can be difficult in that sub-nanometer clusters may be present that are not easily observed. Thus, as the TEM particle sizes for the three activated samples are larger than the mean diameters calculated from first-shell CN values, this suggests there may be a population of smaller clusters which are difficult to image by TEM in the samples.

Selective oxidation of olefins to epoxides is a desirable chemical conversion in the fine chemical industry, and the use of heterogeneous Ag-based catalysts has gained attention in recent years.[65] Specifically, styrene to styrene oxide (StO) conversion is a desirable chemical process in industry as StO is a useful chemical in the production of surface coatings and cosmetics.[65,66] StO is also beneficial to the production of styrene glycol, polyurethanes, and cross-linked polyesters.[66] Both activity and selectivity are important parameters for describing performance of catalysts in a given reaction. Table 2.4 presents the results obtained for the catalytic evaluation of Ag_{25}/carbon as catalysts in styrene oxidation reactions. Catalytic activity was measured in terms of both conversion and an average turnover number (TON), which was determined as moles of converted styrene per moles of Ag in the catalyst. No activity was observed in blank reactions (without catalyst or carbon support) and about 1% conversion of styrene was recorded when air was used as oxidant instead of tert-butyl hydroperoxide (TBHP) in the presence of our catalysts. Significant activity was observed with TBHP as an oxidant and thus data obtained for styrene oxidation reaction with TBHP were used to compare the performances of studied catalysts. Interestingly, carbon supports alone showed about 15% conversion of styrene, on average, under our reaction conditions. The results show that Ag_{25}/carbon catalysts display size-dependent activities with StO as a major product for all examined catalysts in this study. The range of values obtained for selectivity for styrene oxide is in agreement with those reported for Au_{25} clusters in literature.[10,13] For example, Liu *et al.* noted that the activated Au clusters on hydroxyapatite supports showed 100% conversion (TON = 302, t = 12 h) and 92% selectivity towards styrene oxide using TBHP as an oxidant in toluene at 80 ˚C.[10] The TON of as-prepared catalysts was found to be 1114 and it increased to 1325 for catalysts activated at 250 °C. This increase in TON value can be ascribed to significant removal of protecting ligands off the catalyst surface which enables better access of the active sites by the substrate. The subsequent drop in TON values for catalysts activated at higher temperatures is due to particle sintering as indicated by the increase in the CN values in the XAS measurements and average particle sizes in the TEM measurements. The small trend obtained for product selectivity may be due to particle size effects, as the clusters increase in size at higher calcination temperatures.

Table 2.4. Catalytic performances of support, as-prepared and activated Ag_{25}/carbon catalysts.

Catalyst	Activity		Selectivity	
	Conversion (%)	**TON**	**StO (%)**	**BA (%)**
Carbon support	15.3	-	90.9	9.1
Ag_{25}/carbon as-prepared	51.6	1114	95.1	4.9
Ag_{25}/carbon @250 °C	61.4	1325	94.0	6.0
Ag_{25}/carbon @350 °C	49.9	1078	92.6	7.4
Ag_{25}/carbon @450 °C	46.6	1006	89.4	10.6
Reaction conditions: Styrene (8.0 mmol), TBHP (24 mmol), MeCN (5.0 mL), catalyst (20 mg) in a flask under reflux, stirring speed (600 rpm), reaction temperature of (82 °C), reaction time (24 h). Ratio of substrate to metal is 2157:1. TON = moles of converted styrene / moles of Ag.				

It is evident in the literature that TBHP works as a radical initiator, when present in small amount, and then allow the reaction to proceed with oxygen as the main oxidant.[67,68] Using the Ag_{25}/carbon@250 °C catalyst, we performed cycles of oxidation reactions like those reported in Table 2.4, but with a small amount of TBHP and for longer reaction times, and the results obtained are presented in Table 2.5. The reduction in amount of TBHP from 24 mmol (i.e. 300% of styrene amount) to 0.40 mmol (i.e. 5% of styrene amount) leads to decrease in the styrene conversion from 61.4% to 5.8% for a reaction period of 24 h, and to no conversion in the complete absence of TBHP initiator. Whereas, by extending the reaction period to 72 h, a conversion of 23.3% is observed with 0.40 mmol TBHP. This indicates that the reaction proceeds much slower when smaller amounts of TBHP is used as radical initiator and molecular oxygen in air remains a major oxygen atom source for the epoxide formation. Similar observations were reported in separate studies for Au and Ag nanoparticle catalysts.[68,69] Thus, a radical mechanism for styrene epoxidation over mildly activated Ag_{25}/carbon catalysts, in which the thermolysis of *t*-BuOOH (TBHP) occurs on the surface of silver particles to give *t*-BuOO$^{\bullet}$ and H$^{\bullet}$ radicals, is speculated as reported for similar systems.[68,70] It is of note that the selectivity towards epoxide formation is reduced in the case of 0.40 mmol of TBHP, as compared to the case of 24 mmol of TBHP. The decrease in the selectivity is consistent with results in the literature as TBHP itself has been identified to be more selective for epoxide formation.[69] The spent catalyst was subjected to a recycling process that involves washing the spent catalyst with acetone for three times, followed

by oven drying at 110 °C for 30 min. Thereafter, the recycled catalyst was used for 2 more cycles of reaction, and it was found to be both active and selective for styrene oxide. The significant increase in activity after the first cycle of reaction can be due to the removal of organic sulfur species adsorbed on the catalyst surface by steps utilized to recycle the catalyst. The catalyst shows stability in activity and selectivity after the first cycle of the reaction.

Table 2.5. Catalytic performances of mildly activated Ag_{25}/carbon@250 °C catalyst with low amount of TBHP.

Entry		**Activity**		**Selectivity**	
Cycle	**Reaction time**	**Conversion (%)**	**TON**	**StO (%)**	**BA (%)**
First	24 h	5.8	125	60.8	39.2
Second	24 h	7.2	155	59.8	40.2
Third	24 h	7.4	160	59.6	40.4
First	72 h	23.3	502	59.6	40.4
Second	72 h	46.2	997	61.0	39.0
Third	72 h	46.7	1007	61.2	38.8
Reaction conditions: Styrene (8.0 mmol), TBHP (0.40 mmol), MeCN (5.0 mL), catalyst (20 mg) in a flask under reflux, stirring speed (600 rpm), reaction temperature of (82 °C). Ratio of substrate to metal is 2157:1. TON = moles of converted styrene / moles of Ag.					

2.4 Conclusions

Atom-precise $Ag_{25}(SPhMe_2)_{18}^-$ clusters were synthesized and deposited onto carbon supports for catalysis. Carbon-supported Ag_{25} clusters were activated at mild temperatures (250 ^oC) without sintering, while growth in particle sizes was observed at higher calcination temperatures. Upon thermal activation, the protecting thiolate ligands were detached from the surface of Ag_{25} clusters and the products of dethiolation were adsorbed onto the carbon supports, and these sulfur species were further removed at high temperatures. XPS and XAS data both show that the resulting activated Ag clusters have metallic character, and Ag_2S formation was not observed. Both as-prepared and activated Ag_{25}/carbon catalysts showed high selectivity towards styrene oxide, with maximum activities and selectivities seen for clusters activated at 250 ^oC. The catalytic performance of the presumed best catalyst was however reduced when a small amount of

TBHP was used. Results showed that the reaction progressed much slowly using the greenest choice of oxidant, i.e. oxygen in air, as the major oxygen atom source for epoxide formation.

2.5 References

1. M. Haruta, T. Kobayashi, H. Sano, N. Yamada. Novel Gold Catalysts for the Oxidation of Carbon Monoxide at a Temperature far Below 0 °C, *Chem. Lett.* 1987, **16,** 405-408.

2. R. Jin, C. Zeng, M. Zhou, Y. Chen. Atomically Precise Colloidal Metal Nanoclusters and Nanoparticles: Fundamentals and opportunities, *Chem. Rev.* 2016, **116**, 10346-10413.

3. J. Zeng, Q. Zhang, J. Chen, Y. Xia. A Comparison Study of the Catalytic Properties of Au-Based Nanocages, Nanoboxes, and Nanoparticles, *Nano Lett.* 2010, **10,** 30-35.

4. N. Li, X. Lai, P. Zhao, G. Yue, D. Astruc, M. Shuai, S. Su. Gold Nanoparticles as Sensors in the Colorimetric and Fluorescence Detection of Chemical Warfare Agents, *Coord. Chem. Rev.* 2015, **311**, 75-84.

5. M.S. Bootharaju, C.P. Joshi, M.R. Parida, O.F. Mohammed, O.M. Bakr, Angew. Templated Atom-Precise Galvanic Synthesis and Structure Elucidation of a $[Ag_{24}Au(SR)_{18}]^-$ Nanocluster, *Angew. Chem. Int. Ed.* 2016, **55**, 922-926.

6. X. Yuan, X. Dou, K. Zheng, J. Xie. Recent Advances in the Synthesis and Applications of Ultrasmall Bimetallic Nanoclusters, *Part. Part. Syst. Charact.* 2015, **32**, 613-629.

7. J. Wang, G. Wang,J. Zhao. Density-Functional Study of Au_n (n = 2-20) Clusters: Lowest-Energy Structures and Electronic Properties, *Phys. Rev. B* 2002, **66**, 1-6.

8. L. Wang, J. Zhang, Y. Zhu, S. Xu, C. Wang, C. Bian, X. Meng, F.S. Xiao. Strong Metal-Support Interactions Achieved by Hydroxide-to-Oxide Support Transformation for Preparation of Sinter-Resistant Gold Nanoparticle Catalysts, *ACS Catal.* 2017, **7**, 7461-7465.

9. Y. Zhu, H. Qian, M. Zhu, R. Jin. Thiolate-Protected Au(n) Nanoclusters as Catalysts for Selective Oxidation and Hydrogenation Processes, *Adv. Mater.* 2010, **22**, 1915-1920.

10. Y. Liu, H. Tsunoyama, T. Akita, T. Tsukuda. Efficient and Selective Epoxidation of Styrene with TBHP Catalyzed by Au_{25} Clusters on Hydroxyapatite, *Chem. Commun*. 2010, **46**, 550-552.

11. G. Li, D.E. Jiang, S. Kumar, Y. Chen, R. Jin. Size Dependence of Atomically Precise Gold Nanoclusters in Chemoselective Hydrogenation and Active Site Structure, *ACS Catal.* 2014, **4**, 2463-2469.

12. A. Shivhare, D.M. Chevrier, R.W. Purves, R.W.J. Scott. Following the Thermal Activation of $Au_{25}(SR)_{18}$ Clusters for Catalysis by X-ray Absorption Spectroscopy, *J. Phys. Chem. C* 2013, **117**, 20007-20016.

13. V. Sudheeshkumar, A. Shivhare, R.W.J. Scott. Synthesis of Sinter-Resistant Au@silica Catalysts Derived from Au_{25} Clusters, *Catal. Sci. Technol.* 2017, **7**, 272-280.

14. T. Chen, R.R. Nasaruddin, M.J. Hülsey, J. Xie, Q. Yao, N. Yan. Hydride-Induced Ligand Dynamic and Structural Transformation of Gold Nanoclusters during a Catalytic Reaction, *Nanoscale* 2018, **10**, 23113-23121.

15. J. Zhao, R. Jin. Heterogeneous Catalysis by Gold and Gold-Based Bimetal Nanoclusters, *Nano Today* 2018, **18**, 86-102.

16. D.M. Chevrier, R. Yang, A. Chatt, P. Zhang. Bonding Properties of Thiolate-Protected Gold Nanoclusters and Structural Analogs from X-Ray Absorption Spectroscopy, *Nanotechnol. Rev.* 2015, **4**, 193-206.

17. A.I. Frenkel. Applications of Extended X-Ray Absorption Fine-Structure Spectroscopy to Studies of Bimetallic Nanoparticle Catalysts, *Chem. Soc. Rev*. 2012, **41**, 8163-8178.

18. M.A. MacDonald, D.M. Chevrier, P. Zhang, H. Qian, R. Jin. The Structure and Bonding of $Au_{25}(SR)_{18}$ Nanoclusters from EXAFS: The Interplay of Metallic and Molecular Behavior, *J. Phys. Chem. C* 2011, **115**, 15282-15287.

19. K.E. Lee, A. Shivhare, Y. Hu, R.W.J. Scott. Supported Bimetallic AuPd Clusters Using Activated Au_{25} Clusters, *Catal. Today* 2017, **280**, 259-265.

20. M. Urushizaki, H. Kitazawa, S. Takano, R. Takahata, S. Yamazoe, T. Tsukuda. Synthesis and Catalytic Application of Ag_{44} Clusters Supported on Mesoporous Carbon, *J. Phys. Chem. C* 2015, **119**, 27483-27488.

21. Q. Ge, H. Xu, R. Jin, X. Nie, H. Qian. CO Oxidation Catalyzed by Oxide-Supported $Au_{25}(SR)_{18}$ Nanoclusters and Identification of Perimeter Sites as Active Centers, *ACS Nano* 2012, **6**, 6014-6022.

22. G.M. Veith, A.R. Lupini, S. Rashkeev, S.J. Pennycook, D.R. Mullins, V. Schwartz, C.A. Bridges, N.J. Dudney. Thermal Stability and Catalytic Activity of Gold Nanoparticles Supported on Silica, *J. Catal.* 2009, **262**, 92-101.

23. H. Yin, Z. Ma, H. Zhu, M. Chi, S. Dai. Evidence for and Mitigation of the Encapsulation of Gold Nanoparticles within Silica Supports upon High-Temperature Treatment of Au/SiO_2 Catalysts: Implication to Catalyst Deactivation, *Appl. Catal. A Gen*. 2010, **386**, 147-156.

24. J. Fang, J. Li, B. Zhang, X. Yuan, H. Asakura, T. Tanaka, K. Teramura, J. Xie, N. Yan. The Support Effect on the Size and Catalytic Activity of Thiolated Au_{25} Nanoclusters as Precatalysts, *Nanoscale* 2015, **7**, 6325-6333.

25. Y. Zhu, H. Qian, R. Jin. An Atomic-Level Strategy for Unraveling Gold Nanocatalysis from the Perspective of $Au_n(SR)_m$ Nanoclusters, *Chem. Eur. J.* 2010, **16**, 11455-11462.

26. M. Dasog, W. Hou, R.W.J. Scott. Controlled Growth and Catalytic Activity of Gold Monolayer Protected Clusters in Presence of Borohydride Salts, *Chem. Commun*. 2011, **47**, 8569-8571.

27. S.M. Ansar, F.S. Ameer, W. Hu, S. Zou, C.U. Pittman, D. Zhang. Removal of Molecular Adsorbates on Gold Nanoparticles Using Sodium Borohydride in Water, *Nano Lett.* 2013, **13**, 1226-1229.

28. E.W. Elliott, R.D. Glover, J.E. Hutchison. Removal of Thiol Ligands from Surface-Confined Nanoparticles without Particle Growth or Desorption, *ACS Nano* 2015, **9**, 3050-3059.

29. J. Kilmartin, R. Sarip, R. Grau-Crespo, D. Di Tommaso, G. Hogarth, C. Prestipino, G. Sankar. Following the Creation of Active Gold Nanocatalysts from Phosphine-Stabilized Molecular Clusters, *ACS Catal.* 2012, **2**, 957-963.

30. F.X. Xiao, Z. Zeng, S.H. Hsu, S.F. Hung, H.M. Chen, B. Liu. Light-Induced *In Situ* Transformation of Metal Clusters to Metal Nanocrystals for Photocatalysis, *ACS Appl. Mater. Interfaces* 2015, **7**, 28105-28109.

31. Y. Zhu, H. Qian, A. Das, R. Jin. Comparison of the Catalytic Properties of 25-Atom Gold Nanospheres and Nanorods. *Chin. J. Catal.* 2011, **32**, 1149-1155.

32. R. Xu, D. Wang, J. Zhang, Y. Li. Shape-Dependent Catalytic Activity of Silver Nanoparticles for the Oxidation of Styrene, *Chem. Asian J.* 2006, **1**, 888-893.

33. L. Zhou, C.F. Gorin, R.J. Madix. Cesium Promotion in Styrene Epoxidation on Silver Catalysts, *J. Am. Chem. Soc.* 2010, **132**, 434-435.

34. X. Yuan, M.I. Setyawati, A.S. Tan. C.N. Ong, D.T. Leong, J. Xie. Highly Luminescent Silver Nanoclusters with Tunable Emissions: Cyclic Reduction-Decomposition Synthesis and Antimicrobial Properties, *NPG Asia Mater*. 2013, **5**, e39.

35. F.D. David, A.G. Kantor, I.J. Rankine, S.K. Wheeler, J.F. Wheeler, M. Ganguly, J.T. Petty, O.O. Sergev. Ten-Atom Silver Cluster Signaling and Tempering DNA Hybridization, *Anal. Chem.* 2015, **87**, 5302-5309.

36. K.P. Remya, T. Udayabhaskararao, T. Pradeep. Low-Temperature Thermal Dissociation of Ag Quantum Clusters in Solution and Formation of Monodisperse Ag_2S Nanoparticles, *J. Phys. Chem. C* 2012, **116**, 26019-26026.

37. A. Desireddy, B.E. Conn, J. Guo, B. Yoon, R.N. Barnett, B.M. Monahan, K. Kirschbaum, W.P. Griffith, R.L. Whetten, U. Landman, T.P. Bigioni. Ultrastable Silver Nanoparticles, *Nature* 2013, **501**, 399-402.

38. K. Zheng, X. Yuan, J. Xie. Effect of Ligand Structure on the Size Control of Mono- and Bi-Thiolate-Protected Silver Nanoclusters, *Chem. Commun*. 2017, **53**, 9697-9700.

39. C.P. Joshi, M.S. Bootharaju, M.J. Alhilaly, O.M. Bakr. $[Ag_{25}(SR)_{18}]^-$: The "Golden" Silver Nanoparticle, J. *Am. Chem. Soc.* 2015, **137**, 11578-11581.

40. J.D. Padmos, P. Zhang. Surface Structure of Organosulfur Stabilized Silver Nanoparticles Studied with X-ray Absorption Spectroscopy, *J. Phys. Chem. C* 2012, **116**, 23094-23101.

41. C.A. Schneider, W.S. Rasband, K.W. Eliceiri. NIH Image to ImageJ: 25 Years of Image Analysis HHS Public Access, *Nat. Methods* 2012, **9**, 671-675.

42. CasaXPS: Processing Software for XPS, AES, SIMS and More, Teignmouth, UK, 2016.

43. B. Ravel, M. Newville. ATHENA, ARTEMIS, HEPHAESTUS: Data Analysis for X-Ray Absorption Spectroscopy Using IFEFFIT, *J. Synchrotron Radiat.* 2005, **12**, 537-541.

44. K. Momma, F. Izumi. VESTA: A Three-Dimensional Visualization System for Electronic and Structural Analysis, *J. Appl. Crystallogr.* 2008, **41**, 653-658.

45. X.L. Du, X.L. Wang, Y.H. Li, Y.L. Wang, J.J. Zhao, L.J. Fang, L.R. Zheng, H. Tong, H.G. Yang. Isolation of Single Pt Atoms in a Silver Cluster: Forming Highly Efficient Silver-Based Cocatalysts for Photocatalytic Hydrogen Evolution, *Chem. Commun.* 2017, **53**, 9402-9405.

46. H. Yamamoto, H. Yano, H. Kouchi, Y. Obora, R. Arakawa, H. Kawasaki. *N,N*-Dimethylformamide-Stabilized Gold Nanoclusters as a Catalyst for the Reduction of 4-Nitrophenol, *Nanoscale* 2012, **4**, 4148-4154.

47. J. Fang, B. Zhang, Q. Yao, Y. Yang, J. Xie, N. Yan. Recent Advances in The Synthesis and Catalytic Applications of Ligand-Protected, Atomically Precise Metal Nanoclusters, *Coord. Chem. Rev.* 2016, **322**, 1-29.

48. R.R. Nasaruddin, T. Chen, N. Yan, J. Xie. Roles of Thiolate Ligands in the Synthesis, Properties and Catalytic Application of Gold Nanoclusters, *Coord. Chem. Rev.* 2018, **368**, 60-79.

49. J.C. Lascovich, S. Scaglione. Comparison among XAES, PELS and XPS Techniques for Evaluation of Sp^2 Percentage in a-C:H, *Appl. Surf. Sci.* 1994, **78**, 17-23.

50. X. She, M. Flytzani-Stephanopoulos. The Role of Ag-O-Al Species in Silver-Alumina Catalysts for the Selective Catalytic Reduction of NO_x with Methane, *J. Catal.* 2006, **237**, 79-93.

51. G. Corro, E. Vidal, S. Cebada, U. Pal, F. Bañuelos, D. Vargas, E. Guilleminot. Electronic State of Silver in Ag/SiO_2 and Ag/ZnO Catalysts and Its Effect on Diesel Particulate Matter Oxidation: An XPS Study, *Appl. Catal. B Environ.*, 2017, **216**, 1-10.

52. A. Majid, F. Bensebaa, P. L'Ecuyer, G. Pleizier, Y. Deslandes. Modification of the Metallic Surface of Silver by the Formation of Alkanethiol Self-Assembled Monolayers with Subsequent Reaction with Chlorosilanes, *Rev. Adv. Mater. Sci.* 2003, **4**, 25-31.

53. D.G. Castner, K. Hinds, D.W. Grainger. X-ray Photoelectron Spectroscopy Sulfur 2p Study of Organic Thiol and Disulfide Binding Interactions with Gold Surfaces, *Langmuir* 2002, **12**, 5083-5086.

54. D. Schilter. Thiol Oxidation: A Slippery Slope, *Nat. Rev. Chem.* 2017, **1**, 0013.

55. J.P.R. Chauvin, D.A. Pratt. On the Reactions of Thiols, Sulfenic Acids, and Sulfinic Acids with Hydrogen Peroxide, *Angew. Chem. Int. Ed.* 2017, **56**, 6255-6259.

56. B. Zhang, A. Sels, G. Salassa, S. Pollitt, V. Truttmann, C. Rameshan, J. Llorca, W. Olszewski, G. Rupprechter, T. Bürgi, N. Barrabés. Ligand Migration from Cluster to Support: A Crucial Factor for Catalysis by Thiolate-protected Gold Clusters, *ChemCatChem.* 2018, **10**, 5372-5376.

57. J.W. Niemantsverdriet. Spectroscopy in Catalysis: An Introduction, Third edit.; Wiley-VCH Verlag GmbH & Co. KGaA, 2007.

58. Gangishetty, R.W.J. Scott, T.L. Kelly. Thermal Degradation Mechanism of Triangular Ag@SiO_2 Nanoparticles, *Dalton Trans.* 2016, **45**, 9827-9834.

59. J.D. Padmos, D.J. Morris, P. Zhang. The Structure and Bonding Properties of Tiopronin-Protected Silver Nanoparticles as Studied by X-Ray Absorption Spectroscopy, *Can. J. Chem.* 2018, **96**, 749-754.

60. J. Timoshenko, S. Roese, H. Hövel, A.I. Frenkel. Silver Clusters Shape Determination from *In-Situ* XANES Data. *Radiat. Phys. Chem.* 2018, 1-4.

61. F.B.M Duivenvoorden, B.J. Kip, D.C. Koningsberger, R. Prins. Determination of the Metal Particle Size of Supported Pt, Rh, and Ir Catalysts. A Calibration of Hydrogen Chemisorption by EXAFS, *J. Phys. Colloq.* 2007, **47**, 227-230.

62. B.S. Clausen, L. Grabaek, H. Topsoe, L.B. Hansen, P. Stoltze, J.K. Norskov, O.H. Nielsen. A New Procedure for Particle Size Determination by EXAFS Based on Molecular Dynamics Simulations, *J. Catal.* 1993, **141**, 368-379.

63. H. Wei, C. Gomez, J. Liu, N. Guo, T. Wu, R. Lobo-Lapidus, C.L. Marshall, J.T. Miller, R.J. Meyer. Selective Hydrogenation of Acrolein on Supported Silver Catalysts: A Kinetics Study of Particle Size Effects. *J. Catal.* 2013, **298**, 18-26.

64. Summary of Rules for Error Propagation
https://sites.fas.harvard.edu/~scphys/nsta/error_propagation.pdf.

65. X.Y. Dong, Z.W. Gao, K.F. Yang, W.Q. Zhang, L.W. Xu. Nanosilver as a New Generation of Silver Catalysts in Organic Transformations for Efficient Synthesis of Fine Chemicals, *Catal. Sci. Technol.* 2015, **5**, 2554-2574.

66. R. Mckenna, S. Pugh, B. Thompson, D.R. Nielsen. Microbial Production of the Aromatic Building-Blocks (S)-Styrene Oxide and (R)-1,2-Phenylethanediol from Renewable Resources, *Biotechnol. J.* 2013, **8**, 1465-1475.

67. E. Tebandeke, C. Coman, K. Guillois, G. Canning, E. Ataman, J. Knudsen, L.R. Wallenberg, H. Ssekaalo, J. Schnadt, O.F. Wendt. Epoxidation of Olefins with Molecular Oxygen as the Oxidant Using Gold Catalysts Supported on Polyoxometalates, *Green Chem.* 2014, **16**, 1586-1593.

68. Z. Chen, R.L. Luck. Oxidation of Olefins Using Atmospheric Oxygen Atoms Initiated by tert-Butyl hydroperoxide or Hydrogen Peroxide with Silver Nanoparticles Deposited on MCM-41 as Catalysts, *Green Chem.* 2016, **18**, 3354-3359.

69. S. Bawaked, N.F. Dummer, N. Dimitratos, D. Bethell, Q. He, C.J. Kiely, G.J. Hutchings. Solvent-Free Selective Epoxidation of Cyclooctene Using Supported Gold Catalysts, *Green Chem.* 2009, **11**, 1037-1044.

70. M. Vandichel, K. Leus, P. Van Der Voort, M. Waroquier, V. Van Speybroeck. Mechanistic Insight into the Cyclohexene Epoxidation with $VO(acac)_2$ and tert-Butyl hydroperoxide, *J. Catal.* 2012, **294**, 1-18.

Chapter 3

Atom-Precise Ag Clusters as Precursors for Selective Bimetallic AgPd Heterogeneous Catalysts

In this chapter, an indirect method for preparing AgPd bimetallic clusters is documented. Mildly activated Ag clusters on carbon supports were investigated as a precursor for making AgPd bimetallic clusters via a sequential reduction approach. EXAFS analysis suggested a cluster-in-cluster structural arrangement in the carbon-supported bimetallic samples prepared via the sequential reduction approach. Within the range of metal composition ratios studied, there was no limit to the amount of Pd that could be incorporated to make AgPd bimetallic samples via this sequential deposition approach. The catalyst structures and their catalytic performances for selective hydrogenation reactions of alkynes were correlated and alkene selectivity decreased with increases in Pd loading.

This chapter is a manuscript that will be submitted for publication in the near future. I wrote the complete first draft of the manuscript and this was then edited with the guidance of Prof. Robert W.J. Scott. Andrew Bueckert, who was a summer student in our laboratory under my supervision, assisted with the testing of catalysts, and Ahmed Abdellah performed the STEM imaging under the supervision of Dr. V. Sudheeshkumar and Dr. Drew Higgins at Canadian Centre for Electron Microscopy (CCEM), McMaster University, Ontario, Canada.

3.1 Introduction

The synthesis and activation of bimetallic clusters is an active research area towards making model heterogeneous catalysts for selective hydrogenation and oxidation reactions.[1-3] Bimetallic clusters can show superior physicochemical and catalytic properties compared to monometallic cluster catalysts due to synergistic interactions between the constituent metals.[3-6] Several factors including choice of metals and method of preparation influence the constituent atom arrangement; this can contribute to superior catalytic performance of bimetallic systems compared to monometallic systems.[3,7] Careful synthetic protocols are needed to achieve pure, atom-precise bimetallic clusters with controlled cluster size, composition, and structure.[3,8] Both direct synthesis and post-synthesis treatment strategies are well documented in literature and largely used for preparing atom-precise Au- and Ag-based bimetallic catalysts.[6,9,10] Direct synthesis methods often have both thermodynamic limitations and purification challenges which can limit the possible compositions of bimetallic clusters made by such routes.[9,11,12] Post-synthesis strategies involving the secondary reaction of atom-precise clusters can also afford excellent structural and compositional control of clusters, and potentially allow for greater compositional flexibility.[12,13] The sequential deposition approach reported herein is a post-synthesis strategy which entails the use of mildly activated metal clusters on supports as precursors for making bimetallic heterogeneous catalysts.[14]

The $Au_{25}(SR)_{18}$ cluster motif remains the most researched atom-precise metal cluster system owing to its early discovery, facile preparation, great stability, and ease of functionalization.[15] Our group and others have developed Au and AuPd cluster catalysts for oxidation and hydrogenation reactions, with on-going efforts to achieve stability of these clusters against sintering upon activation.[8,11,14,16-19] Unlike Au cluster systems, the design and development of Ag clusters are still limited due to susceptibility of Ag to oxidation. However, Ag cluster systems are gaining interest given their similar chemistry and the higher relative abundance and lower cost of Ag compared to Au. Of major interest amongst them is the atom-precise $Ag_{25}(SR)_{18}^-$ clusters that are similar (but not identical) to $Au_{25}(SR)_{18}^-$ clusters in terms of atomic arrangements and ligand counts. The crystal structure of $Ag_{25}(SR)_{18}^-$ clusters shows four voids that enable solvent coordination which promotes higher stability of the clusters.[20] Recently, I prepared activated Ag clusters on carbon supports without the formation of Ag_2O or Ag_2S and hypothesized

that such mildly activated Ag clusters could serve as precursor for making AgPd bimetallic heterogeneous catalysts (Chapter 2). Previous results in our group have shown that Pd atoms can be selectively reduced on the surface of activated Ag nanoparticles via galvanic reactions,[1] and the use of smaller sized Ag clusters as precursors for this reaction is of research interest in designing Ag-based bimetallic catalysts. Herein, I report the sequential reduction of Pd onto activated Ag_{25} clusters on carbon supports to make carbon-supported AgPd bimetallic clusters. The bimetallic cluster structures were further elucidated using element specific X-ray absorption spectroscopy (XAS), followed by catalytic evaluation of these heterogeneous catalysts in selective hydrogenation reactions.

Pd catalysts are known to be highly active catalysts for alkyne hydrogenations, but have intrinsically poor selectivity to alkenes because of over-hydrogenation to alkanes.[21] However, the selectivity of Pd catalysts can be improved by addition of secondary metals that enable isolation of Pd active sites.[22] Specifically, Ag is a remarkably good secondary metal to suppress the over-hydrogenation of alkynes to alkanes by Pd catalysts in industrial processes.[23] Glyzdova *et al.* posited that dilution of Pd atoms can prevent adsorption of acetylene in a strong multisite mode and improve ethylene selectivity.[24] A DFT study by Zhao *et al.* showed that there is a shift in the Pd d-band center in Pd alloys and this favours ethylene desorption over its further hydrogenation to ethane in the selective hydrogenation of acetylene.[25] Mitsudome *et al.* reported 99% selectivity for 1-octene in the hydrogenation of 1-octyne at room temperature and 1 bar pressure over Pd@Ag nanoparticle catalysts with core-shell structures.[26] We previously investigated the hydrogenation of allyl alcohol, 3-buten-1-ol, and 3-hexyn-1-ol over AgPd catalysts prepared via galvanic exchange between Ag nanoparticle seeds and K_2PdCl_4, and showed that presence of Ag significantly improved the selectivity of hydrogenation over isomerization products.[1] The selective hydrogenation of 2-methyl-3-butyn-2-ol (MBY) to 2-methyl-3-buten-2-ol (MBE) is another model hydrogenation reaction of industrial interest. While formation of the alkane product, 2-methyl-2-butanol (MBA) is less desirable, MBE is a key product in the manufacture of vitamins and aroma compounds, and high selectivity to MBE is desirable due to the hurdles in the separation of MBE/MBA mixtures.[27,28]

This work probes the location and speciation of Pd in heterogeneous AgPd bimetallic clusters prepared via a sequential deposition (SD) strategic route. Using X-ray absorption

spectroscopy (XAS) and other techniques, our results show that the mildly activated Ag_{25} clusters on carbon supports serve as an excellent precursor to make AgPd/carbon bimetallic catalysts. The constituent metal ratio influences the relative position of the Pd in the resulting AgPd bimetallic system, and the resulting structure is correlated to the catalytic performance of the AgPd bimetallic clusters as selective heterogeneous catalysts for the hydrogenation of MBY. The SD-AgPd/carbon catalysts show cluster-in-cluster atoms arrangements, with no limit to the amount of Pd that can be incorporated to form the AgPd bimetallic structures. AgPd catalysts with high Ag/Pd ratios strategically positions Pd in subsurface sites which enables the suppression of over-hydrogenation products of MBY, resulting in high MBE selectivity. Conversely, AgPd bimetallic catalysts with high Pd loadings have more Pd atoms on the surface and show high MBY conversion but poor MBE selectivity due to the over-hydrogenation of MBY.

3.2 Experimental

3.2.1 Materials

Silver nitrate ($AgNO_3$, ≥99.0%), palladium (II) acetate ($Pd(OAc)_2$, 99.9%), 100% ethanol (EtOH), 2-methyl-3-butyn-2-ol (MBY, 98%), and high purity acetonitrile (MeCN) were procured from Sigma Aldrich. Dichloromethane (CH_2Cl_2, DCM), methanol (MeOH, HPLC grade), sodium borohydride ($NaBH_4$, 98%), and tetrahydrofuran (high purity, THF) were purchased from Fisher Scientific. 2,4-Dimethylbenzenethiol ($HSPhMe_2$, C_8H_9SH, 95%), 2-propanol (isopropanol, HPLC grade, 99.7+%), and tetraphenylphosphonium bromide (Ph_4PBr) were procured from Alfa Aesar, while activated carbon (Powder, CX0657-1) was purchased from EMD. All chemicals are commercially available and were used as received without any further purification. In all experiments, Milli-Q (Millipore, Bedford, MA) deionized water with a resistivity of 18.2 MΩ cm was used. Glassware was thoroughly cleaned using aqua regia, rinsed with deionized water, and then dried completely before use.

3.2.2 Preparation of Carbon-Supported Ag Monometallic and AgPd Bimetallic Clusters

The 2,4-dimethylbenzenethiolate-protected Ag clusters were prepared as described in section 2.2.2. The wetness impregnation method was employed to immobilize Ag clusters onto carbon supports to give a final metal loading of 2.2 wt %, as determined by elemental analysis. Typically, 20 mL of a DCM solution of $Ag_{25}(SPhMe_2)_{18}^-$ clusters was added to 2.0 g of activated

carbon and stirred for 30 min, after which the colourless supernatant was removed under vacuum using a rotatory evaporator, and then a Schlenk line for complete removal of solvent, to obtain the carbon-supported Ag clusters (Ag/carbon) in dried form. The dried Ag/carbon sample was then calcined at 250 °C for 2 h at a ramping rate of 10 °C/min under air flow using a Lindberg/Blue M furnace to make the Ag/carbon precursor. The Ag/carbon sample was then washed twice with chloroform to remove disulfide and oxidized sulfur byproducts created by the activation of the $Ag_{25}(SPhMe_2)_{18}^-$ clusters by thermal treatment. The final SD-Ag/carbon sample was dried under ambient conditions and used as a precursor to prepare carbon-supported AgPd bimetallic clusters via a sequential deposition (SD) method. For the SD-1:1-Ag:Pd/carbon sample, 200 mg of the Ag/carbon sample (4.17×10^{-5} moles Ag) was dispersed in 5 mL of THF, and 8.34×10^{-5} moles (14.7 mg) of ascorbic acid and 4.17×10^{-5} moles Pd (9.4 mg Pd(II) acetate) were sequentially added, followed by stirring for 10 min. This was then followed by washing with an ethanol-water (1:1) mixture, followed by solvent removal using a Schlenk line vacuum. Other SD-x:y-Ag:Pd/carbon samples (where x:y is 12:1, 6:1, 2:1, 1:1, 1:2, and 1:6) were prepared in the same way by varying the amount of Pd and ascorbic acid added to the system.

3.2.3 Characterization Techniques

UV-Vis absorption spectroscopy and X-ray photoelectron spectroscopy (XPS) measurements were collected as described in section 2.2.4. Electrospray ionization mass spectrometry (ESI-MS) measurements were performed on a Thermo Fisher Q-Exactive mass spectrometer operating at the maximum resolving power of 140,000 (at m/z 200), using a m/z range of 2000-6000. The sample was continuously introduced to the heated electrospray ionization source at 10 µL/min. A spray voltage of 3.5-4.0 kV was used with sheath and auxiliary gas settings of 12 and 2 respectively, and a probe temperature of 50 °C. Prior to sample injection, purified monometallic Ag clusters were dissolved in DCM and 20 µL of the cluster solution (1 mg/mL) was further diluted with 1980 µL MeCN solvent. This diluted cluster solution was then vortexed for 2 min before injecting into the instrument for sample analysis in the negative ionization mode of ESI-MS.

Elemental composition was determined using Varian SpectrAA 55 atomic absorption spectroscope equipped with a multi-element hollow cathode lamp. 50 mg of catalyst sample (Ag/carbon) was placed in 4 mL of aqua regia (prepared with ultrapure reagents; HNO_3: HCl =

1:3) for 24 h. The sample in aqua regia was passed through a cellulose filter to get rid of undissolved support and then the filtrate was diluted to 10 mL by deionized water for elemental analysis. Another 4.0 mL of aqua regia was diluted to 10 mL with deionized water and was used as the blank. Transmission electron microscopy (TEM) images were collected using a Hitachi HT7700 TEM operated at 100 kV. TEM samples were prepared by drop casting cluster solutions onto a carbon coated 300 mesh copper TEM grid (Electron Microscopy Sciences, Hatfield, PA) and drying at ambient condition prior to TEM analysis. Scanning transmission electron microscopy (STEM) images were collected by a Thermo Scientific Talos 200X high-angle annular dark-field scanning transmission electron microscopy (HAADF-STEM) operating at 200 kV. Elemental mapping was done using the Pd and Ag L peaks, respectively, from the energy dispersive X-ray spectra at each data point. The sample for STEM analysis was prepared by drop-casting the cluster solution (dispersed in isopropanol) onto a holey carbon-coated 200 mesh Cu grid. Typically, average particle sizes were manually determined by measuring 100 particles from images obtained for each sample using the ImageJ software program.[29]

X-ray absorption spectroscopy (XAS) studies at the Ag K-edge and Pd K-edge were conducted at the Biological X-ray Absorption Spectroscopy (BioXAS) beamline 07ID-2 (Energy range 4-32 keV; resolution 1 x 10^{-4} $\Delta E/E$; spot size 5 mm x 0.5 mm (W x H)) at the CLS. Energy selection of the Ag and Pd K-edge was done using a Si(220) double-crystal Si monochromator, with a water-cooled toroidal Rh coated Si mirror before the monochromator and a second Rh-coated Si (focusing) mirror after the monochromator. Ionization chambers were filled with Ar gas and samples were measured in fluorescence mode at room temperature using a 32-element Ge detector. A GUI based data acquisition manager software (AquaMan) and a Python-based automation package were employed for data acquisition. The energy of the X-rays was calibrated by using Ag and Pd foils (25514 eV and 24350 eV respectively) for their K-edge measurements. The data processing was performed using the IFEFFIT software package.[30] The XANES spectra were obtained by subtracting the atomic absorption background and normalizing the spectra to the edge height. The k^2-weighted spectra were subjected to a Fourier transform (FT) in R space for the k range of 2.8-12 $Å^{-1}$ for Ag and Pd data. Ag fcc bulk lattice parameters were used to fit the Ag-foil spectrum, keeping the first shell coordination number fixed (CN = 12) at first to determine the amplitude reduction factor (S_0^2). Similar data fitting was performed for Pd fcc bulk lattice parameters for the Pd-foil spectrum. From these fits, amplitude reduction factors of 0.80 and 0.79

were determined for the Ag-foil and Pd-foil, respectively, and these values were used for the subsequent bimetallic sample fits.

3.2.4 Catalyst Evaluation

Hydrogenation reactions were carried out in a 50 mL three-neck round bottom flask. Prior to sealing all the three necks, an egg-shaped magnetic stirrer, 25.0 mg of catalyst, and 5.0 mL of EtOH were added to the reaction flask which was then purged with continuous flow of H_2 gas for 10 min. Thereafter, the system was filled with ca. 1.5 atm H_2 gas and allowed to equilibrate for 10 min, during which there was no observable leakage as monitored by a differential pressure manometer (407910, Extech Instrument). 2.0 mmol of 2-methyl-3-butyn-2-ol (MBY) was quickly added to start the reaction, and the reaction mixture was stirred at 1400 rpm for 180 min at 25 °C. After the reaction, the suspension was centrifuged to remove the solid catalyst and the liquid sample containing the catalytic products was analyzed by gas chromatography. The gas chromatograph (7890A, Agilent Technologies) was equipped with a flame ionization detector and a HP-5 column. For recycling experiments, the catalyst was washed twice in isopropanol, dried under vacuum, and reused in subsequent reaction cycles. The average TON was calculated as moles of substrate converted per moles of total metal (e.g. Ag+Pd).

3.3 Results and Discussion

The atom-precise $Ag_{25}(SR)_{18}^-$ clusters were formed upon reduction of a Ag(I)-thiolate complex with a freshly prepared aqueous solution of $NaBH_4$ in the presence of tetraphenyl phosphonium (Ph_4P^+) counter ions as previously reported.[20] The ESI-MS of the thiolate-protected Ag clusters shows a prominent molecular ion peak at m/z = 5166.3 and isotope distribution peaks are separated by a m/z value of 1; the m/z peak value affirms -1 as overall charge for the Ag clusters (Figure 3.1(a)), which is consistent with the value reported for atom-precise $Ag_{25}(SPhMe_2)_{18}^-$ clusters in the literature.[31] Figure 3.1(b) shows the UV-Vis spectrum of thiolate-protected Ag clusters with distinctive peaks at 334 nm, 392 nm, 490 nm, and 678 nm for the $Ag_{25}(SPhMe_2)_{18}^-$ clusters, which are also consistent with literature values.[20] The $Ag_{25}(SPhMe_2)_{18}^-$ clusters were then immobilized on carbon supports. TEM imaging of the intact clusters on carbon supports (Figure 3.2(a)) was challenging due the small size of the clusters and poor contrast between the clusters and support, nevertheless some clusters can be distinguished. Improved

contrast was observed for the carbon-supported Ag clusters after thermal activation at 250 °C, and an average particle size of 1.6 ± 0.4 nm was measured (Figure 3.2(b)) which indicates a mild amount of sintering has taken place. Previous work showed oxidative desorption of thiolate ligands off cluster surfaces under such mild heat treatments with consequent mild growth in cluster size (Chapter 2), while disulfides and other products of thiol oxidation adsorb onto the support.[32]

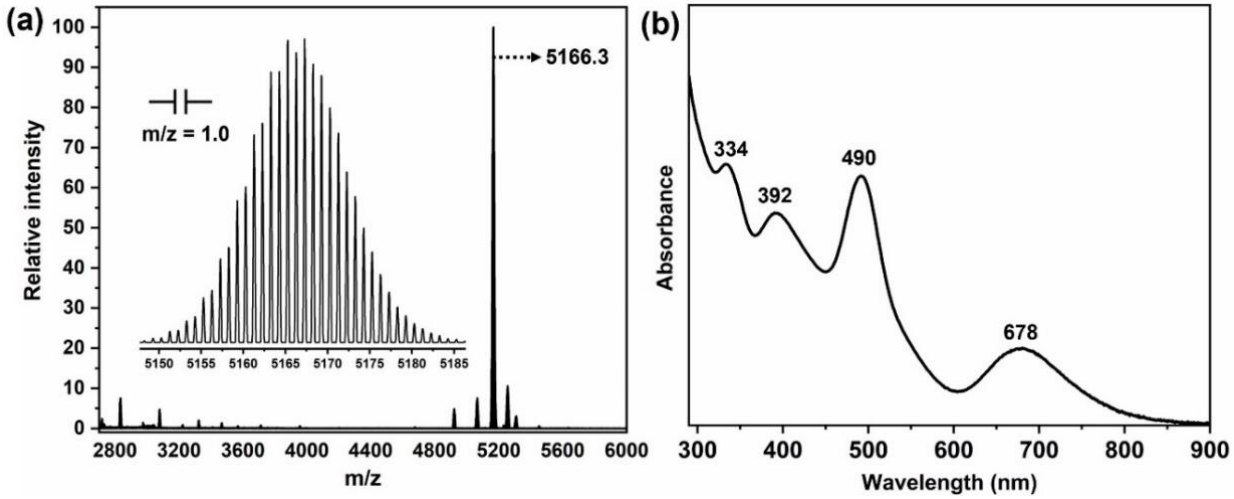

Figure 3.1. (a) ESI-MS spectrum and (b) UV-Vis absorption spectrum of $Ag_{25}(SPhMe_2)_{18}^-$ clusters in DCM.

Figure 3.3 shows the S 2p XPS spectra of the as-prepared carbon-supported $Ag_{25}(SR)_{18}^-$ cluster sample and those of thermally treated samples at 250 °C before and after washing with $CHCl_3$. The S $2p_{3/2}$ peak at 162.2 eV attributed to Ag-thiolate species is present in the as-prepared sample while calcined samples show S 2p peaks at higher binding energies and these peaks are features of organic disulfide and other oxidized sulfur species.[33] Quantification of the survey XPS spectra shows that the S species content decreases from 0.6% in the activated sample to 0.2% after the $CHCl_3$ wash, as the disulfides and other S species are soluble in $CHCl_3$,[34] and thus can be removed from the sample. The Ag $3d_{5/2}$ peak at ~368.1 eV suggests that Ag remains in metallic state upon activation of Ag clusters at 250 ^oC,[35] and was not affected by the $CHCl_3$ wash as indicated by the Ag 3d XPS spectra (Figure 3.4).

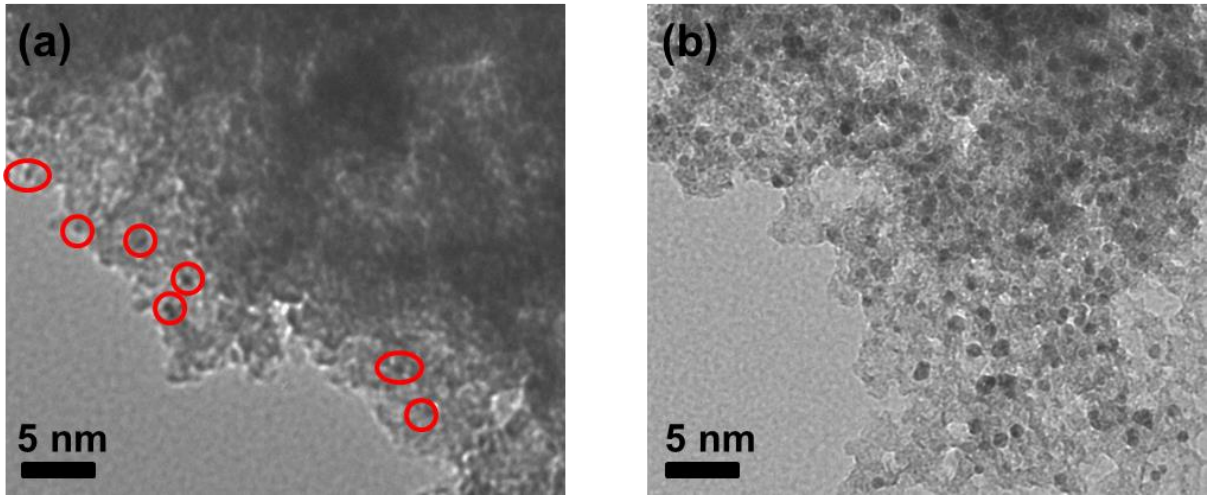

Figure 3.2. TEM images of carbon-supported $Ag_{25}(SR)_{18}$ clusters before (a) and after (b) thermal activation at 250 °C. The red circles in a) were added to show the location of $Ag_{25}(SR)_{18}$ clusters.

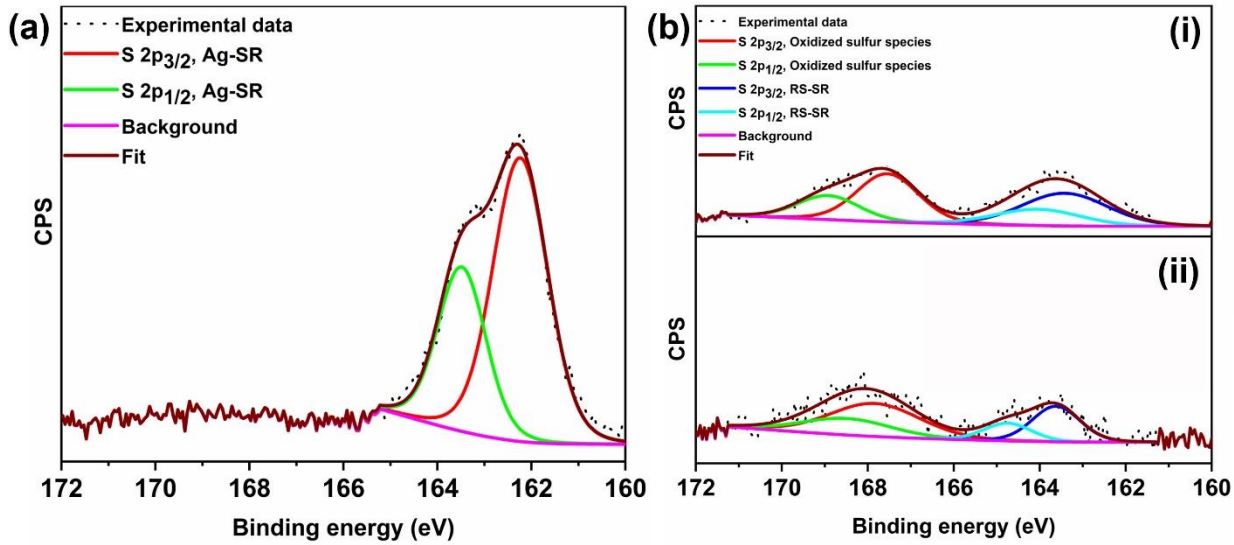

Figure 3.3. XPS S 2p XPS spectra of carbon-supported Ag clusters (a) as prepared and (b) thermally treated at 250 °C, (i) before and (ii) after $CHCl_3$ wash.

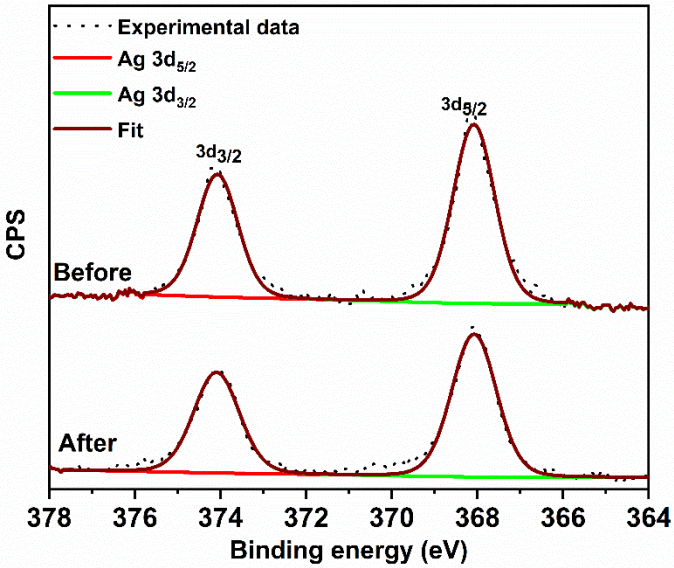

Figure 3.4. XPS Ag 3d spectra of carbon-supported Ag clusters thermally treated at 250 °C before and after $CHCl_3$ wash.

In the sequential deposition (SD) synthesis, Pd acetate was sequentially reduced with ascorbic acid onto the activated Ag clusters on carbon supports (labelled SD-Ag/carbon) to make AgPd bimetallic clusters with different Ag:Pd ratios (labelled SD-x:y-Ag:Pd/carbon); where x and y are the mole ratios as determined by elemental analysis (which were quite close to the synthetic mole ratios used). To ascertain the formation of bimetallic structures and rule out the possibility of secondary nucleation of pure Pd particles in the synthesis, STEM imaging was performed. Figures 3.5 and 3.6 show representative images obtained for the SD-6:1-Ag:Pd/carbon sample; individual particles show large populations of both Ag and Pd but without no obvious core-shell atomic arrangement. No Pd-only particles were seen which indicates the lack of secondary nucleation of new Pd particles during the synthesis, which is consistent with other work by our group and others using ascorbic acid as a mild reducing agent.[14,36]

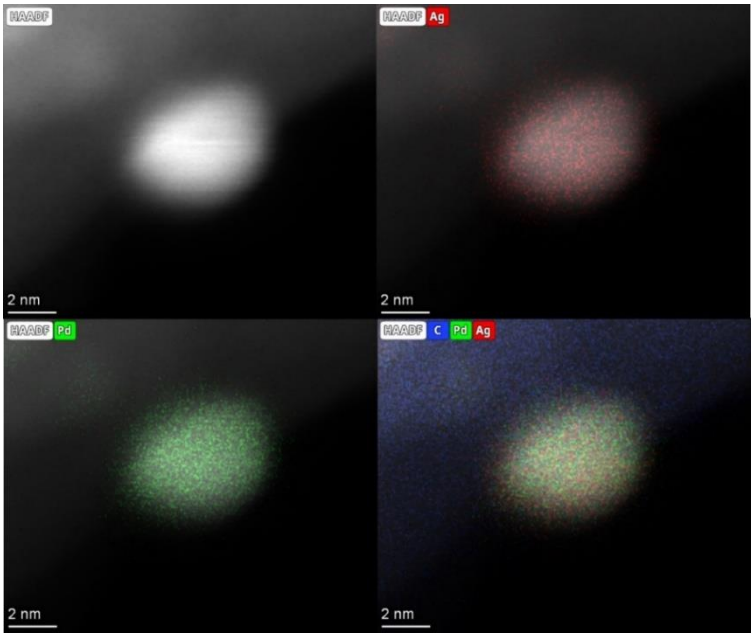

Figure 3.5. Representative STEM images of an individual particle in a SD-6:1-Ag:Pd/carbon sample. The blue, red, and green colour maps are for the contributions from C, Ag, and Pd, respectively in the sample determined by Energy Dispersive X-ray Spectroscopy.

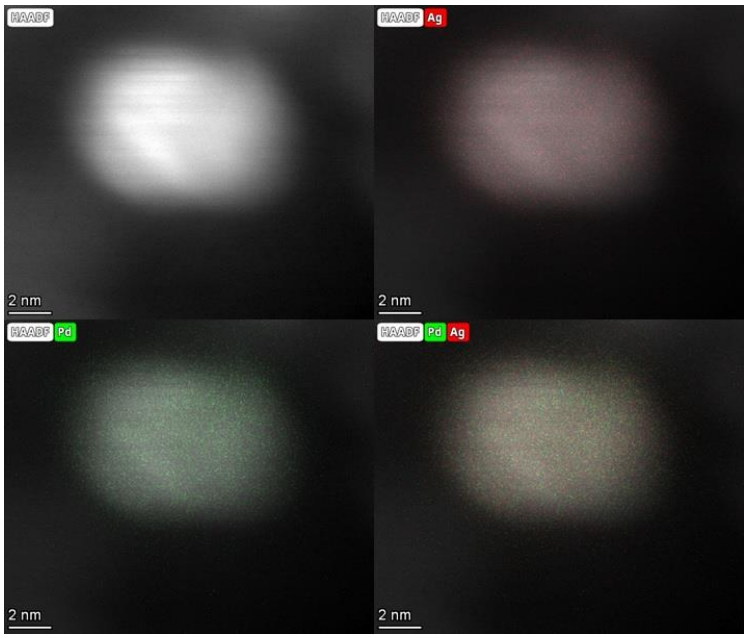

Figure 3.6. STEM images of another particle of the SD-6:1-Ag:Pd/carbon sample. The red and green colour mappings are for the contributions from Ag and Pd, respectively in the sample determined by Energy Dispersive X-ray Spectroscopy.

The SD-x:y-Ag:Pd/carbon samples were further characterized using XAS, a widely used technique to study the structure of bimetallic systems. XAS data can afford information about the oxidation state and local environment of a specific element of interest. Figure 3.7(a) shows the Ag K-edge XANES spectra for SD-Ag/carbon and the series of SD-x:y-Ag:Pd/carbon samples, as well as standard Ag_2O and Ag foils. In particular, all the SD-x:y-Ag:Pd/carbon samples have Ag foil-like XANES spectra which suggest that Ag is in a zerovalent fcc environment in all samples. Notably, the XANES spectrum obtained for the SD-Ag/carbon sample does not match up well with that of Ag foil, and this is due to small size of Ag clusters in SD-Ag/carbon sample. Figure 3.7(b) shows the corresponding XANES data for Pd K-edge measurements; all the SD-x:y-Ag:Pd/carbon samples show a Pd fcc-like metallic environment, with a strong K-edge feature for Pd at 24350 eV. The white line at the respective edges is attributed to the dipole-allowed 1s to 5p transition,[37] and all SD-x:y-Ag:Pd/carbon samples show similar near edge features to metal foils at both edges to suggest that Ag and Pd atoms are in Ag(0) and Pd(0) fcc environments, respectively (Figure 3.7). The amplitude of the photoelectron wave at high k decreases for the SD-x:y-Ag:Pd/carbon samples as compared to bulk Ag and Pd foils which suggests that small particles are formed with a large fraction of atoms on the surface.

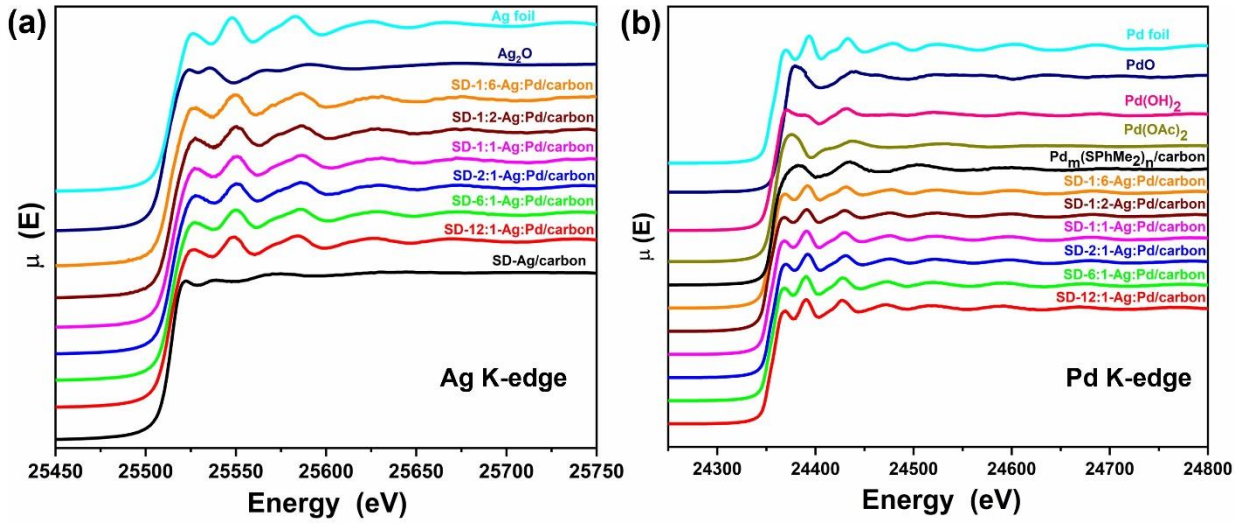

Figure 3.7. XANES spectra for (a) Ag K-edge of SD-Ag/carbon and SD-x:y-Ag:Pd/carbon samples, alongside standards and bulk metal foil; (b) Pd K-edge data of SD-x:y-Ag:Pd/carbon samples alongside standards and bulk metal foil.

EXAFS measurements are specifically sensitive to the bonding environment of the absorbing atom. As shown in k-space EXAFS plots (Figure 3.8), the SD-x:y-Ag:Pd samples show EXAFS oscillation patterns that have slight differences in amplitude and periodicity than those for the monometallic standards which suggests the presence of bimetallic clusters. This is consistent with the STEM images that show bimetallic structures of Ag and Pd atoms for individual particles in the sample (Figures 3.5 and 3.6). Figure 3.9(a) shows the Ag K-edge Fourier transformed EXAFS spectra of SD-Ag/carbon, the series of SD-x:y-Ag:Pd/carbon samples, and Ag_2O and Ag foil standards in R-space. The Ag_2O standard sample shows a major peak at around 1.56 Å (without phase shift correction) which is attributed to Ag-O contributions and this feature is absent in all other samples. However, an Ag-M (where M is Ag or Pd) feature in the 2.62 Å region is present in all samples to suggest a metallic state of Ag in the SD-x:y-Ag:Pd/carbon samples. Both Ag and Pd have nearly identical backscattering and phase effects on the photoelectron wave due to their similar atomic number, and thus they are almost indistinguishable around the central atom. Consequently, for modelling purposes both Ag-Ag and Ag-Pd scattering paths are fit as Ag-M interactions during the fitting of the experimental data collected for Ag K-edge measurements (and similarly Pd-M interactions for Pd-Pd and Pd-Ag interactions in the Pd K-edge measurements). Figure 3.9(b) shows the Pd K-edge Fourier transformed EXAFS measurements for the SD-x:y-Ag:Pd/carbon samples, alongside other standards and Pd foil in R-space. The peaks at around 1.55 Å for Pd-O and 1.84 Å for Pd-S bonds are absent in the SD-x:y-Ag:Pd/carbon samples. These samples only show a prominent peak that is attributed to Pd-M (where M is Ag or Pd) in the region of 2.50 Å. This is consistent with literature values for similar systems for Pd in zerovalent states.[38,39] Thus, both constituent metals in the SD-x:y-Ag:Pd/carbon samples are in metallic states.

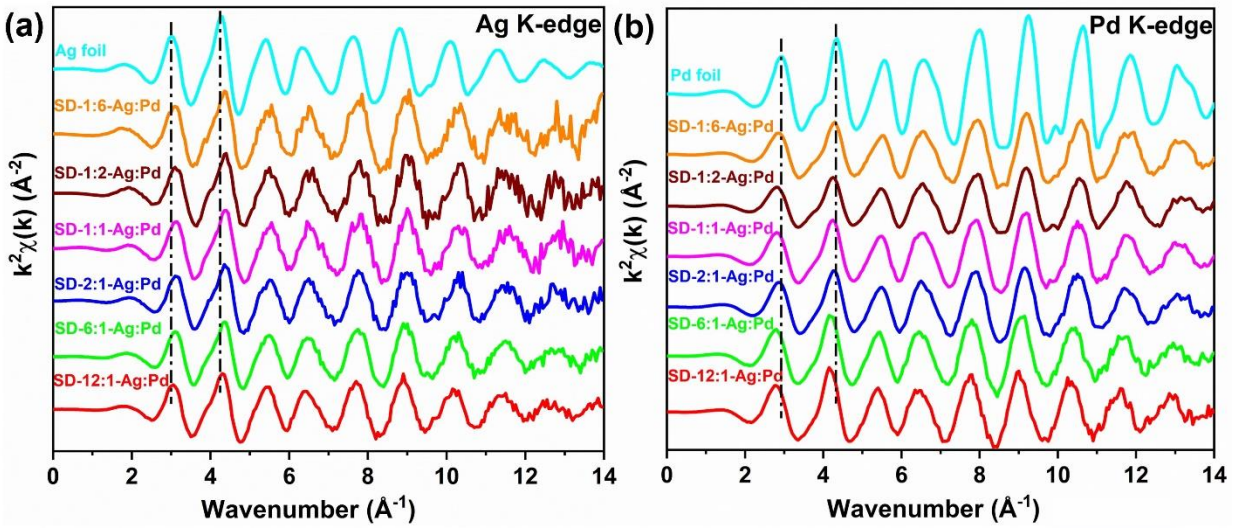

Figure 3.8. (a) Ag K-edge and (b) Pd K-edge EXAFS spectra in k-space for SD-x:y-Ag:Pd/carbon samples and bulk metal foils.

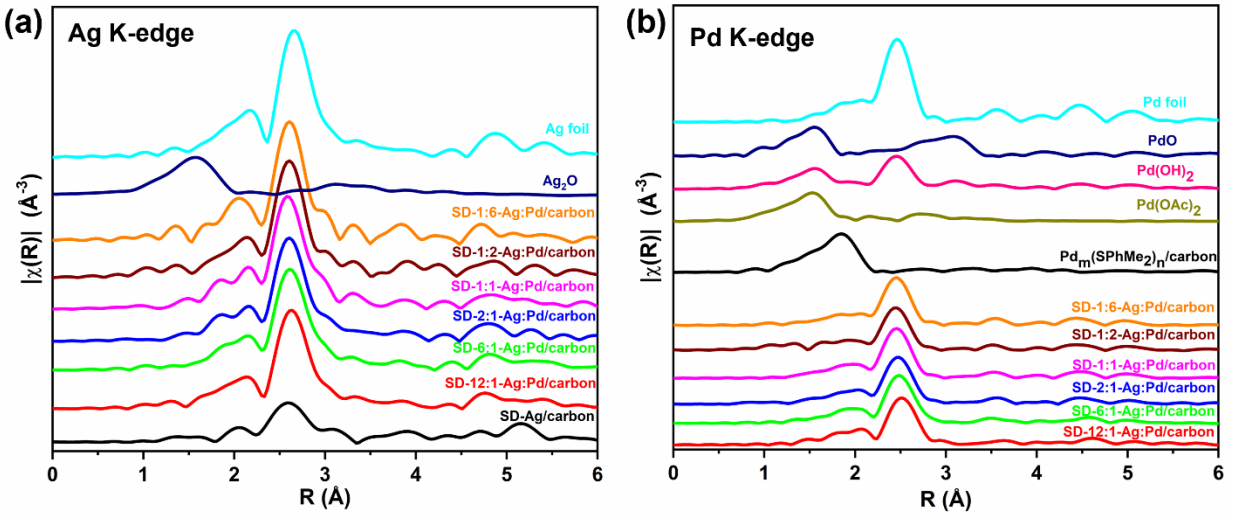

Figure 3.9. (a) Ag K-edge and (b) Pd K-edge Fourier transformed EXAFS spectra in R-space for SD-x:y-Ag:Pd/carbon samples, alongside standards and bulk metal foils.

EXAFS data fittings can give insight into the structural arrangement of atoms in bimetallic systems. Figure 3.10 shows the representative fits of experimental data for the SD-12:1-Ag:Pd/carbon sample for both Ag and Pd K-edge measurements in both k-space and R-space, using a fcc alloy model while Table 3.1 presents a summary of EXAFS fitting parameters for all sequentially reduced AgPd systems. Upon thermal activation there is desorption of thiolate ligands

off the Ag cluster surface (Chapter 2). The activated monometallic Ag clusters have a coordination number (CN) of 3.8(6) which indicates their small size, while bimetallic samples show larger Pd-M and Ag-M CNs to suggest that growth of particle size occurs during the ascorbic acid reduction (Table 3.1), which is consistent with the STEM images above (Figures 3.5 and 3.6). All bimetallic SD-x:y-Ag:Pd/carbon samples show coordination numbers (CNs) less than 12, at both edges, to suggest that small particles were formed with a large fraction of atoms on the surface. The SD-x:y-Ag:Pd/carbon samples show Ag-M distances that are slightly shorter than the Ag-Ag bond distance of 2.88 Å in standard Ag foils. Similarly, their modelled Pd-M distances show deviations from typical Pd-Pd bond distances of 2.75 Å in standard Pd fcc foils. These differences in bond distance strongly indicate the presence of heteroatomic bonding in the SD-x:y-Ag:Pd/carbon samples.[39-41] The trend in the CN values with the variation in constituent mole ratios in the AgPd clusters suggests that Ag@Pd core-shell structures are definitely not formed at higher Pd loadings. The cluster architectures are best described as cluster-in-cluster structures for the SD-x:y-Ag:Pd/carbon bimetallic samples with high Pd loadings in which both Ag and Pd have some atoms on the surface.[1] Notably, lower CN values are seen for Ag-M than Pd-M for samples with low Pd loadings, which suggests that Pd atoms are predominantly in sub-surface locations in these clusters (despite being reduced onto the Ag) and Ag atoms dominate the surface in these samples.[42] This is consistent with the observation made recently by Gedara *et al.* that Ag atoms can migrate to cover Pd islands on Ag(111) in minutes at room temperature.[43] However, this trend reverses at higher Pd loadings, and much lower Pd-M CNs are seen for Pd-rich AgPd clusters which suggests most Pd is on the surface of such clusters (Scheme 3.1). Given the large changes in the architectures of the AgPd clusters at different Pd loadings, we wanted to see how these structural changes affect the catalytic performance of these samples for alkyne hydrogenation reactions.

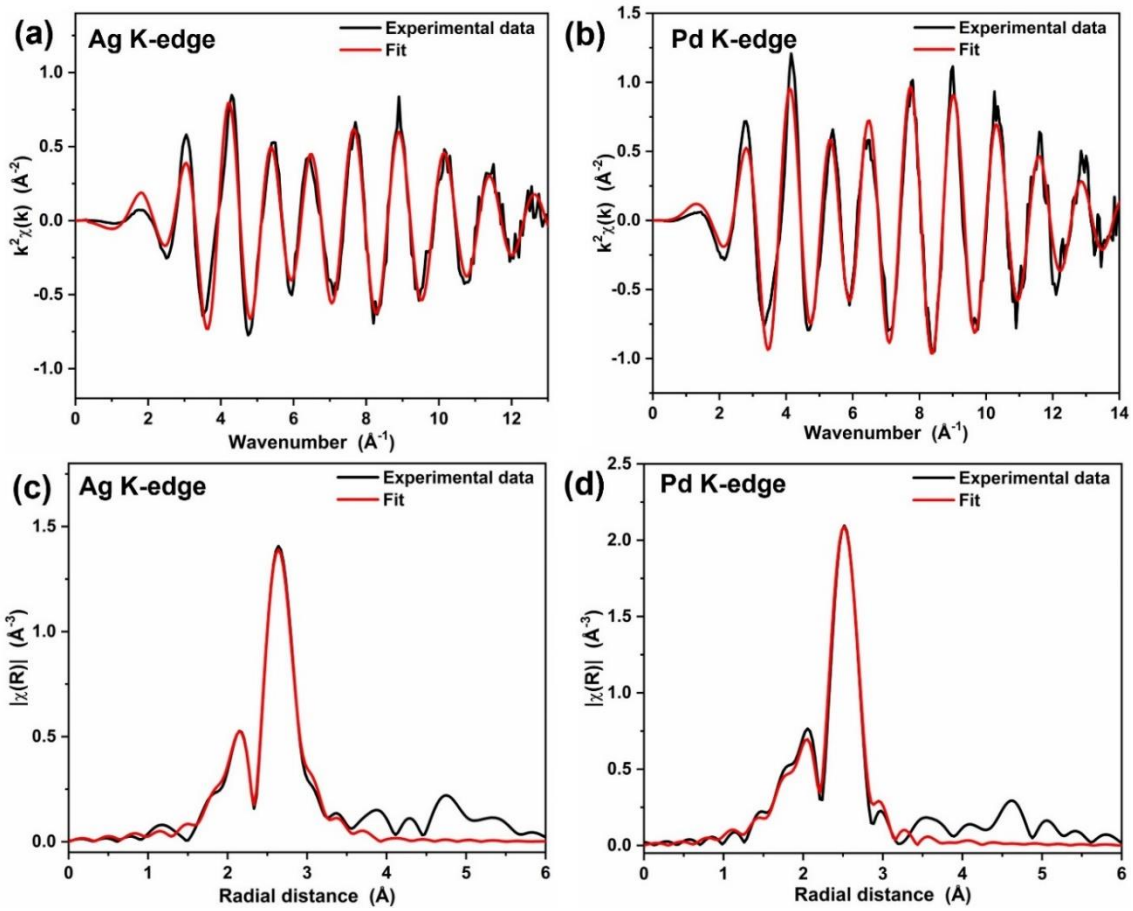

Figure 3.10. Experimental data of the Fourier transformed EXAFS and theoretical EXAFS fit for a representative SD-12:1-Ag:Pd/carbon sample for Ag and Pd K-edge measurements in (a,b) k-space and (c,d) R-space.

Table 3.1. Summary of EXAFS fitting parameters for SD-x:y-Ag:Pd/carbon samples.

SD-x:y Ag:Pd /carbon	**Fitting parameters**							
	Ag-M*				**Pd-M***			
	CN	R/Å	σ^2/Å^2	E_o shift /eV	CN	R/Å	σ^2/Å^2	E_o shift /eV
Ag	3.8(6)	2.826(6)	0.0080(2)	0.7(5)	-	-	-	-
12:1 Ag:Pd	8.4(4)	2.833(3)	0.0094(4)	0.4(3)	10.8(7)	2.786(4)	0.0082(5)	-7.9(4)
6:1 Ag:Pd	7.8(4)	2.819(3)	0.0088(4)	1.2(3)	10.5(5)	2.769(3)	0.0081(4)	-8.7(3)
2:1 Ag:Pd	7.7(4)	2.809(3)	0.0086(4)	1.3(3)	8.9(4)	2.748(3)	0.0072(4)	-7.7(3)
1:1 Ag:Pd	8.4(5)	2.807(3)	0.0086(5)	1.9(5)	8.7(5)	2.741(3)	0.0067(4)	-9.2(4)
1:2 Ag:Pd	7.9(4)	2.803(3)	0.0080(4)	1.2(3)	6.6(5)	2.734(4)	0.0061(5)	-9.3(5)
1:6 Ag:Pd	9.0(5)	2.806(4)	0.0086(5)	0.4(3)	7.1(4)	2.735(3)	0.0059(4)	-8.3(4)
*M is Ag or Pd.								

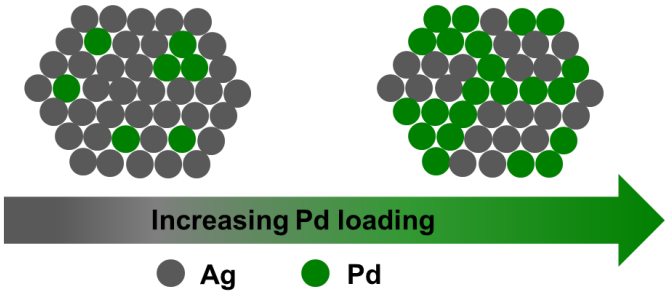

Scheme 3.1. Illustration of cluster-in-cluster architecture with Pd atoms predominantly in sub-surface sites for clusters with low Pd loadings moving to clusters with a greater percentage of Pd atoms on the surface as the Pd loading increases.

The catalytic performance of these heterogeneous catalysts was evaluated for the chemoselective hydrogenation of MBY to MBE and the results are presented in Table 3.2. Turnover numbers were used to compare the catalytic activity in order to normalize the activity for slight changes in the total amount of Ag+Pd over the SD-x:y-Ag:Pd/carbon samples. No measurable MBY conversion was observed in the absence of catalyst, but we noted that the carbon support alone shows very low (3.8%) MBY conversion, which may be due to impurities. As shown in Table 3.2, all AgPd bimetallic catalysts, except for the SD-12:1-Ag:Pd/carbon catalyst, showed

significantly greater catalytic activity compared to monometallic Ag catalysts in the hydrogenation of MBY. For instance, the bimetallic SD-12:1-Ag:Pd/carbon catalyst has a TON of 92.2 as compared with a TON value of 53.1 for the monometallic Ag catalyst. The catalytic activity significantly increases with Pd loading and the maximum TON of 194.7 was seen for the SD-1:1-Ag:Pd/carbon catalyst. The SD-1:1-Ag:Pd/carbon catalyst had nearly similar Ag-M and Pd-M CN values obtained for Ag and Pd, 8.4(5) and 8.7(5) respectively (Table 3.1), which shows that optimum catalytic activity seems to be correlated with roughly equal amounts of each metal on the surface of the clusters. Changes in the Pd loading (and consequently the structure) of the AgPd catalysts had drastic consequences towards the selective hydrogenation of MBY to MBE. The SD-12:1-Ag:Pd/carbon catalyst showed a MBE selectivity of 96.6% and this decreased to 0% for the bimetallic SD-1:6-Ag:Pd/carbon catalyst (in which MBA was the only product seen). Pd catalysts intrinsically have poor selectivity for hydrogenation of alkynes to alkenes because of over-hydrogenation to alkanes,[21] and similarly poor selectivities to alkene products are likely for catalysts whose surface is largely dominated by Pd atoms. Thus, the trend in MBE selectivity can be explained in term of the location of the Pd atoms in the bimetallic catalysts. In samples with high Pd loadings, Pd atoms are predominantly on the cluster surface which leads contiguous Pd surfaces which are active for the complete hydrogenation of MBY to MBA, and thus such AgPd catalysts show poor MBE selectivity. Meanwhile, EXAFS data show that Ag atoms dominate the catalyst surface in bimetallic samples with low Pd loading, and these samples have higher MBE selectivity, which indicates that having predominantly subsurface Pd atoms suppresses the over-hydrogenation of MBY to MBA. The MBE selectivity decreases progressively with Pd loading in the AgPd bimetallic samples. It is noteworthy that the suppression of over-hydrogenation products is more effective when Pd is significantly diluted by Ag. The SD-1:1-Ag:Pd/carbon catalyst with the maximum catalytic activity shows a moderate MBE selectivity of 30.3%, while AgPd bimetallic catalysts with lower Pd loadings had slightly lower activities but much higher selectivities to MBE. Rebrov *et al*. reported an MBE selectivity of 90% with a titania-supported ZnPd bimetallic catalyst prepared with a molar ratio of 3:1 (Zn:Pd).[44] They noted a further increase in MBE selectivity to 97% with the addition of pyridine to the reaction mixtures. Although differences in operating conditions limit an extensive comparison of the catalytic performance of this system with state-of-the-art catalysts, it is noteworthy that the high selectivities of catalysts with low Pd loading reported in this work, are attained without addition of any additives. Others

have also observed that the presence of Ag on Pd surface suppresses the over-hydrogenation of alkynes like acetylene and 1-octyne.[26,45] Finally, a recyclability study was done to see if the AgPd bimetallic catalysts retained their activity and selectivity over several cycles. Note this study was done at moderate conversions (25-45%) to ensure that any catalyst deactivation would be readily apparent. AgPd bimetallic catalysts with lower Pd loadings maintained both their activity and high MBE selectivity over three reaction cycles (Table 3.3).

Table 3.2. Catalytic performance of carbon-supported Ag monometallic and SD-x:y-Ag:Pd bimetallic catalysts for the hydrogenation of 2-methyl-3-butyn-2-ol (MBY).

SD-x:y-Ag:Pd /carbon	**TON**	**MBE Selectivity (%)**
Ag	53.1	84.7
12:1 Ag:Pd	92.2	96.6
6:1 Ag:Pd	147.9	93.3
2:1 Ag:Pd	151.0	79.9
1:1 Ag:Pd	194.7	30.3
1:2 Ag:Pd	131.8	8.5
1:6 Ag:Pd	56.7	0
Reaction conditions: MBY (2.0 mmol), EtOH (5.0 mL), catalyst (25 mg), hydrogen gas (1.5 atm), stirring speed (1400 rpm), temperature (25 °C), time (3 h).		

Table 3.3. Recyclability test of selected SD-x:y-Ag:Pd/carbon catalysts for hydrogenation reactions of MBY.

SD-x:y-Ag:Pd /carbon	**Cycle**	**TON**	**MBE Selectivity (%)**
12:1 Ag:Pd	Cycle-1	92.2	96.6
	Cycle-2	94.0	96.0
	Cycle-3	90.8	95.8
6:1 Ag:Pd	Cycle-1	147.9	93.3
	Cycle-2	145.8	92.8
	Cycle-3	146.8	93.0
Reaction conditions: MBY (2.0 mmol), EtOH (5.0 mL), catalyst (25 mg), hydrogen gas (1.5 atm), stirring speed (1400 rpm), temperature (25 °C), time (3 h).			

3.4 Conclusions

This work establishes structure-activity relationships for carbon-supported AgPd catalysts prepared via the sequential deposition approach for the selective hydrogenation of MBY. $Ag_{25}(SR)_{18}$ clusters could be activated on carbon supports at 250 °C with very mild sintering and were shown to be good precursors for the subsequent formation of AgPd bimetallic clusters by sequentially reducing $Pd(OAc)_2$ using an ascorbic acid reducing agent. XAS data shows cluster-in-cluster AgPd heterogeneous bimetallic clusters are formed at high Pd loadings rather than perfect core-shell heterogeneous bimetallic clusters, while at low Pd loadings nearly all the Pd is in subsurface sites. Bimetallic AgPd catalysts showed superior activity to monometallic Ag catalysts and high Ag/Pd ratios favoured better MBE selectivity in the hydrogenation reactions. High Ag/Pd ratios in the sample strategically positioned Pd atoms in subsurface locations which enabled the suppression of over-hydrogenation of MBY, and thus resulting in high MBE selectivity.

3.5 References

1. C.F. Calver, P. Dash, R.W.J. Scott. Selective Hydrogenations with Ag-Pd Catalysts Prepared by Galvanic Exchange Reactions, *ChemCatChem*, 2011, **3**, 695-697.

2. T. Balcha, J. Strobl, C. Fowler, P. Dash, R.W.J. Scott. Selective Aerobic Oxidation of Crotyl Alcohol Using AuPd Core-Shell Nanoparticles, *ACS Catal.* 2011, **1**, 425-436.

3. X. Yuan, X. Dou, K. Zheng, J. Xie. Recent Advances in the Synthesis and Applications of Ultrasmall Bimetallic Nanoclusters, *Part. Part. Syst. Charact.* 2015, **32**, 613-629.

4. D. Jana, A. Dandapat, G. De. Au@Pd Core-Shell Nanoparticle Incorporated Alumina Sols and Coatings: Transformation of Au@Pd to Au-Pd Alloy Nanoparticles, *J. Phys. Chem. C*, 2009, **113**, 9101-9107.

5. R. Ferrando, J. Jellinek, R.L. Johnston. Nanoalloys: From Theory to Applications of Alloy Clusters and Nanoparticles, *Chem. Rev.*, 2008, **108**, 845-910.

6. Y. Liu, X. Chai, X. Cai, M. Chen, R. Jin, W. Ding, Y. Zhu. Central Doping of a Foreign Atom into the Silver Cluster for Catalytic Conversion of CO_2 toward C-C Bond Formation, *Angew. Chem. Int. Ed.* 2018, **57**, 9775-9779.

7. A. Zaleska-Medynska, M. Marchelek, M. Diak, E. Grabowska. Noble Metal-Based Bimetallic Nanoparticles: The Effect of the Structure on The Optical, Catalytic and Photocatalytic Properties, *Adv. Colloid Interface Sci.*, 2016, **229**, 80-107.

8. S. Xie, H. Tsunoyama, W. Kurashige, Y. Negishi, T. Tsukuda. Enhancement in Aerobic Alcohol Oxidation Catalysis of Au_{25} Clusters by Single Pd Atom Doping, *ACS Catal.* 2012, **2**, 1519-1523.

9. C.A. Fields-Zinna, M.C. Crowe, A. Dass, J.E.F. Weaver, R.W. Murray. Mass Spectrometry of Small Bimetal Monolayer-Protected Clusters, *Langmuir* 2009, **25**, 7704-7710.

10. S. Wang, Y. Song, S. Jin, X. Liu, J. Zhang, Y. Pei, X. Meng, M. Chen, P. Li, M. Zhu. Metal Exchange Method Using Au_{25} Nanoclusters as Templates for Alloy Nanoclusters with Atomic Precision, *J. Am. Chem. Soc.*, 2015, **137**, 4018-4021.

11. H. Qian, D.-e. Jiang, G. Li, C. Gayathri, A. Das, R.R. Gil, R. Jin. Monoplatinum Doping of Gold Nanoclusters and Catalytic Application, *J. Am. Chem. Soc.*, 2012, **134**, 16159-16162.

12. M. Kim, K.L.D.M. Weerawardene, W. Choi, S.M. Han, J. Paik, Y. Kim, M-G. Choi, C.M. Aikens, D. Lee. Insights into the Metal-Exchange Synthesis of $MAg_{24}(SR)_{18}$ (M = Ni, Pd, Pt) Nanoclusters, *Chem. Mater.* 2020, **32**, 10216-10226.

13. Y. Niihori, S. Hossain, S. Sharma, B. Kumar, W. Kurashige, Y. Negishi. Understanding and Practical Use of Ligand and Metal Exchange Reactions in Thiolate-Protected Metal Clusters to Synthesize Controlled Metal Clusters, *Chem. Rec.* 2017, **17**, 473-484.

14. K.E. Lee, A. Shivhare, Y. Hu, R.W.J. Scott. Supported Bimetallic AuPd Clusters Using Activated Au_{25} Clusters, *Catal. Today* 2017, **280**, 259-265.

15. X. Kang, H. Chong, M. Zhu. $Au_{25}(SR)_{18}$: The Captain of the Great Nanocluster Ship, *Nanoscale* 2018, **10**, 10758-10834.

16. Y. Negishi, W. Kurashige, Y. Niihori, T. Iwasa, K. Nobusada. Isolation, Structure, and Stability of a Dodecanethiolate-Protected Pd_1Au_{24} Cluster, *Phys. Chem. Chem. Phys.* 2010, **12**, 6219-6225.

17. Qian, E. Barry, Y. Zhu, R. Jin. Doping 25-Atom and 38-Atom Gold Nanoclusters with Palladium, *Acta Phys.-Chim. Sin.* 2011, **27**, 513-519.

18. M.A. Tofanelli, T.W. Ni, B.D. Phillips, C.J. Ackerson. Crystal Structure of the $PdAu_{24}(SR)_{18}^0$ Superatom, *Inorg. Chem.* 2016, **55**, 999-1001.

19. V. Sudheeshkumar, A. Lushington, X. Sun, R.W.J. Scott. Thermal Stability of Alumina-Overcoated Au_{25} Clusters for Catalysis, *ACS Appl. Nano. Mater*. 2018, **1**, 6904-6911.

20. C.P. Joshi, M.S. Bootharaju, M.J. Alhilaly, O.M. Bakr. $[Ag_{25}(SR)_{18}]^-$: The "Golden" Silver Nanoparticle, J. *Am. Chem. Soc.* 2015, **137**, 11578-11581.

21. H. Zhou, X. Yang, L. Li, X. Liu, Y. Huang, X. Pan, A. Wang, J. Li, T. Zhang. PdZn Intermetallic Nanostructure with Pd-Zn-Pd Ensembles for Highly Active and Chemoselective Semi-Hydrogenation of Acetylene, *ACS Catal.* 2016, **6**, 1054-1061.

22. G.X. Pei, X.Y. Liu, A. Wang, A.F. Lee, M.A. Isaacs, L. Li, X. Pan, X. Yang, X. Wang, Z. Tai, K. Wilson, T. Zhang. Ag Alloyed Pd Single-Atom Catalysts for Efficient Selective Hydrogenation of Acetylene to Ethylene in Excess Ethylene, *ACS Catal.* 2015, **5**, 3717-3725.

23. P.A. Sheth, M. Neurock, C.M. Smith. First-Principles Analysis of the Effects of Alloying Pd with Ag for the Catalytic Hydrogenation of Acetylene-Ethylene Mixtures, *J. Phys. Chem. B* 2005, **109**, 12449-12466.

24. D.V. Glyzdova, A.A. Vedyagin, A.M. Tsapina, V.V. Kaichev, A.L. Trigub, M.V. Trenikhin, D.A. Shlyapin, P.G. Tsyrulnikov, A.V. Lavrenov. A Study on Structural Features of Bimetallic Pd-M/C (M: Zn, Ga, Ag) Catalysts for Liquid-Phase Selective Hydrogenation of Acetylene, *Appl. Catal. A*, 2018, **563**, 18-27.

25. Z-J. Zhao, J. Zhao, X. Chang, S. Zha, L. Zeng, J. Gong. Competition of C-C Bond Formation and C-H Bond Formation for Acetylene Hydrogenation on Transition Metals: A Density Functional Theory Study, *AIChE J.*, 2019, **65**, 1059-1066.

26. T. Mitsudome, T. Urayama, K. Yamazaki, Y. Maehara, J. Yamasaki, K. Gohara, Z. Maeno, T. Mizugaki, K. Jitsukawa, K. Kaneda. Design of Core-Pd/Shell-Ag Nanocomposite Catalyst for Selective Semihydrogenation of Alkynes, *ACS Catal.*, 2016, **6**, 666-670.

27. N. Semagina, M. Grasemann, N. Xanthopoulos, A. Renken, L. Kiwi-Minsker. Structured Catalyst of Pd/ZnO on Sintered Metal Fibers for 2-methyl-3-butyn-2-ol Selective Hydrogenation, *J. Catal.* 2007, **251**, 213-222

28. S. Vernuccio, R. Goy, Ph. Rudolf von Rohr, J. Medlock, W. Bonrath. Hydrogenation of 2-methyl-3-butyn-2-ol over a Pd/ZnO Catalyst: Kinetic Model and Selectivity Study, *React. Chem. Eng.*, 2016, **1**, 445-453.

29. C.A. Schneider, W.S. Rasband, K.W. Eliceiri. NIH Image to ImageJ: 25 Years of Image Analysis HHS Public Access, *Nat. Methods* 2012, **9**, 671-675.

30. B. Ravel, M. Newville. ATHENA, ARTEMIS, HEPHAESTUS: Data Analysis for X-ray Absorption Spectroscopy Using IFEFFIT, *J. Synchrotron Radiat.* 2005, **12**, 537-541.

31. M.S. Bootharaju, C.P. Joshi, M.R. Parida, O.F. Mohammed, O.M. Bakr, Angew. Templated Atom-Precise Galvanic Synthesis and Structure Elucidation of a $[Ag_{24}Au(SR)_{18}]^-$ Nanocluster, *Angew. Chem. Int. Ed.* 2016, **55**, 922-926.

32. B. Zhang, C. García, A. Sels, G. Salassa, C. Rameshan, J. Llorca, K. Hradil, G. Rupprechter, N. Barrabés, T. Bürgi. Ligand and Support Effects on the Reactivity and Stability of $Au_{38}(SR)_{24}$ Catalysts in Oxidation Reactions, *Catal. Commun.* 2019, **130**, 105768.

33. J.P.R. Chauvin, D.A. Pratt. On the Reactions of Thiols, Sulfenic Acids, and Sulfinic Acids with Hydrogen Peroxide, *Angew. Chem. Int. Ed.* 2017, **56**, 6255-6259.

34. Y. Wang, S. Fu, Y. Jia, C. Qian, X. Chen. Solubility of Benzyl Disulfide in Five Organic Solvents between (283.45 and 333.15) K, *J. Chem. Eng. Data*, 2013, **58**, 2483-2486.

35. G. Corro, E. Vidal, S. Cebada, U. Pal, F. Bañuelos, D. Vargas, E. Guilleminot. Electronic State of Silver in Ag/SiO_2 and Ag/ZnO Catalysts and Its Effect on Diesel Particulate Matter Oxidation: An XPS Study, *Appl. Catal. B Environ.*, 2017, **216**, 1-10.

36. M.K. Gangishetty, A.M. Fontes, M. Malta, T.L. Kelly, R.W.J. Scott. Improving the Rates of Pd-Catalyzed Reactions by Exciting the Surface Plasmons of AuPd Bimetallic Nanotriangles, *RSC Adv.*, 2017, 7, 40218-40226.

37. M.K. Gangishetty, R.W.J. Scott, T.L. Kelly. Thermal Degradation Mechanism of Triangular Ag@SiO_2 Nanoparticles, *Dalton Trans.* 2016, **45**, 9827-9834.

38. K. Mori, M. Dojo, H. Yamashita. Pd and Pd–Ag Nanoparticles within a Macroreticular Basic Resin: An Efficient Catalyst for Hydrogen Production from Formic Acid Decomposition, *ACS Catal.*, 2013, **3**, 1114-1119.

39. M. Navlani-García, K. Mori, A. Nozaki, Y. Kuwahara, H. Yamashita. Screening of Carbon-Supported PdAg Nanoparticles in the Hydrogen Production from Formic Acid, *Ind. Eng. Chem. Res.*, 2016, **55**, 7612-7620.

40. P. Verma, Y. Kuwahara, K. Mori, H. Yamashita. Synthesis and Characterization of a Pd/Ag Bimetallic Nanocatalyst on SBA-15 Mesoporous Silica as a Plasmonic Catalyst, *J. Mater. Chem. A.*, 2015, **3**, 18889-18897.

41. C. Hu, X. Mu, J. Fan, H. Ma, X. Zhao, G. Chen, Z. Zhou, N. Zheng. Interfacial Effects in PdAg Bimetallic Nanosheets for Selective Dehydrogenation of Formic Acid, *ChemNanoMat*, 2016, **2**, 28-32.

42. V. Sudheeshkumar, M. Alyari, M. Gangishetty, R.W.J. Scott. Galvanic Synthesis of AgPd Bimetallic Catalysts from Ag Clusters Dispersed in a Silica Matrix, *Catal. Sci. Technol.* 2020, **10**, 8421-8428.

43. B.S.A. Gedara, M. Muir, A. Islam, D. Liu, M. Trenary. Room Temperature Migration of Ag Atoms to Cover Pd Islands on Ag(111), *J. Phys. Chem. C*, 2021, **125**, 27828-27836.

44. E.V. Rebrov, E.A. Klinger, A. Berenguer-Murcia, E.M. Sulman, J.C. Schouten. Selective Hydrogenation of 2-Methyl-3-butyne-2-ol in a Wall-Coated Capillary Microreactor with a $Pd_{25}Zn_{75}/TiO_2$ Catalyst, *Org. Process Res. Dev.*, 2009, **13**, 991-998.

45. M.R. Ball, K.R. Rivera-Dones, E.B. Gilcher, S.F. Ausman, C.W. Hullfish, E.A. Lebrón, J.A. Dumesic. AgPd and CuPd Catalysts for Selective Hydrogenation of Acetylene, *ACS Catal.*, 2020, **10**, 8567-8581.

Chapter 4

Exploring the Structure of Atom-Precise Silver-Palladium Bimetallic Clusters Prepared via Improved Single-Pot Co-Reduction Synthesis Protocol

This chapter explores the structure of atom-precise AgPd bimetallic clusters prepared via an improved single-pot co-reduction synthesis protocol. UV-Vis absorption spectroscopy and mass spectrometry techniques ascertained the optical fingerprint and atomic composition of the bimetallic of $Ag_{24}Pd_1(SR)_{18}^{2-}$ clusters. Element-specific XPS and XAS analyses indicated that the single dopant Pd atom is positioned at surface/staple site of the clusters.

This chapter is adapted from work published in *J. Chem. Phys*. 2021, **155**, 084301. I perfomed all the experimental work in this article. Dr. Randy W. Purves assisted with the mass spectrometry experiments at the Centre for Veterinary Drug Residues, Canadian Food Inspection Agency (CFIA). I wrote the complete first draft of the manuscript and this was then edited with the guidance of Prof. Robert W.J. Scott prior to its publication.

4.1 Introduction

The development of model heterogeneous catalysts using atom-precise metallic clusters is a very active research area.[1,2] Generally, nanoscale-sized clusters of noble metal atoms show excellent catalytic activity due to their possession of well-defined active sites, high surface area, modified surface geometries, and modulated electronic properties compared to bulk materials.[3,4] In addition to the size, tailoring the composition and morphology can afford robust nanocatalysts with outstanding catalytic activity and selectivity.[3] Bimetallic clusters are commonly more catalytically active than their monometallic analogues due to the synergetic effect of two metals, and the choice of method of synthesis can remarkably influence the success of making pure, high-yield, compositionally precise bimetallic clusters.[1,5] The use of thiolate ligands is ubiquitous with the co-reduction strategy of making atom-precise ligand protected clusters possibly owing to strong sulfur-metal interactions that enable good stability in solution, facile synthesis, and controlled cluster compositions.[6] Unlike Au systems, atom-precise Ag monometallic and Ag-based bimetallic clusters are less studied in the literature, perhaps due to the predisposition of silver (Ag) to oxidation, although Ag cluster systems are gaining interest given the higher relative abundance and lower cost of Ag compared to Au.

Bimetallic clusters systems have been prepared successfully via co-reduction and galvanic approaches to give compositionally-pure systems.[7-9] Atom-precise bimetallic systems can be a greater characterization challenge as there can also be subtle changes in the relative positions of each type of metal atom in the cluster.[9-11] Thus, it is essential to explore the position of the dopant atom in such bimetallic systems to properly establish structure-activity relationships of the resulting bimetallic cluster catalysts. It is difficult to determine the surface structures of small bimetallic clusters in the range of 1-2 nm sizes by using electron microscopy techniques. Using X-ray crystallography methods, many studies have shown that single atom dopants in Au_{25} and Ag_{25} clusters often occupy the central core position, however, there are examples in which other positions are occupied by the dopant atom. Notably, Zheng *et al.* showed that single Au atoms started in staple positions on Ag clusters and diffused towards the core over time.[12] Also, Negishi and co-workers recently showed that Cu preferentially substitutes for Au in the staple position of $Au_{25}(SR)_{18}^-$ clusters regardless of the synthesis method used, and that the Cu substitution also

occurred at the cluster core-surface of the Au clusters when the amount of Cu substitution is increased or when the central Au atom is substituted by Pt.[13]

X-ray absorption spectroscopy (XAS) is a good alternative choice for structural elucidation and this technique has been largely used by our research group and others as a crucial tool for the structural determination of bimetallic nanoparticles and clusters with thiolate ligands.[14-18] Several research groups have reported singly-doped Ag based bimetallic clusters,[9,19,20] but none have employed XAS to probe the position of the dopant atom. Zheng and co-workers carried out a total structure and electronic structure analysis of $Ag_{24}M(SPhCl_2)_{18}^{2-}$, (M = Pd or Pt) clusters, and found that the obtained 25-metal-atom bimetallic clusters have a cluster structure similar to that of widely investigated $Au_{25}(SR)_{18}$.[19] In a separate study, Bakr and co-workers reported the successful synthesis and structural elucidation of $Ag_{25}(SPhMe_2)_{18}^{-}$ and $Ag_{24}Pd(SPhMe_2)_{18}^{2-}$ clusters with core-shell morphologies.[20] Both studies noted that the Pd dopant atom replaces the core central atom using X-ray crystallography methods,[19,20] and such single Pd atom doping of Ag_{25} leads to both improved cluster stability and enhanced catalytic efficiency.[9] We note that X-ray crystallography methods cannot typically unambiguously distinguish Pd versus Ag locations given their similar atomic numbers, which leaves the question on the actual position of the dopant Pd atom potentially unanswered.[19,21] Moreover, it is not clear how many Pd atoms can be doped into parent Ag clusters while maintaining the compositional purity of the resulting bimetallic clusters prepared via the co-reduction strategy. Intuitively, multiple doping of secondary metal atoms cannot be ruled out, especially when the amount of the dopant metal ions is stoichiometrically high in the co-reduction synthesis procedure. While mass spectrometry can afford information about the atomic composition, a technique such as XAS can be an important alternative tool to understand the structure of such atom-precise bimetallic clusters.

Herein, we explore the possibility of making compositionally-pure Ag clusters doped with variable amounts of Pd, and report the use of XAS to explore the structure of atom-precise AgPd bimetallic cluster systems. In this study, both Pd and Ag ions were reduced simultaneously to form thiolate-stabilized bimetallic clusters, followed by deposition of the bimetallic clusters onto carbon supports. Mass spectrometry was used to examine the purity and atomic composition of the clusters and UV-Vis absorption spectroscopy revealed the electronic properties of the clusters, while X-ray photoelectron spectroscopy (XPS) and X-ray absorption spectroscopy (XAS) were employed

to probe the metallic speciation and structure of bimetallic AgPd heterogeneous catalysts. Our results show that only singly-doped Pd in Ag clusters occurs even with equimolar ratios of Ag(I) and Pd(II) ions in the synthesis, whereas at higher Pd loadings, the resulting samples are not compositionally pure and Pd salts are not fully reduced. In comparison with monometallic Ag_{25} clusters, the absorption peaks of the obtained bimetallic $Ag_{24}Pd_1$ cluster system are blue shifted due to incorporation of Pd atoms. Interestingly, XPS and XAS results show the bimetallic clusters have multivalent Ag atoms and Pd(II) ions with significant thiolate interactions. These results suggest that single Pd atoms predominantly occupy the staple position of individual clusters, or possibly alternatively icosahedral surface sites. Single-atom doping of Pd allows for the formation of thiolate-protected $Ag_{24}Pd_1$ bimetallic clusters and this work distinctly shows that the Pd atom is not positioned in the core position of the icosahedral cluster.

4.2 Experimental

4.2.1 Materials

All chemicals are similar to those mentioned in section 3.2.1. Palladium (II) chloride ($PdCl_2$) used in the experiments described in this chapter was procured from Sigma Aldrich.

4.2.2 Synthesis of the Purified, Alkanethiolate-Protected Ag and AgPd Clusters

Monometallic $Ag_{25}(SPhMe_2)_{18}^-$ clusters were prepared as described in section 2.2.2, and the x:y Ag:Pd bimetallic clusters were synthesized using a literature procedure with slight modifications.[20] In a typical synthesis of the bimetallic system, metal solution **A** (0.22 mmol of $AgNO_3$ dissolved in 2.0 mL of MeOH, under 10 min sonication) and metal solution **B** (0.22 mmol of $Pd(OAc)_2$ dissolved in 2.0 mL of MeOH, under 10 min sonication) were mixed in a 50 mL flask and stirred at 600 rpm for 2 min, followed by the addition of 0.66 mmol of 2,4-dimethylbenzenethiol ($HSPhMe_2$) to give a brownish-coloured opaque mixture that became dispersed with the addition of 18 mL of DCM. This solution was continuously stirred at the same speed for 20 min before adding freshly prepared 0.50 mL of methanolic solution containing 0.014 mmol of PPh_4Br. Afterwards, 0.50 mL of an ice-cold aqueous solution containing 0.40 mmol of $NaBH_4$ was added dropwise and the reaction mixture was continuously stirred for 18 h. Within the first hour, the colour of the solution changed from light brown to a dark brown, which indicates the reduction of metal-thiolate mixture.

The crude solution was centrifuged (8500 rpm for 30 min) to remove a solid that presumably contains undissolved metal salts and/or thiol ligands. The obtained supernatant was then concentrated under a rotary evaporator to about 5 mL before adding 20 mL of methanol to precipitate the metal clusters. The precipitate was collected by centrifugation and extracted into 20 mL of DCM. The DCM solution of the clusters was again centrifuged (8500 rpm for 60 min) to remove an insoluble yellow solid. Then, the deep red colored supernatant was dried under vacuum, and the obtained purified and dried bimetallic clusters were stored in a glass vial under ambient conditions for further studies. In making the series of clusters using x:y Ag:Pd ratios (where x and y are synthetic mole ratios for Ag and Pd respectively), the concentration of solution A was maintained while the moles of Pd were varied in solution B. For example, the 2:1 Ag:Pd sample was prepared with the intended metal composition of 0.22 mmol Ag and 0.11 mmol Pd (for clarity this nomenclature will be used throughout this manuscript). The atom-precise composition was assigned based on the results from electrospray ionization mass spectrometry (ESI-MS) measurements (see below).

4.2.3 Preparation of Carbon-Supported Atom-Precise Metallic Clusters

The wetness impregnation method was employed to immobilize x:y Ag:Pd cluster samples onto carbon supports, with a final metal loading of ca. 2 wt%. For example, 19.8 mg of clusters was dissolved in 2.0 mL of DCM followed by adding 200 mg of activated carbon and stirring for 2 h. Afterwards, the colourless supernatant was completely removed under vacuum using a Schlenk line apparatus. Then, the as-prepared dried, carbon-supported cluster samples were analyzed by XPS and XAS methods.

4.2.4 Characterization Techniques

UV-Vis absorption spectroscopy and X-ray photoelectron spectroscopy (XPS) measurements were collected as described in section 2.2.4, while X-ray absorption spectroscopy (XAS) measurements were collected as described in section 3.2.3. All cluster solutions were analyzed in the negative ionization mode in ESI-MS measurements, and the isotopic distribution was simulated using open-sourced mMass 5.5.0 software.[22,23]

4.3 Results and Discussion

The formation of silver-palladium (AgPd) bimetallic clusters was achieved using a single-pot synthetic approach that involves co-reduction of Ag(I) and Pd(II) ions in the presence of 2,4-dimethylbenzenethiolate ligands, and using $NaBH_4$ as the reducing agent. For the established procedure in the literature, $PdCl_2$ was added to a preformed Ag-thiolate complex.[9] We noted the presence of a greater amount of insoluble materials prior to purification using this strategy, presumably due to incomplete solubility of the Pd precursor. A modified method, reported herein, involves homogenizing a methanolic solution of each metal ion precursor separately before mixing in a single-pot, followed by addition of thiolate ligands. While either $PdCl_2$ or $Pd(OAc)_2$ could be used as the Pd species, $Pd(OAc)_2$ showed improved solubility in methanol and showed improvements in the fractions of compositionally pure clusters (see below). The formation of a dark-brown solution upon addition of $NaBH_4$ to the Ag(I)-Pd(II)-thiolate complex indicates the formation of thiolate protected AgPd bimetallic clusters. The Ag:Pd ratio was changed by varying the amount of Pd(II) added while other variables were maintained.

Figure 4.1 presents the UV-Vis absorption spectra of different samples of purified, unsupported thiolate-protected AgPd bimetallic clusters synthesized using variable Ag:Pd ratios, in which x:y is the synthetic molar ratio used in the synthesis. The Ag-only clusters show a spectrum which is consistent with the literature for clusters containing 25 Ag atoms precisely: $Ag_{25}(SPhMe_2)_{18}^-$, with characteristic peaks at 334 nm, 392 nm, 490 nm, and 678 nm for nearly monodisperse $Ag_{25}(SR)_{18}^-$ clusters.[24] The broad peak at around 678 nm is due to the HOMO-LUMO transition due to the Ag_{13} icosahedral core in the Ag_{25} structure. In contrast, the HOMO-LUMO peaks of the AgPd bimetallic samples with high Ag loadings are blue-shifted by ~11 nm and such a change in the UV-Vis absorption spectrum is a characteristic feature of bimetallic AgPd samples, as the incorporation of a dopant atom results in moderation of the electronic properties of the clusters.[18] A similar electronic perturbation is reported in literature for $Au_{25}L_{18}^-$ clusters when doped with single Pd atoms.[10,25] Upon introducing more Pd in the system, no significant change in the UV-Vis spectra is seen until equimolar Pd was present in the synthesis. The four characteristic peaks assigned to metallic clusters are clearly visible up to a 1:1 Ag:Pd synthetic ratio, beyond which the spectra show no cluster signatures. The preservation of a yellowish-orange colour in the case of the Pd-only system, and absence of HOMO-LUMO transitions, suggests no

reduction of the Pd(II)-thiolate complex with $NaBH_4$ under the same experimental conditions used for the reduction of the other samples. This shows that the Pd(II)-S bonds are seemingly more resistant to borohydride reduction than Ag(I)-S bonds. This is consistent with earlier work by Murray and co-workers who found that Pd thiolate complexes are very resistant to reduction.[26]

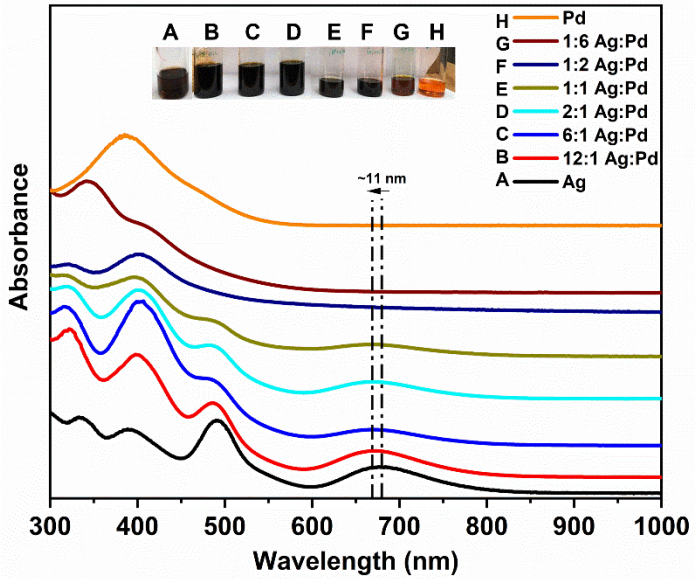

Figure 4.1. UV-Vis absorption spectra of (A-H) AgPd bimetallic syntheses with varying constituent metal ratios using $Pd(OAc)_2$ as the Pd precursor. The x:y Ag:Pd ratios in the legend refer to the synthetic molar ratios used. The inset in the upper left shows photographs of the resulting solutions.

Mass spectrometry is a useful technique for providing information about the atomic composition, and to some extent, purity, of atom-precise cluster systems. Figure 4.2(a) shows the mass spectrum of the monometallic $Ag_{25}(SPhMe_2)_{18}^-$ clusters. The clusters show a prominent molecular ion peak at around m/z = 5166 and isotope distribution peaks that are separated by a m/z value of 1, which confirms an overall -1 charge for the $[Ag_{25}(SPhMe_2)_{18}]^-$ clusters and is consistent with the literature.[20,24] When solid $PdCl_2$ was added into the Ag(I)-thiolate mixture, a less pure and polydisperse sample was formed as seen in the nature of the obtained mass spectrum (Figure 4.2(b)). High resolution molecular ion peaks at m/z = 2582, m/z = ~2602, and m/z = 5166 can be seen, which suggest the presence of both a bimetallic and monometallic Ag_{25} analogue in the system. In contrast, when a homogenized methanolic solution of $PdCl_2$ was used, a sole prominent molecular ion peak was seen at m/z = 2582 (Figure 4.2(c)), which is consistent with

monodisperse $Ag_{24}Pd_1(SPhMe_2)_{18}^{2-}$ bimetallic clusters.[9] Importantly, the difference in mass spectra for similar samples with the same metal precursor but a slight difference in method of synthesis, emphasizes the significance of synthetic protocol in achieving pure and monodisperse AgPd bimetallic cluster samples.

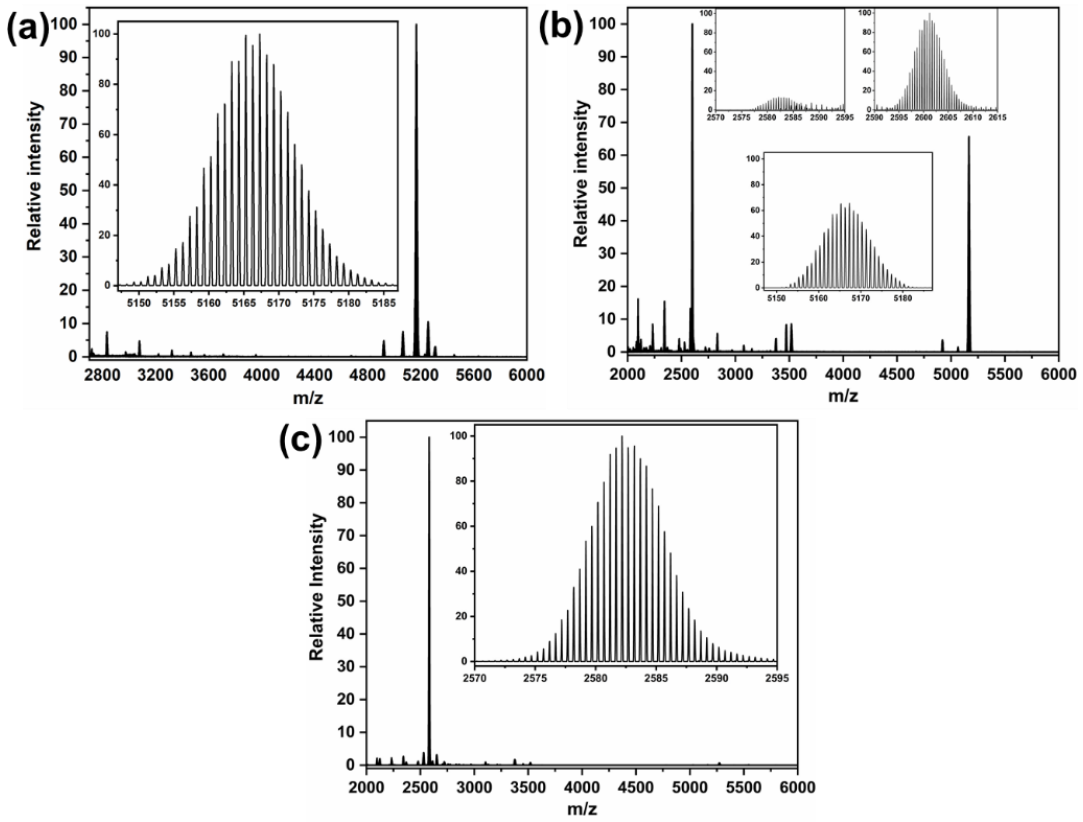

Figure 4.2. Mass spectra of (a) $Ag_{25}(SPhMe_2)_{18}^-$ clusters (b) 12:1 Ag:Pd sample prepared with dispersed $PdCl_2$ solid, no sonication (c) 12:1 Ag:Pd sample prepared with sonicated $PdCl_2$ solution.

$Pd(OAc)_2$ was found to be much easier and faster to solubilize in methanol than $PdCl_2$ under sonication and in our modified method a series of AgPd bimetallic samples was prepared using $Pd(OAc)_2$ as the Pd precursor. Figure 4.3(a) shows the mass spectrum of 12:1 Ag:Pd bimetallic samples prepared using this modified single-pot synthesis method. The mass spectra of samples prepared with similar metal loading of 12:1 Ag:Pd, regardless of Pd precursor (Figure 4.2(c) versus Figure 4.3(a)), show high similarity to further show that the monodispersity of AgPd bimetallic clusters is more sensitive to the synthetic protocol than the Pd precursor type. Near identical mass spectra were obtained for bimetallic samples with synthetic ratios ranging from 12:1

Ag:Pd to 2:1 Ag:Pd (Figure 4.3). The prominent molecular ion peak at m/z = 2582 is consistent with that of bimetallic clusters comprising of a single Pd atom in the cluster and 24 Ag atoms, i.e., $Ag_{24}Pd_1(SPhMe_2)_{18}^{2-}$ clusters.[9,20] The experimental and simulated mass spectra match completely, which also confirms the atomic composition of the atom-precise $Ag_{24}Pd_1(SPhMe_2)_{18}^{2-}$ bimetallic clusters (Figure 4.3(d)). Note that despite the much higher Pd loading in the synthesis for the 6:1 Ag:Pd and 2:1 Ag:Pd systems, single-atom doping is predominant. However, mass spectrometry cannot uniquely identify the position of the Pd in the cluster, thus XPS and XAS studies were undertaken to understand the Ag and Pd speciation in these samples.

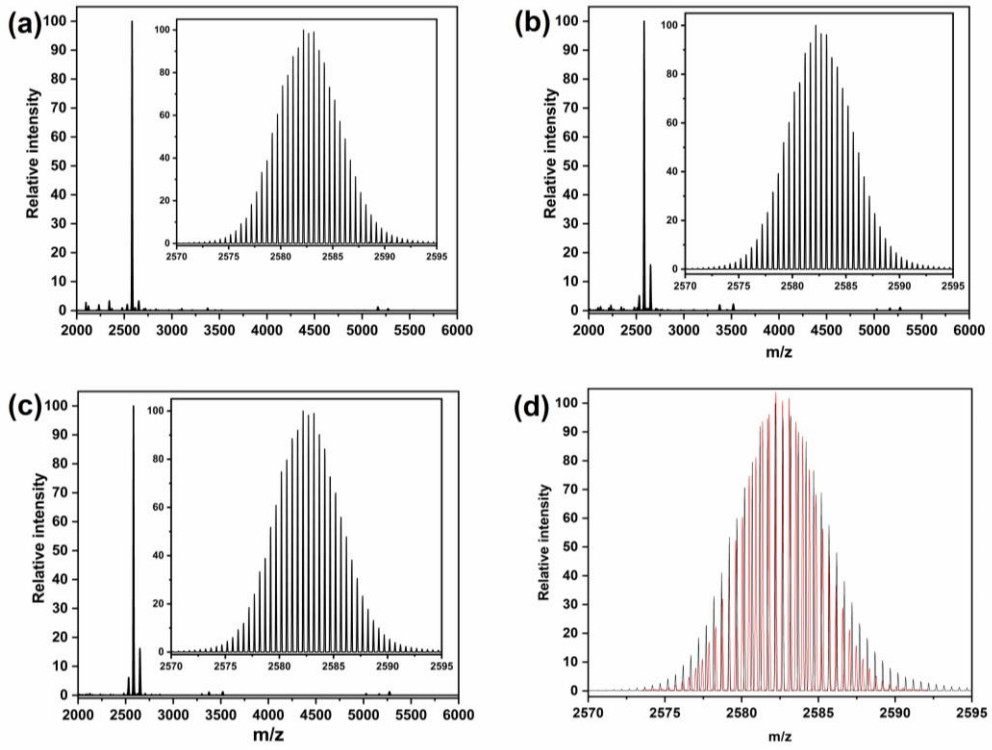

Figure 4.3. Mass spectra of as-prepared thiolate-protected AgPd bimetallic clusters samples made using synthetic ratios of (a) 12:1 Ag:Pd, (b) 6:1 Ag:Pd, (c) 2:1 Ag:Pd; and (d) overlay of experimental (**black**) and simulated (**red**) spectra of atom-precise $Ag_{24}Pd_1(SPhMe_2)_{18}^{2-}$ clusters.

The crystal structure of $Ag_{25}(SPhMe_2)_{18}^{-}$, reported elsewhere,[24] was visualized using the VESTA software package,[27] to reflect the atomic arrangement and ligand counts. There exists one Ag atom at the center and twelve Ag atoms on the surface of the icosahedral core, while the remaining twelve Ag atoms and eighteen S atoms from thiolate ligands constitute atoms in the staple positions (Scheme 4.1(a)). In atom-precise $Ag_{25-x}Pd_x(SPhMe_2)_{18}^{2-}$ clusters the Pd dopant

atoms can exist in the central core (Scheme 4.1(b)), the core surface (Scheme 4.1(c)), or staple position (Scheme 4.1(d)) and by extension, depending on the number of dopant atoms in the composition of bimetallic clusters, the dopant can either occupy one site type or two or more of these positions simultaneously. In the case of a single dopant atom in the composition of bimetallic clusters, the situation is less complicated, and the position of the dopant can be carefully explored. For this bimetallic system, Bark and co-workers reported that the single Pd dopant atom occupies central core position of $Ag_{24}Pd_1(SPhMe_2)_{18}^{2-}$ using X-ray crystallography methods.[20] However, a recent study by Zheng *et al.* suggests that sometimes staple atoms can move towards the core over time in related systems, and thus both kinetic and thermodynamic products may be possible.[12] More element specific techniques like XPS and XAS can be employed to better unravel the structure of AgPd bimetallic clusters.

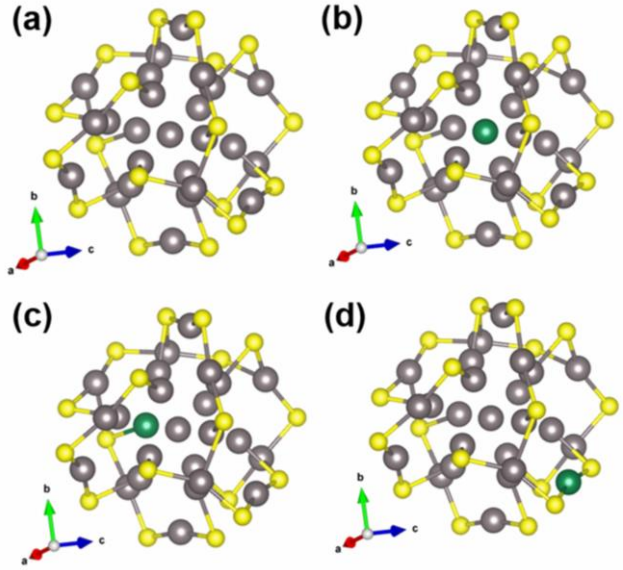

Scheme 4.1. Pictorial representation of possible location of dopant in the atom-precise bimetallic clusters compared with monometallic analogue. Green depicts Pd, grey depicts Ag while yellow represents S.

Through a wetness incipient impregnation method, after full purification, clusters were deposited onto carbon support to give total metal loading of 2% wt. and the atom-precise, carbon-supported, thiolate-protected monometallic and bimetallic clusters were dried at room temperature before XPS and XAS measurements. Previous work showed that this method allows for the successful immobilization of clusters without compromising the cluster structure and no Ag

oxidation is seen (Chapter 2). Figure 4.4 shows the XPS spectra of a representative 12:1 Ag:Pd/carbon sample which was shown to be compromised of $Ag_{24}Pd_1(SPhMe_2)_{18}^{2-}$ clusters by mass spectrometry. XPS survey maps show the presence of C, O, Ag, Pd, and S as the constituent elements and Table 4.1 presents a summary of the fitting parameters. The C 1s spectrum (Figure 4.4(a)) was fitted with multiple Gaussian components having peaks with binding energies at 289.9 eV, 285.9 eV, and 284.8 eV, and these can be attributed to C=O, C-O, and C-C/C-H species respectively, which is consistent with species commonly found on activated carbon surfaces.[28] The O 1s spectrum shows an asymmetric peak that indicates the presence of more than one kind of oxygen species (Figure 4.4(b)) on the carbon surface. The deconvolution of the spectrum gives two peaks centering at 533.1 and ~531.2 eV that can be ascribed to C=O and C-O species from the activated carbon surface, respectively, and thus the absence of metal oxide species.[29] Figure 4.4(c) presents the multiple-component XPS analysis of carbon-supported $Ag_{25}(SPhMe_2)_{18}^{-}$ and $Ag_{24}Pd_1(SPhMe_2)_{18}^{2-}$ clusters to show the site-specific speciation of Ag atoms using method described by Zhang and co-workers.[30] Each of the Ag peaks (both Ag $3d_{5/2}$ and Ag $3d_{3/2}$) was fitted with three components and the peak area ratio was constrained to 1:~12:~12 for Ag_{center}:$Ag_{surface}$:Ag_{staple}. The components of Ag $3d_{5/2}$ peak of $Ag_{25}(SPhMe_2)_{18}^{-}$/carbon sample have binding energies of 367.2 eV, 368.5 eV, and 368.9 eV respectively to show that the central Ag atom is most metallic with oxidation state of 0, the surface Ag atoms are a mixture of both metallic and non-metallic natures with oxidation states between 0 and +1, while the Ag atoms at the staple sites are in +1 oxidation state.[30,31] The Ag 3d peaks are slightly shifted to lower binding energies due to electronic perturbation resulting from incorporation of the Pd atom in the bimetallic system.[9] Figure 4.4(d) shows one set of Pd $3d_{5/2}$ and Pd $3d_{3/2}$ peaks at 337.5 eV and 342.8 eV, respectively, which are inconsistent with Pd atoms in the zerovalent state (Pd $3d_{5/2}$ = 334.5 eV and Pd $3d_{3/2}$ = 339.8 eV),[32] but rather closer to typical values for Pd thiolate species (Pd $3d_{5/2}$ = 336.7 eV and Pd $3d_{3/2}$ = 342.5 eV).[33,34]

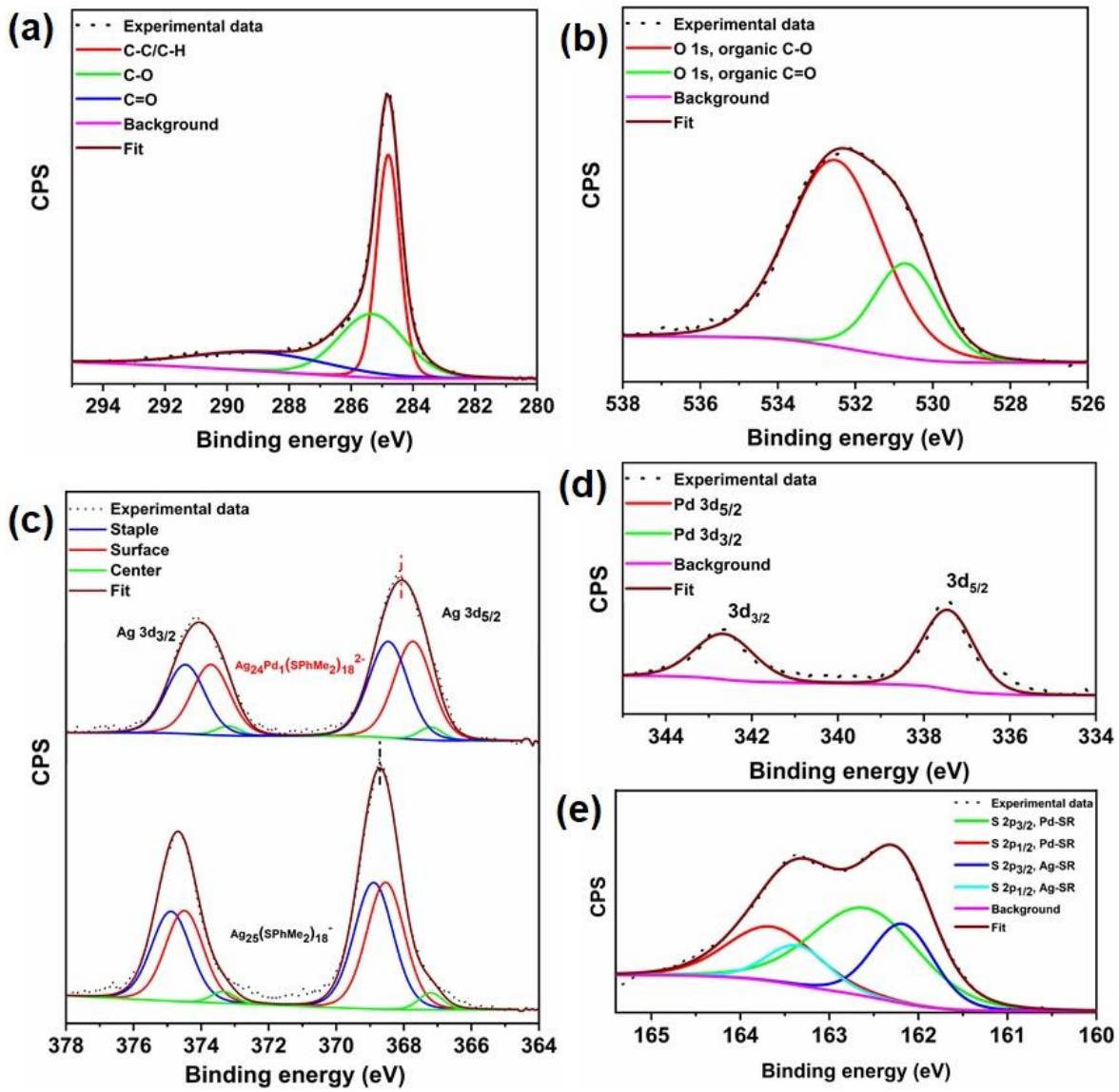

Figure 4.4. XPS spectra of carbon-supported $Ag_{24}Pd_1(SPhMe_2)_{18}^{2-}$ clusters synthesized using a Ag:Pd ratio of 12:1; (a) C 1s, (b) O 1s, (c) Ag 3d, (d) Pd 3d, and (e) S 2p plots.

Table 4.1. XPS fitting parameters for carbon-supported $Ag_{24}Pd_1(SPhMe_2)_{18}^{2-}$ clusters made using a 12:1 Ag:Pd synthetic ratio.

Element	Assignment	Spin-orbit	Position (eV)	FWHM	Area %
O 1s	C=O		533.1	2.84	74
	C-O		531.2	1.96	26
Ag 3d	Ag in Core	5/2	367.2	0.84	2
	Ag on Surface		367.7	1.32	28
	Ag in Staple		368.5	1.36	28
	Ag in Core	3/2	373.2	0.84	2
	Ag on Surface		373.7	1.32	20
	Ag in Staple		374.5	1.36	20
Pd 3d	Pd-thiolate	5/2	337.5	1.41	60
		3/2	342.8	1.62	40
C 1s	C-C/C-H		284.8	0.82	46
	C-O		285.9	2.98	31
	C=O		289.9	4.75	23
S 2p	Ag-thiolate	3/2	162.7	1.43	44
		1/2	163.8	1.18	22
	Pd-thiolate	3/2	162.3	0.82	23
		1/2	163.5	0.82	11

Deconvolution of the high-resolution spectrum of S 2p spectrum, shown in Figure 4.4(e), shows two peaks with spin-orbit splitting of ~1.2 eV indicating the presence of metal-thiolate species.[35] The peaks at 162.3 eV for S $2p_{3/2}$ and 163.5 eV for S $2p_{1/2}$ are assigned as Pd-S (*i.e.*, Pd-thiolate), whereas peaks at 162.7 eV for S $2p_{3/2}$ and 163.8 eV for S $2p_{1/2}$ are attributed to Ag-S (Ag-thiolate) interactions.[29,35] Altogether, XPS results indicate that thiolate ligands remain attached to the surface of the AgPd bimetallic cluster surface and that the carbon-supported bimetallic clusters show multivalent (0 and +1) Ag atoms and a non-zerovalent state for Pd atoms, with no indication of PdO or Ag_2O formation. Thus, XPS results indicate that the Pd atom does

not occupy the central core position. The non-zerovalent state of Pd atoms is seen for all synthesis ratios up to Ag:Pd of 2:1, as shown in Figure 4.5. This is consistent with mass spectrometry results for this sample such that $Ag_{24}Pd_1(SPhMe_2)_{18}^{2-}$ clusters are the only species formed up to a Ag:Pd ratio of 2:1, and no clusters are seen at higher Pd loadings. Only the 1:6 Ag:Pd/carbon sample with a higher loading of Pd (and no cluster signature in the UV-Vis) shows Pd(0) peaks in addition to the non-zerovalent Pd prominent peaks at 336.1 eV ($3d_{5/2}$) and 341.3 eV ($3d_{3/2}$) (Figure 4.5(b)).

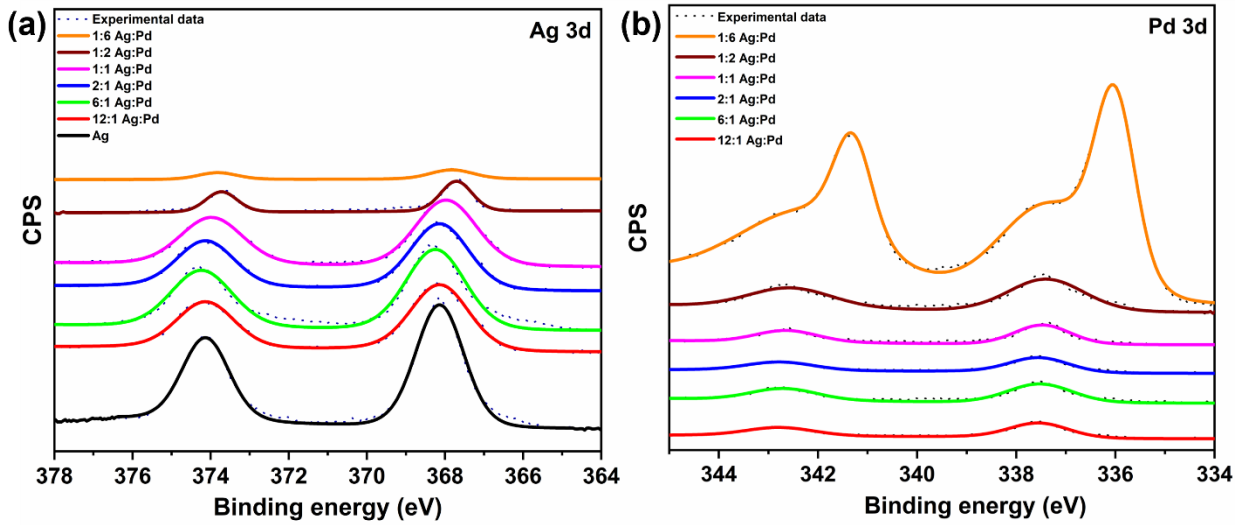

Figure 4.5. XPS spectra of a series of carbon-supported x:y Ag:Pd bimetallic clusters: (a) Ag 3d and (b) Pd 3d.

XAS provides information about the oxidation state and local environment of a specific element and this technique was employed to further explore the position of dopant atoms. Figure 4.6 shows the Pd K-edge XAS spectra obtained for carbon-supported $Ag_{24}Pd_1(SPhMe_2)_{18}^{2-}$ clusters synthesized using a 12:1 Ag:Pd ratio, and $Pd(OAc)_2$, $Pd(OH)_2$, PdO, and Pd foil standard samples. The Pd K-edge XANES spectra (Figure 4.6(a)) shows a strong K-edge feature for Pd at 24,350 eV, which is assigned to the dipole-allowed 1s to 5p transition. Inspection of the spectra of the $Ag_{24}Pd_1(SPhMe_2)_{18}^{2-}$ clusters suggest that it is in a Pd(II) state rather than a Pd(0) state as seen for the Pd foil reference. All x:y Ag:Pd/carbon samples and the $Pd_m(SPhMe_2)_n$/carbon sample show similar near edge features to suggest that the chemical environments around Pd atoms are the same (Figure 4.7(a)). Figure 4.6(b) shows the Pd K edge R-space EXAFS spectra of the carbon-supported $Ag_{24}Pd_1(SPhMe_2)_{18}^{2-}$ sample, along with $Pd(OAc)_2$, $Pd(OH)_2$, PdO, and Pd foil standards (Note the spectra are not phase shift corrected). EXAFS measurements are sensitive to

the bonding environment of the absorbing atom. The $Ag_{24}Pd_1(SPhMe_2)_{18}^{2-}$ clusters show a strong single peak at ~1.9 Å which is consistent with Pd in a thiolate environment, and this is consistent with the Pd dopant atom is most likely occupying a staple position or possibly a position on the icosahedral surface. Similarly the carbon-supported 12:1 Ag:Pd, 6:1 Ag:Pd, 2:1 Ag:Pd, and 1:1 Ag:Pd and $Pd_m(SPhMe_2)_n^-$ samples all show a peak at around 1.9 Å that is attributed to a Pd-S contribution (Figure 4.7(b)) The Pd-O feature at *ca.* 1.60 Å is only present in $Pd(OAc)_2$, $Pd(OH)_2$, and PdO standards. Moreover, the Pd-M (where M is Pd or Ag) feature in the 2.50 Å region is weak or absent to further indicate that the Pd dopant atom does not occupy central core positions in the x:y Ag:Pd bimetallic samples, and that the majority of the Pd is likely in a staple position in individual clusters, though we can not unambiguously rule out some Pd on the icosahedral surface of some clusters. The XAS data at the Pd K-edge indicate Pd bonding with thiolate ligands and no noticeable Pd-O interactions.

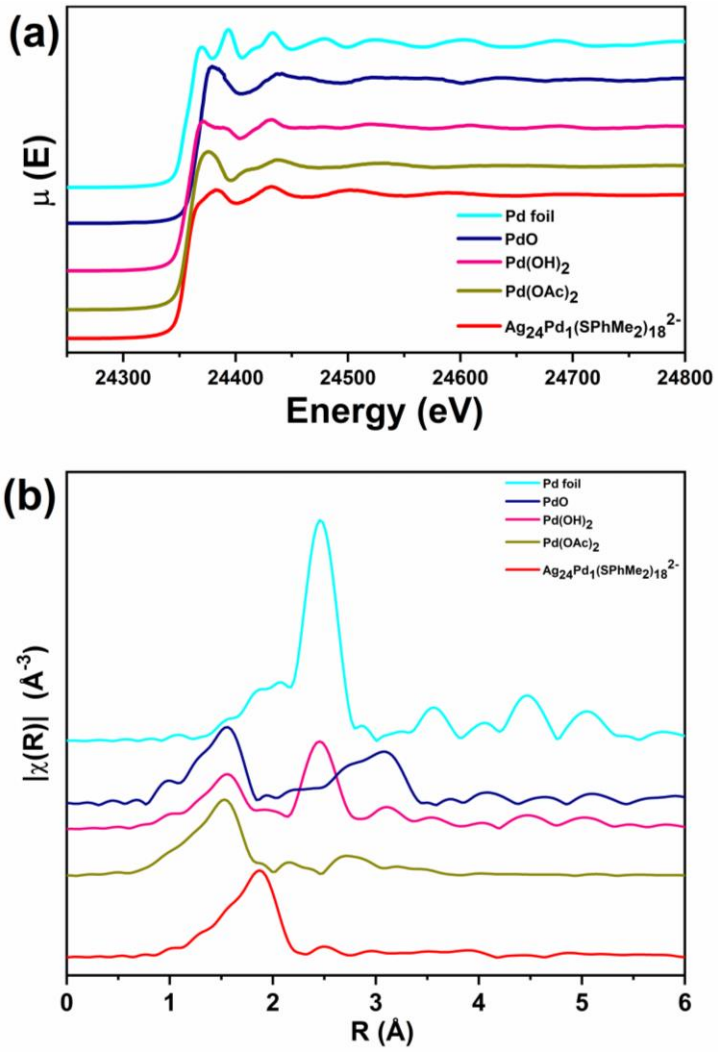

Figure 4.6. XAS Pd K-edge (a) XANES and (b) R-space EXAFS plots of carbon-supported $Ag_{24}Pd_1(SPhMe_2)_{18}^{2-}$ clusters in comparison with $Pd(OAc)_2$, $Pd(OH)_2$, PdO and Pd foil standards.

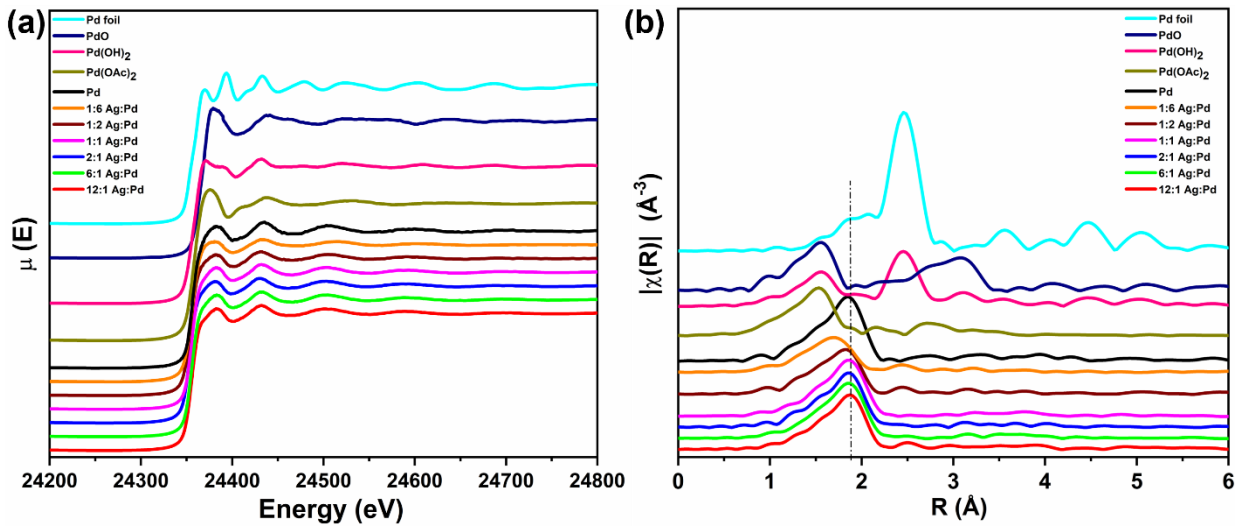

Figure 4.7. XAS Pd K-edge (a) XANES and (b) R-space EXAFS plots of carbon-supported x:y Ag:Pd bimetallic clusters in comparison with $Pd(OAc)_2$, $Pd(OH)_2$, PdO and Pd foil standards.

One concern about the Pd(II) data showing a thiolate environment in both XPS and XAS data was the possibility of Pd(II) thiolate impurities in the cluster solutions. Multiple solvent extractions and redissolutions of clusters were done in the purification step, and a series of chromatographic separations was attempted and showed no indication of a trace of impurities in the cluster samples. So, the prominent Pd-S peak is ascribed to the sample rather than any impurities. It is noteworthy that these observations are not consistent with the earlier studies that reported Pd dopant atom as the core central atom in a similar $Ag_{24}Pd_1(SPhMe_2)_{18}^{2-}$ system using single crystal X-ray diffraction (SC-XRD) methods.[19,20] Typically, the SC-XRD method cannot distinguish transition metals of similar atomic numbers; also it involves sample crystallization which may bias the structure determination by favoring certain structures over others.[19,21] Besides these highlighted limitations of the SC-XRD method, the observed difference, with respect to the position of the dopant atom, may be related to subtle changes in my synthesis protocols. In my synthesis procedure, both Ag and Pd ions are present initially before adding the thiolate ligand and other reagents, whereas the Pd precursor was added to a preformed Ag-thiolate complex in earlier reported procedures.[9,20] XPS and XAS data shown above both indicate the Pd dopant atom predominantly occupies a staple position in individual clusters (or possibly an icosahedral surface position) in the structure of AgPd bimetallic clusters. It is noteworthy that similar staple positions for Pd have recently been reported for dopant Pd atoms in a $Pd_2Au_{36}(SC_2H_4Ph)_{24}$ system using

combined experimental and theoretical EXAFS analysis.[21] Aikens and co-workers performed robust theoretical calculations and predicted centrally doped structures to be the most stable structure of $PdAg_{24}$ clusters. It was however noted that where there is no interaction between the nd levels and superatomic levels, other factors such as the strength of RS-M-SR bonds in the ligand shell, or the energetics of 1S and 1P levels may come into play in understanding the relative stability of the isomer structures which have dopant metal atoms in the staple site.[36] Our group, and others,[26] have noted Pd thiolate bonds can be quite resistant to borohydride reduction, which may be due to increased RS-M-SR bond strengths. This likely positions the Pd dopant in the staple position due to faster Ag reduction during the co-reduction protocol used in this work.

Figure 4.8(a) shows the Ag K-edge XANES spectra obtained for $Ag_{25}(SPhMe_2)_{18}^-$ /carbon and $Ag_{24}Pd_1(SPhMe_2)_{18}^{2-}$/carbon samples, alongside that of Ag_2O and Ag foil as standards. The spectra show a strong K-edge feature for Ag at 25,514 eV which is assigned to the dipole-allowed 1s to 5p transition. The Ag K-edge spectra are quite similar for $Ag_{25}(SPhMe_2)_{18}^-$ /carbon and $Ag_{24}Pd_1(SPhMe_2)_{18}^{2-}$/carbon samples, suggesting Ag has the same environment in both samples. $Ag_{25}(SPhMe_2)_{18}^-$/carbon and nearly all x:y Ag:Pd/carbon samples show similar near edge features (Figure 4.9(a)), which suggests that the neighboring atoms are likely the same. The only exception is the 1:6 Ag:Pd/carbon sample which has distinct features, possibly because some Pd(0) is in the Ag coordination sphere for that sample. Figure 4.8(b) shows the Ag K-edge EXAFS R-space spectra of the $Ag_{25}(SPhMe_2)_{18}^-$/carbon and $Ag_{24}Pd_1(SPhMe_2)_{18}^{2-}$/carbon samples; notably both have similar R-space spectra which contain major Ag-S contributions and minor Ag-Ag contributions. The weaker Ag-Ag interactions are likely due to the fact that there are multiple bonding modes in the clusters (Chapter 2). The Ag-S feature in the 1.85 Å region is consistent with the presence of protecting thiolate ligands on the surface of metal clusters. The Ag_2O standard sample shows a major Ag-O peak at around 1.62 Å which is assigned to Ag-O contributions and is absent in both samples. Figure 4.9(b) shows the Ag K-edge EXAFS R-space spectra for all synthetic AgPd ratios; interestingly the Ag-Ag metallic peaks become more prominent at Ag:Pd ratios of 1:1 and 1:2, which suggest a more metallic environment for these samples (earlier UV-Vis data showed that these samples did not have cluster signatures and thus are likely larger nanoparticles). In summary, XPS and XAS data show that the $Ag_{24}Pd_1(SPhMe_2)_{18}^{2-}$/carbon samples have a metal framework structure similar to that of $Ag_{25}(SPhMe_2)_{18}^-$/carbon and that the single Pd dopant atom predominantly occupies the staple position in individual clusters (or

possibly occasionally the icosahedral surface site) in the structure of atom-precise $Ag_{24}Pd_1(SPhMe_2)_{18}^{2-}$/carbon catalysts.

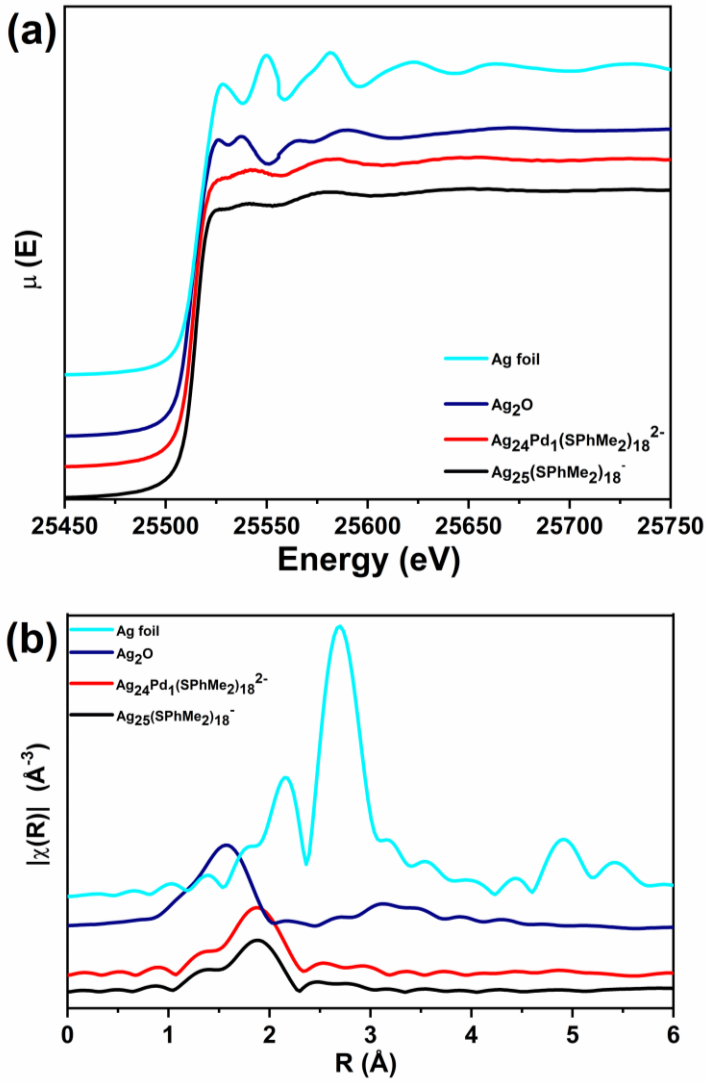

Figure 4.8. XAS Ag K-edge (a) XANES and (b) R-space EXAFS plots of carbon-supported $Ag_{25}(SPhMe_2)_{18}^-$ and $Ag_{24}Pd_1(SPhMe_2)_{18}^{2-}$ bimetallic clusters in comparison with Ag_2O and Ag foil standards.

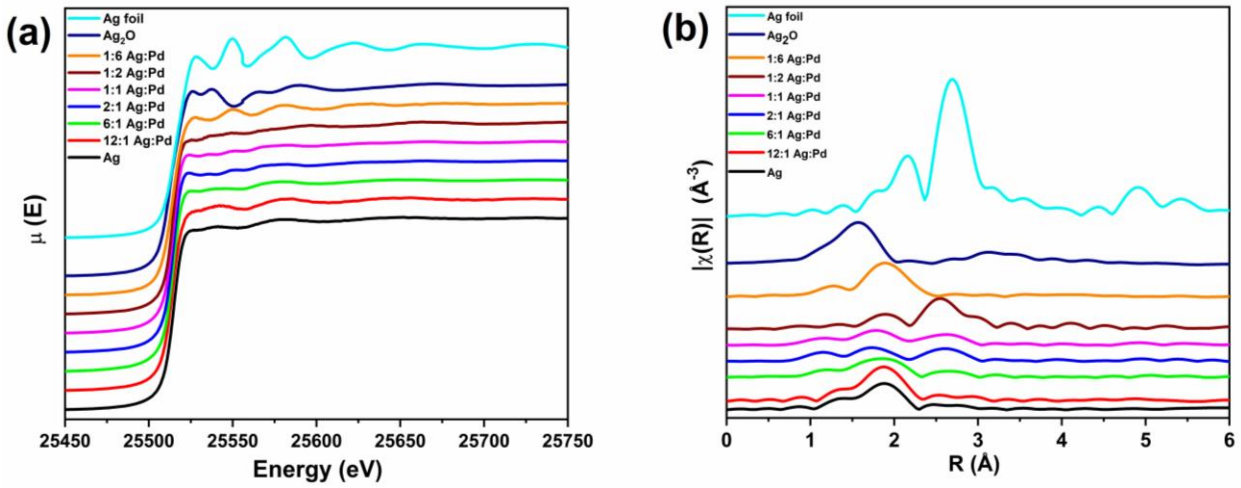

Figure 4.9. XAS Ag K-edge (a) XANES and (b) R-space EXAFS plots of carbon-supported $Ag_{25}(SPhMe_2)_{18}^-$ and x:y Ag:Pd bimetallic clusters in comparison with Ag_2O and Ag foil standards.

4.4 Conclusions

The use of atom-precise, ligand-protected metal clusters has exceptional promise towards the fabrication of model supported-nanoparticle heterogeneous catalysts which have controlled sizes and compositions. One of the major setbacks of the co-reduction strategy of making bimetallic clusters is achieving monodispersity of the clusters. AgPd bimetallic clusters were prepared via an improved co-reduction strategy. The method of preparation, rather than Pd precursor type, was crucial to achieving improved purity. Interestingly, atom-precise $Ag_{24}Pd_1(SPhMe_2)_{18}^{2-}$ bimetallic clusters are the only species seen up to Ag:Pd synthetic ratios of 2:1. At higher Pd loadings, monodisperse clusters are not seen, and no clusters at all are seen when Pd is present in large excess. Single Pd doping leads to changes in the optical properties of the clusters. XPS and XAS results reveal that the single Pd dopant predominantly occupies the staple position in individual clusters, although may alternatively occupy icosahedral surface positions, in the atom-precise $Ag_{24}Pd_1(SPhMe_2)_{18}^{2-}$ bimetallic clusters. The position of the doping metal will lead to changes in the electronic structure, stability, and catalytic properties of the resulting $Ag_{24}Pd_1(SPhMe_2)_{18}^{2-}$ bimetallic clusters.

4.5 References

1. A. Ghosh, O.F. Mohammed, O.M. Bakr. Atomic-Level Doping of Metal Clusters, *Acc. Chem. Res.* 2018, **51**, 3094-3103.

2. R. Jin, C. Zeng, M. Zhou, Y. Chen. Atomically Precise Colloidal Metal Nanoclusters and Nanoparticles: Fundamentals and Opportunities, *Chem. Rev.* 2016, **116**, 10346-10413.

3. G. Yue, S. Su, N. Li, M. Shuai, X. Lai, D. Astruc, P. Zhao. Gold Nanoparticles as Sensors in the Colorimetric and Fluorescence Detection of Chemical Warfare Agents, *Coord. Chem. Rev.* 2016, **311**, 75-84.

4. J. Zeng, Q. Zhang, J. Chen, Y. Xia. A Comparison Study of the Catalytic Properties of Au-Based Nanocages, Nanoboxes, and Nanoparticles, *Nano Lett.* 2010, **10**, 30-35.

5. S.K. Barik, T-H. Chiu, Y-C. Liu, M-H. Chiang, F. Gam, I. Chantrenne, S. Kahlal, J-Y. Saillard, C.W. Liu. Mono- and Hexa-Palladium Doped Silver Nanoclusters Stabilized by Dithiolates, *Nanoscale* 2019, **11**, 14581-14586.

6. Z. Luo, V. Nachammai, B. Zhang, N. Yan, D.T. Leong, D.-e. Jiang, J. Xie. Toward Understanding the Growth Mechanism: Tracing All Stable Intermediate Species from Reduction of Au(I)-Thiolate Complexes to Evolution of Au_{25} Nanoclusters, *J. Am. Chem. Soc.* 2014, **136**, 10577-10580.

7. X. Yuan, X. Dou, K. Zheng, J. Xie. Recent Advances in the Synthesis and Applications of Ultrasmall Bimetallic Nanoclusters, *Part. Part. Syst. Charact.* 2015, **32**, 613-629.

8. B. Huang, Y. Pei. On the Mechanism of Inter-Cluster Alloying Reactions: Two-Stage Metal Exchange of $[Au_{25}(PET)_{18}]^-$ and $[Ag_{25}(DMBT)_{18}]^-$ Clusters, *J. Mater. Chem. A* 2020, **8**, 10242-10251.

9. Y. Liu, X. Chai, X. Cai, M. Chen, R. Jin, W. Ding, Y. Zhu. Central Doping of a Foreign Atom into the Silver Cluster for Catalytic Conversion of CO_2 toward C-C Bond Formation, *Angew. Chem. Int. Ed.* 2018, **57**, 9775-9779.

10. H. Qian, D-e. Jiang, G. Li, C. Gayathri, A. Das, R.R. Gil, R. Jin. Monoplatinum Doping of Gold Nanoclusters and Catalytic Application, *J. Am. Chem. Soc.* 2012, **134**, 16159-16162.

11. M.A. Tofanelli, T.W. Ni, B.D. Phillips, C.J. Ackerson. Crystal Structure of the $PdAu_{24}(SR)_{18}^{0}$ Superatom, *Inorg. Chem.* 2016, **55**, 999-1001.

12. K. Zheng, V. Fung, X. Yuan, D-e. Jiang, J. Xie. Real Time Monitoring of the Dynamic Intracluster Diffusion of Single Gold Atoms into Silver Nanoclusters, *J. Am. Chem. Soc.* 2019, **141**, 18977-18983.

13. S. Hossain, D. Suzuki, T. Iwasa, R. Kaneko, T. Suzuki, S. Miyajima, Y. Iwamatsu, S. Pollitt, T. Kawawaki, N. Barrabés, G. Rupprechter, Y. Negishi. Determining and Controlling Cu-Substitution Sites in Thiolate-Protected Gold-Based 25-Atom Alloy Nanoclusters, *J. Phys. Chem. C* 2020, **124**, 22304-22313.

14. K.E. Lee, A. Shivhare, Y. Hu, R.W.J. Scott. Supported Bimetallic AuPd Clusters Using Activated Au_{25} Clusters, *Catal. Today* 2017, **280**, 259-265.

15. C.F. Calver, P. Dash, R.W.J. Scott. Selective Hydrogenations with Ag-Pd Catalysts Prepared by Galvanic Exchange Reactions, *ChemCatChem*, 2011, **3**, 695-697.

16. M.A. MacDonald, D.M. Chevrier, P. Zhang, H. Qian, R. Jin. The Structure and Bonding of $Au_{25}(SR)_{18}$ Nanoclusters from EXAFS: The Interplay of Metallic and Molecular Behavior, *J. Phys. Chem. C* 2011, **115**, 15282-15287.

17. S. Yamazoe, T. Tsukuda. X-ray Absorption Spectroscopy on Atomically Precise Metal Clusters, *Bull. Chem. Soc. Jpn.* 2019, **92**, 193-204.

18. I. López-Hernández, V. Truttmann, C. Garcia, C.W. Lopes, C. Rameshan, M. Stöger-Pollach, N. Barrabés, G. Rupprechter, F. Rey, A.E. Palomares. AgAu Nanoclusters Supported on Zeolites: Structural Dynamics During CO Oxidation, *Catal. Today* 2022, **384**, 166-176.

19. J. Yan, H. Su, H. Yang, S. Malola, S. Lin, H. Häkkinen, N. Zheng. Total Structure and Electronic Structure Analysis of Doped Thiolated Silver $[MAg_{24}(SR)_{18}]^{2-}$ (M = Pd, Pt) Clusters, *J. Am. Chem. Soc.* 2015, **137**, 11880-11883.

20. M.S. Bootharaju, C.P. Joshi, M.R. Parida, O.F. Mohammed, O.M. Bakr. Templated Atom-Precise Galvanic Synthesis and Structure Elucidation of a $[Ag_{24}Au(SR)_{18}]^-$ Nanocluster, *Angew. Chem. Int. Ed.* 2016, **55**, 922-926.

21. B. Zhang, S. Kaziz, H. Li, D. Wodka, S. Malola, O. Safonova, M. Nachtegaal, C. Mazet, I. Dolamic, J. Llorca, E. Kalenius, L.M.L. Daku, H. Hakkinen, T. Bürgi, N. Barrabés. $Pd_2Au_{36}(SR)_{24}$ Cluster: Structure Studies, *Nanoscale* 2015, **7**, 17012-17019.

22. M. Strohalm, D. Kavan, P. Novák, M. Volný, V. Havlíček. mMass 3: A Cross-Platform Software Environment for Precise Analysis of Mass Spectrometric Data, *Anal. Chem.* 2010, **82**, 4648-4651.

23. M. Strohalm, M. Hassman, B. Košata, M. Kodíček. mMass Data Miner: An Open Source Alternative for Mass Spectrometric Data Analysis, *Rapid Commun. Mass Spec.* 2008, **22**, 905-908.

24. C.P. Joshi, M.S. Bootharaju, M.J. Alhilaly, O.M. Bakr. $[Ag_{25}(SR)_{18}]^-$: The "Golden" Silver Nanoparticle, *J. Am. Chem. Soc.* 2015, **137**, 11578-11581.

25. Y. Negishi, T. Iwai, M. Ide. Continuous Modulation of Electronic Structure of Stable Thiolate-Protected Au_{25} Cluster by Ag Doping, *Chem. Commun.* 2010, **46**, 4713-4715.

26. F.P. Zamborini, S.M. Gross, R.W. Murray. Synthesis, Characterization, Reactivity, and Electrochemistry of Palladium Monolayer Protected Clusters, *Langmuir* 2001, **17**, 481-488.

27. K. Momma, F. Izumi. VESTA: A Three-Dimensional Visualization System for Electronic and Structural Analysis, *J. Appl. Crystallogr.* 2008, **41**, 653-658.

28. J.C. Lascovich, S. Scaglione. Comparison among XAES, PELS and XPS Techniques for Evaluation of Sp^2 Percentage in a-C:H, *Appl. Surf. Sci.* 1994, **78**, 17-23.

29. D.G. Castner, K. Hinds, D.W. Grainger. X-ray Photoelectron Spectroscopy Sulfur 2p Study of Organic Thiol and Disulfide Binding Interactions with Gold Surfaces, *Langmuir* 2002, **12**, 5083-5086.

30. Z. Chen, A.G. Walsh, X. Wei, M. Zhu, P. Zhang. Site-Specific Electronic Properties of $[Ag_{25}(SR)_{18}]^-$ Nanoclusters by X-Ray Spectroscopy, *Small* 2021, **17**, 2005162.

31. G. Corro, E. Vidal, S. Cebada, U. Pal, F. Bañuelos, D. Vargas, E. Guilleminot. Electronic State of Silver in Ag/SiO_2 and Ag/ZnO Catalysts and Its Effect on Diesel Particulate Matter Oxidation: An XPS Study, *Appl. Catal. B Environ.* 2017, **216**, 1-10.

32. S.K. Sengar, B.R. Mehta, Govind. Size and Alloying Induced Shift in Core and Valence Bands of Pd-Ag and Pd-Cu Nanoparticles, *J. Appl. Phys.* 2014, **115**, 124301.

33. G. Corthey, A.A. Rubert, A.L. Picone, G. Casillas, L.J. Giovanetti, J.M. Ramallo-López, E. Zelaya, G.A. Benitez, F.G. Requejo, M. José-Yacamán, R.C. Salvarezza, M.H. Fonticelli. New Insights into the Chemistry of Thiolate-Protected Palladium Nanoparticles, *J. Phys. Chem. C* 2012, **116**, 9830-9837.

34. X. Zhao, L. Zhou, W. Zhang, C. Hu, L. Dai, L. Ren, B. Wu, G. Fu, N. Zheng, Thiol Treatment Creates Selective Palladium Catalysts for Semihydrogenation of Internal Alkynes, *Chem.* 2018, **4**, 1080-1091.

35. A. Majid, F. Bensebaa, P. L'Ecuyer, G. Pleizier, Y. Deslandes. Modification of the Metallic Surface of Silver by the Formation of Alkanethiol Self-Assembled Monolayers with Subsequent Reaction with Chlorosilanes, *Rev. Adv. Mater. Sci.* 2003, **4**, 25-31.

36. F. Alkan, P. Pandeya, C.M. Aikens. Understanding the Effect of Doping on Energetics and Electronic Structure for Au_{25}, Ag_{25}, and Au_{38} Clusters, *J. Phys. Chem. C* 2019, **123**, 9516-9527.

Chapter 5

Atom-Precise Silver-Palladium Bimetallic Clusters on Carbon Supports as Selective Hydrogenation Catalysts

This chapter details the catalytic performance of atom-precise bimetallic $Ag_{24}Pd_1(SPhMe_2)_{18}^{2-}$ clusters made by the direct synthesis method for the semi-hydrogenation of terminal and internal alkynols. EXAFS analysis indicated better stability upon thermal activation for bimetallic $Ag_{24}Pd_1(SPhMe_2)_{18}^{2-}$ clusters as compared to monometallic $Ag_{25}(SR)_{18}^{-}$ clusters. The bimetallic systems showed better catalytic activities than monometallic systems for the selective hydrogenation of 3-hexyn-1-ol and 3-methyl-3-butyn-2-ol.

This chapter is a manuscript that is in preparation for publication. I wrote the complete first draft of the manuscript and this was then edited with the guidance of Prof. Robert W.J. Scott. Catalytic studies were done with the assistance of Andrew Bueckert, who was a summer student in our laboratory under my supervision.

5.1 Introduction

Atom-precise, ligand-protected metal clusters are relevant for the design of model heterogeneous catalysts.[1-5] Nanosized metal clusters can offer both atom economy for catalysis and possess modified electronic properties, surface geometries, and unique structures, and thus can exhibit catalytic performance than bulk materials.[6,7] Atom-precise $Au_{25}(SR)_{18}^-$ clusters are heavily studied in the literature and the analogous Ag system is also gaining research attention.[8,9] Compared to monometallic catalysts, bimetallic catalysts often show superior physicochemical and catalytic properties due to synergy of properties of the constituent metals,[4,10-15] and preparation of selective bimetallic catalysts with control over atom counts allow one to access bimetallic clusters with controlled cluster size, composition, and structure.[10-14] Bimetallic clusters with a single foreign metal atom dopant are attracting great interest, as such subtle atom replacement can afford bimetallic clusters with significantly different physicochemical and catalytic properties. For instance, several studies have shown that a single atom doping of Au_{25} clusters lead to both improved cluster stability and enhanced catalytic efficiency.[13,14,16-19] Meanwhile, Qian *et al.* noted similar catalytic activity for $Pd_1Au_{24}(SC_2H_4Ph)_{18}$ and $Au_{25}(SC_2H_4Ph)_{18}$ clusters in the selective hydrogenation reaction of α,β-unsaturated ketones to α,β-unsaturated alcohols, which indicated that the central Pd atom could not affect the catalytic properties significantly since the central atom was not the active site of the catalyst.[17] In contrast, Xie *et al.* observed no catalytic activity for ligand-on $Pd_1Au_{24}(SC_{12}H_{25})_{18}$/CNT and $Au_{25}(SC_{12}H_{25})_{18}$/CNT catalysts, whereas activated catalysts (via thermal activation in vacuum) were active for aerobic oxidation of benzyl alcohol and that single Pd atom doping significantly enhanced the catalytic performance of activated Au_{25} clusters.[19] Using *operando* Diffuse Reflectance Infrared Fourier Transform Spectroscopy (DRIFTS), Garcia *et al.* showed that migration of the Pd dopant atom from the Au cluster core to the cluster surface is responsible for increased activity of titania-supported $PdAu_{24}$ catalysts for CO oxidation.[20] These divergent observations show that the enhanced catalytic performance by $Pd_1Au_{24}(SR)_{18}$ with a single Pd atom at the central position is yet to be clearly rationalized completely.

Atom-precise Ag-based bimetallic clusters are less studied compared to their Au-based bimetallic counterparts and have similar atomic arrangements and ligand counts. Bakr and co-workers prepared $Pd_1Ag_{24}(SR)_{18}^{2-}$ clusters and noted, via crystallography, that the Pd dopant atom

replaces the core central atom.[21] Like the Au system, improvement in stability and catalytic performance has been observed for $Pd_1Ag_{24}(SR)_{18}^{2-}$ clusters when compared with $Ag_{25}(SR)_{18}^{-}$ clusters,[12,15,21] but catalytic studies of bimetallic Ag-based clusters are presently limited. Zhu and co-workers reported that the centrally-doped bimetallic $Pd_1Ag_{24}(SR)_{18}^{2-}$ clusters display superior catalytic performances to $Ag_{25}(SR)_{18}^{2-}$ clusters in the carboxylation reaction of CO_2 with terminal alkynes via C-C bond formation to give propiolic acid.[15] The rationale as to how such subtle modification by a single atom in the center of the cluster results in significant enhancements in the catalytic efficiency still needs to be unraveled. Alternatively, positioning the active metal on the catalyst surface for better accessibility by the substrates can significantly improve the catalytic performance.[14,20] In addition, the optimum catalytic potential of these ligand-protected bimetallic clusters can be achieved by partial or complete desorption of protecting ligands.[9,19,22] At present, there is no information on the nature of bimetallic $Pd_1Ag_{24}(SR)_{18}^{2-}$ clusters upon activation and there is possibility of oxidation and/or phase separation upon thermal activation.

In Chapter 4, I reported the synthesis of atom-precise bimetallic $Ag_{24}Pd_1(SR)_{18}^{2-}$ clusters and showed via element-specific X-ray absorption spectroscopy that the single Pd dopant atom did not reside in the central core position of the overall structure. The Pd dopant atom is in the surface/staple environment and thus should be more accessible for catalysis. Notably, Ag is a poor hydrogenation catalyst by itself while Pd is very active, albeit with intrinsic poor selectivity.[23,24] So, a bimetallic cluster system that comprises of atomically isolated Pd on a Ag cluster surface, like in the case of singly-doped $Ag_{24}Pd_1(SR)_{18}^{2-}$ clusters, is an intriguing model single-atom hydrogenation catalyst that should allow for selective hydrogenations of alkynes to alkenes. Several research groups, including ours, have reported AgPd bimetallic systems as excellent selective hydrogenation catalysts.[25-33] Single-atom alloy AgPd catalysts with isolated Pd atoms were found to be active for the hydrogenation of acrolein.[31] Khan *et al.* described a system of having a Pd-rich surface to dissociate H_2 and catalyze hydrogenation reactions, as well as an Ag-rich core to prevent the occurrence of sub-surface H, for an ideal highly-selective AgPd bimetallic catalyst.[26] Moreover, in Chapter 3, I showed that AgPd bimetallic catalysts prepared via the sequential reduction of Pd onto the surface of Ag clusters show structure-dependent selectivity for hydrogenation reactions, with high selectivity for selective hydrogenations at low Pd levels.

In this study, the structural characterization and catalytic evaluation of atom-precise $Ag_{24}Pd_1(SPhMe_2)_{18}^{2-}$ bimetallic clusters, prepared via a modified direct synthesis method, were done in comparison with the corresponding $Ag_{25}(SPhMe_2)_{18}^{2-}$ monometallic clusters. Clusters were examined both with and without low temperature activation on carbon supports. Both intact and activated clusters were characterized using element-specific X-ray absorption spectroscopy to follow the structure evolution upon activation, and then evaluated as selective heterogeneous catalysts for the hydrogenation of alkynols. Results further affirm that Pd atoms selectively occupy a staple position in the clusters while Ag atoms occupy the core and surface of the icosahedral cluster cores and the remaining staple positions. Upon activation, both Ag-M and Pd-M (where M is Ag or Pd) interactions increase upon increasing the activation temperature. Pd-S interactions remain for calcined samples at 250 °C, but they are absent in samples calcined at 450 °C. Bimetallic $Ag_{24}Pd_1(SR)_{18}^{2-}$ clusters showed better thermal stability and catalytic activity than homonuclear $Ag_{25}(SR)_{18}^{2-}$ clusters on carbon supports. The $Ag_{24}Pd_1(SR)_{18}^{2-}$ clusters showed excellent selectivity for the selective hydrogenation of 2-methyl-3-butyn-2-ol (MBY) and 3-hexyn-1-ol (HY) to their respective alkenols. Upon mild activation at 250 °C, catalytic activities were not significantly different from intact clusters, albeit the presence of residual thiolate ligands on the activated $Ag_{24}Pd_1$ clusters increased the selectivity towards alkenols.

5.2 Experimental

5.2.1 Materials

Silver nitrate ($AgNO_3$, ≥99.0%), palladium (II) acetate ($Pd(OAc)_2$, 99.9%), acetonitrile (MeCN, 99.9%), ethanol (EtOH, 100%), 2-methyl-3-butyn-2-ol (MBY, 98%), and 3-hexyn-1-ol (HY, 98%) were procured from Sigma Aldrich. Dichloromethane (CH_2Cl_2, DCM), methanol (MeOH, HPLC grade), acetone (C_3H_6O, 99.5%), hexane (C_6H_{14}, 98.5%), sodium borohydride ($NaBH_4$, 98%), and 1% wt Pd/Al_2O_3 catalyst were bought from Fisher Scientific. 2,4-Dimethylbenzenethiol ($HSPhMe_2$, C_8H_9SH, 95%), tetraphenylphosphonium bromide (Ph_4PBr), and 2-propanol (isopropanol, HPLC grade, 99.7+%) were procured from Alfa Aesar, while activated carbon (Powder, CX0657-1) was bought from EMD. In all experiments, Milli-Q (Millipore, Bedford, MA) deionized water with resistivity of 18.2 MΩ cm was used. Glassware was thoroughly cleaned using aqua regia, rinsed with deionized water, and then dried completely before use. All chemicals were used as received without any further purification.

5.2.2 Synthesis of Atom-Precise Thiolate-Protected Ag_{25} and $Ag_{24}Pd_1$ Clusters

Monometallic $Ag_{25}(SPhMe_2)_{18}^-$ clusters were prepared as described in section 2.2.2. Bimetallic $Ag_{24}Pd_1(SR)_{18}^{2-}$ clusters were prepared via a method described in section 4.2.2 using 0.22 mmol of $AgNO_3$ and 0.018 mmol of $Pd(OAc)_2$, as the synthetic metal compositions.

5.2.3 Preparation and Activation of Carbon-Supported Atom-Precise Metal Clusters

The carbon-supported metal clusters were prepared by immobilizing metal clusters onto carbon supports via the wetness impregnation method, to give a final metal loading of ca. 1 wt%. Typically, 2.0 mL of a DCM solution of the metal clusters was added to 200 mg of activated carbon and stirred for 30 min. Afterwards, the mixture was allowed to settle, and the colourless supernatant was removed under vacuum to obtain the carbon-supported metal clusters. This powder was then allowed to dry completely under ambient conditions. Activated samples were prepared by calcining samples of the as-prepared carbon-supported metal clusters at 250 °C and 450 °C for 2 h at a ramping rate of 10 °C/min under air flow using a Lindberg/Blue M furnace.

5.2.4 Characterization Techniques

UV-Vis absorption spectroscopy and X-ray photoelectron spectroscopy (XPS) measurements were collected as described in section 2.2.4. Elemental compositions and ESI-MS measurements were performed as described in section 3.2.3. X-ray absorption near-edge structure (XANES) measurements at the Pd L_3-edge and S K-edge were conducted in fluorescence yield (FY) mode at the Soft X-ray Micro Characterization Beamline (SXRMB) 06B1-1 (Energy range 1.7-10 keV; resolution 1 x 10^{-4} $\Delta E/E$ Si (111); spot size 4 mm x ~1 mm) at the Canadian Light Source (CLS). Several mg of each powdered sample was placed on carbon tape which was mounted on the Cu plate sample holder. The Cu plate was then placed inside the vacuum chamber with a vacuum of 3 x 10^{-5} torr. High energy XAS (Ag K-edge and Pd K-edge) measurements were conducted at the Biological X-ray Absorption Spectroscopy (BioXAS) beamline 07ID-2 at the CLS as described in section 3.2.3. The k^2-weighted spectra were subjected to a Fourier transform (FT) in R space for the k range of 3.0-11.8 $Å^{-1}$ and 3.0-13.8 $Å^{-1}$ for Ag and Pd data respectively. Ag fcc bulk lattice parameters were used to fit the Ag-foil spectrum, keeping the first shell coordination number fixed (CN = 12) at first to determine the amplitude reduction factor (S_0^2). Similar data fitting was performed for Pd fcc bulk lattice parameters for the Pd-foil spectrum. From

these fits, amplitude reduction factors of 0.85 were determined for both Ag-foil and Pd-foil, and this value was used for the subsequent sample fits.

5.2.5 Catalyst Evaluation

The hydrogenation reaction was carried out in a 50 mL three-neck round bottom flask. Prior to sealing all the three necks, an egg-shaped magnetic stirrer, 25.0 mg of catalyst, and 5.0 mL of solvent (typically ethanol, except for initial solvent studies) were added to the reaction flask which was then purged with continuous flow of H_2 gas for 10 min. Thereafter, the system was filled with ca. 1.5 atm H_2 gas and allowed to equilibrate for 10 min, during which there was no observable leakage as monitored by a differential pressure manometer (407910, Extech Instrument). 2.0 mmol of alkynol (MBY or HY) was quickly added by syringe to start the reaction, and the reaction mixture was stirred at different speeds (200-1600 rpm) for 180 min at 25 °C. After the reaction, the solid catalyst was removed by centrifugation, and the liquid sample containing the catalytic products was analyzed by gas chromatography (7890A, Agilent Technologies), equipped with a flame ionization detector and a HP-5 column. For recycling experiments, the catalyst was washed twice in isopropanol, dried under vacuum, and reused in subsequent reaction cycles. Selectivity was calculated as the ratio of a particular product to the sum of all products, expressed as a percentage. The stereoselectivity of a product isomer is the ratio of the amount of its Z-configuration product to the total amount of its Z- and E-isomer products, expressed as a percentage.

5.3 Results and Discussion

The reduction of the metal-thiolate complex mixture by $NaBH_4$ addition resulted in the formation of thiolate-protected metal clusters whose atom compositions were ascertained by mass spectrometry measurements. Figure 5.1(a) shows the mass spectra of $Ag_{25}(SPhMe_2)_{18}^-$ and $Ag_{24}Pd_1(SPhMe_2)_{18}^{2-}$ clusters. The $Ag_{25}(SPhMe_2)_{18}^-$ monometallic clusters show a prominent peak at m/z of 5166 with isotopic distribution peaks separated by m/z value of 1. In contrast, the $Ag_{24}Pd_1(SPhMe_2)_{18}^{2-}$ bimetallic clusters show a prominent peak at m/z of 2582 with isotopic distribution peaks separated by m/z value of 0.5. These values are consistent with values of ~5167 and ~2582 reported in the literature for monodisperse $Ag_{25}(SPhMe_2)_{18}^-$ and $Ag_{24}Pd_1(SPhMe_2)_{18}^{2-}$ clusters, respectively.[15,21] Atom-precise thiolate-protected metal clusters have distinct optical

features in the visible light region, and thus UV-Vis absorption spectroscopy is an excellent characterization technique to follow the synthesis of these atom-precise thiolate-protected metal clusters. Figure 5.1(b) shows the UV-Vis absorption spectra both $Ag_{25}(SPhMe_2)_{18}^-$ and $Ag_{24}Pd_1(SPhMe_2)_{18}^{2-}$ clusters in DCM solvent. The clusters exhibit broad multiband optical absorptions in the UV-Vis region. The $Ag_{25}(SPhMe_2)_{18}^-$ clusters particularly show characteristic peaks at 334 nm, 392 nm, 490 nm, and 678 nm which are consistent with nearly monodisperse $Ag_{25}(SR)_{18}^-$ clusters.[34] The absorption peak at 678 nm is ascribed to the HOMO-LUMO transition in the Ag_{25} structure, and it undergoes a hypsochromic shift of ~11 nm upon incorporation of dopant Pd to form $Ag_{24}Pd_1(SPhMe_2)_{18}^{2-}$ clusters. Such a hypsochromic shift in the optical absorption spectra is consistent with the previous studies on Pd-doped M_{25} (where M is Ag or Au) clusters.[12,13,15,16,21] Except for the hypsochromic shift, the overall optical features are similar to the $Ag_{25}(SPhMe_2)_{18}^-$ clusters which suggests an analogous structural framework for both $Ag_{25}(SPhMe_2)_{18}^-$ and $Ag_{24}Pd_1(SPhMe_2)_{18}^{2-}$ clusters.[12,21] Both ESI-MS and UV-Vis data clearly showed that highly monodisperse and pure atom-precise $Ag_{25}(SPhMe_2)_{18}^-$ and $Ag_{24}Pd_1(SR)_{18}^{2-}$ clusters were produced, which is consistent with previous work (Chapter 4).

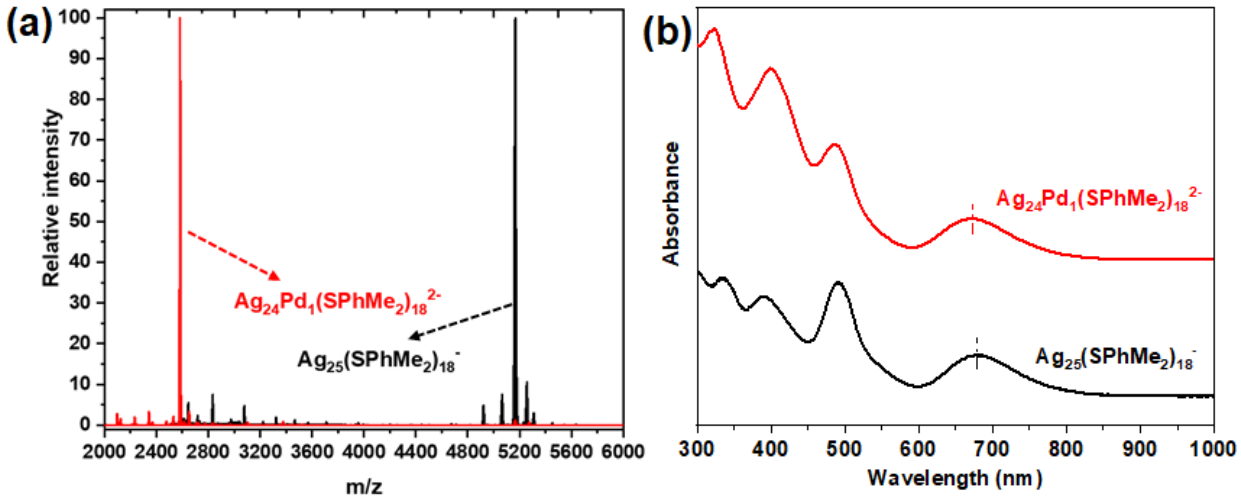

Figure 5.1. (a) ESI-MS spectra and (b) UV-Vis absorption spectra of unsupported $Ag_{25}(SPhMe_2)_{18}^-$ monometallic and $Ag_{24}Pd_1(SPhMe_2)_{18}^{2-}$ bimetallic clusters.

The atom-precise metallic and bimetallic clusters were immobilized onto carbon supports for heterogeneous catalysis. The carbon-supported samples were further characterized using element-specific X-ray spectroscopy and Table 5.1 summarizes the results obtained from the

multiple-component XPS analysis of $Ag_{25}(SPhMe_2)_{18}^-$ and $Ag_{24}Pd_1(SPhMe_2)_{18}^{2-}$ clusters on carbon supports. For the Ag 3d peaks, the peak area ratio was constrained to 1:~12:~12 for Ag_{center}:$Ag_{surface}$:Ag_{staple} to show the site-specific speciation of Ag atoms as described by Chen *et al*.[35] The components of the Ag $3d_{5/2}$ peaks of carbon-supported $Ag_{25}(SPhMe_2)_{18}^-$ clusters have binding energies of 367.2 eV, 368.5 eV, and 368.9 eV for Ag at center, surface, and staple positions, respectively. Similar Ag $3d_{5/2}$ binding energies of 367.2 eV, 367.7 eV, and 368.5 eV were obtained for the carbon-supported $Ag_{24}Pd_1(SPhMe_2)_{18}^{2-}$ sample. Notably, the Ag 3d peak components assigned to Ag atoms in the surface and staple sites are slightly shifted to lower binding energies to indicate electronic perturbation due to incorporation of the Pd atom.[15] In both systems, the Ag atom in the center position is most metallic with oxidation state of 0, the Ag atoms in surface position have oxidation states between 0 and +1 to suggest a mixture of both non-metallic and metallic natures, while the Ag atoms at the staple sites are in +1 oxidation state.[35] The Pd $3d_{5/2}$ peak at 337.3 eV for the $Ag_{24}Pd_1$ clusters is consistent with a Pd(II) oxidation state in a thiolate environment.[36] The $Ag_{24}Pd_1$ clusters have S $2p_{3/2}$ peaks at 162.7 eV and 162.3 eV which suggests two metal-thiolate (i.e. Ag-thiolate and Pd-thiolate) interactions are present in bimetallic clusters, whereas only one metal-thiolate interaction (S $2p_{3/2}$ peak at 162.6 eV) is seen for the monometallic Ag_{25} clusters. In summary, XPS results show that thiolate ligands are present on the metal cluster surface and that the dopant Pd is a Pd(II) species which is therefore likely present on either the core surface or in a staple environment and thus should be accessible for catalysis.

Table 5.1. Multiple component XPS analysis of atom-precise $Ag_{25}(SPhMe_2)_{18}^-$ and $Ag_{24}Pd_1(SPhMe_2)_{18}^{2-}$ clusters on carbon supports.

Element	Element	Assignment	Position (eV)	FWHM	Area %
$Ag_{25}(SPhMe_2)_{18}^-$/carbon	Ag $3d_{5/2}$	Ag in Center	367.2	0.84	2
		Ag on Surface	368.5	1.32	28
		Ag in Staple	368.9	1.36	28
	Ag $3d_{3/2}$	Ag in Center	373.3	0.84	2
		Ag on Surface	374.5	1.32	20
		Ag in Staple	374.9	1.36	20
	S $2p_{3/2}$	Ag-thiolate	162.6	1.38	66
	S $2p_{1/2}$		163.9	1.21	34
$Ag_{24}Pd_1(SPhMe_2)_{18}^{2-}$ /carbon	Ag $3d_{5/2}$	Ag in Center	367.2	0.84	2
		Ag on Surface	367.7	1.32	28
		Ag in Staple	368.5	1.36	28
	Ag $3d_{3/2}$	Ag in Center	373.2	0.84	2
		Ag on Surface	373.7	1.32	20
		Ag in Staple	374.5	1.36	20
	Pd $3d_{5/2}$	Pd-thiolate	337.3	1.41	60
	Pd $3d_{3/2}$		342.7	1.62	40
	S $2p_{3/2}$	Ag-thiolate	162.7	1.41	44
	S $2p_{1/2}$		163.8	1.18	22
	S $2p_{3/2}$	Pd-thiolate	162.3	0.82	23
	S $2p_{1/2}$		163.5	0.82	11

The presence of ligands on the surface of a cluster can influence the catalytic performance as the protecting ligand may limit the accessibility of active site by the substrates.[9,19,22] Thermal treatment (calcination) is one of the simple and efficient ways of activating (i.e. removing the ligand from) ligand-protected clusters.[9] The carbon-supported, atom-precise monometallic and bimetallic clusters were activated at different temperatures and both the as-prepared and activated samples were further characterized using element-specific XAS methods. XAS can provide information about the local environment as well as the oxidation states of a specific element. Figure

5.2 presents the Ag K-edge XAS data for as-prepared and thermally-activated $Ag_{25}(SPhMe_2)_{18}^-$ and $Ag_{24}Pd_1(SPhMe_2)_{18}^{2-}$ clusters on carbon supports. The Ag K-edge XANES spectra are similar for as-prepared carbon-supported $Ag_{25}(SPhMe_2)_{18}^-$ and $Ag_{24}Pd_1(SPhMe_2)_{18}^{2-}$ clusters to indicate that the chemical environment of Ag is similar in both samples (Figures 5.2(a) and 5.2(b)). Meanwhile, there is a difference in the spectra obtained for the metallic and bimetallic cluster samples upon thermal activation. For the $Ag_{25}(SPhMe_2)_{18}^-$ clusters there is growth in the intensity of the multi-scattering peak at ca. 25,548 eV after calcination which increases at higher calcination temperatures, while for the bimetallic sample growth of this peak is only seen for the $Ag_{24}Pd_1(SPhMe_2)_{18}^{2-}$ clusters calcined at 450 °C (and little to no change is seen at 250 °C). Figure 5.2(c) shows the Ag K-edge EXAFS data for the monometallic system. The Ag-S peak (~1.85 Å) disappears with a consequent increase in the Ag-Ag peak for the sample calcined at 250 °C indicating mild sintering of clusters at this temperature. The Ag-Ag peak grows further at a calcination temperature of 450 °C which indicates that cluster sintering becomes particularly problematic beyond 250 °C. Figure 5.2(d) shows the analogous Ag K-edge data for the Pd-doped system (i.e. $Ag_{24}Pd_1(SPhMe_2)_{18}^{2-}$); nearly no growth in the Ag-Ag peak is seen at 250 °C whereas the Ag-Ag peak increases in intensity significantly at 450 °C, which points to significant sintering at higher temperatures but no sintering at 250 °C. The absence of a Ag-O peak around 1.60 Å in both systems suggests that there is no formation of Ag_2O (Figures 5.2(c) and 5.2(d)). These results indicate that the single Pd atom in $Ag_{24}Pd_1(SPhMe_2)_{18}^{2-}$ bimetallic clusters enables increased stability to thermal treatment than the analogous $Ag_{25}(SPhMe_2)_{18}^-$ monometallic clusters.

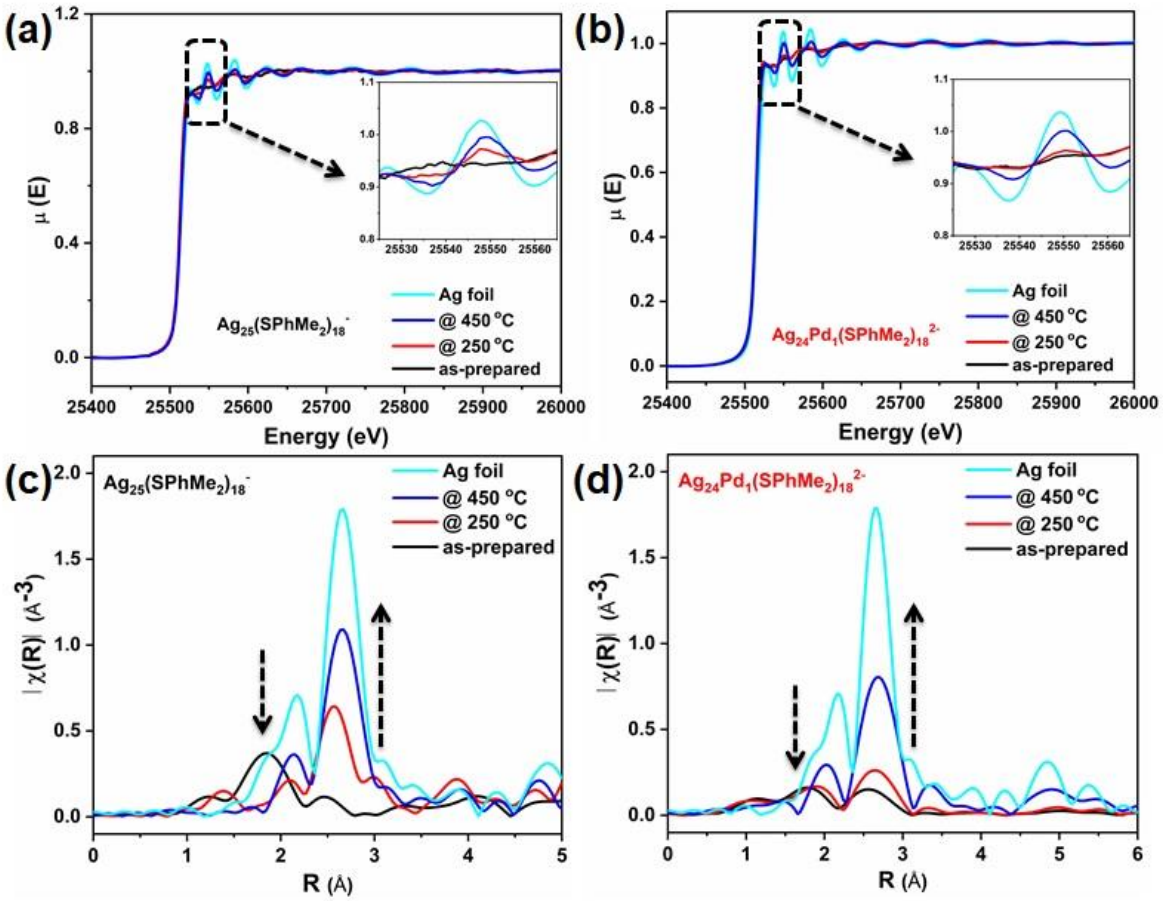

Figure 5.2. The Ag K-edge XANES (a, b) and Ag K-edge EXAFS (c, d), spectra of as-prepared and activated carbon-supported $Ag_{25}(SPhMe_2)_{18}^-$ monometallic (a, c) and $Ag_{24}Pd_1(SPhMe_2)_{18}^{2-}$ bimetallic (b, d), clusters samples.

XANES can be an excellent probe of the speciation of constituent metals of clusters upon activation. Figure 5.3(a) presents the Pd K-edge XANES spectra obtained for as-prepared and activated carbon-supported $Ag_{24}Pd_1(SPhMe_2)_{18}^{2-}$ bimetallic clusters. A close look at the near edge features shows that the chemical environment of Pd atoms changes for the bimetallic sample calcined at 450 °C; Pd is neither in thiolate environment as in the as-prepared sample nor in a fcc Pd zerovalent metallic state like in standard Pd foil. The Pd K-edge EXAFS data show that in the as-prepared, carbon-supported $Ag_{24}Pd_1(SPhMe_2)_{18}^{2-}$ bimetallic clusters, Pd is in a thiolate environment as suggested by the presence of Pd-S peak at about 1.9 Å (Figure 5.3(b)), which is consistent with previous work (Chapter 4). Interestingly, at 250 °C, this peak is still seen, showing that the Pd-S thiolate interaction is much stronger than Ag-S thiolate interactions (as seen in Figure

5.2). Upon activation of carbon-supported $Ag_{24}Pd_1(SPhMe_2)_{18}^{2-}$ bimetallic clusters at 450 °C, there is disappearance of the Pd-S peak with consequent emergence of a prominent Pd-M peak (where M is Pd or Ag) at 2.55 Å, as well as a very weak Pd-O feature at ~1.60 Å (Figure 5.3(b)).

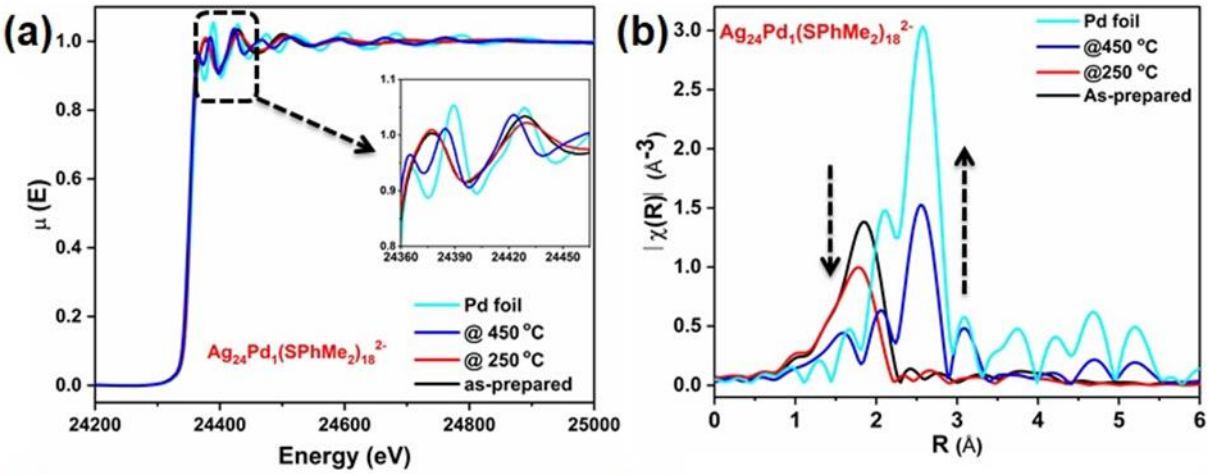

Figure 5.3. (a) Pd K-edge XANES, and (b) Pd K-edge EXAFS, spectra of as-prepared and activated carbon-supported $Ag_{24}Pd_1(SPhMe_2)_{18}^{2-}$ bimetallic cluster samples.

Figure 5.4 presents the fits of experimental EXAFS data for the activated sample at 450 °C for both Ag and Pd K-edge measurements in both k-space and R-space using a fcc model, while Table 5.2 presents a summary of EXAFS fitting parameters (note that data for samples calcined at 250 °C were not amenable to EXAFS fitting due to poor S/N in the Ag K-edge data). At both Ag and Pd K-edges, the Ag-M and Pd-M coordination numbers (CNs) for the bimetallic sample calcined at 450 °C are significantly less than 12, which is consistent with the presence of small clusters with a large fraction of surface atoms. Also, the activated sample shows a Ag-M distance (2.836(6) Å) that is slightly shorter than the Ag-Ag bond distance of 2.88 Å in standard Ag foils. Similarly, the modelled Pd-M distance of 2.787(7) Å is slightly larger than typical Pd-Pd bond distance of 2.75 Å in a standard Pd fcc foil. These differences in bond distance also strongly indicate the presence of heteroatomic bonding in the activated sample;[37-39] i.e. no indication of phase separation is seen upon activation at 450 °C. This is consistent with the result obtained for bimetallic AgPd/carbon catalysts with similar metal compositions prepared via an indirect method of catalyst preparation (Chapter 3). The fit of the Pd K-edge EXAFS data also suggests a small amount of PdO_x species are present on the surface of the clusters. The greater $CN_{Pd\text{-}M}$ of 6.5(9) (compared to a $CN_{Ag\text{-}M}$ value of 5.0(4)) also suggests there may be slightly more subsurface Pd

atoms in the final clusters, which is an indication of structural changes upon calcination. Using scanning tunneling microscopy (STM) and machine-learning molecular dynamics simulations, others have also observed migration of some Ag atoms to cover Pd islands on Ag(111), especially at elevated temperatures, with the degree of Ag encapsulation depending on temperature and coverage of Pd deposited onto the Ag(111) surface.[40] Notably, incomplete encapsulation will expose some Pd atoms for possible surface oxidation.

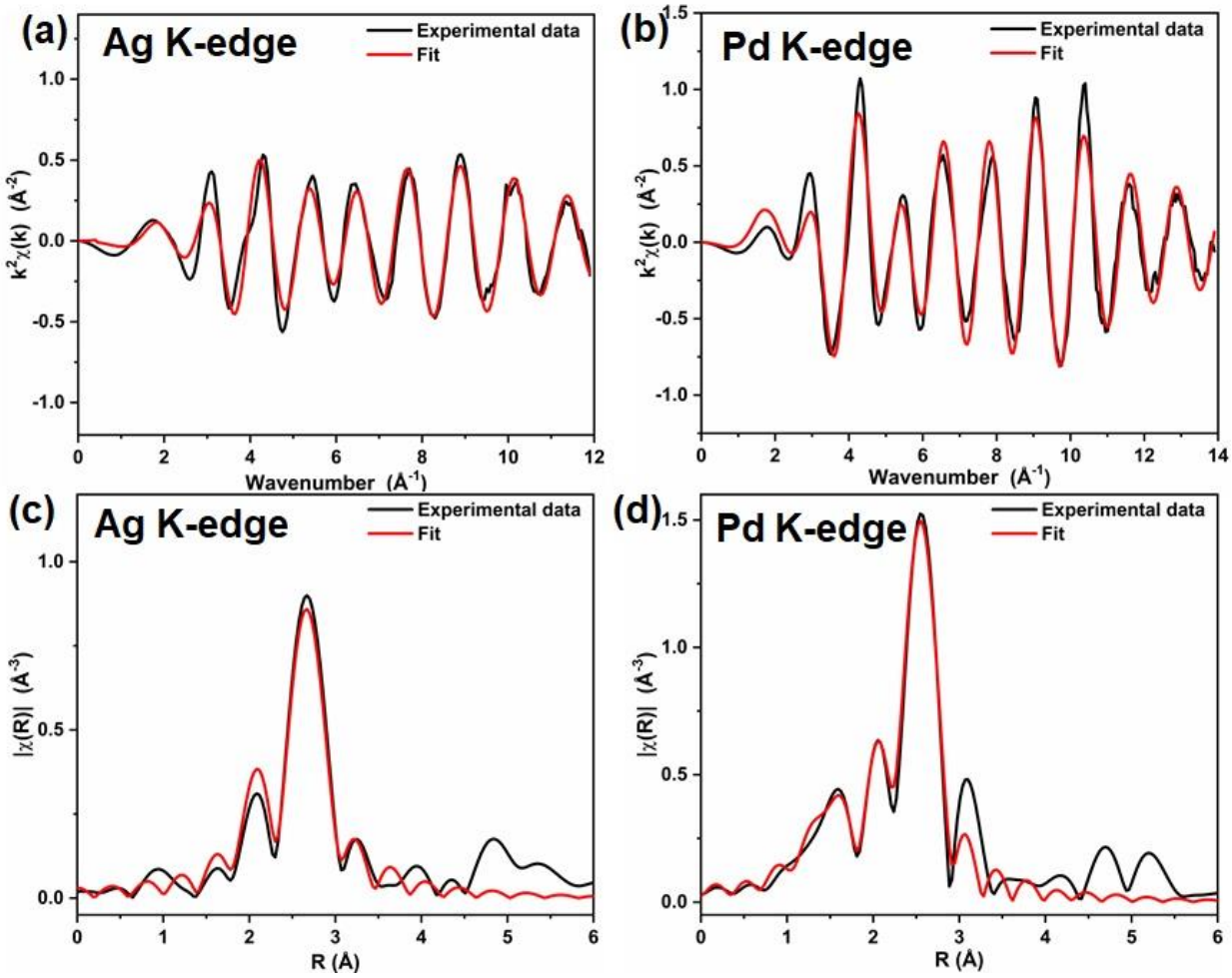

Figure 5.4. Experimental data of the Fourier transformed EXAFS and theoretical EXAFS fits for the carbon-supported $Ag_{24}Pd_1$@450 °C sample for Ag and Pd K-edge measurements in (a,b) k-space and (c,d) R-space.

Table 5.2. Summary of EXAFS fitting parameters for the carbon-supported $Ag_{24}Pd_1$@450 °C sample.

Bond type	**CN**	**R/Å**	**σ^2 /Å^2**	**E_o Shift (eV)**	**R (%)**
Pd-O	1.0(5)	1.98(2)	0.003(1)	-3.4(9)	1.3
Pd-M	6.5(9)	2.787(7)	0.006(1)		
Ag-M	5.0(4)	2.836(6)	0.008(1)	0.7(5)	1.6
where M is Ag or Pd.					

Figure 5.5(a) shows Pd L_3-edge XANES measurements for as-prepared and activated carbon-supported bimetallic samples. The L_3-edge Pd XANES white line is sensitive to 4d vacancies in Pd and a positive shift in the white line after calcination at 450 °C suggests a small increase in oxidation state of Pd.[41] Thus the Pd L_3-edge white line is consistent with a small degree of surface oxidation of Pd to PdO_x in sample activated at 450 °C. Figure 5.5(b) shows S K-edge XANES measurements for carbon-supported samples activated at different temperatures. The peak assignments are based on values reported in the literature for sulfur-metal (S-M) and sulfur-carbon (S-C) interactions.[42] The peak around 2472 eV is characteristic of S-M interactions (where M is Ag or Pd in this case) and the S-M peak significantly loses intensity for samples activated at 450 °C to indicate the oxidative desorption of thiolate ligands off the metal surface (Figure 5.5(b)). The S-C peak still has strong intensity after calcination of the sample at 450 °C which suggests that although thiols are being removed from the metal surfaces, significant disulfide and/or sulfonate species still exist on the surface.[42]

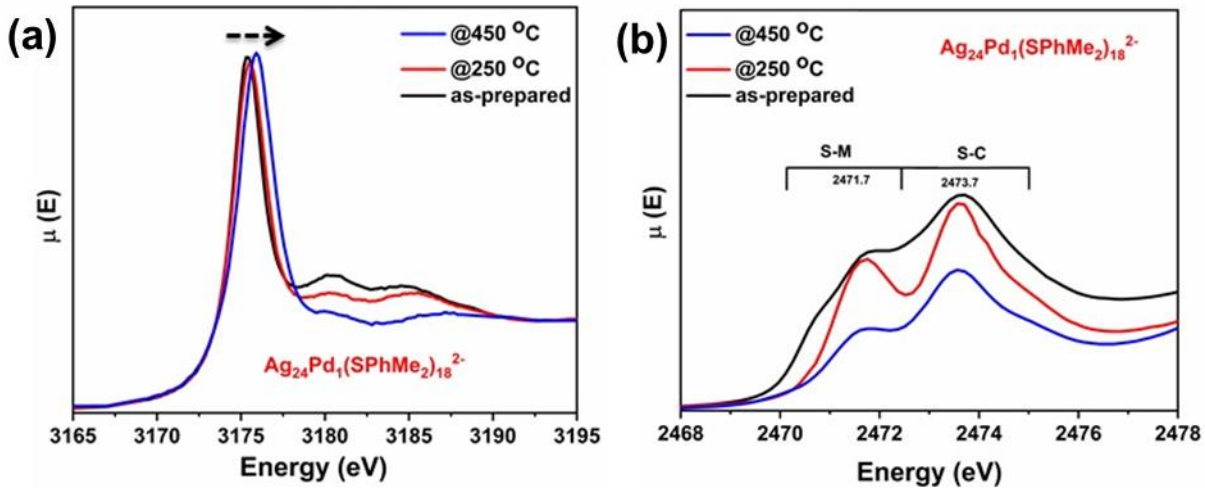

Figure 5.5. (a) Pd L_3-edge EXAFS, and (b) S K-edge XANES spectra of as-prepared and activated carbon-supported $Ag_{24}Pd_1(SPhMe_2)_{18}^{2-}$ bimetallic cluster samples.

Selective hydrogenation of the carbon-carbon triple bonds of alkynols is an essential chemical reaction for the production of fine chemicals.[43-46] Carbon-supported Ag_{25} and $Ag_{24}Pd_1$ clusters were evaluated as heterogeneous catalysts for the selective hydrogenation of 2-methyl-3-butyn-2-ol (MBY) and 3-hexyn-1-ol (HY) as model examples of internal and terminal alkynol substrates. Pd-only catalysts have intrinsically poor selectivity for the hydrogenation of alkynes to alkenes, as they tend to give the alkanes; double hydrogenation products.[24,47-49] Many research groups, including ours, have shown that the incomplete hydrogenation of alkynes to alkenes can be achieved via suppression of Pd by alloying with other metals, including Ag.[25,28,32,33,47-50] The use of Ag-only catalysts for hydrogenation reactions is less common and a certain level of activity can be seen under optimized reaction conditions.[51-53] Considering the three-phase nature of hydrogenation of liquid alkynes over solid catalysts, the choice of solvent and stirring speed were considered as two important parameters to be optimized to address possible mass transfer limitations in this reaction. The MBY hydrogenation reaction was carried out with ethanol as solvent over carbon-supported Ag catalysts at different stirring speeds, ranging from 200 rpm to 1600 rpm. Figure 5.6(a) shows the results indicating there was no mass transfer limitation at high stirring speeds, and a maximum 15.7% MBY conversion is attained at a stirring speed of 1400 rpm, and thus subsequent reactions were carried out at this stirring rate. Note that conditions were chosen to ensure that only moderate yields were seen for the Ag only system as it was anticipated that $Ag_{24}Pd_1$ systems would have higher activities (see below). Figure 5.6(b) presents the solvent

effect on MBY conversion. The order of MBY conversion in the studied solvents is acetone < water < acetonitrile < hexane < methanol < ethanol, but the trend cannot be explained with a particular solvent property (Table 5.2). Others have shown that solvents affect the enthalpy of hydrogen adsorption on the catalyst surface to give differences in catalyst performance for MBY hydrogenation reactions,[45,54] and that a combination of factors like hydrogen solubility and solvent properties, such as polarity, dipole moment, and dielectric constant, affect solvent influence on hydrogenation reactions.[45,55] Hydrogenation reactions over different catalysts were performed at a stirring speed of 1400 rpm and using ethanol as a solvent.

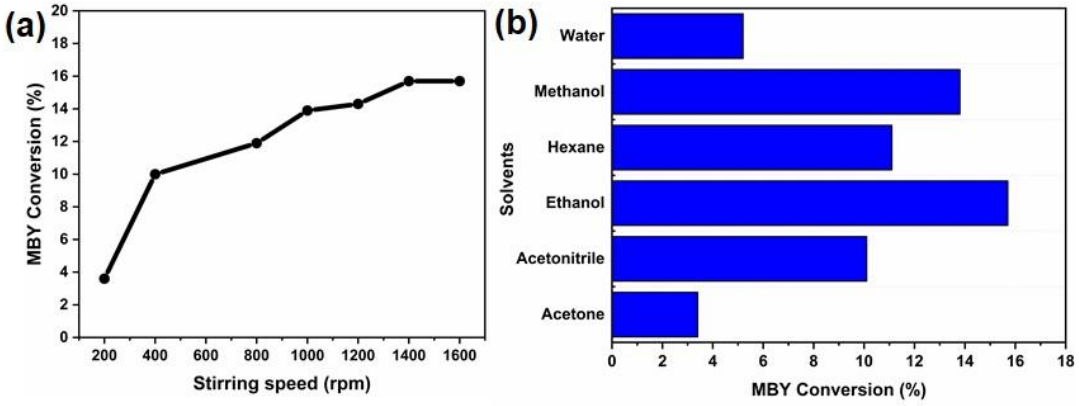

Figure 5.6. Effect of (a) stirring speed (in ethanol) and (b) solvent on catalytic activity of carbon-supported $Ag_{25}(SPhMe_2)_{18}^-$ catalysts for the hydrogenation reaction of MBY.

Table 5.3. Solvent parameters for solvents used for hydrogenation reactions of MBY with carbon-supported $Ag_{25}(SPhMe_2)_{18}^-$ catalysts.

Solvent	Dipole moment (D)	Dielectric constant	Relative polarity	MBY Conversion (%)
Acetone	2.85	21.0	0.355	3.4
Acetonitrile	3.50	37.5	0.460	10.1
Ethanol	1.70	24.0	0.654	15.7
Hexane	0	1.9	0.009	11.1
Methanol	1.60	33.0	0.762	13.8
Water	1.85	80.1	1.000	5.2

Table 5.4 presents the catalytic performances of studied catalysts in the selective hydrogenation of a terminal alkynol (MBY) and an internal alkynol (HY) to their respective alkenols. There was no measurable substrate conversion in the reactions carried out in the absence of catalyst. The intact $Ag_{25}(SR)_{18}^-$ catalyst has 15.7 % MBY conversion with 85.0 % MBE selectivity and there is no significant change in the catalytic performance after calcination at 250 °C, which indicates that the presence of the thiolate ligand has no significant effect on the Ag-only catalyst performance. The intact bimetallic $Ag_{24}Pd_1(SR)_{18}^{2-}$ catalyst gave 34.2 % MBY conversion with 96.2% MBE selectivity. The superior catalytic performance is likely due to both electronic interactions between Ag and Pd and the presence of single-atom Pd species.[30] The activated $Ag_{24}Pd_1$@250 °C catalyst showed similar activity to the intact clusters, albeit with a slightly lower MBE selectivity of 91.5%. This contrasts with the $Ag_{24}Pd_1$@450 °C catalyst which showed significantly lower MBE selectivity (73.4%). This is consistent with EXAFS data which clearly shows that there is a loss of single-atom Pd character for the $Ag_{24}Pd_1$@450 °C catalyst sample (Figure 5.3(b) and Table 5.2). This shows that the presence of protecting thiolate ligands (via residual Pd-thiolate bonds) on the $Ag_{24}Pd_1$ catalyst hinders the over-hydrogenation of MBY and allows improved MBE selectivity. Others have shown that the addition of sulfur-containing additives to reaction mixture can improve MBE selectivity over Pd catalyst.[56,57] Nikoshvili *et al.* reported 98.7% MBE selectivity at 95% MBY conversion in ethanol (T = 40 °C, P = 3 bar) over a Pd catalyst supported on hypercrosslinked polystyrene.[45] Others have also noted that the presence of Ag on Pd surfaces suppresses the over-hydrogenation of alkynes like acetylene, acrolein, and 1-octyne.[30-32,49]

The catalysts were also tested for the hydrogenation of another alkynol substrate, 3-hexyn-1-ol (HY). The HY substrate has an internal triple bond, and the selective hydrogenation of this substrate enables the evaluation of both chemoselectivity and stereoselectivity of catalysts. Similar activity and selectivity trends were observed for the Ag_{25} and $Ag_{24}Pd_1$ catalysts in the hydrogenation of 3-hexyn-1-ol (HY), albeit with slightly lower selectivity to the alkenol product. The highest selectivity towards Z-HE was seen for intact $Ag_{24}Pd_1$ (80.3%) and $Ag_{24}Pd_1$@250 °C systems (78.5%). Again, a decrease in selectivity was seen for the $Ag_{24}Pd_1$@450 °C catalyst. The stereoselectivity to the Z-3-hexen-1-ol (Z-HE) product was ≥ 80% for all catalysts. This is consistent with results in the literature which indicate that Z-isomers are typically commonly obtained products over solid catalysts like Pd metal due to steric constraints.[33,46,58-60] The

monometallic Pd (1% wt Pd/Al_2O_3) catalyst shows poor selectivity for both substrates due to over-hydrogenation to alkanols compared to other catalysts tested under the same conditions. Finally, a recyclability study was performed, and the selected bimetallic catalysts showed similar activity and selectivity over three cycles (Table 5.5).

Table 5.4. Catalytic performance of carbon-supported metal clusters catalysts in hydrogenation reactions of MBY and HY alkynols.

Catalyst	2-Methyl-3-butyn-2-ol (MBY)		3-Hexyn-1-ol (HY)		
	MBY Conversion (%)	**MBE Selectivity (%)**	**HY Conversion (%)**	**Z-HE Chemo-selectivity (%)**	**Z-HE Stereo-selectivity (%)**
$Ag_{25}(SR)_{18}$	15.7	85.0	27.5	64.4	84.1
Ag_{25}@250 ºC	15.5	84.7	30.5	63.6	84.7
$Ag_{24}Pd_1(SR)_{18}$	34.2	96.2	44.2	80.3	85.0
$Ag_{24}Pd_1$@250 ºC	35.6	91.5	42.7	78.5	87.4
$Ag_{24}Pd_1$@450 ºC	37.8	73.4	40.0	64.0	84.2
Pd	100	0	99.5	0.1	20.0

Reaction conditions: Alkynol (2.0 mmol), EtOH (5.0 mL), catalyst (25 mg) in a flask charged with H_2(g), stirring speed (1400 rpm), reaction temperature of (25 °C), reaction time (3 h). Ratio of substrate to metal is 500:1. The Pd sample is s commercial 1% wt Pd/Al_2O_3 catalyst.

Table 5.5. Recyclability tests of selected catalysts in hydrogenation reactions of terminal and internal alkynes.

Catalyst	Cycle	2-Methyl-3-butyn-2-ol (MBY)		3-Hexyn-1-ol (HY)		
		MBY Conversion (%)	MBE Selectivity (%)	HY Conversion (%)	Z-HE Chemo-selectivity (%)	Z-HE Stereo-selectivity (%)
$Ag_{24}Pd_1$	First	34.2	96.2	44.2	80.3	85.0
	Second	33.9	96.8	42.1	82.6	86.6
	Third	34.0	95.7	42.8	82.1	86.1
$Ag_{24}Pd_1$ @250 °C	First	35.6	91.5	42.7	78.5	87.4
	Second	33.8	92.4	41.3	77.9	86.5
	Third	34.2	91.1	40.0	78.2	85.3
Reaction conditions: Alkynol (2.0 mmol), EtOH (5.0 mL), catalyst (25 mg) in a flask charged with H_2(g), stirring speed (1400 rpm), reaction temperature of (25 °C), reaction time (3 h). Ratio of substrate to metal is 500:1.						

5.4 Conclusions

Atom-precise $Ag_{25}(SR)_{18}^-$ and $Ag_{24}Pd_1(SR)_{18}^{2-}$ bimetallic clusters were synthesized and examined as selective hydrogenation catalysts for alkynols. Element-specific X-ray spectroscopy results indicated that the single Pd dopant atom in $Ag_{24}Pd_1(SR)_{18}^{2-}$ bimetallic clusters is located in the thiolate environment and thus is more accessible for catalysis. $Ag_{24}Pd_1(SR)_{18}^{2-}$ bimetallic clusters exhibited better thermal stability (upon calcination at 250 °C) and catalytic activity compared to $Ag_{25}(SR)_{18}^-$ monometallic clusters on carbon supports. Atom-precise $Ag_{24}Pd_1(SR)_{18}^{2-}$ bimetallic clusters activated on carbon supports at 450 °C showed significant sintering and reduced activity and selectivity compared to catalysts activated at milder 250 °C calcination conditions. The atom-precise $Ag_{24}Pd_1(SR)_{18}^{2-}$ bimetallic clusters on carbon supports are selective for the hydrogenation of both terminal and internal alkynols to alkenols, and the presence of residual

protecting thiolate ligands improved the performance of the catalysts for the selective hydrogenation of the alkynol substrates to alkenols.

5.5 References

1. Y. Zhu, H. Qian, R. Jin. An Atomic-Level Strategy for Unraveling Gold Nanocatalysis from the Perspective of $Au_n(SR)_m$ Nanoclusters, *Chem. Eur. J.* 2010, **16**, 11455-11462.

2. A. Shivhare, S.J. Ambrose, H. Zhang, R.W. Purves, R.W.J. Scott. Stable and Recyclable Au_{25} Clusters for The Reduction of 4-Nitrophenol, *Chem. Commun.* 2013, **49**, 276-278.

3. R. Jin, C. Zeng, M. Zhou, Y. Chen. Atomically Precise Colloidal Metal Nanoclusters and Nanoparticles: Fundamentals and Opportunities, *Chem. Rev.* 2016, **116**, 10346-10413.

4. A. Ghosh, O.F. Mohammed, O.M. Bakr. Atomic-Level Doping of Metal Clusters, *Acc. Chem. Res.* 2018, **51**, 3094-3103.

5. L. Liu, A. Corma. Metal Catalysts for Heterogeneous Catalysis: From Single Atoms to Nanoclusters and Nanoparticles, *Chem. Rev.* 2018, **118**, 4981-5079.

6. J. Zeng, Q. Zhang, J. Chen, Y. Xia. A Comparison Study of the Catalytic Properties of Au-Based Nanocages, Nanoboxes, and Nanoparticles, *Nano Lett.* 2010, **10**, 30-35.

7. G. Yue, S. Su, N. Li, M. Shuai, X. Lai, D. Astruc, P. Zhao. Gold Nanoparticles as Sensors in the Colorimetric and Fluorescence Detection of Chemical Warfare Agents, *Coord. Chem. Rev.* 2016, **311**, 75-84.

8. X. Kang, H. Chong, M. Zhu. $Au_{25}(SR)_{18}$: The Captain of the Great Nanocluster Ship, *Nanoscale* 2018, **10**, 10758-10834.

9. V. Sudheeshkumar, K.O. Sulaiman, R.W.J. Scott. Activation of Atom-Precise Clusters for Catalysis, *Nanoscale Adv.* 2020, **2**, 55-69.

10. Q. Zhang, J. Xie, J. Liang, J.Y. Lee. Synthesis of Monodisperse Ag-Au Alloy Nanoparticles with Independently Tunable Morphology, Composition, Size, and Surface Chemistry and Their 3-D Superlattices, *Adv. Funct. Mater.* 2009, **19**, 1387-1398.

11. X. Yuan, X. Dou, K. Zheng, J. Xie. Recent Advances in the Synthesis and Applications of Ultrasmall Bimetallic Nanoclusters, *Part. Part. Syst. Charact.* 2015, **32,** 613-629.

12. J. Yan, H. Su, H. Yang, S. Malola, S. Lin, H. Häkkinen, N. Zheng. Total Structure and Electronic Structure Analysis of Doped Thiolated Silver $[MAg_{24}(SR)_{18}]^{2-}$ (M = Pd, Pt) Clusters, *J. Am. Chem. Soc.* 2015, **137**, 11880-11883.

13. M.A. Tofanelli, T.W. Ni, B.D. Phillips, C.J. Ackerson. Crystal Structure of the $PdAu_{24}(SR)_{18}^{0}$ Superatom, *Inorg. Chem.* 2016, **55**, 999-1001.

14. C. Yao, Y.-j. Lin, J. Yuan, L. Liao, M. Zhu, L.-h. Weng, J. Yang, Z. Wu. Mono-cadmium vs Mono-mercury Doping of Au_{25} Nanoclusters, *J. Am. Chem. Soc.* 2015, **137**, 15350-15353.

15. Y. Liu, X. Chai, X. Cai, M. Chen, R. Jin, W. Ding, Y. Zhu. Central Doping of a Foreign Atom into the Silver Cluster for Catalytic Conversion of CO_2 toward C-C Bond Formation, *Angew. Chem. Int. Ed.* 2018, **57**, 9775-9779.

16. Y. Negishi, W. Kurashige, Y. Niihori, T. Iwasa, K. Nobusada. Isolation, Structure, and Stability of a Dodecanethiolate-Protected Pd_1Au_{24} Cluster, *Phys. Chem. Chem. Phys.* 2010, **12**, 6219-6225.

17. H. Qian, E. Barry, Y. Zhu, R. Jin. Doping 25-Atom and 38-Atom Gold Nanoclusters with Palladium, *Acta Phys.-Chim. Sin.* 2011, **27**, 513-519.

18. H. Qian, D-e. Jiang, G. Li, C. Gayathri, A. Das, R.R. Gil, R. Jin. Monoplatinum Doping of Gold Nanoclusters and Catalytic Application, *J. Am. Chem. Soc.* 2012, **134**, 16159-16162.

19. S. Xie, H. Tsunoyama, W. Kurashige, Y. Negishi, T. Tsukuda. Enhancement in Aerobic Alcohol Oxidation Catalysis of Au_{25} Clusters by Single Pd Atom Doping, *ACS Catal.* 2012, **2**, 1519-1523.

20. C. Garcia, V. Truttmann, I. Lopez, T. Haunold, C. Marini, C. Rameshan, E. Pittenauer, P. Kregsamer, K. Dobrezberger, M. Stöger-Pollach, N. Barrabés, G. Rupprechter. Dynamics of Pd Dopant Atoms inside Au Nanoclusters during Catalytic CO Oxidation, *J. Phys. Chem. C* 2020, **124**, 23626-23636.

21. M.S. Bootharaju, C.P. Joshi, M.R. Parida, O.F. Mohammed, O.M. Bakr, Angew. Templated Atom-Precise Galvanic Synthesis and Structure Elucidation of a $[Ag_{24}Au(SR)_{18}]^-$ Nanocluster, *Angew. Chem. Int. Ed.* 2016, **55**, 922-926.

22. T. Yoskamtorn, S. Yamazoe, R. Takahata, J.I. Nishigaki, A. Thivasasith, J. Limtrakul, T. Tsukuda. Thiolate-Mediated Selectivity Control in Aerobic Alcohol Oxidation by Porous Carbon-Supported Au_{25} Clusters, *ACS Catal.* 2014, **4**, 3696-3700.

23. G. Vilé, D. Baudouin, I. Remediakis, C. Copéret, N. López, J. Pérez-Ramírez. Silver Nanoparticles for Olefin Production: New Insights into the Mechanistic Description of Propyne Hydrogenation, *ChemCatChem*, 2013, **5**, 3750-3759.

24. H. Zhou, X. Yang, L. Li, X. Liu, Y. Huang, X. Pan, A. Wang, J. Li, T. Zhang. PdZn Intermetallic Nanostructure with Pd-Zn-Pd Ensembles for Highly Active and Chemoselective Semi-Hydrogenation of Acetylene, *ACS Catal.* 2016, **6**, 1054-1061.

25. P.A. Sheth, M. Neurock, C.M. Smith. First-Principles Analysis of the Effects of Alloying Pd with Ag for the Catalytic Hydrogenation of Acetylene-Ethylene Mixtures, *J. Phys. Chem. B*, 2005, **109**, 12449-12466.

26. N.A. Khan, S. Shaikhutdinov, H.-J. Freund. Acetylene and Ethylene Hydrogenation on Alumina Supported Pd-Ag Model Catalysts, *Catal. Lett.* 2006, **108**, 159-164.

27. S. González, K.M. Neyman, S. Shaikhutdinov, H.J. Freund, F. Illas. On the Promoting Role of Ag in Selective Hydrogenation Reactions over Pd-Ag Bimetallic Catalysts: A Theoretical Study, *J. Phys. Chem. C.* 2007, **111**, 6852-6856.

28. C.F. Calver, P. Dash, R.W.J. Scott. Selective Hydrogenations with AgPd Catalysts Prepared by Galvanic Exchange Reactions, *ChemCatChem*, 2011, **3**, 695-697.

29. P.T. Witte, P.H. Berben, S. Boland, E.H. Boymans, D. Vogt, J.W. Geus, J.G. Donkervoort. BASF NanoSelect™ Technology: Innovative Supported Pd- And Pt-Based Catalysts for Selective Hydrogenation Reactions, *Top. Catal.* 2012, **55**, 505-511.

30. G.X. Pei, X.Y. Liu, A. Wang, A.F. Lee, M.A. Isaacs, L. Li, X. Pan, X. Yang, X. Wang, Z. Tai, K. Wilson, T. Zhang. Ag Alloyed Pd Single-Atom Catalysts for Efficient Selective Hydrogenation of Acetylene to Ethylene in Excess Ethylene, *ACS Catal.* 2015, **5**, 3717-3725.

31. P. Aich, H. Wei, B. Basan, A.J. Kropf, N.M. Schweitzer, C.L. Marshall, J.T. Miller, R. Meyer. Single-Atom Alloy Pd-Ag Catalyst for Selective Hydrogenation of Acrolein, *J. Phys. Chem. C* 2015, **119**, 18140-18148.

32. T. Mitsudome, T. Urayama, K. Yamazaki, Y. Maehara, J. Yamasaki, K. Gohara, Z. Maeno, T. Mizugaki, K. Jitsukawa, K. Kaneda. Design of Core-Pd/Shell-Ag Nanocomposite Catalyst for Selective Semihydrogenation of Alkynes, *ACS Catal.*, 2016, **6**, 666-670.

33. V. Sudheeshkumar, M. Alyari, M. Gangishetty, R.W.J. Scott. Galvanic Synthesis of AgPd Bimetallic Catalysts from Ag Clusters Dispersed in a Silica Matrix, *Catal. Sci. Technol.* 2020, **10**, 8421-8428.

34. C.P. Joshi, M.S. Bootharaju, M.J. Alhilaly, O.M. Bakr. $[Ag_{25}(SR)_{18}]^-$: The "Golden" Silver Nanoparticle, J. *Am. Chem. Soc.* 2015, **137**, 11578-11581.

35. Z. Chen, A.G. Walsh, X. Wei, M. Zhu, P. Zhang. Site-Specific Electronic Properties of $[Ag_{25}(SR)_{18}]^-$ Nanoclusters by X-Ray Spectroscopy, *Small* 2021, **17**, 2005162.

36. G. Corthey, A.A. Rubert, A.L. Picone, G. Casillas, L.J. Giovanetti, J.M. Ramallo-López, E. Zelaya, G.A. Benitez, F.G. Requejo, M. José-Yacamán, R.C. Salvarezza, M.H. Fonticelli. New Insights into the Chemistry of Thiolate-Protected Palladium Nanoparticles, *J. Phys. Chem. C* 2012, **116**, 9830-9837.

37. M. Navlani-García, K. Mori, A. Nozaki, Y. Kuwahara, H. Yamashita. Screening of Carbon-Supported PdAg Nanoparticles in the Hydrogen Production from Formic Acid, *Ind. Eng. Chem. Res.* 2016, **55**, 7612-7620.

38. P. Verma, Y. Kuwahara, K. Mori, H. Yamashita. Synthesis and Characterization of a Pd/Ag Bimetallic Nanocatalyst on SBA-15 Mesoporous Silica as a Plasmonic Catalyst, *J. Mater. Chem. A.* 2015, **3**, 18889-18897.

39. C. Hu, X. Mu, J. Fan, H. Ma, X. Zhao, G. Chen, Z. Zhou, N. Zheng. Interfacial Effects in PdAg Bimetallic Nanosheets for Selective Dehydrogenation of Formic Acid, *ChemNanoMat* 2016, **2**, 28-32.

40. B.S.A. Gedara, M. Muir, A. Islam, D. Liu, M. Trenary. Room Temperature Migration of Ag Atoms to Cover Pd Islands on Ag(111), *J. Phys. Chem. C* 2021, **125**, 27828-27836.

41. Z. Zhang, A.G. Walsh, P. Zhang. Dynamic Structure of Metal Nanoclusters from Synchrotron X-ray Spectroscopy, *J. Phys. Chem. C* 2021, **125**, 5982-5994.

42. B. Zhang, A. Sels, G. Salassa, S. Pollitt, V. Truttmann, C. Rameshan, J. Llorca, W. Olszewski, G. Rupprechter, T. Bürgi, N. Barrabés. Ligand Migration from Cluster to Support: A Crucial Factor for Catalysis by Thiolate-protected Gold Clusters, *ChemCatChem.* 2018, **10**, 5372-5376.

43. F. Roessler. Catalytic Hydrogenation in the Liquid Phase, *Chimia* 2003, **57**, 791-798.

44. B. Chen, U. Dingerdissen, J.G.E. Krauter, H.G.J. Lansink Rotgerink, K. Möbus, D.J. Ostgard, P. Panster, T.H. Riermeier, S. Seebald, T. Tacke, H.Trauthwein. New Developments in Hydrogenation Catalysis Particularly in Synthesis of Fine and Intermediate Chemicals, *Appl. Catal. A* 2005, **280**, 17-46.

45. L. Nikoshvili, E. Shimanskaya, A. Bykov, I. Yuranov, L. Kiwi-Minsker, E. Sulman. Selective Hydrogenation of 2-Methyl-3-butyn-2-ol over Pd-Nanoparticles Stabilized in Hypercrosslinked Polystyrene: Solvent Effect, *Catal. Today* 2015, **241**, 179-188.

46. J.A. Delgado, O. Benkirane, C. Claver, D. Curulla-Ferré, C. Godard. Advances in the Preparation of Highly Selective Nanocatalysts for the Semi-Hydrogenation of Alkynes Using Colloidal Approaches, *Dalton Trans.* 2017, **46**, 12381-12403.

47. D.V. Glyzdova, A.A. Vedyagin, A.M. Tsapina, V.V. Kaichev, A.L. Trigub, M.V. Trenikhin, D.A. Shlyapin, P.G. Tsyrulnikov, A.V. Lavrenov. A Study on Structural Features of Bimetallic Pd-M/C (M: Zn, Ga, Ag) Catalysts for Liquid-Phase Selective Hydrogenation of Acetylene, *Appl. Catal. A* 2018, **563**, 18-27.

48. Z-J. Zhao, J. Zhao, X. Chang, S. Zha, L. Zeng, J. Gong. Competition of C-C Bond Formation and C-H Bond Formation for Acetylene Hydrogenation on Transition Metals: A Density Functional Theory Study, *AIChE J.* 2019, **65**, 1059-1066.

49. M.R. Ball, K.R. Rivera-Dones, E.B. Gilcher, S.F. Ausman, C.W. Hullfish, E.A. Lebrón, J.A. Dumesic. AgPd and CuPd Catalysts for Selective Hydrogenation of Acetylene, *ACS Catal.* 2020, **10**, 8567-8581.

50. E.V. Rebrov, E.A. Klinger, A. Berenguer-Murcia, E.M. Sulman, J.C. Schouten. Selective Hydrogenation of 2-Methyl-3-butyne-2-ol in a Wall-Coated Capillary Microreactor with a $Pd_{25}Zn_{75}/TiO_2$ Catalyst, *Org. Process Res. Dev.* 2009, **13**, 991-998.

51. M. Bron, D. Teschner, A. Knop-Gericke, F.C. Jentoft, J. Kröhnert, J. Hohmeyer, C. Volckmar, B. Steinhauer, R. Schlögl, P. Claus. Silver As Acrolein Hydrogenation Catalyst: Intricate Effects of Catalyst Nature and Reactant Partial Pressures, *Phys. Chem. Chem. Phys.* 2007, **9**, 3559-3569.

52. A. Andoni, R.A. van Santen. Propenal Hydrogenation on Silver Surface- A Theoretical Approach, *Chem. Eng. Trans*. 2013, **34**, 19-24.

53. S. Wang, H. Huang, S. Tsareva, C. Bruneau, C. Fischmeister. Silver-Catalyzed Hydrogenation of Ketones under Mild Conditions. *Adv. Synth. Catal.* 2019, **361**, 786-790.

54. G.D. Zakumbaeva, L.A. Beketaeva, L.B. Shapovalova. Influence of Ruthenium Dispersity on its Adsorption and Catalytic Properties, *React. Kinet. Catal. Lett.* 1978, **8**, 235-240.

55. P.A. Rautanen, J.R. Aittamaa, A.O.I. Krause. Solvent Effect in Liquid-Phase Hydrogenation of Toluene, *Ind. Eng. Chem. Res.* 2000, **39**, 4032-4039.

56. M. Crespo-Quesada, M. Grasemann, N. Semagina, A. Renken, L. Kiwi-Minsker. Kinetics of the Solvent-Free Hydrogenation of 2-Methyl-3-butyn-2-ol over a Structured Pd-Based Catalyst, *Catal. Today* 2009, **147**, 247-254.

57. X. Zhao, L. Zhou, W. Zhang, C. Hu, L. Dai, L. Ren, B. Wu, G. Fu, N. Zheng, Thiol Treatment Creates Selective Palladium Catalysts for Semihydrogenation of Internal Alkynes, *Chem.* 2018, **4**, 1080-1091.

58. T. Montsch, M. Heuchel, Y. Traa, E. Klemm, C. Stubenrauch. Selective Hydrogenation of 3-Hexyn-1-ol with Pd Nanoparticles Synthesized via Microemulsions, *Appl. Catal. A: Gen.* 2017, **539**, 19-28.

59. C.W.A. Chan, A. Mahadi, M. M.-J. Li, E.C. Corbos, C. Tang, G. Jones, W.C.H. Kuo, J. Cookson, C.M. Brown, P.T. Bishop, S.C.E. Tsang. Interstitial Modification of Palladium Nanoparticles with Boron Atoms as a Green Catalyst for Selective Hydrogenation, *Nat. Commun.* 2014, **5**, 5787.

60. S. Paganelli, A. Angi, N. Pajer, O. Piccolo. A Smart Heterogeneous Catalyst for Efficient Chemo- and Stereoselective Hydrogenation of 3-Hexyn-1-ol, *Catalysts* 2021, **11**, 14.

Chapter 6

Taking A Different Road: Following Ag_{25} and Au_{25} Cluster Activation via *In Situ* Differential Pair Distribution Function Analysis

In the previous chapters, catalyst materials were mostly characterized using microscopy, X-ray photoelectron spectroscopy and X-ray absorption spectroscopy. X-ray diffraction is also an excellent method of characterizing nanomaterials. Although atom-precise metal clusters are typically too small to produce Bragg peaks, total scattering measurements with pair distribution function (PDF) analysis can be done. This chapter examines the suitability of PDF analysis towards the characterization of atom-precise metal clusters, particularly in gaining insights into their structural changes during thermal activation processes. Both TEM and *in situ* total scattering/PDF analyses showed that Ag clusters behaved differently than Au clusters upon activation. The interatomic distances measured by differential PDF (dPDF) analysis agreed with those measured by single-crystal crystallographic and EXAFS methods. Furthermore, the dPDF analysis clearly showed the structural transformation of the atom-precise clusters to fcc-like structures upon thermal activation at intermediate temperatures, while the Ag system began to fracture again at higher temperatures.

This chapter is a manuscript that is in preparation for publication. I wrote the complete first draft of the manuscript and this was then edited with the guidance of Prof. Robert W.J. Scott. Dr. Graham King assisted with the experimental set up for total scattering measurements at the BXDS-HEW beamline at the Canadian Light Source, Saskatoon, Canada. The PDF data refinement and modelling was performed in collaboration with Muhammad Zubair and Dr. Nicholas Bedford at the University of New South Wales, Sydney, Australia.

6.1 Introduction

The structural evolution and catalytic reactivity of atom-precise, ligand-protected coinage metal clusters are of great research interest.[1,2] Owing to their definite structure and monodispersity, ultrasmall metal clusters are excellent model catalysts that can enable insights into structure-performance correlations at the atomic scale.[3] Among ligand-protected metal clusters, atom-precise thiolate-protected metal clusters are widely studied due to strong metal-sulfur interactions that enable good stability in solution, simple synthesis, and controlled cluster compositions.[4] With its early discovery, facile preparation, excellent stability, and interesting catalytic properties, $Au_{25}(SR)_{18}$ is one of the most studied atom-precise metal clusters.[5] Meanwhile, other twenty-five metal atom clusters have also been reported for coinage metals like Ag and Cu,[6,7] but only the $Ag_{25}(SR)_{18}$ cluster system shows similar atomic arrangements and ligand counts to those of $Au_{25}(SR)_{18}$ clusters as revealed by crystallographic methods. Several groups including ours have reported the catalytic performance of $Au_{25}(SR)_{18}^-$ and $Ag_{25}(SR)_{18}^-$ on various supports like carbon and metal oxides (Chapter 2).[8-14] Accessing the optimum catalytic potential of these ligand-protected noble metal clusters often necessitates partial or complete removal of the ligands, *i.e.* activation of catalysts, to enable adequate substrate access to the active site of the catalysts.[11,15,16]

Thermal activation is one of the most common and simplest approaches to activate atom-precise clusters, and it involves the oxidation or decomposition of ligands from the cluster surface by thermal calcination in air or inert atmospheres.[14,16] It is important to be able to follow the growth of the resulting activated clusters by sintering upon such thermal treatments. Both our group and others have shown growth in cluster size upon thermal activation of Au clusters on supports, with the eventual particle size depending on the type of support, activation temperature, and duration of heating, and there are continuous efforts to achieve stability of these clusters against sintering.[10,13,14,16-18] Shivhare *et al.* examined the activation of phenylethanethiolate- and hexanethiolate-protected $Au_{25}(SR)_{18}$ clusters on carbon supports, and EXAFS Au L_3-edge analyses clearly showed that thiolate ligand removal began at temperatures as low as 125 ˚C and was nearly complete at 250 ˚C.[10] EXAFS modelling and TEM images showed that average particle sizes increased due to sintering as the calcination temperature increased. Yan and coworkers studied the activation of 6-mercaptohexanoic acid-protected $Au_{25}(SR)_{18}$ clusters on different supports by calcination under nitrogen stream at 300 ˚C for 2 h and noted significant sintering of

the clusters on many supports, though some supports such as Degussa P25 titania and hydroxyapatite supports mitigated sintering.[17] Tsukuda and colleagues observed that the activation of glutathionate-protected $Au_{25}(SR)_{18}$ clusters on hydroxyapatite supports at 300 ˚C *in vacuo* for 2 h resulted in complete removal of thiolate ligands with a slight increase in cluster size (from 1.0 ± 0.4 nm to 1.4 ± 0.6 nm).[18] Though the activation of $Au_{25}(SR)_{18}$ clusters has attracted significant research attention, thermal activation of analogous $Ag_{25}(SR)_{18}$ clusters has been less studied. Our group reported the activation of $Ag_{25}(SR)_{18}$ clusters on carbon supports for 2 h in air and observed desorption of thiolate ligands off Ag clusters surface with minimal cluster size growth at a temperature of 250 ˚C, though significant sintering was observed at 450 ˚C (Chapter 2). However, a number of research groups, including ours, have previously noted that larger Ag nanoparticles tend to fracture at higher temperatures.[19-21] Thus, examining the thermal behaviour of Ag clusters with a wider range of activation temperatures was of research interest.

The most common ways to follow the particle growth of atom-precise metal clusters upon thermal activation include high-resolution transmission electron microscopy (HRTEM) and extended X-ray absorption fine structure spectroscopy (EXAFS) measurements. Unlike HRTEM which is considered as a localized technique, EXAFS is a bulk technique and the average coordination number for a given element obtained from EXAFS data fittings can be correlated to the average particle size.[22,23] However, EXAFS studies of metal clusters predominately probe the first coordination sphere, along with the second or third to a lesser extent, thus giving somewhat limited information about the materials under study. In contrast, pair distribution function (PDF) analyses can cover length scales of ~1-200 Å, and thus provide bulk structural information not available from most other techniques.[24,25] Atomic PDF analysis is a bulk technique that enables non-element specific and long order measurements along with quick data collection.[22] Notably, PDF analysis is a total scattering technique and can be used to learn about the structures of particles which are too small to produce Bragg peaks, making it a very suitable technique for metal cluster characterization.[26] Qualitatively, particle size can be determined by observing when G(r), the probability of finding a pair of atoms separated by distance-r, tends to zero.[22,24] EXAFS and HRTEM data are still valuable complementary techniques that can provide independent constraints which can be used for the structure modeling of experimental PDF data.[27,28]

Several groups have shown the suitability of PDF analysis in the characterization of Au nanoparticles,[24,26,29-31] but this technique has yet to be extended to very small atom-precise metal clusters. Herein, we show *in situ* heating total scattering measurements of $Au_{25}(SR)_{18}^-$ clusters and $Ag_{25}(SR)_{18}^-$ clusters on alumina supports collected at the recently commissioned Brockhouse X-ray Diffraction and Scattering - High Energy Wiggler (BXDS-HEW) beamline at the Canadian Light Source (CLS). Both $Au_{25}(SR)_{18}^-$ clusters and $Ag_{25}(SR)_{18}^-$ clusters were synthesized, purified, and successfully immobilized on alumina supports without compromising their structures. Thereafter, the alumina-supported metal clusters were thermally activated in air and characterized using both *ex situ* TEM measurements and *in situ* total scattering/PDF analyses. TEM measurements on Au and Ag cluster systems complement differential PDF (dPDF) results, in which the alumina background scattering signal is subtracted from the scattering data. For the Au cluster system, dPDF measurements show that the particle size continuously increases with activation temperature, which is consistent with previous studies. Conversely, the initial growth in particle size in the Ag cluster system ceases and then decreases significantly at higher activation temperatures, which is likely due to the thermal oxidation of Ag and resulting instability of Ag oxides, which quickly break back down into smaller Ag clusters.

6.2 Experimental

6.2.1 Materials

Hydrogen tetrachloroaurate (III) trihydrate ($HAuCl_4.3H_2O$, 99.9% on a metal basis), silver nitrate ($AgNO_3$, ≥99.0%), tetraoctylammonium bromide (TOAB, 98%), 11-mercaptoundecanoic acid ($HS\text{-}(CH_2)_{10}\text{-}COOH$, 11-MUA, 95%), alumina (Al_2O_3, NIST742, pore size = 58 Å), and 100% ethanol (EtOH) were purchased from Sigma Aldrich. 2,4-Dimethylbenzenethiol (C_8H_9SH, $HSPhMe_2$, 95%) and tetraphenylphosphonium bromide (Ph_4PBr) were purchased from Alfa Aesar. Sodium borohydride ($NaBH_4$, 98%), acetic acid (≥99.7%), tetrahydrofuran (THF, high purity), dichloromethane (CH_2Cl_2, DCM), methanol (MeOH, HPLC grade), were purchased from Fisher Scientific. Milli-Q (Millipore, Bedford, MA) deionized water (18 MΩ cm) was used throughout, and all chemicals are used as received from commercial manufacturer without any further purification.

6.2.2 Synthesis and Purification of Atom-Precise, Thiolate-Protected M_{25} (M = Au or Ag) Clusters

The $Au_{25}(11\text{-MUA})_{18}$ clusters were synthesized and purified according to an established procedure.[32] In a typical synthesis, 0.609 mmol of TOAB was added to 20 mL of THF containing dissolved 0.508 mmol of $HAuCl_4.3H_2O$ and the mixture was stirred at 600 rpm until a reddish-brown solution was obtained in the reaction flask. At this point, the stirring speed was reduced to 200 rpm and a solution of 2.54 mmol of 11-MUA dissolved in 5.0 mL of THF was added dropwise. The resulting solution quickly turned colourless. Afterwards, the colourless solution was cooled in an ice bath and stirred at 1000 rpm while adding ice cold $NaBH_4$ (2.03 mmol in 2.0 mL of water) dropwise until $Au_{25}(SR)_{18}^-$ features were seen by UV-Vis absorption spectroscopy. Then, the solution was centrifuged at 6000 rpm for 2 min and the coloured supernatant solution of $Au_{25}(11\text{-MUA})_{18}$ clusters in THF was obtained. In the purification step, freshly prepared ice cold $NaBH_4$ (2.03 mmol in 2 mL of water) was again slowly added dropwise to the $Au_{25}(11\text{-MUA})_{18}$ clusters in THF, while vigorously stirring in an ice-bath, until a fine brown precipitate suspended in a colourless solution was observed. Then, centrifugation was used to obtain a brown solid that was washed twice with fresh THF. The $Au_{25}(11\text{-MUA})_{18}$ clusters were re-dissolved in water to form a brown coloured solution and re-precipitated as a brown suspension upon protonation of the carboxylate groups using few drops of dilute acetic acid (pH = ~3). The solid was then collected using centrifugation and stored in a glass vial under ambient conditions.

The $Ag_{25}(SPhMe_2)_{18}^-$ clusters were synthesized following the procedure reported in section 2.2.2.

6.2.3 Preparation of Alumina-Supported Metal Clusters (M_{25}/alumina) Samples

The isolated and purified thiolate-protected M_{25} clusters (M = Au or Ag) were immobilized onto alumina supports via the wetness impregnation method, to give a final metal loading of *ca.* 2 wt%. Typically, 2.0 mL of a THF solution of each atom-precise, ligand-protected metal cluster solution was added to 200 mg of the alumina support and stirred for 30 min, followed by complete removal of solvent under vacuum using a Schenk line apparatus. Afterwards, the alumina supported M_{25} clusters (Au_{25}/alumina or Ag_{25}/alumina) were dried in air for another 15 min. The dried samples in powder form were then packed in sample vials and used directly for *in situ* PDF

measurements. For *ex situ* measurements, as-prepared M_{25}/alumina samples were thermally calcined at 250 °C, 350 °C, 450 °C, 550 °C, and 650 °C under air flow for 2 h in a Lindberg/Blue M furnace with a ramping rate of 10 °C/min.

6.2.4 Characterization Techniques

UV-Vis absorption spectroscopy measurements and thermal gravimetric analyses (TGA) were performed as described in section 2.2.4. Transmission electron microscopy (TEM) images were collected and analyzed as described in section 3.2.3. Total scattering measurements were performed at the Brockhouse X-ray Diffraction and Scattering – High Energy Wiggler (BXDS-HEW) beamline (Energy range 20 – 94 keV; beam size 2-10 mm x ~100 μm (W x H); energy resolution 1 x 10^{-3} Δd/d; monochromator crystal Si (111); Flux 5 x 10^{9} – 2 x 10^{13}) at the Canadian Light Source (CLS). Experimental conditions were the same for all measurements and all diffraction patterns were collected in a wide-angle transmission geometry with area detectors positioned close to the sample. The Q-range was tuned for each sample to give the best balance between statistical noise and real space resolution. Total exposure times differed between different temperature measurements for a sample but were typically less than five minutes. Samples were carefully packed into a one-end-closed quartz capillary (0.8 mm in diameter) and each loaded quartz capillary was positioned between heating filaments along the beam direction (Figure 6.1).[33] Beam alignment was done to ensure that the beam hit the sample through the quartz capillary only, but not the heating filaments and/or temperature probe as these materials could contribute significantly to beam scattering. The whole set-up was monitored closely throughout the measurement using an in-house camera installed inside the beamline hutch. The temperature was monitored by a Eurotherm® temperature controller with a thermocouple as a temperature probe inserted into the capillary. Both the set and measured temperature were in close agreement with ca. 5% error at temperatures below 200 °C and ca. 2% error at higher temperatures. Diffraction patterns were collected using a Q_{max} of 24 $Å^{-1}$. Diffraction data treatment and pair distribution function (PDF) data extraction were done using PDFgetX3.[34] In analyzing the data, instrumental resolution parameters ($Q_{damping}$ and $Q_{broading}$) were calibrated using a standard crystalline Ni sample measured directly before the alumina support and alumina-supported metal cluster samples. Differential PDFs (dPDFs) of metal cluster samples were obtained by subtracting a PDF of an alumina sample at a particular temperature from the PDF of alumina-supported metal cluster

sample collected at the same temperature. Similar differential PDF measurements have been recently reported for the structural studies of adsorbates on nanomaterials.[35,36] Simulations of PDF data for Au and Ag fcc structures, as well as the modelling of experimental dPDF data were performed using PDFGui.[37]

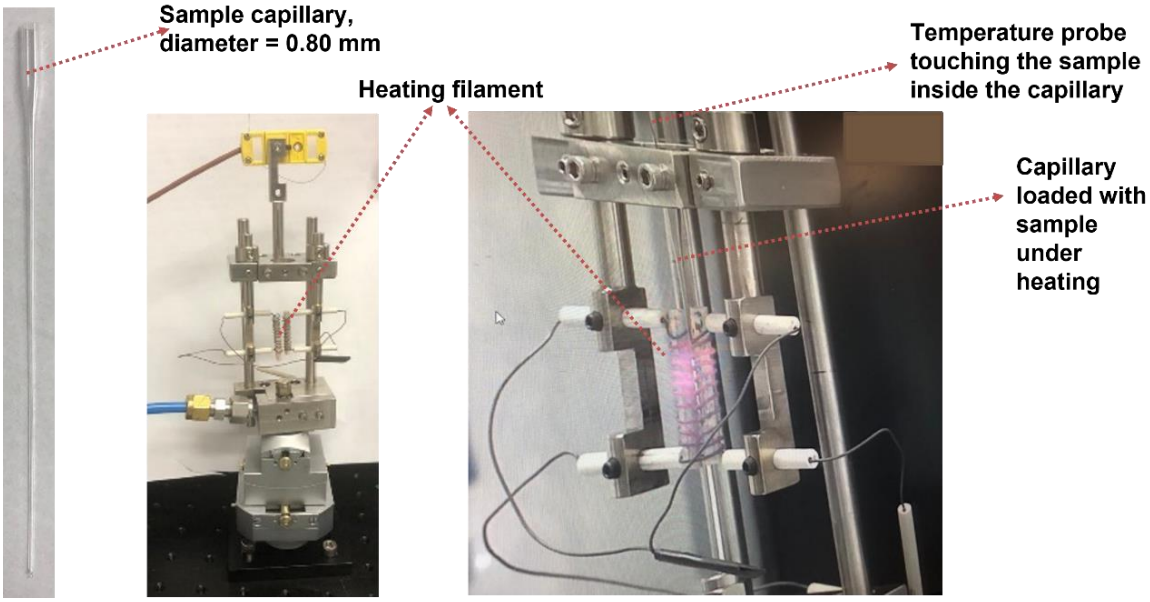

Figure 6.1. Set up for *in situ* heating at Brockhouse beamline, Canadian Light Source.

6.3 Results and Discussion

Atom-precise metal clusters have unique absorption behavior in the visible region of light due to their discrete electronic energy levels. This makes UV-Vis absorption measurements a facile technique to follow the preparation of atom-precise metal clusters in solution. Figure 6.2 shows the UV-Vis spectra of the thiolate-protected Au_{25} and Ag_{25} clusters in THF. The thiolate-protected $Au_{25}(11\text{-MUA})_{18}^{-}$ clusters show expected characteristic peaks at 398 nm, 446 nm, and 680 nm that are a clear indication of Au_{25} clusters.[32] The choice of the carboxylate-terminated thiolate ligand for the Au system allows thorough purification of the Au clusters as we observed poor solubility of the carboxylic acid-terminated clusters in water in acidic conditions as well as poor solubility of the deprotonated clusters in THF under basic conditions. Attempts to make similar acid-terminated Ag clusters were not successful, hence alkanethiolate ligands were used in preparing analogous atom-precise Ag clusters. The UV-Vis absorption spectrum of thiolate-protected Ag_{25} clusters, as presented in Figure 6.2(b), shows distinctive peaks at 334 nm, 392 nm, 490 nm, and

688 nm which indicates the presence of nearly monodisperse $Ag_{25}(SPhMe_2)_{18}^-$ clusters.[38] In both cases, the UV-Vis absorption results give clear evidence for the formation of 25-metal-atom clusters, and the lowest energy peak in each case has been ascribed to the HOMO-LUMO transition due to the M_{13} icosahedral core in the M_{25} structure (where M is Au or Ag).[38,39] We have previously performed mass spectrometry (ESI and MALDI-TOF) analyses to further bolster these assignments of $Au_{25}(11\text{-MUA})_{18}^-$ and $Ag_{25}(SPhMe_2)_{18}^-$ clusters for the Au and Ag systems, respectively.[32]

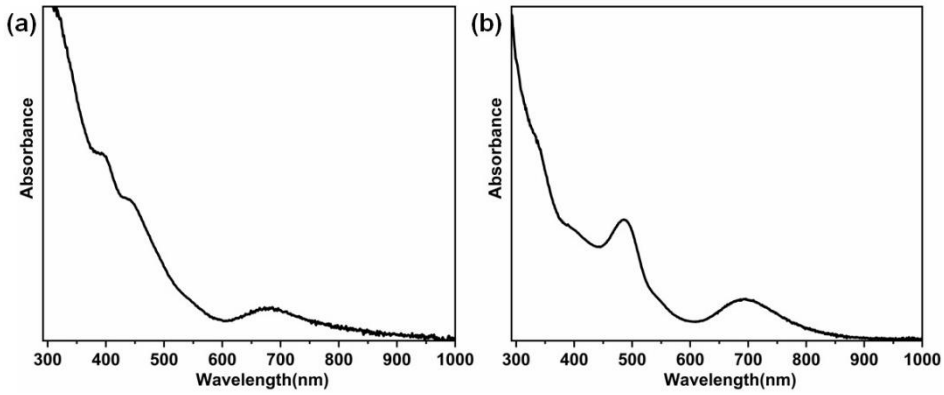

Figure 6.2. UV-Vis absorption spectra of (a) $Au_{25}(11\text{-MUA})_{18}^-$ and (b) $Ag_{25}(SPhMe_2)_{18}^-$ clusters in THF.

The purified atom-precise metal clusters were immobilized onto alumina supports for further studies. While the presence of protecting thiolate ligands on metal clusters enables the synthesis of these well-defined structures, the deprotection of metal clusters with little to no cluster growth is often considered necessary in establishing the size-dependent catalytic performance of metal clusters.[16] We employed the simplest and most studied activation approach which involves the thermal treatment of alumina-supported metal clusters samples in air. It is noteworthy here that the difference in terminal groups of the thiolate ligand is of less importance in this study as there is clear evidence in the literature that the cleavage of the metal-sulfur bond occurs in the same temperature range for atom-precise Au and Ag clusters, regardless of the terminal group on the thiolate ligand.[14,40] What is rather crucial is the structural behavior of these metal clusters, especially at relatively high temperatures when the complete deprotection (i.e. removal of thiolate ligands) has already occurred. TEM analysis is a conventional method for examining metal cluster stability against sintering. Figure 6.3 presents TEM images of the as-prepared and calcined

$Au_{25}(11\text{-MUA})_{18}^{-}/Al_2O_3$ samples at different temperatures. The average particle sizes were measured to be 1.4 ± 0.2 nm for the as-prepared $Au_{25}(11\text{-MUA})_{18}^{-}/Al_2O_3$ sample and increased to 4.9 ± 2.8 nm, 5.1 ± 3.0 nm, 7.5 ± 3.2 nm, 7.8 ± 3.0 nm, and 11.2 ± 2.1 nm for $Au_{25}(11\text{-MUA})_{18}^{-}/Al_2O_3$ samples calcined at 250 °C, 350 °C, 450 °C, 550 °C, and 650 °C, respectively. These values indicate growth of the Au clusters via sintering and growth becomes significant at high activation temperatures. The observed particle size growth with increasing calcination temperature is consistent with previous results for similar Au systems which showed measured particle sizes of 7.1 ± 6.0 nm and 11.7 ± 4.0 nm for alumina-supported Au samples calcined at 250 °C and 650 °C respectively.[41] Moreover, we have previously shown via *in situ* HRTEM studies that deprotected metal clusters migrate on supports and then agglomerate to form bigger particles.[42]

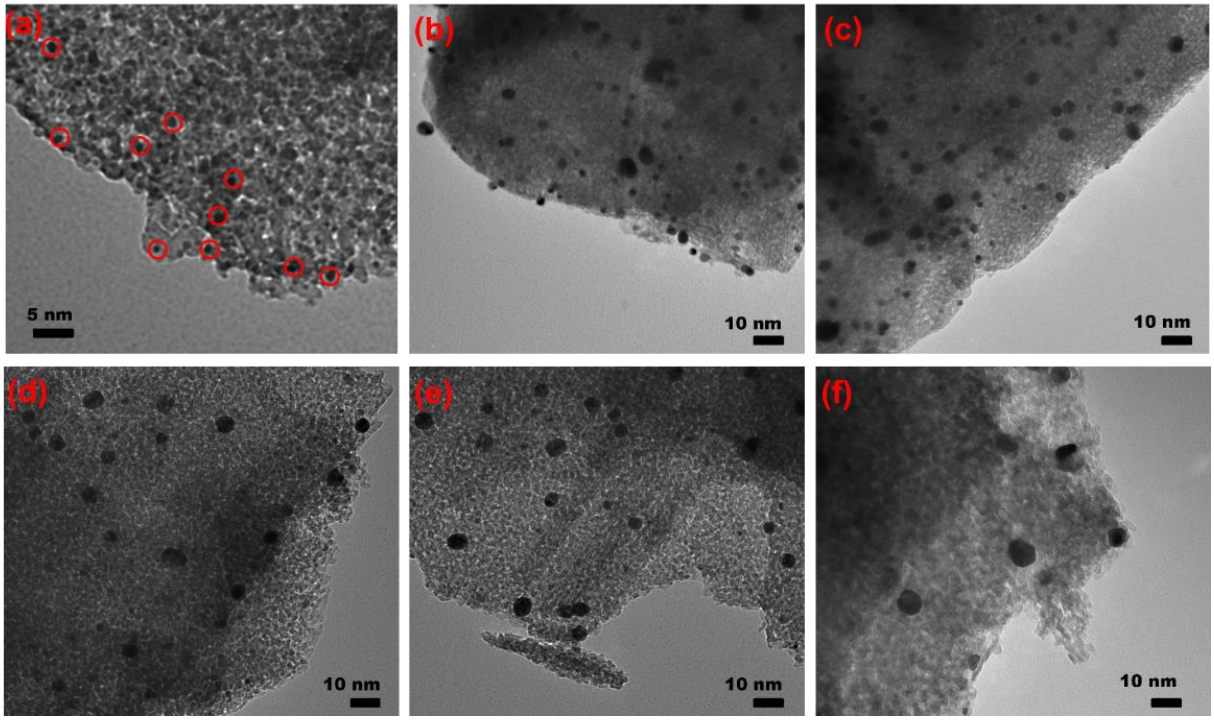

Figure 6.3. TEM images of (a) as-prepared $Au_{25}(11\text{-MUA})_{18}^{-}/Al_2O_3$; clusters are highlighted with red circles, and calcined samples at (b) 250 °C, (c) 350 °C, (d) 450 °C, (e) 550 °C, and (f) 650 °C.

Figure 6.4 presents the TEM images of as-prepared and thermally activated Ag clusters on alumina supports at different temperatures. The average particle sizes were measured to be 1.1 ± 0.3 nm for the as-prepared $Ag_{25}(SPhMe_2)_{18}^{-}/Al_2O_3$ sample and changed to 3.4 ± 1.2 nm, 3.2 ± 0.8

nm, 3.2 ± 0.4 nm, 1.5 ± 0.3 nm, and 1.3 ± 0.2 nm for $Ag_{25}(SPhMe_2)_{18}^-/Al_2O_3$ samples calcined at 250 °C, 350 °C, 450 °C, 550 °C, and 650 °C, respectively. Like the Au system, the analogous Ag system shows early growth in average particle size with increasing activation temperature up to activation temperature of 450 °C, beyond which the Ag particles then undergo thermal degradation to form Ag fragments as suggested by decrease in average particle sizes measured for Ag samples calcined at high temperatures. Further discussion on the mechanism by which this happens will be detailed below.

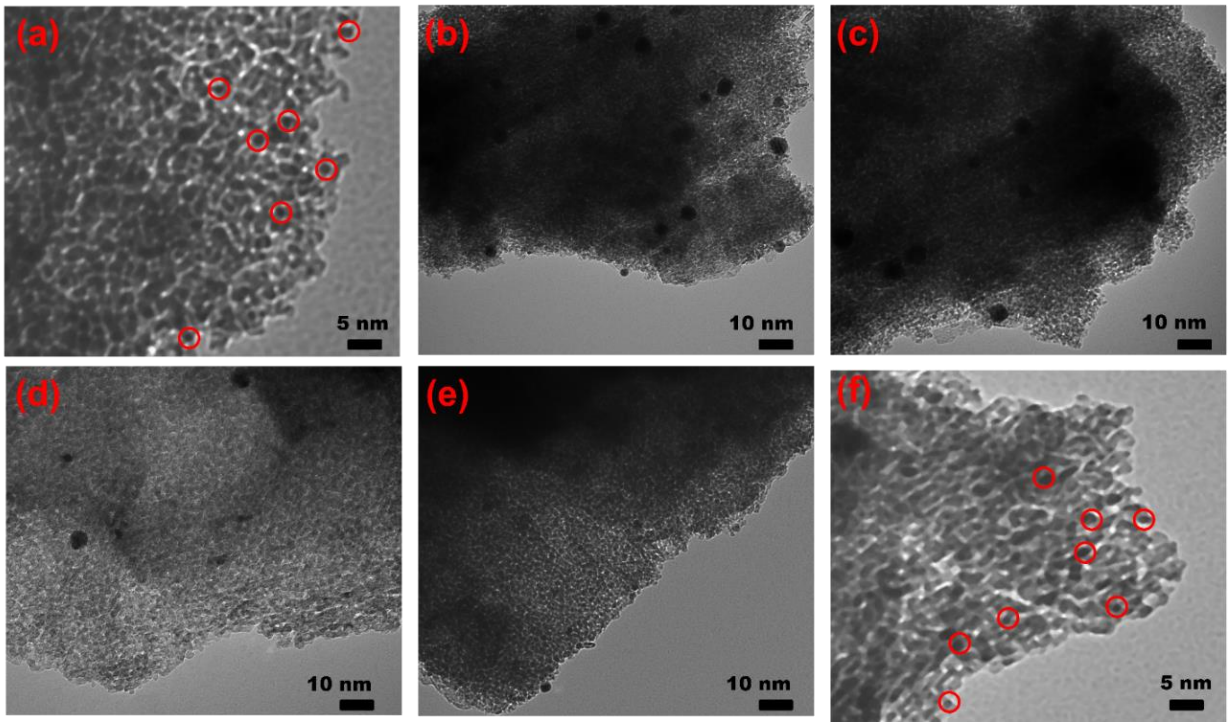

Figure 6.4. TEM images of (a) as-prepared $Ag_{25}(SPhMe_2)_{18}^-/Al_2O_3$ and calcined samples at (b) 250 °C, (c) 350 °C, (d) 450 °C, (e) 550 °C, and (f) 650 °C. Clusters are highlighted with red circles in (a) and (f).

X-ray absorption spectroscopy (XAS) is also a useful technique to follow cluster integrity upon thermal deprotection of supported-cluster materials and complements local TEM measurements. Atomic structural information can be obtained from the EXAFS fitting analyses.[43] Previous EXAFS studies involving thermal calcination of both Ag and Au cluster systems showed significant changes in peaks that are attributed to metal-sulfur (M-S) and metal-metal (M-M) interactions at moderate temperatures.[10] Previous EXAFS data for Ag K-edge measurements

showed the disappearance of Ag-S peaks with a simultaneous increase of Ag-Ag interactions at a calcination temperature of 250 °C (Chapter 2). Au L_3-edge EXAFS analysis of a similar Au_{25} system showed that the thiolate ligands start to be removed from the Au surface at 125 °C and were nearly completely removed from the Au surface at 250 °C.[10] During the activation process in both cases, peaks due to first shell M-S interactions appearing just below 2 Å slowly disappear to indicate the removal of thiolate ligands. This disappearance of the first shell M-S interaction is accompanied by a growth in intensity of the first shell M-M peaks in the 2.5 to 3.0 Å region.

In order to further follow the structural changes right from the beginning of the ligand desorption all the way to fragmentation of the resulting Ag nanoparticles, total scattering data was collected under *in situ* heating conditions on the newly commissioned BXDS-HEW beamline at the CLS. The resulting atomic PDF analysis directly complements previous EXAFS studies in unravelling the structural changes in both these systems. Obtaining a decent spatial resolution for the local structure of materials requires the acquisition of diffraction data at large Q-range (where $Q = 4\pi\sin\theta/\lambda$; *i.e.* at high diffraction angles and very short wavelength) using X-ray radiation, with both excellent counting statistics and optimum background containment.[44,45] These special requirements for PDF measurements are met by the synchrotron facilities such as the BXDS-HEW beamline of the CLS. With the additional set up for *in situ* heating of samples (Figure 6.1), the total scattering from the same sample area was measured while increasing the calcination temperature. Figure 6.5 presents the PDF data for the alumina support under *in situ* heating at different temperatures, which shows the structural stability of the alumina support over the range of temperatures of our study (25 °C - 650 °C). The PDF pattern is consistent with γ-alumina reported in the literature, with peaks at 1.86 Å and 2.78 Å assigned to Al-O and Al-Al interatomic distances.[36,46] It follows that any observable changes in the PDF plots for alumina-supported metal clusters upon calcination can be attributed to the structural changes of the metal clusters upon thermal treatment. This forms the basis for performing dPDF analyses to clearly reveal the change in PDF data that can be attributed to changes in the metal cluster structures upon thermal activation.

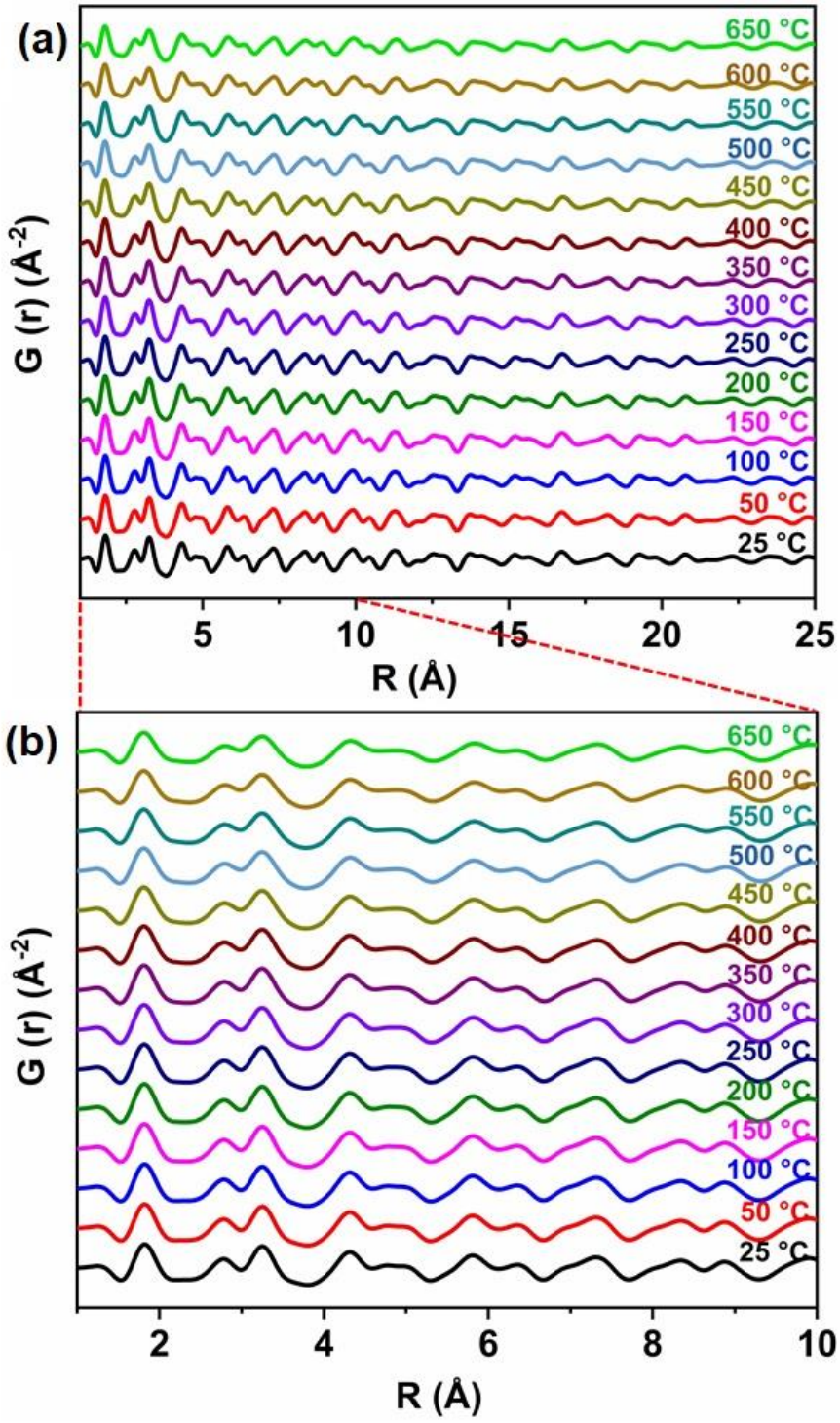

Figure 6.5. Atomic PDF profile of γ-alumina support under *in situ* heating at different temperatures over (a) long distance, and (b) short distance.

Figure 6.6 shows the dPDF data plot for the $Au_{25}(MUA)_{18}^-$ cluster system under *in situ* heating at different temperatures. The ligand-on Au_{25} clusters show a peak (at 2.27 Å) that can be assigned to Au-S interatomic distances, and multiple peaks (at 2.78 Å, 3.16 Å, and 3.43 Å) that are respectively attributed to Au_{core}-$Au_{surface}$, $Au_{surface}$-$Au_{surface}$, and $Au_{surface}$-Au_{staple} distances; these peaks reflect the multiple bonding modes in the as-prepared Au clusters sample at a temperature of 25 °C. The measured values for these interatomic distances are in close agreement with those reported from SC-XRD and EXAFS methods for similar $Au_{25}(SR)_{18}$ systems (Table 6.1). The SC-XRD structure of $Au_{25}(SR)_{18}^-$ clusters shows the clusters have a Au_{13} icosahedral core that is surrounded by six -S-Au-S-Au-S- staple motifs whose terminal sulfur atoms are directly attached to the icosahedral core.[47] So, there are two different sulfur-binding modes and different Au-Au interatomic distances (such as Au_{core}-$Au_{surface}$, $Au_{surface}$-$Au_{surface}$, $Au_{surface}$-Au_{staple}) in the structure of $Au_{25}(SR)_{18}$ clusters.

Table 6.1. Summary of interatomic distances obtained from different methods for thiolate-protected Au_{25} and Ag_{25} clusters.

Interatomic distance	**Au system**			**Ag system**		
	SC-XRD[a]	**EXAFS[b]**	**dPDF**	**SC-XRD[c]**	**EXAFS[d]**	**dPDF**
	(Å)	(Å)	(Å)	(Å)	(Å)	(Å)
M - S	2.32-2.38	2.32(1)	2.27	2.38-2.45	2.401(6)	2.39
$M_{central}$ - $M_{surface}$	2.79(1)	2.82(3)	2.78	2.76(1)	2.81(2)	2.78
$M_{surface}$ - $M_{surface}$	2.93(6)	3.03(4)	3.16	2.86(4)	N/A	3.04
$M_{surface}$ - M_{staple}	3.16(4)	3.31(9)	3.43	2.91(4)	N/A	3.32

a. Crystallographic data of $Au_{25}(SCH_2CH_2Ph)_{18}$ clusters reported in ref. 47.

b. EXAFS fittings of alumina-supported Au_{25}(11-MUA)$_{18}$ sample reported in ref. 41.

c. Crystallographic data of $Ag_{25}(SPhMe_2)_{18}^-$ clusters reported in ref. 38.

d. EXAFS fittings of carbon-supported $Ag_{25}(SPhMe_2)_{18}^-$ sample reported in Chapter 2. Fitting for Ag-S contribution and a single Ag-Ag contribution were done. (N/A means 'data not available').

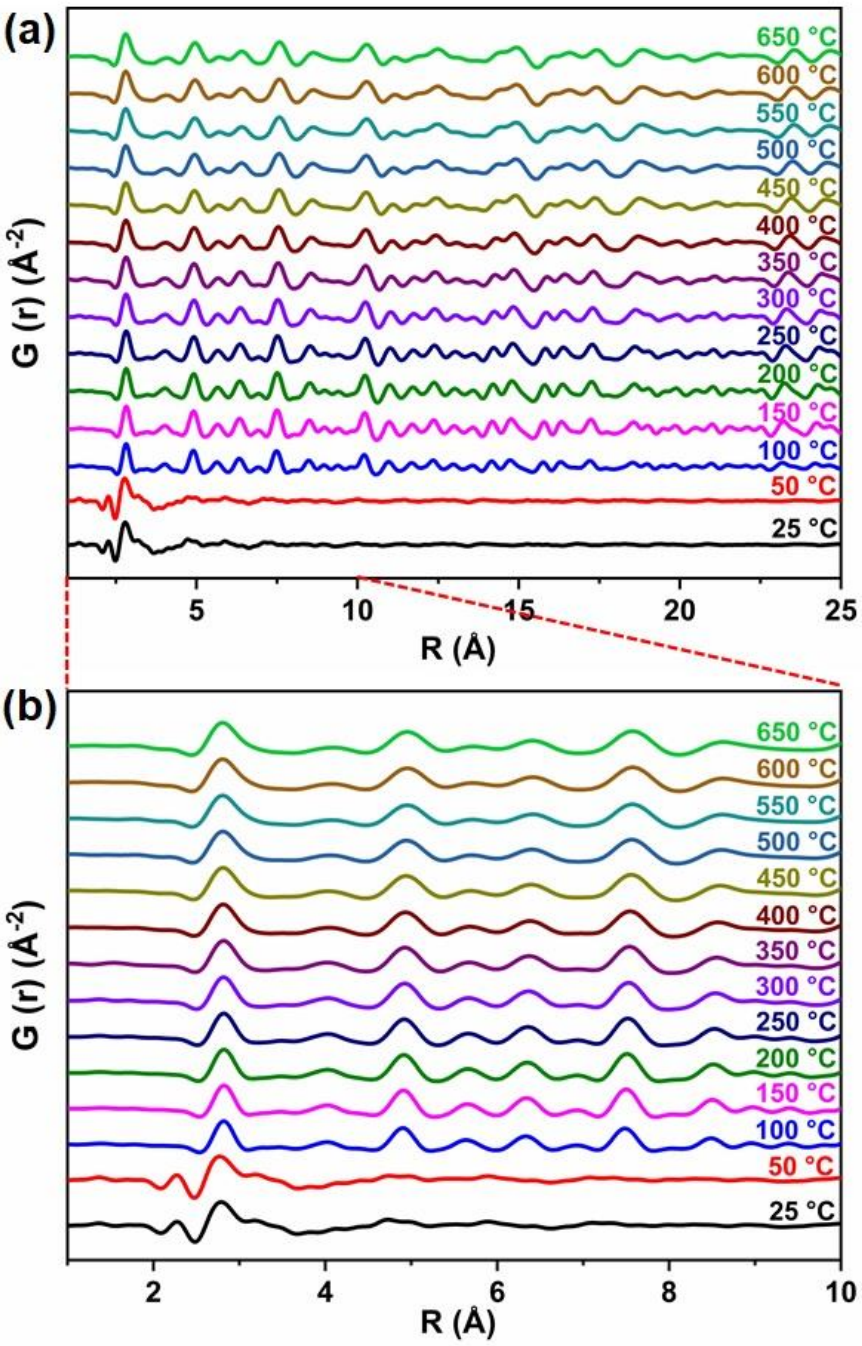

Figure 6.6. dPDF profiles of $Au_{25}(MUA)_{18}^-$ clusters upon *in situ* heating at different temperatures over (a) long distance, and (b) short distance.

A closer look of the dPDF spectra pattern reveals the structural changes in the Au cluster system with increases with activation temperatures. Upon *in situ* thermal treatment, the observable structural changes begin as low as 100 °C (Figure 6.6(b)), which indicates the start of ligand

desorption off the Au metal surface at this temperature. Meanwhile, the available EXAFS Au L_3-edge data obtained from *ex situ* measurements of a similar Au cluster system showed that the thiolate ligands start desorption from the Au surface at 125 °C.[10] It is likely that the desorbed/oxidized ligands are still on the support at this point, as TGA results (Figure 6.7) show a mass loss only occurs beyond 150 °C. As reported elsewhere for a similar Au system, the consequence of ligand desorption is particle migration and coalescence, which then leads to Au particle growth at higher temperatures.[42] For calcination temperatures of 100 °C and beyond, the Au-S peak and Au-Au cluster peaks observed for intact $Au_{25}(SR)_{18}^-$ clusters disappear, with consequent emergence of peaks at 2.83 Å, 4.02 Å, 4.89 Å, 5.64 Å, 6.33 Å, 6.92 Å, 7.51 Å, 8.48 Å etc., which are consistent with Au-Au distances observed for a fcc Au system (for a simulated Au fcc PDF, see Figure 6.8(a)). Subsequent changes at higher temperatures are minimal and mostly due to cluster sintering and thermal expansion effects, the latter of which shows up as slight peak broadening for Au samples between the calcination temperatures of 100 °C and 650 °C (Figure 6.6(b)). The dPDF data at 250 °C was fit with a fcc Au model (Figure 6.9), and refined values were 4.020(1) Å for the unit cell lattice parameters and 0.0107(3) $Å^2$ for the isotropic atomic displacement parameter (U_{iso}).

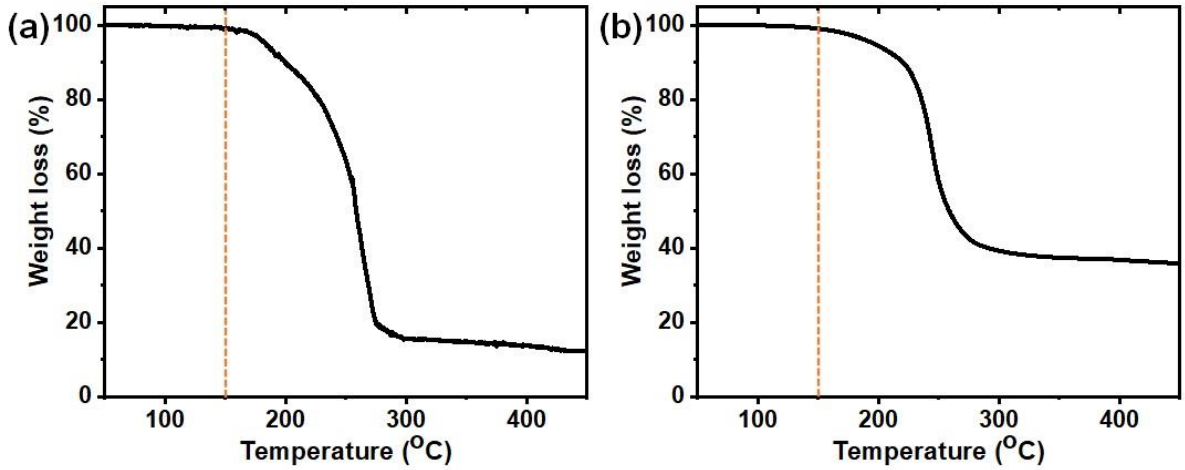

Figure 6.7. Thermal gravimetric analysis profiles of (a) $Au_{25}(11\text{-MUA})_{18}^-$ and (b) $Ag_{25}(SPhMe_2)_{18}^-$ clusters.

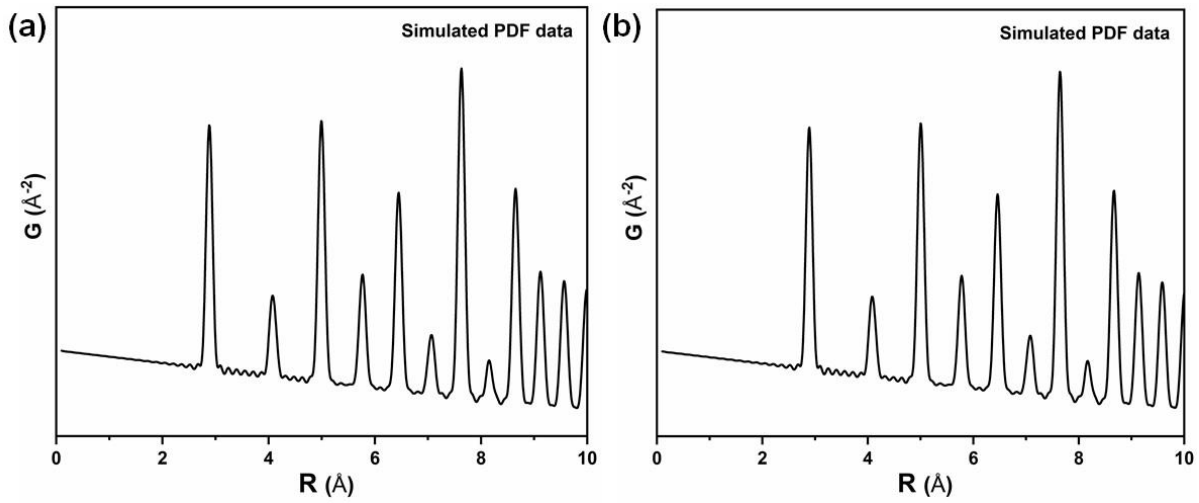

Figure 6.8. Simulated atomic PDF plot for (a) Au and (b) Ag fcc models at higher Q_{max} of 40 $Å^{-1}$ for better resolution.

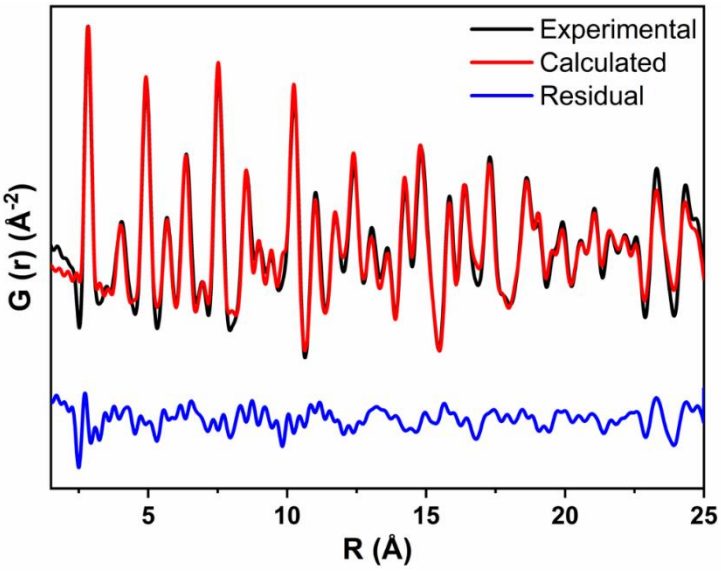

Figure 6.9. Fit of experimental dPDF with calculated PDF plot of Au fcc models for Au sample thermally treated at 250 °C.

A correlation plot offers a swift way of looking at large dataset to determine when (i.e., over which datasets) the sample is changing. Pearson correlation is a purely mathematical tool that can be used to compare spectra, with Pearson correlograms typically showing how similar datasets are to each other. Figure 6.10 presents the similarity maps obtained from the Pearson correlation analysis over the entire r-range for the Au sample. The rapid change in colour seen at 100 °C is due to the structural phase transition from the pristine core-shell structure of the intact clusters to

nanoparticles with a fcc Au structure. These structural changes are due to sintering of metal clusters upon the thermal removal of protecting thiolate ligand from the pristine atom-precise Au_{25} clusters starting from thermal treatment at 100 °C. Intuitively, transient structure (core-shell) collapse and atom reconstruction would precede particle migration and coalescence. While the *in situ* heating method and total scattering measurement nature of atomic PDF technique should potentially enable insights into possible structural changes that occur in this region, more work still needs to be done to collect well-calibrated temperature data over the 100 ºC to 150 ºC temperature range. While it is evident from TEM results that the eventual Au particle size depends on the activation temperature (Figure 6.3), the particle size is qualitatively defined by observing when G(r) tends to zero,[22,24] for atomic PDF plot obtained for a sample at a particular temperature. Notably, the dPDF data at high G(r) do show that there is continuous increase in particle size with increase in activation temperature and this is consistent with the TEM results. However, Fourier artefacts at high G(r) prevent a quantitative estimate of particle size from the dPDF data in this work. Others have also seen sintering of Au clusters upon thermal activation at temperatures above 250 ºC for supported Au clusters and noted that some supports can mitigate sintering by showing strong interactions with Au clusters.[14,16]

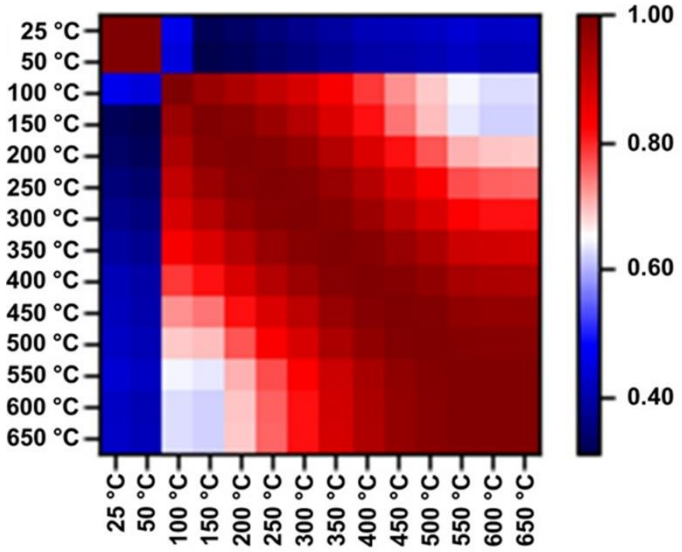

Figure 6.10. Similarity mapping from Pearson correlation matrix analysis of temperature series of dPDF profiles for the Au cluster system upon *in situ* heating.

In spite of the similarity of $Ag_{25}(SR)_{18}^-$ to $Au_{25}(SR)_{18}^-$ in term of atom and ligand count as well as core-shell structure, a more careful comparison of their crystal structures reveals a slight difference in the arrangement of staples around the cluster core. In contrast to a situation in $Au_{25}(SR)_{18}^-$, where all the twelve staple Au atoms occupy the center of the triangular face centers of the Au_{13} icosahedral core in $Au_{25}(SR)_{18}^-$ crystal structure, the crystal structure of $Ag_{25}(SR)_{18}^-$ shows that three of the staple Ag atoms lie away from the triangular face centers with the remaining nine staple Ag atoms lay on the triangular face centers of the Ag_{13} icosahedral core.[38] This atomic arrangement enables weak intermotif interactions in $Ag_{25}(SR)_{18}^-$. Figure 6.11 shows the dPDF data plot for $Ag_{25}(SPhMe_2)_{18}^-$ clusters on alumina, which shows obvious structural changes starting at around 200 °C, a much higher temperature than that seen for the analogous Au cluster system. The intermotif interactions may be responsible for better stability of $Ag_{25}(SR)_{18}^-$ against thermal dethiolation until 200 °C. The weak peak at 1.96 Å is attributed to the interaction between Ag clusters and the alumina surface (i.e. a Al-O-Ag interaction). The voids in the Ag structure (areas where the core could be coordinated by solvents) may be allowing weak Al-O-Ag interactions of the support with intact clusters. At room temperature, the Ag clusters also show four other peaks at 2.39 Å, 2.78 Å, 3.04 Å, and 3.32 Å which are due Ag-S and three Ag-Ag interactions due to multiple bonding modes in the clusters (Table 6.1). Similar multiple bonding modes were identified in the EXAFS data of atom-precise $Ag_{25}(SR)_{18}^-$ clusters on carbon supports (Chapter 2).

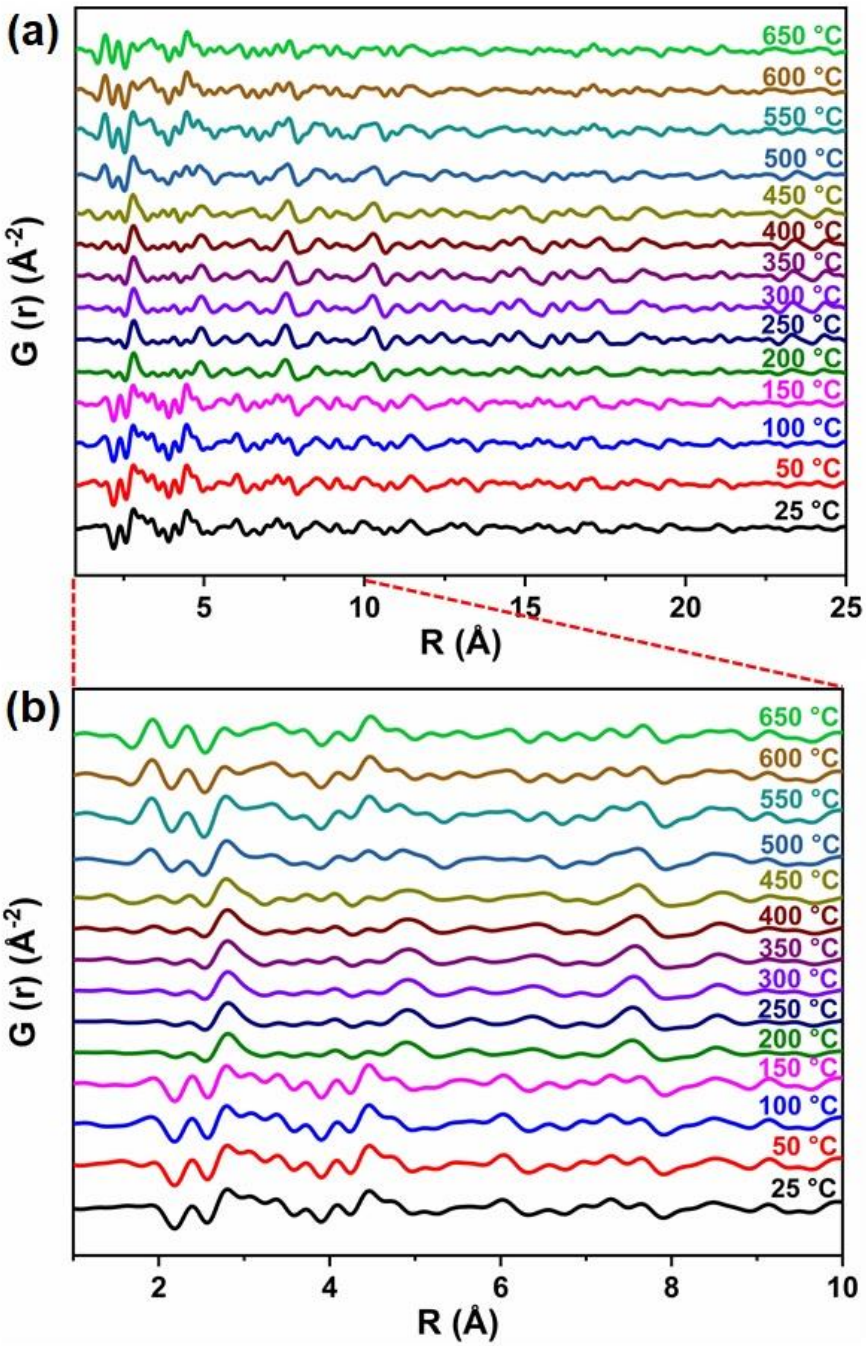

Figure 6.11. dPDF profiles of $Ag_{25}(SPhMe_2)_{18}$ clusters under *in situ* heating at different temperatures over (a) long distance, and (b) short distance.

While the dPDF spectra for the Ag clusters are consistent at activation temperatures below 200 °C which shows the preservation of the cluster structure, there are significant changes in the spectra of the activated Ag clusters within the temperature range of 200 °C - 450 °C (Figure 6.11).

Notably, the differential PDF treatment of Ag clusters was more problematic due to weaker scattering of Ag compared to Au, and thus poorer signal-to-noise ratios were obtained in the resulting dPDFs for the Ag system. Nonetheless, the Ag-S peak at 2.39 Å is significantly suppressed to indicate the dethiolation of Ag clusters, while weak peaks emerge at around 2.0 and 2.3 Å which can be assigned to Al-O and Ag-O interactions of activated clusters with the alumina support (e.g. Al-O-Ag interactions), and thus are present in all activated samples. Importantly, new Ag-Ag peaks are seen at higher peak positions at 2.81 Å, 3.41 Å, and 3.74 Å, etc. (Figure 6.11(b)). The first prominent peak at 2.81 Å can be assigned to first shell Ag-Ag interactions that emerge due to an increase in cluster size, and thus particle growth to form Ag nanoparticles with a fcc structure. This value is in close agreement with the values of 2.826(6) Å - 2.859(6) Å earlier reported for Ag-Ag interactions from the single-shell EXAFS fittings for fcc Ag particles in the same range of activation temperatures (Chapter 2). The simulated atomic PDF for Ag fcc (Fig 6.8(b)) shows first seven major peaks at around 2.88 Å, 4.05 Å, 4.98 Å, 5.79 Å, 6.47 Å, 7.07 Å, and 7.64 Å, which are consistent with several of the new and prominent peaks in the samples thermally treated within the temperature range of 200 °C - 450 °C. An excellent fit was obtained for the dPDF data for sample treated at 250 °C when modelled with a Ag fcc structure (Figure 6.12). The refined values were 4.023(6) Å for the fcc lattice parameter, and 0.011(3) $Å^2$ for the isotropic atomic displacement parameter (U_{iso}).

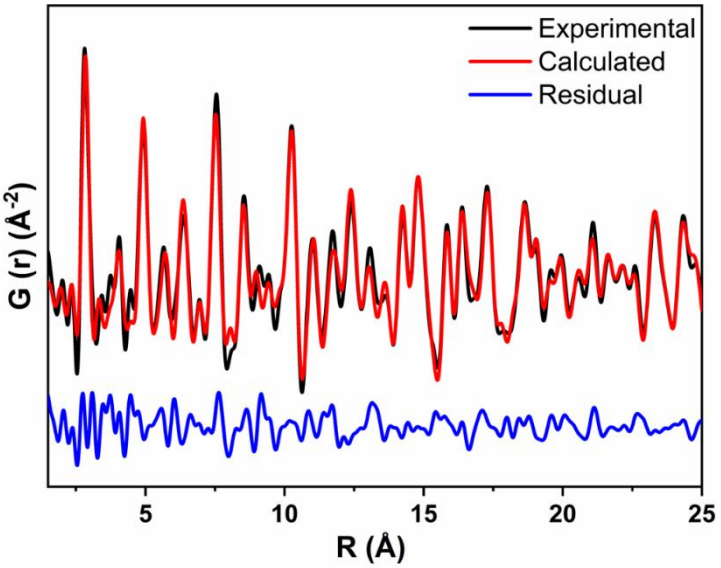

Figure 6.12. Fit of experimental dPDF with calculated PDF plot of Ag fcc models for Ag sample thermally treated at 250 °C.

Unlike in the analogous Au system, the observed particle growth in the Ag system ceases and the particle size declines significantly beyond 450 °C. Beyond the activation temperature of 450 °C, there is a re-emergence of a set of weaker Ag-Ag interactions at 2.80 Å, 3.05 Å, 3.35 Å, and 3.71 Å, assigned to multiple bonding modes in the small-sized Ag clusters that are presumably formed from the fragmentation of Ag nanoparticles as supported by the TEM results (Figure 6.4). The similarity maps obtained from the Pearson correlation analysis for the Ag sample clearly show the re-emergence of PDF features that are highly correlated with unactivated samples (Figure 6.13). For samples treated beyond 450 °C, new peaks at 1.92 Å and 2.33 Å, ascribed to Al-O and Ag-O interactions, respectively (i.e. Al-O-Ag interactions, see below for more discussion), become prominent; these are possibly be due to a higher population of Ag atoms interacting with the alumina support and/or Ag oxide cluster formation.[48,49] The peak at 1.92 Å is likely due to Al-O interactions and may indicate a small amount of silver aluminate, $AgAlO_2$, has formed on the surface; indeed, She and Flytzani-Stphanopoulos have shown that $AgAlO_2$ species can form when heating co-gels of alumina and silver salts at 650 ^oC.[50] Meanwhile, the new peak at 2.33 Å is likely due to Ag-O interactions of the Ag clusters with the support; others have shown Ag-O bond distances are typically around 2.3 Å.[49,51] Others have also shown that the surface of Ag nanoparticles gets easily oxidized to AgO_x during annealing in air,[52,53] whereas AgO_x is thermodynamically unstable and dissociates into Ag and O_2 at higher temperatures.[19] The PDF data at high temperatures is consistent with Ag nanoparticles being oxidized to form a large proportion of small Ag and or AgO_x clusters, and possibly some $AgAlO_2$ formation. Thus, the Ag system undergoes mild particle growth at low activation temperature, followed by thermal degradation and fragmentation into small-sized Ag clusters at relatively high temperatures. This behaviour is completely different from the Au cluster behaviour discussed above, and thus shows that activation protocols need to be developed separately for different metal cluster systems.

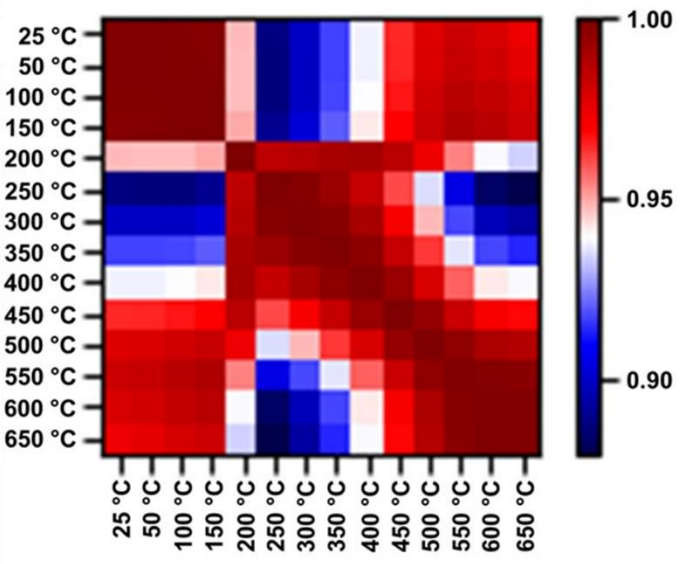

Figure 6.13. Similarity mapping from Pearson correlation matrix analysis of temperature series of dPDF profiles for the Ag cluster system upon *in situ* heating.

6.4 Conclusions

Synchrotron sources offer broad opportunities for studying catalyst materials and alternative experimental techniques such as total scattering that can complement more common characterization methods such as TEM and EXAFS. We have shown here that differential PDF analysis is an excellent complementary method for investigating *in situ* structural changes in atom-precise metal clusters during thermal activation. The interatomic distances in atom-precise $Au_{25}(SR)_{18}^-$ and $Ag_{25}(SR)_{18}^-$ clusters as measured by the differential PDF method are in good agreement with those measured by crystallography and EXAFS methods. Notably, Au clusters behave significantly differently than analogous Ag clusters upon thermal activation. The Au system shows continuous growth in particle size with increasing activation temperature due to particle migration and coalescence upon thermal deprotection and particle reconstruction. Conversely, the analogous Ag system exhibits discontinuous growth in particle size due to thermal oxidation and degradation of Ag at high activation temperatures to give small-sized Ag fragments. Aside the nature of the metals, the underlying subtle differences in staple atom arrangements can also contribute to the observed difference in the activation temperature as the starting point of structural changes that follow the cleavage of metal-thiolate bonds in the atom-precise $Au_{25}(SR)_{18}^-$ and $Ag_{25}(SR)_{18}^-$ clusters. Further studies will look to allow for measurements with more precise

temperature control such that subtle changes upon thiol deprotection and cluster rearrangement at low temperatures, and under inert gas flow, can be followed in detail.

6.5 References

1. B. Yin, Z. Luo. Coinage Metal Clusters: From Superatom Chemistry to Genetic Materials, *Coord. Chem. Rev.* 2021, **429**, 213643.

2. Y. Watanabe. Atomically Precise Cluster Catalysis Towards Quantum Controlled Catalysts, *Sci. Technol. Adv. Mater.* 2014, **15**, 063501.

3. Y. Du, H. Sheng, D. Astruc, M. Zhu. Atomically Precise Noble Metal Nanoclusters as Efficient Catalysts: A Bridge Between Structure and Properties, *Chem. Rev.* 2020, **120**, 526-622.

4. M.S. Bootharaju, C.P. Joshi, M.R. Parida, O.F. Mohammed, O.M. Bakr. Templated Atom-Precise Galvanic Synthesis and Structure Elucidation of a $[Ag_{24}Au(SR)_{18}]^-$ Nanocluster, *Angew. Chem. Int. Ed.* 2016, **55**, 922-926.

5. X. Kang, H. Chong, M. Zhu. $Au_{25}(SR)_{18}$: The Captain of the Great Nanocluster Ship, *Nanoscale* 2018, **10**, 10758-10834.

6. T-A.D. Nguyen, Z.R. Jones, B.R. Goldsmith, W.R. Buratto, G. Wu, S.L. Scott, T.W. Hayton. A Cu_{25} Nanocluster with Partial Cu(0) Character, *J. Am. Chem. Soc.* 2015, **137**, 13319-13324.

7. C. Sun, N. Mammen, S. Kaappa, P. Yuan, G. Deng, C. Zhao, J. Yan, S. Malola, K. Honkala, H. Häkkinen, B.K. Teo, N. Zheng. Atomically Precise, Thiolated Copper-Hydride Nanoclusters as Single-Site Hydrogenation Catalysts for Ketones in Mild Conditions, *ACS Nano* 2019, **13**, 5975-5986.

8. X. Nie, H. Qian, Q. Ge, H. Xu, R. Jin. CO Oxidation Catalyzed by Oxide-Supported $Au_{25}(SR)_{18}$ Nanoclusters and Identification of Perimeter Sites as Active Centers, *ACS Nano* 2012, **6**, 6014-6022.

9. Y. Zhu, H. Qian, R. Jin. An Atomic-Level Strategy for Unraveling Gold Nanocatalysis from the Perspective of $Au_n(SR)_m$ Nanoclusters, *Chem. Eur. J.* 2010, **16**, 11455-11462.

10. A. Shivhare, D.M. Chevrier, R.W. Purves, R.W.J. Scott. Following the Thermal Activation of $Au_{25}(SR)_{18}$ Clusters for Catalysis by X-ray Absorption Spectroscopy, *J. Phys. Chem. C* 2013, **117**, 20007-20016.

11. T. Yoskamtorn, S. Yamazoe, R. Takahata, J-i. Nishigaki, A. Thivasasith, J. Limtrakul, T. Tsukuda. Thiolate-Mediated Selectivity Control in Aerobic Alcohol Oxidation by Porous Carbon-Supported Au_{25} Clusters, *ACS Catal.* 2014, **4**, 3696-3700.

12. J. Li, R.R. Nasaruddin, Y. Feng, J. Yang, N. Yan, J. Xie. Tuning the Accessibility and Activity of $Au_{25}(SR)_{18}$ Nanocluster Catalysts via Ligand Engineering, *Chem. Eur. J.* 2016, **22**, 14816-14820.

13. C. García, S. Pollitt, M. van der Linden, V. Truttmann, C. Rameshan, R. Rameshan, E. Pittenauer, G. Allmaier, P. Kregsamer, M. Stöger-Pollach, N. Barrabés, G. Rupprechter, Support Effect on the Reactivity and Stability of $Au_{25}(SR)_{18}$ and $Au_{144}(SR)_{60}$ Nanoclusters in Liquid Phase Cyclohexane Oxidation, *Catal. Today* 2019, **336**, 174-185.

14. T. Kawawaki, Y. Kataoka, M. Hirata, Y. Iwamatsu, S. Hossain, Y. Negishi. Toward the Creation of High-Performance Heterogeneous Catalysts by Controlled Ligand Desorption from Atomically Precise Metal Nanoclusters, *Nanoscale Horiz.* 2021, **6**, 409-448.

15. S. Campisi, M. Schiavoni, C.E. Chan-Thaw, A. Villa. Untangling the Role of the Capping Agent in Nanocatalysis: Recent Advances and Perspectives, *Catalysts* 2016, **6**, 185.

16. V. Sudheeshkumar, K.O. Sulaiman, R.W. J. Scott. Activation of Atom-Precise Clusters for Catalysis, *Nanoscale Adv.* 2020, **2**, 55-69

17. J. Fang, J. Li, B. Zhang, X. Yuan, H. Asakura, T. Tanaka, K. Teramura, J. Xie, N. Yan. The Support Effect on the Size and Catalytic Activity of Thiolated Au_{25} Nanoclusters as Precatalysts, *Nanoscale* 2015, **7**, 6325-6333.

18. Y. Liu, H. Tsunoyama, T. Akita, T. Tsukuda. Efficient and Selective Epoxidation of Styrene with TBHP Catalyzed by Au_{25} Clusters on Hydroxyapatite, *Chem. Commun*. 2010, **46**, 550-552.

19. M.K. Gangishetty, R.W.J. Scott, T.L. Kelly. Thermal Degradation Mechanism of Triangular $Ag@SiO_2$ Nanoparticles, *Dalton Trans.* 2016, **45**, 9827-9834.

20. K.E. Lee, A.V. Hesketh, T.L. Kelly. Chemical Stability and Degradation Mechanisms of Triangular Ag, Ag@Au, and Au Nanoprisms, *Phys. Chem. Chem. Phys.* 2014, **16**, 12407-12414.

21. B. Tang, J. An, X. Zheng, S. Xu, D. Li, J. Zhou, B. Zhao, W. Xu. Silver Nanodisks with Tunable Size by Heat Aging, *J. Phys. Chem. C* 2008, **112**, 18361-18367.

22. S.J.L. Billinge, I. Levin. The Problem with Determining Atomic Structure at the Nanoscale, *Science* 2007, **316**, 561-565.

23. A.I. Frenkel, A. Yevick, C. Cooper, R. Vasic. Modeling the Structure and Composition of Nanoparticles by Extended X-Ray Absorption Fine-Structure Spectroscopy, *Annu. Rev. Anal. Chem.* 2011, **4**, 23-39.

24. Th. Proffen, K.L. Page, R. Seshadri, A. Cheetham. Pair Distribution Function for Nanoparticle Studies, *Las Alamos Science* 2006, **30**, 161-163.

25. K. Page, T.C. Hood, Th. Proffen, R.B. Neder. Building and Refining Complete Nanoparticle Structures with Total Scattering Data, *J. Appl. Cryst.* 2011, **44**, 327-336.

26. H. Nakotte, C. Silkwood, K. Page, H-W. Wang, D. Olds, B. Kiefer, S. Manna, D. Karpov, E. Fohtung, E.E. Fullerton. Pair Distribution Function Analysis Applied to Decahedral Gold Nanoparticles, *Phys. Scr.* 2017, **92**, 114002.

27. S. Le Roux, S. Martin, R. Christensen, Y. Ren, V. Petkov. Three Dimensional Structure of Multicomponent $(Na_2O)_{0.35}[(P_2O_5)_{1-x}\ (B_2O_3)_x]_{0.65}$ Glasses by High Energy X-Ray Diffraction and Constrained Reverse Monte Carlo Simulations, *J. Phys.: Condens. Matter* 2011, **23**, 035403.

28. T.L. Christiansen, S.R. Cooper, K.M.Ø. Jensen. There's No Place Like Real-Space: Elucidating Size Dependent Atomic Structure of Nanomaterials Using Pair Distribution Function Analysis, *Nanoscale Adv.* 2020, **2**, 2234-2254.

29. V. Petkov, Y. Peng, G. Williams, B. Huang, D. Tomalia, Y. Ren. Structure of Gold Nanoparticles Suspended in Water Studied by X-Ray Diffraction and Computer Simulations, *Phys. Rev. B: Condens. Matter Mater. Phys.* 2005, **72**, 195402.

30. K.M.Ø. Jensen, P. Juhás, M.A. Tofanelli, C.L. Heinecke, G. Vaughan, C.J. Ackerson, S.J.L. Billinge. Polymorphism in Magic-Sized $Au_{144}(SR)_{60}$ Clusters, *Nat. Commun.* 2016, **7**, 11859.

31. S. Banerjee, C.-H. Liu, J.D. Lee, A. Kovyakh, V. Grasmik, O. Prymak, C. Koenigsmann, H. Liu, L. Wang, A.M.M. Abeykoon, S.S. Wong, M. Epple, C.B. Murray, S.J.L. Billinge. Improved Models for Metallic Nanoparticle Cores from Atomic Pair Distribution Function (PDF) Analysis, *J. Phys. Chem. C* 2018, **122**, 29498-29506.

32. A. Shivhare, L. Wang, R.W.J. Scott. Isolation of Carboxylic Acid-Protected Au_{25} Clusters Using a Borohydride Purification Strategy, *Langmuir* 2015, **31**, 1835-1841.

33. P.J. Chupas, K.W. Chapman, C. Kurtz, J.C. Hanson, P.L. Lee, C.P. Grey. A Versatile Sample-Environment Cell for Non-Ambient X-Ray Scattering Experiments, *J. Appl. Cryst.* 2008, **41**, 822-824.

34. P. Juhás, T. Davis, C.L. Farrow, S.J.L. Billinge. PDFgetX3: A Rapid and Highly Automatable Program for Processing Powder Diffraction Data into Total Scattering Pair Distribution Functions, *J. Appl. Crystallogr.* 2013, **46**, 560-566.

35. R. Harrington, D.B. Hausner, N. Bhandari, D.R. Strongin, K.W. Chapman, P.J. Chupas, D.S. Middlemiss, C.P. Grey, J.B. Parise. Investigations of Surface Structures by Powder Diffraction: A Differential Pair Distribution Function Study on Arsenate Sorption on Ferrihydrite, *Inorg. Chem.* 2010, **49**, 325-330.

36. W. Li, R. Harrington, Y. Tang, J.D. Kubicki, M. Aryanpour, R.J. Reeder, J.B. Parise, B.L. Phillips. Differential Pair Distribution Function Study of the Structure of Arsenate Adsorbed on Nanocrystalline γ-Alumina, *Environ. Sci. Technol.* 2011, **45**, 9687-9692.

37. C.L. Farrow, P. Juhas, J.W. Liu, D. Bryndin, E.S. Bozin, J. Bloch, Th. Proffen, S.J.L. Billinge. PDFfit2 and PDFgui: Computer Programs for Studying Nanostructure in Crystals, *J. Phys.: Condens. Matter* 2007, **19**, 335219.

38. C.P. Joshi, M.S. Bootharaju, M.J. Alhilaly, O.M. Bakr. $[Ag_{25}(SR)_{18}]^-$: The "Golden" Silver Nanoparticle, J. *Am. Chem. Soc.* 2015, **137**, 11578-11581.

39. M. Zhu, C.M. Aikens, F.J. Hollander, G.C. Schatz, R. Jin. Correlating the Crystal Structure of a Thiol-Protected Au_{25} Cluster and Optical Properties, *J. Am. Chem. Soc*. 2008, **130**, 5883-

40. J. Yan, H. Su, H. Yang, S. Malola, S. Lin, H. Häkkinen, N. Zheng. Total Structure and Electronic Structure Analysis of Doped Thiolated Silver $[MAg_{24}(SR)_{18}]^{2-}$ (M = Pd, Pt) Clusters, *J. Am. Chem. Soc.* 2015, **137**, 11880-11883.

41. V. Sudheeshkumar, A. Lushington, X. Sun, R.W.J. Scott. Thermal Stability of Alumina-Overcoated Au_{25} Clusters for Catalysis, *ACS Appl. Nano. Mater*. 2018, **1**, 6904-6911.

42. V. Sudheeshkumar, C. Soong, S. Dogel, R.W.J. Scott, Probing the Thermal Stability of (3-Mercaptopropyl)-trimethoxysilane-Protected Au_{25} Clusters by *in situ* Transmission Electron Microscopy, *Small* 2021, **17**, 2004539.

43. Z. Zhang, A.G. Walsh, P. Zhang. Dynamic Structure of Metal Nanoclusters from Synchrotron X-ray Spectroscopy, *J. Phys. Chem. C* 2021, **125**, 5982-5994.

44. C.L. Farrow, S.J.L. Billinge. Relationship between the Atomic Pair Distribution Function and Small-Angle Scattering: Implications for Modeling of Nanoparticles, *Acta Cryst.* 2009, **A65**, 232-239.

45. B.H. Toby, T. Egami. Accuracy of Pair Distribution Function Analysis Applied to Crystalline and Non-Crystalline Materials, *Acta Cryst.* 1992, **A48**, 336-346.

46. L. Samain, A. Jaworski, M. Edén, D.M. Ladd, D-K. Seo, F.J. Garcia-Garcia, U. Häussermann. Structural Analysis of Highly Porous γ-Al_2O_3, *J. Solid State Chem.* 2014, **217**, 1-8.

47. M.W. Heaven, A. Dass, P.S. White, K.M. Holt, R.W. Murray. Crystal Structure of Gold Nanoparticle $[N(C_8H_{17})_4][Au_{25}(SCH_2CH_2Ph)_{18}]$, *J. Am. Chem. Soc.* 2008, **130**, 3754-3755.

48. A. Shivhare, R.W.J. Scott. Following the Thermal and Chemical Activation of Supported Au Clusters using X-ray Absorption Spectroscopy, *RSC Adv.* 2016, **6**, 62579-62584.

49. E.V. Trushin, I.L. Zilberberg. Anion-Radical Oxygen Centers in Small $(AgO)_n$ Clusters: Density Functional Theory Predictions, *Chem. Phys. Lett.* 2013, **560**, 37-41.

50. X. She, M. Flytzani-Stephanopoulos. The Role of Ag-O-Al Species in Silver-Alumina Catalysts for the Selective Catalytic Reduction of NOx with Methane, *J. Catal.* 2006, **237**, 79-93.

51. K.P. Huber, G. Herzberg. Molecular Spectra and Molecular Structure: IV. Constants of Diatomic Molecules, Van Nostrand-Reinhold, New York, 1979.

52. Z.W. Lei, M. Liu, W. Ge, Z.P. Fu, K. Reinhardt, R.J. Knize, Y. Lu. Morphology and Optical Absorption Change of Ag/SiO_2 Core-Shell Nanoparticles Under Thermal Annealing, *Appl. Phys. Lett.* 2012, **101**, 272-283.

53. K. Chatterjee, S. Banerjee, D. Chakravorty. Plasmon Resonance Shifts in Oxide-Coated Silver Nanoparticles, *Phys. Rev. B* 2002, **66**, 085421.

Chapter 7

General Discussion, Concluding Remarks and Future Directions

7.1 General Discussion and Concluding Remarks

Heterogeneous catalysis occurs at the active metal surface and/or active metal-support interface and minimizing metal particle sizes affords higher surface energies and enables higher catalytic activity of metal nanoparticles compared to bulk metals. Further downsizing of conventional metal nanoparticles to ultra-small metal clusters with uniform composition enhances the utilization of metal atoms, and besides the cluster size, atom composition and arrangements are crucial in designing selective heterogenous catalyst materials. The design and catalytic applications of atom-precise metal clusters have attracted tremendous research attention as their detailed characterization affords information that enables atom-level structure-activity relationship studies of the catalysts. Atom-precise $Ag_{25}(SR)_{18}^-$ clusters are an analogue of well studied $Au_{25}(SR)_{18}^-$ clusters and both are similar in terms of metal and ligand count, overall cluster charge, and their morphologies. This thesis contributes to the body of knowledge about the design, preparation, characterization of both atom-precise $Ag_{25}(SR)_{18}^-$ monometallic and Ag-based bimetallic clusters as precursors for selective heterogenous catalyst materials. Ag is an attractive choice among noble metals for heterogeneous catalysis design owing to its lower cost (at the time of writing, Ag is 50 times cheaper than Pd and 70 times cheaper than Au and Pt) and high abundancy. Carbon-supported Ag-based bimetallic clusters were made via both direct and indirect preparation methods, where the indirect preparation methods entailed post-synthesis treatments of atom-precise $Ag_{25}(SR)_{18}^-$ clusters.

The first objective was to examine the activation of atom-precise $Ag_{25}(SR)_{18}^-$ clusters on carbon supports by conventional thermal treatment methods. Results showed that Ag-thiol bonds were selectively oxidized from the clusters upon mild heat treatments without formation of Ag_2O or Ag_2S and no significant sintering, and that the activated Ag clusters on carbon supports showed particle size dependent activity for styrene oxidation reactions (Chapter 2). Carbon-supported Ag cluster samples calcined at 250 °C showed mild cluster growth and were evaluated as a precursor onto which Pd ions were added by a sequential deposition (SD) method to make bimetallic AgPd/carbon samples (Chapter 3) as the second objective of this thesis. By varying the amount of

Pd, SD-x:y-Ag:Pd/carbon samples with different Ag:Pd ratios were made and characterized using XAS and XPS. While the XANES results showed that Ag and Pd are in zerovalent states, the results from EXAFS data fittings suggested cluster-in-cluster structural arrangements in the carbon-supported bimetallic samples prepared by the sequential deposition approach. Moreover, there was no limit to the amount of Pd that could be incorporated to make AgPd bimetallic samples via this sequential deposition approach, albeit the final clusters were not atom-precise. It was proven that activated Ag clusters on carbon supports were a good precursor for making carbon-supported AgPd bimetallic clusters. A drawback of this method is the lack of atom precision in the final AgPd bimetallic samples, as some growth of the clusters to nanoparticles was seen. For AgPd bimetallic catalysts with low Pd loadings, Pd atoms occupy subsurface sites while Ag atoms are predominately on the catalyst surface. Conversely, most Pd atoms occupy surface sites for catalysts with higher Pd loadings. Bimetallic AgPd catalysts showed better activity than monometallic Ag catalysts and low Pd loadings favoured better 2-methyl-3-buten-2-ol (MBE) selectivity in the hydrogenation reactions of 2-methyl-3-butyn-2-ol (MBY). The dominance of catalyst surface by Ag atoms, rather than Pd atoms, atoms enabled the suppression of over-hydrogenation of MBY, and thus high MBE selectivity with such catalysts.

Subsequently, an improved single-pot co-reduction (CR) synthesis protocol was explored to make compositionally pure Ag clusters doped with variable amounts of Pd (Chapter 4) as the third objective of the thesis. The purity and atomic composition of these CR-x:y-Ag:Pd bimetallic clusters were chemically confirmed by mass spectrometry. Only singly-doped Pd in Ag clusters, i.e. atom-precise $Ag_{24}Pd_1(SR)_{18}^{2-}$ clusters, occurred even with equimolar ratios of Ag(I) and Pd(II) ions in the direct synthesis (otherwise referred to as co-reduction approach), whereas at higher Pd loadings, the resulting samples were not compositionally pure and Pd salts were not fully reduced. As compared with the monometallic $Ag_{25}(SR)_{18}^{-}$ clusters, the absorption peaks of the obtained bimetallic $Ag_{24}Pd_1(SR)_{18}^{2-}$ cluster system were blue shifted due to incorporation of Pd. Multiple component XPS analysis and XAS results showed that the carbon-supported $Ag_{24}Pd_1(SR)_{18}^{2-}$ bimetallic clusters have multivalent Ag atoms and Pd(II) ions with significant thiolate interactions. These results suggested that single Pd atoms predominantly occupied the staple position of individual clusters, or possibly alternatively on icosahedral vertex sites. It was noted that Pd-thiolate bonds can be quite resistant to borohydride reduction due to increased RS-M-SR bond strengths. This likely positions the Pd dopant in a non-central position due to faster Ag reduction

during the co-reduction protocol used in this work. In a follow up study (to pursue the fourth objective), carbon-supported $Ag_{24}Pd_1(SR)_{18}^{2-}$ bimetallic clusters were subjected to thermal treatments, and the Pd-thiolate bonds in the metal-ligand shell were found to be more thermally stable in carbon-supported $Ag_{24}Pd_1(SR)_{18}^{2-}$ bimetallic clusters than the Ag-thiolate bonds in the earlier studied carbon-supported $Ag_{25}(SR)_{18}^{-}$ monometallic clusters (Chapter 5). This further showed that the Pd dopant occupies the ligand-shell environment. Thus, a well-defined structure with an unprecedented level of atomic precision was implemented in AgPd catalysts prepared by the co-reduction protocol. This design employs the strong cooperative effects induced by a single catalytically active heteroatom (Pd) to tailor the performance of the passive host metal (Ag) while concomitantly minimizing precious metal usage. Besides the improved thermal stability, carbon-supported $Ag_{24}Pd_1(SR)_{18}^{2-}$ bimetallic clusters catalysts also showed superior catalytic activities as compared to homonuclear $Ag_{25}(SR)_{18}^{2-}$ cluster catalysts for the semi-hydrogenation reactions of MBY and HY (3-hexyn-1-ol) as model terminal and internal alkynol substrates. Moreover, the presence of residual thiolate ligands led to higher alkenol selectivity, as well as excellent stereoselectivity towards the Z-isomer of 3-hexen-1-ol (Chapter 5). Altogether, the eventual structure of the carbon-supported AgPd bimetallic clusters depends on the choice of synthesis protocol. The carbon-supported AgPd bimetallic clusters, regardless of the method of preparation, showed superior catalytic activities to monometallic Ag clusters and the selectivity of the hydrogenation reactions towards semi-hydrogenation products is sensitive to the surface structure of AgPd catalysts (Chapter 3 and 5).

The fifth, and final objective of this thesis, was to use pair distribution function analysis (PDF) to investigate the structural transformation of Ag and Au metal clusters on supports upon *in situ* thermally activation for heterogeneous catalysis. Unlike in earlier work (Chapter 2-5), where XAS was extensively used in probing the catalyst structures, herein, an *in situ* differential PDF analysis was employed as a novel structural characterization technique to follow the activation of atom-precise Ag_{25} and Au_{25} clusters for heterogeneous catalysis (Chapter 6). The $Au_{25}(SR)_{18}^{-}$ cluster system was chosen as a Au standard for comparison with the $Ag_{25}(SR)_{18}^{-}$ cluster system. Synchrotron X-ray total scattering measurements, along with PDF analyses proved to be a complementary characterization technique to both transmission electron microscopy (TEM) and extended X-ray absorption fine structure (EXAFS) spectroscopy methods for detailed structural studies of atom-precise metal clusters. The interatomic distances in atom-precise

$Au_{25}(SR)_{18}^-$ and $Ag_{25}(SR)_{18}^-$ clusters as measured by the differential PDF (dPDF) method agreed with those measured by crystallography and EXAFS methods. Furthermore, the dPDF analysis clearly showed the structural transformation of the atom-precise clusters to fcc-like structures upon thermal activation, though Ag and its analogous Au systems remarkably behaved in a different way at higher temperatures. The Ag system exhibited discontinuous growth in particle size due to thermal oxidation and degradation of Ag at high activation temperatures to give small-sized Ag fragments. Meanwhile, the analogous Au system showed continuous growth in particle size with increasing activation temperature due to particle migration and coalescence upon thermal deprotection and particle reconstruction.

Summarily, the major conclusions from all these studies are as follows: (1) atom-precise $Ag_{25}(SPhMe_2)_{18}^-$ clusters can be carefully activated on carbon supports, via conventional thermal treatments, without formation of Ag_2O or Ag_2S or significant sintering of clusters; (2) the carbon-supported $Ag_{25}(SPhMe_2)_{18}^-$ clusters are active for selective oxidation of styrene to styrene oxide; (3) the mildly activated Ag clusters on carbon supports at 250 °C can make good precursors for the design of carbon-supported AgPd bimetallic clusters with cluster-in-cluster atomic arrangements; (4) atom-precise $Ag_{24}Pd_1(SR)_{18}^{2-}$ clusters are predominantly formed via the improved single-pot co-reduction synthesis protocol, and the Pd dopant resides in non-central core position; (5) bimetallic AgPd catalysts have superior activities to monometallic Ag catalysts for the selective hydrogenation of alkynols to alkenols and the selectivity of the hydrogenation reactions is sensitive to the surface structure of AgPd catalysts; (6) X-ray absorption spectroscopy (XAS) is a reliable characterization technique for getting insights to the structure of bimetallic AgPd heterogeneous catalysts; (7) differential PDF analysis is an excellent complementary method of probing the structural changes in atom-precise metal clusters under *in situ* thermal activation; and (8) Ag systems perform considerably differently than analogous Au systems at the atomic scale upon thermal activation.

7.2 Future Directions

7.2.1 Enhancement of Thermal Stability of Ag_{25} Clusters by Encapsulation in Hollow Metal Oxide Shells

While Chapter 2 work showed that $Ag_{25}(SR)_{18}^-$ clusters can be successfully activated with minimal sintering at low temperatures, some catalytic applications may require higher temperatures and thus improved control of sintering is desired. Besides strong metal-support interactions, sintering due to particle migration and agglomeration can be minimized by building confinement around the metal clusters. Our group has previously reported silica encapsulation of carboxylic acid-terminated thiolate-protected $Au_{25}(SR)_{18}^-$ clusters.[1] Improved sinter resistance of Au clusters was seen upon silica encapsulation, albeit with the introduction of minor mass transfer issues upon introduction of the silica shell. Such silica encapsulation strategies have yet to be extended to the $Ag_{25}(SR)_{18}^-$ system. With the recent successful development of carboxylic acid terminated thiolate-protected Ag_{25} clusters,[2] metal oxide (e.g. silica) shells can be built around $Ag_{25}(MHA)_{18}$ (where MHA is 6-mercaptohexanoic acid) clusters using similar sol-gel chemistry as reported for $Au_{25}(MUA)_{18}^-$ (where MUA is 11-mercaptoundecanoic acid) systems. Meanwhile, others have shown that the mass transfer limitation introduced by metal oxide shells can be overcome by using hollow shell encapsulation,[3-6] and a common strategy for designing hollow shells around clusters is to first have encapsulation with two shells of different materials, and then do selective etching of the inner shell.[6] With these strategies in mind, thermal stability of Ag_{25} clusters can possibly be enhanced via encapsulation in hollow silica shells that can protect the clusters yet still allow for significant mass transfer of substrates to the catalysts surface.

Firstly, carbon shell encapsulated Ag clusters can be made using a reported synthesis method in the literature with triblock copolymer $EO_{106}PO_{70}EO_{106}$ (F127, where EO is ethylene oxide and PO is propylene oxide) as a carbon precursor.[7-9] In a typical synthesis, aqueous F127 and the $Ag_{25}(MHA)_{18}$ clusters can be put in a sealed autoclave and kept at 100 ˚C for 1 h, after which the carbon shell encapsulated $Ag_{25}(MHA)_{18}$ clusters can be collected by centrifugation. This step can be followed by silica shell encapsulation using sol-gel polymerization of tetraethylorthosilicate (TEOS) in ammonia medium.[1] The inner shell thickness can be controlled by optimizing the concentration of F127, while the outer shell thickness can be tuned by changing the concentration of TEOS, ammonia, and reaction time.[1,10] The eventual Ag_{25}@carbon@SiO_2

sample could then be annealed at 500 ˚C under nitrogen atmosphere for selective calcination of the inner carbon shell. N_2-physisorption measurements could be performed to measure the porosity of the shell, while TEM and EXAFS measurements would give insight to the thermal stability of Ag_{25} clusters encapsulated in hollow silica shell.

7.2.2 Post-Synthesis Treatments of $Ag_{25}(SR)_{18}^-$ Clusters for Heterogeneous $Ag_{25-x}Pd_x$ Bimetallic Catalyst Design

The improved single-pot co-reduction synthesis protocol discussed in Chapter 4 predominantly formed atom-precise $Ag_{24}Pd_1(SR)_{18}^{2-}$ clusters, regardless of the varying ratios of constituent metals. Meanwhile doping the parent Ag_{25} clusters with more Pd atoms could improve the catalytic activity of the eventual $Ag_{25-x}Pd_x(SR)_{18}^{2-}$ bimetallic catalysts for hydrogenation reactions. Galvanic metal exchange is another promising strategy for incorporating foreign metals into parent clusters to form bimetallic systems with atom precision.[11] Using the metal exchange approach, carbon-supported $Ag_{25-x}Pd_x(SR)_{18}^{2-}$ bimetallic catalysts can be prepared as illustrated in Figure 7.1.

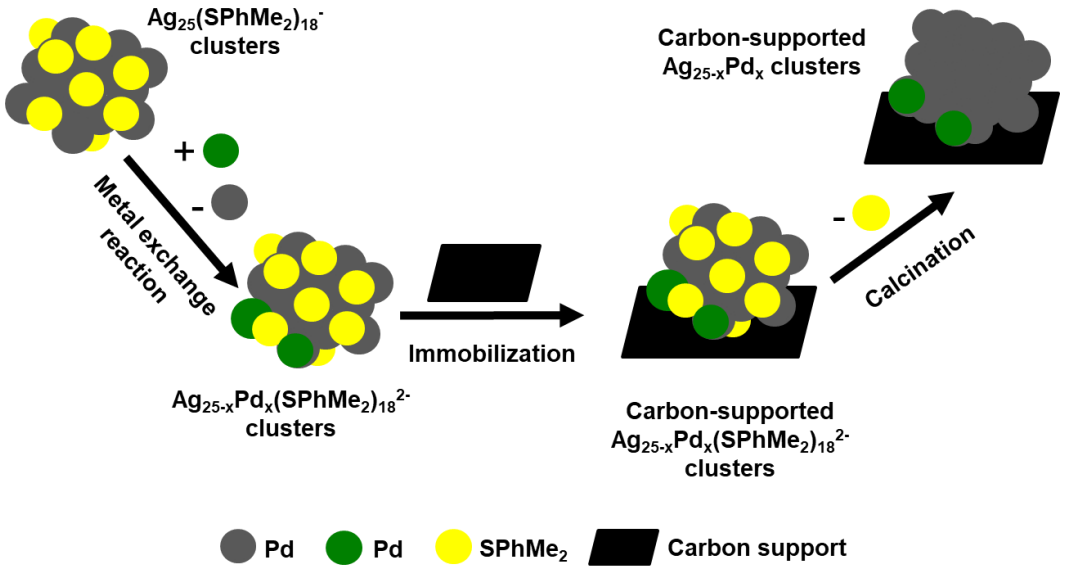

Figure 7.1. Illustration of preparation of heterogeneous $Ag_{25-x}Pd_x(SR)_{18}^{2-}$ bimetallic clusters by metal exchange of $Ag_{25}(SR)_{18}^-$ clusters with Pd salts.

As a proof of concept, $Ag_{25-x}Pd_x(SR)_{18}^{2-}$ bimetallic clusters were prepared with different loadings of Pd (using $Pd(OAc)_2$) through a series of metal exchange (ME) reactions. For brevity, the ME-Ag_xPd_y description is used where x and y represent the synthetic ratio of parent $Ag_{25}(SR)_{18}^-$ clusters and Pd ions, respectively. The exact stoichiometric formula of the products could potentially be confirmed with MS measurements. Carbon-supported bimetallic clusters were characterized by XAS measurements and results are presented in Figure 7.2. The Ag L_3-edge XAS results suggest the presence of trace of Ag^+ species as byproducts of the metal exchange reaction. The Pd L_3-edge XANES spectra show that the ME-Ag_xPd_y/carbon samples exhibit a reduction in white line intensity compared to the $Pd(OAc)_2$ precursor, especially for samples with low loading of Pd, which suggests partial reduction of Pd^{2+} ions by the parent $Ag_{25}(SR)_{18}^-$ clusters. Finally, the S K-edge XAS data show that the characteristic peak of S-M interactions (where M is Ag or Pd) around 2471 eV is more intense and slightly blue-shifted in ME-Ag_xPd_y/carbon samples than in the homonuclear Ag/carbon sample which suggests that Pd exchanges Ag in the surface or staple positions of the clusters.

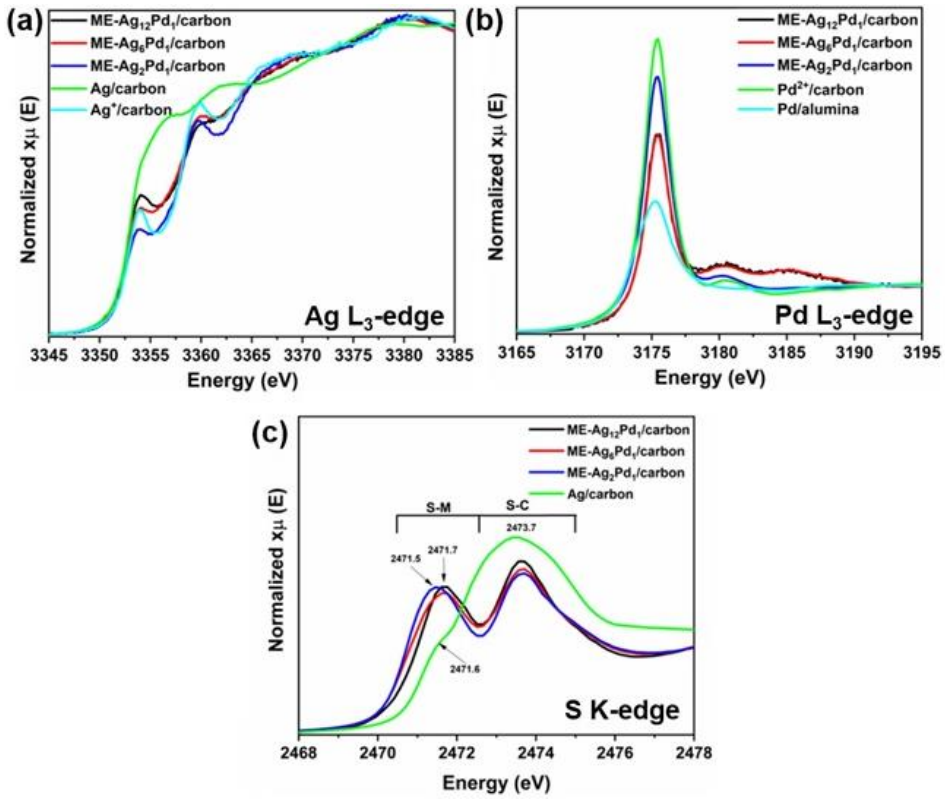

Figure 7.2. XANES spectra of (a) Ag L_3-edge (b) Pd L_3-edge, and (c) S K-edge measurements for ME-Ag_xPd_y/carbon samples.

Besides ascertaining the exact formula for each bimetallic system in the future, the study can be extended by conducting multielement and multiedge XAS measurements for activated samples (i.e. samples after calcination). The activation of Ag clusters has been successful at relatively low temperatures, but bimetallic AgPd systems in this thesis did not show complete Pd-thiolate removal until much higher temperatures. The use of higher temperatures to activate bimetallic clusters can be challenging due to thermal-induced sintering, and possible phase separation of the bimetallic systems. This problem can potentially limit their use as catalysts for high temperature reactions. Alternatively, alumina supports can also be examined as our group is aware of significant support effects on the activation process, and that sintering is reduced on alumina supports compared to activated carbon supports.[12,13] Moreover, robust and sintering resistant catalysts can be achieved with zirconia-modified alumina support as described elsewhere.[14] Accordingly, the partial coverage of metal cluster surfaces by zirconia can restrain cluster growth and improve the metal-support interactions during high temperature reactions.

7.2.3 *In situ* Pair Distribution Function Analysis of Atom-Precise, Thiolate-Protected Bimetallic Cluster Catalysts

Results discussed in Chapter 6 demonstrate the suitability of dPDF measurements in revealing the structural changes in atom-precise monometallic clusters under thermal activation. A follow up work in progress is to employ this concept to examine the structural changes of atom-precise bimetallic clusters upon calcination. Bimetallic $Pd_1M_{24}(SR)_{18}^{2-}$ (M = Au, Ag) clusters were prepared using direct synthesis methods reported in Chapter 4 and elsewhere,[15] for Ag and Au systems, respectively. The composition, purity, and monodispersity of the bimetallic clusters systems can be confirmed by UV-Vis absorption and MS measurements. The purified bimetallic clusters can be immobilized onto alumina supports and characterized by XPS and XAS methods to give insight into the structure of these as-prepared, supported bimetallic clusters catalysts. The alumina supported bimetallic clusters samples can be subjected to *in situ* heating while collecting total scattering measurements at the Brockhouse beamline at the CLS. Chapter 6 work showed that alumina support is structurally stable within a wide temperature range (25 - 650 °C), and thus dPDF will reveal structural changes of the bimetallic clusters only. Given that the alumina support can scatter significantly, samples with 5-10% wt. metal loading would be more ideal for such dPDF measurements. The outcome of the dPDF analysis can be compared with respective

monometallic analogues to show the influence a single Pd dopant atom on the structural stability of Pd_1M_{24} bimetallic system. The proposed research work is important in terms of developing sinter-resistant bimetallic clusters for heterogeneous catalysis, which are ideal model catalysts for many selective oxidation and hydrogenation reactions in the petrochemical industry.

7.3. References

1. V. Sudheeshkumar, A. Shivhare, R.W.J. Scott. Synthesis of Sinter-Resistant Au@silica Catalysts Derived from Au_{25} Clusters, *Catal. Sci. Technol.* 2017, **7**, 272-280.

2. K. Zheng, X. Yuan, J. Xie. Effect of Ligand Structure on the Size Control of Mono- and Bi-Thiolate-Protected Silver Nanoclusters, *Chem. Commun*. 2017, **53**, 9697-9700.

3. S. Wang, M. Zhang, W. Zhang. Yolk-Shell Catalyst of Single Au Nanoparticle Encapsulated within Hollow Mesoporous Silica Microspheres, *ACS Catal*. 2011, **1**, 207-211.

4. Z.A. Qiao, P. Zhang, S.H. Chai, M. Chi, G.M. Veith, N.C. Gallego, M. Kidder, S. Dai. Lab-in-a-Shell: Encapsulating Metal Clusters for Size Sieving Catalysis, *J. Am. Chem. Soc.* 2014, **136**, 11260-11263.

5. J. Liu, S.Z. Qiao, J.S. Chen, X.W.D. Lou, X. Xing, G.Q.M. Lu. Yolk/Shell Nanoparticles: New Platforms for Nanoreactors, Drug Delivery and Lithium-Ion Batteries, *Chem. Commun.* 2011, **47**, 12578-12591.

6. P.M. Arnal, M. Comotti, F. Schüth. High-Temperature-Stable Catalysts by Hollow Sphere Encapsulation, *Angew. Chem. Int. Ed.* 2006, **45**, 8224-8227.

7. X. Sun, Y. Li. Colloidal Carbon Spheres and Their Core/Shell Structures with Noble-Metal Nanoparticles, *Angew. Chem. Int. Ed.* 2004, **43**, 597-601.

8. M.M. Titirici, M. Antonietti, A. Thomas. A Generalized Synthesis of Metal Oxide Hollow Spheres Using a Hydrothermal Approach, *Chem. Mater*. 2006, **18**, 3808-3812.

9. J. Liu, S.B. Hartono, Y.G. Jin, Z. Li, G.Q. Lu, S.Z. Qiao. A Facile Vesicle Template Route to Multi-Shelled Mesoporous Silica Hollow Nanospheres, *J. Mater. Chem.* 2010, **20**, 4595-4601.

10. Y. Kobayashi, H. Inose, T. Nakagawa, K. Gonda, M. Takeda, N. Ohuchi, A. Kasuya. Control of Shell Thickness in Silica-Coating of Au Nanoparticles and their X-ray Imaging Properties, *J. Colloid. Interf. Sci.* 2011, **358**, 329-333.

11. M. Kim, K.L.D.M. Weerawardene, W. Choi, S.M. Han, J. Paik, Y. Kim, M-G. Choi, C.M. Aikens, D. Lee. Insights into the Metal-Exchange Synthesis of $MAg_{24}(SR)_{18}$ (M = Ni, Pd, Pt) Nanoclusters, *Chem. Mater.* 2020, **32**, 10216-10226.

12. A. Shivhare, D.M. Chevrier, R.W. Purves, R.W.J. Scott. Following the Thermal Activation of $Au_{25}(SR)_{18}$ Clusters for Catalysis by X-ray Absorption Spectroscopy, *J. Phys. Chem. C* 2013, **117**, 20007-20016.

13. A. Shivhare, R.W.J. Scott. Following the Thermal and Chemical Activation of Supported Au Clusters Using X-Ray Absorption Spectroscopy, *RSC Adv.* 2016, **6**, 62579-62584.

14. Q. Liu, F. Gu, Z. Zhong, G. Xu, F. Su. Anti-Sintering ZrO_2-Modified Ni/α-Al_2O_3 Catalyst for CO Methanation, *RSC Adv.* 2016, **6**, 20979-20986.

15. Y. Negishi, W. Kurashige, Y. Niihori, T. Iwasa, K. Nobusada. Isolation, Structure, and Stability of a Dodecanethiolate-Protected Pd_1Au_{24} Cluster, *Phys. Chem. Chem. Phys.* 2010, **12**, 6219-6225